OPTIMUM DESIGN OF STRUCTURES AND MATERIALS IN ENGINEERING XII

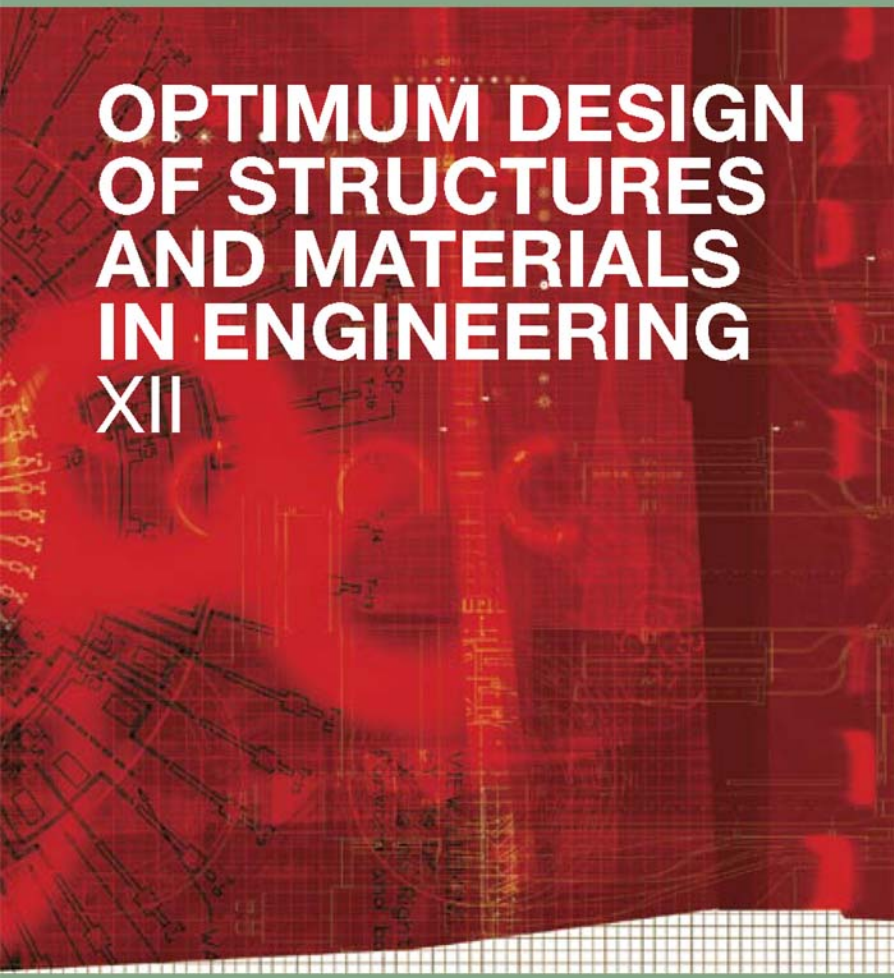

WIT PRESS

Editors
W.P. De Wilde,
C A Brebbia &
S. Hernandez

Computer Aided Optimum Design in Engineering XII

WIT PRESS

WIT Press publishes leading books in Science and Technology.
Visit our website for new and current list of titles.
www.witpress.com

WIT eLibrary

Home of the Transactions of the Wessex Institute.
Papers presented at OPTI 2012 are archived in the WIT eLibrary in
volume 125 of WIT Transactions on The Built Environment (ISSN 1743-3509).
The WIT eLibrary provides the international scientific community with immediate and
permanent access to individual papers presented at WIT conferences.
Visit the WIT eLibrary at www.witpress.com.

TWELFTH INTERNATIONAL CONFERENCE ON OPTIMUM DESIGN OF STRUCTURES AND MATERIALS IN ENGINEERING

OPTI XII

CONFERENCE CHAIRMEN

S. Hernández
University of A Coruña, Spain

C.A. Brebbia
Wessex Institute of Technology, UK

W.P. de Wilde
Vrije Universiteit Brussel, Belgium

INTERNATIONAL SCIENTIFIC ADVISORY COMMITTEE

B. Alzahabi
R. Derksen
E. Kita
S. Kravanja
F. Navarrina
K. Shea
L. Simoes
K. Yamazaki

Organised by
Wessex Institute of Technology, UK
University of A Coruña, Spain
Vrije Universiteit Brussel, Belgium

Sponsored by
WIT Transactions on the Built Environment
International Journal of Computational Experiments and Measurements

WIT Transactions

Transactions Editor

Carlos Brebbia
Wessex Institute of Technology
Ashurst Lodge, Ashurst
Southampton SO40 7AA, UK

Editorial Board

Computer Aided Optimum Design in Engineering XII

EDITORS

S. Hernández
University of A Coruña, Spain

C.A. Brebbia
Wessex Institute of Technology, UK

W.P. de Wilde
Vrije Universiteit Brussel, Belgium

WITPRESS Southampton, Boston

Editors:

S. Hernández
University of A Coruña, Spain

C.A. Brebbia
Wessex Institute of Technology, UK

W.P. de Wilde
Vrije Universiteit Brussel, Belgium

Published by

WIT Press
Ashurst Lodge, Ashurst, Southampton, SO40 7AA, UK
Tel: 44 (0) 238 029 3223; Fax: 44 (0) 238 029 2853
E-Mail: witpress@witpress.com
http://www.witpress.com

For USA, Canada and Mexico

Computational Mechanics Inc
25 Bridge Street, Billerica, MA 01821, USA
Tel: 978 667 5841; Fax: 978 667 7582
E-Mail: info@compmech.com
http://www.witpress.com

British Library Cataloguing-in-Publication Data

A Catalogue record for this book is available
from the British Library

ISBN: 978-1-84564-598-4
eISBN: 978-1-84564-599-1
ISSN: 1746-4498 (print)
ISSN: 1743-3509 (on-line)

The texts of the papers in this volume were set individually by the authors or under their supervision. Only minor corrections to the text may have been carried out by the publisher.

Printed in Great Britain by Lightning Source, UK.

Preface

OPTI 2012, the twelfth edition in the series of international conferences devoted to Optimum Design of Structures and Materials was held in the New Forest in UK, during 20-22 June 2012, organized by the University of Coruña (Spain), the Wessex Institute of Technology (UK) and the Vrije Universiteit of Brussels (Belgium).

The OPTI conferences started in Southampton, UK,(1989) followed by Boston, USA (1991); Zaragoza, Spain (1993); Miami, USA (1995); Rome, Italy (1997); Orlando, USA (1999); Bologna, Italy (2001); Detroit, USA (2003); Skiathos, Greece (2005); Myrtle Beach, USA (2007) and the Algarve, Portugal (2009).

The main objective of these events were to provide a friendly and useful forum for networking amongst researchers, engineers from the industry and professors from the academia involved in optimization and therefore allowing them to discuss ideas and practical and theoretical approaches in design optimization and also helping them to be aware about the advances in this scientific discipline.

Currently, optimization techniques have much to offer to those involved in design in almost any engineering field because the formulation of optimum design has improved dramatically since it was mostly an academic concept unable to produce solutions for real industrial problems. The enhancement of numerical methods, the development of new optimization algorithms, the appearance of powerful commercial computer codes with easy to use graphical interfaces and the revolution in computer architecture has made possible for optimization methodologies to be an essential factor in engineering design.

This book contains most of the papers presented at OPTI 2012. The conference attracted contributions describing case studies in engineering fields as electrical transmission towers, masonry constructions, thin walled structures, short cobels, cable and arch structures, bridges and aircraft structures. The scope of approaches range from size to shape or topology optimization and several strategies such as meta-models, bionic procedures, isogeometric formulations, reliability methods and optimization under uncertainties can be found out in the book.

The Editors would like to express their gratitude to all authors for their contributions. They are also grateful to the members of the International Scientific Advisory Committee (ISAC) who reviewed the manuscripts efficiently and timely and hence ensuring their technical quality.

The Editors
June 2012

Contents

Section 1: Structural optimization

Section 2: Shape and topology optimization

Section 3: Optimization in civil engineering

Section 4: Aerospace structures

Section 5: Evolutionary methods in design optimization

This page intentionally left blank

Section 1
Structural optimization

This page intentionally left blank

Limit spans of cable and arch structures

P. Latteur[1] & W. P. De Wilde[2]
[1]*Tractebel Engineering, Belgium*
[2]*Vrije Universiteit Brussel (VUB), Belgium*

Abstract

The limit span is reached when a structure cannot bear any other load than its self-weight, while the maximum resistance of the material or an excessive deflection is reached. Former publications have shown that the indicators of volume W and of displacement Δ are dimensionless numbers which allow optimizing efficiently the strength and self-weight or the stiffness of structures. In this context, this survey establishes the analytical expressions of limit spans of cables and arches.
Keywords: limit span, maximum span, ultimate span, self-weight, deflections, limit, buckling, volume, morphological indicators, indicator of volume, indicator of displacement.

1 Introduction

During the last decades, structures with ever increasing spans have been designed: e.g. the Viaduct of Millau (France), a technological and scientific masterwork, is a perfect illustration of this statement.

It is thus perfectly legitimate to ask oneself: "what are the theoretical limits of structural spans?", and also "what are the factors influencing this limit?"

The latter question is not trivial as the answer depends on the typology of the structure: a beam is subject to bending, an arch to compression, a cable only works in traction and one finds both compression and traction in trusses.

Considering the specifications of the Eurocodes, defining performances of a structure from both points of view of *strength* (ultimate limit state, in short ULS) and *stiffness* (serviceability limit state or SLS), and taking into account local instability phenomena (buckling), one can distinguish between:

WIT Transactions on The Built Environment, Vol 125, © 2012 WIT Press
www.witpress.com, ISSN 1743-3509 (on-line)
doi:10.2495/OP120011

- *strength limit span*, reached when the material strength is exceeded under the self-weight of the structure;
- *stiffness limit span*, reached when the maximum deflection, under self-weight, is exceeded, or when instability phenomena occur.

By material strength one has to think in terms of yield stress (e.g. for steel) or ultimate strength: one is then thinking of an "*ultimate limit span*". The considered strength will be noted as σ. In order to establish the subsequent diagrams, one considered:

- for VHS steel: σ = 1000 Mpa; (VHS: very high yield strength steel)
- for HS steel: σ = 300 Mpa; (HS: high yield strength steel)
- for mild steel: σ = 140 Mpa;
- for aluminium: σ = 55 Mpa;
- for timber: σ = 10 Mpa;
- for reinforced (RC) or prestressed concrete (PC): σ = 15 Mpa.

Generalizing the concept of limit span, one could define it as the *maximum span* a structure can withstand, sustaining its self-weight, plus a given load F.

To establish those limit spans the authors make use of the theory of so-called "morphological indicators", developed in the context of arches in [1–3].

A *morphological indicator* is a number which has three characteristics:

- it is a dimensionless number
- it is the image of a physical value (volume of material, stiffness of a structure…)
- its value depends on the overall geometry of the structure (e.g. through the (geometrical) *slenderness* of the structure, being the ratio L/H between the dimensions of the smallest window in which the structure can be included, L/H>1, or on the geometry of the transverse sections of the structural components through what one calls *form factors*.

As either volume indicator W or displacement indicator Δ allow to find structures of minimum volume, resp. maximal stiffness (= with minimal deflection), it should be logical to consider their use in the determination of limit spans of different structural typologies.

This study is considering the problem for both iso- and hyperstatic arches and cables, necessitating an essentially different approach, as cables are only subject to traction, whereas arches are subject to compression and possible instability phenomena have thus to be taken into account.

The volume indicator W can be expressed as:

$$W \overset{\Delta}{=} \frac{\sigma V}{FL} = function\left(\frac{L}{H}, \Psi\right) \quad \text{with} \quad \Psi \overset{\Delta}{=} \frac{\mu \sigma L}{\sqrt{qEF}}$$

in which expression Ψ is the buckling indicator, introduced by Latteur [3] carrying the information about the impact of possible buckling phenomena on the total volume of the structure. The value σ is the limit strength of the material

and is depending on both the type of material and the type of calculation, be it elastic or nonlinear.

Finally, it is useful to remind the three morphological indicators which were named "*form factors*" and characterising the geometry of the transverse sections of the elements. Those dimensionless numbers are defined by:

$$q = \frac{I}{\Omega^2} \qquad Z = \frac{\Omega h^2}{16I} \qquad s = \frac{\Omega}{h^2}$$

Figures 1–3 show the values of these form factors for eg. tubular sections.

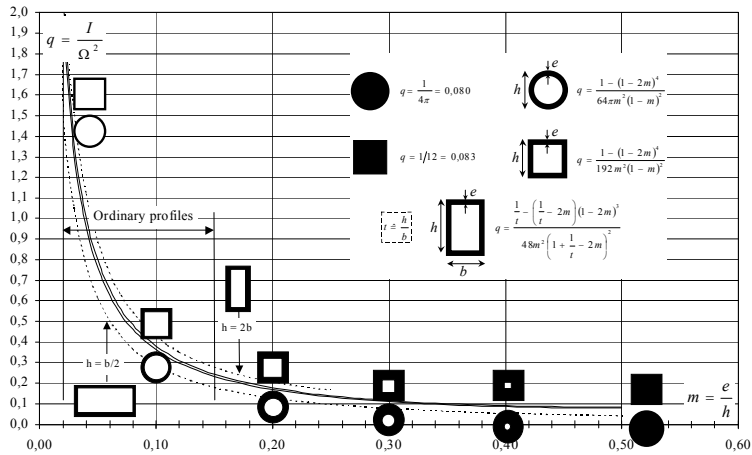

Figure 1: Graph of $q = I/\Omega^2$.

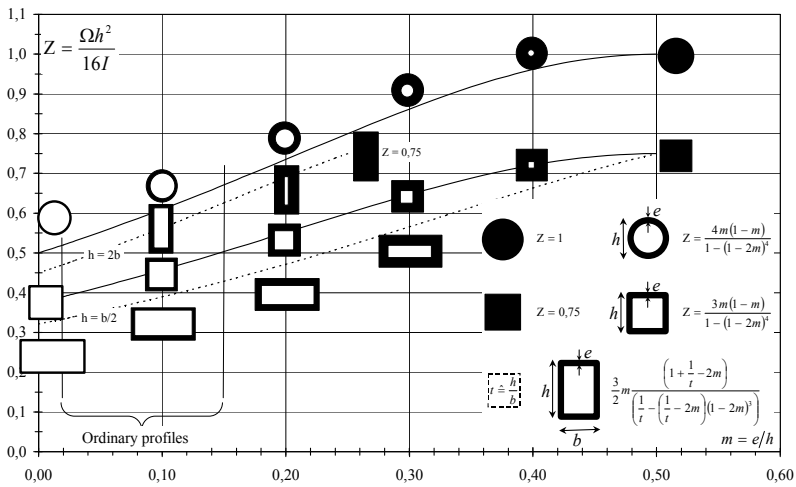

Figure 2: Graph of $Z = \Omega h^2/16I$.

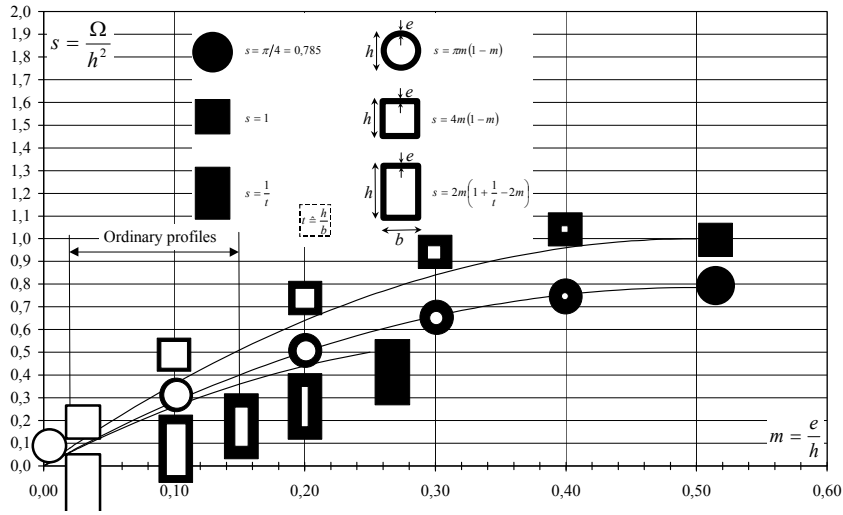

Figure 3: Graph of $s = \Omega/h^2$.

2 Limit span of cables

A large span cable, when subject to its own weight takes the form of a catenary curve. On the other hand, a cable in a suspension bridge can, if the self-weight of the cable is not dominant, be assimilated with a parabolic curve.

In this context one can establish a first calculation of limit spans on the basis of parabolic curves, but a second calculation should also be achieved on the basis of a catenary form, in order to compare and assess the results.

2.1 Hypothesis 1: the cable can be assimilated with a parabola

As a cable structure can only support traction, its volume indicator W can be found by taking W for an arch with constant section, loaded in pure compression, neglecting buckling for the latter [2, §4.1, end of page]:

$W = \dfrac{\sigma V}{FL} = W^{(L/H)}$, in which:

$$W^{(L/H)} = \frac{1}{16}\frac{L}{H}\sqrt{1+16\left(\frac{H}{L}\right)^2}\left(\sqrt{1+16\left(\frac{H}{L}\right)^2}+\frac{L}{4H}\ln\left(\frac{4H}{L}+\sqrt{1+16\left(\frac{H}{L}\right)^2}\right)\right)$$

W depends only on the value of the slenderness L/H en reaches a minimum for L/H = 2,926. Self-weight is ρV and assumed to be uniformly distributed, which yields:

$$\frac{\sigma V}{(F+\rho V)L} = W^{(L/H)}$$

If one now defines ε = F/(ρV) being the ratio between the resultant of externally applied loads F and the self-weight:

$$\frac{\sigma}{(1+\varepsilon)\rho L} = W$$

which yields a value for the limit span when ε → 0:

$$\boxed{L_{\max} = \frac{1}{(1+\varepsilon)}\left(\frac{\sigma}{\rho}\right)\frac{1}{W}}$$

and thus:

$$L_{\lim} = \frac{\sigma}{\rho}\frac{1}{W}$$

Fig. 4 shows the limit values for the previously defined materials. These can be corrected in function of the value taken by $\varepsilon = F/(\rho V)$:

$$\left(\frac{1}{1+\varepsilon}\right) = 0{,}91 \quad for \quad \varepsilon = 10\%$$
$$= 0{,}83 \quad for \quad \varepsilon = 20\%$$
$$= 0{,}67 \quad for \quad \varepsilon = 50\%$$
$$= 0{,}50 \quad for \quad \varepsilon = 100\%$$
$$= 0{,}33 \quad for \quad \varepsilon = 200\%$$
$$= 0{,}17 \quad for \quad \varepsilon = 500\%$$
$$= 0{,}09 \quad for \quad \varepsilon = 1000\%$$

One can also rewrite the above expression, thus finding the value of ε for a given span:

$$\varepsilon = \left(\frac{\sigma}{\rho}\right)\frac{1}{LW} - 1$$

For any material, the maximum span L_{lim} of a cable is found for L/H=2,926:

- for VHS steel (σ = 1000 Mpa, ρ = 77 kN/m^3) : L_{lim} = 16707 m;
- for HS steel (σ = 300 Mpa, ρ = 77 kN/m^3) : L_{lim} = 5012 m;
- for mild steel (σ = 140 Mpa, ρ = 77 kN/m^3) : L_{lim} = 2339 m;
- for aluminium (σ = 55 Mpa, ρ = 27 kN/m^3) : L_{lim} = 2622 m;

Those spans decrease dramatically for larger or lower values of L/H.

Remark: one of the longest span of a cable car today is that of Trockener Steg, Switzerland and has a span of 2900 m for a value L/H=9.

Fig. 4 shows that for L/H=9 and the selected materials, the limit span is 10000m. However, applying the stress reduction factor of 3 (uncertainties about loads, fatigue, material uncertainties…) one finds a limit span of 3333 m, which proves that the design engineers produced a nearly optimal design. Let us also draw the attention on the fact that nowadays limit stress values are increased to approx. 2000 MPa.

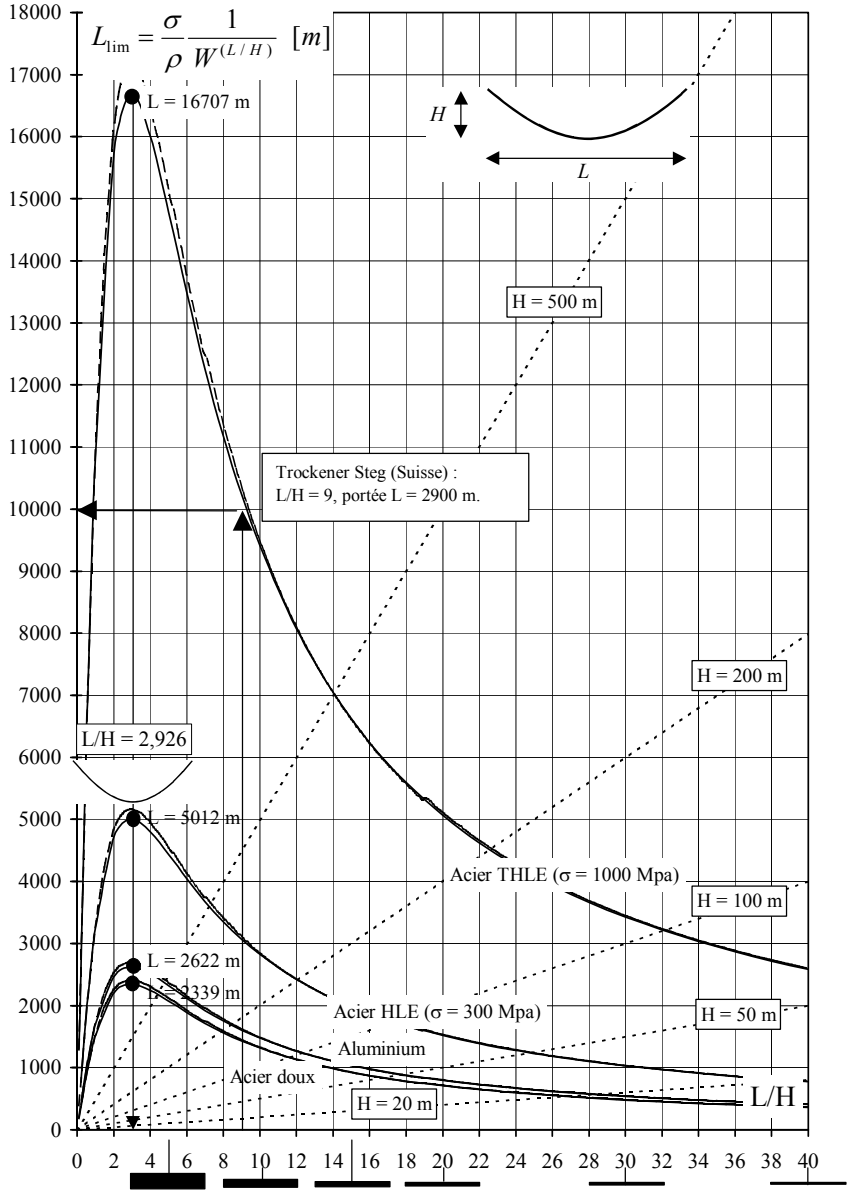

Figure 4: Limit span of cables; continuous lines: hypothesis "parabolic cable" and in long dotted lines: hypothesis "catenary cable". (acier doux = mild steel; portée = span; Acier THLE= VHS steel; Acier HLE = HS steel).

2.2 Catenary cable form

A cable which is only subject to its self-weight takes the form of a catenary. If R is representing the thrust force (horizontal component of the reaction at the abutments), one can write following equations:

$$\textit{Total length of the cable: } L_0\textit{:}\quad L_0=\frac{2R}{mg}\,SinHyp\left(\frac{mgL}{2R}\right) \tag{1}$$

$$\textit{Deflection of the cable y:}\quad y(x)=\frac{R}{\rho\Omega}\left(CosHyp\left(\frac{\rho\Omega L}{2R}\right)-CosHyp\left[\frac{\rho\Omega}{R}\left(\frac{L}{2}-x\right)\right]\right) \tag{2}$$

$$\textit{Normal force in the cable:}\quad N(x)=R.CosHyp\left[\frac{\rho\Omega}{R}\left(\frac{L}{2}-x\right)\right] \tag{3}$$

$$\textit{Local coordinate on the cable:}\quad s(x)=\frac{R}{\rho\Omega}\left(\frac{\rho\Omega L_0}{2RH}-SinHyp\left[\frac{\rho\Omega}{R}\left(\frac{L}{2}-x\right)\right]\right) \tag{4}$$

If Ω is the (constant) cable section, the limit span is reached when

$$N\left(x=0\right)=\sigma\Omega \tag{5}$$

Equation (2) transforms into:

$$\frac{H}{L}=\beta_1\left(CosHyp\left(\frac{1}{2\beta_1}\right)-1\right),$$

in which $\beta_1=\dfrac{R}{\rho\Omega L}$ is a solution of the implicit equation. Eqn (3) then becomes:

$$\beta_2=CosHyp\left[\frac{1}{2\beta_1}\right],$$

with $\beta_2=\dfrac{N(x=0)}{R}$ as a solution of this equation.

If one notes that $\beta_1\beta_2=\dfrac{N\left(x=0\right)}{\rho\Omega L}$, condition eqn (5) transforms into:

$$L_{\lim}=\frac{\sigma}{\rho}\frac{1}{\beta_1\beta_2}\qquad\text{and}\qquad \boxed{L_{\max}=\frac{1}{\left(1+\varepsilon\right)}\left(\frac{\sigma}{\rho}\right)\frac{1}{\beta_1\beta_2}}$$

This relation defines the curves in long dotted lines in fig. 4: they undoubtedly prove that the approximation of the deflection by a parabola is both safe and very acceptable.

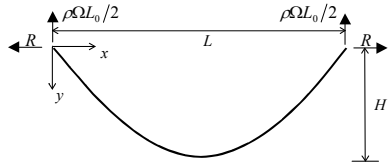

Figure 5: Catenary cable form.

3 Limit spans of arches

Fig 6 shows the ratio between l_{arc}, the length of the arch, and its span L, which one can call g(L/H) and which only depends on the slenderness L/H.

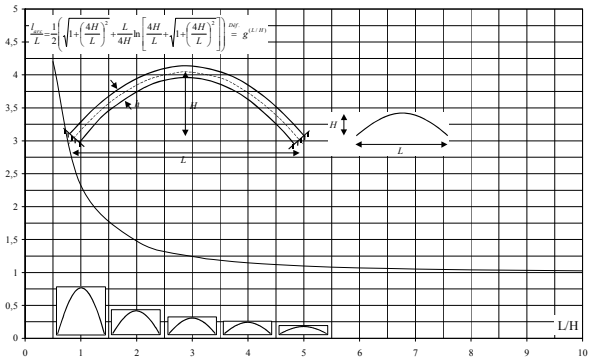

Figure 6: $l_{arc}/L = g^{(L/H)}$ is shown as a function of the slenderness.

The limit span is studied from the point of view of strength. Indeed, one shows that the deformation of a uniformly loaded arch is very small, and that strength determines the limit span.

Let one consider parabolic arches with constant section; its volume indicator is [2, eqn (4)]:

$$W = \frac{\sigma V}{F_{tot} L} = \Psi . W^{(C)}$$

with $W^{(C)}$ the volume indicator for the elements in compression:

$$W^{(C)} \overset{\Delta}{=} \frac{1}{2\sqrt{\gamma}} \left(\sqrt{1+\left(\frac{4H}{L}\right)^2} + \frac{L}{4H} \ln \left[\frac{4H}{L} + \sqrt{1+\left(\frac{4H}{L}\right)^2} \right] \right) = Function(L/H)$$

where parameter γ takes the type of arch into account and is only dependent on the L/H ratio:

$$F = \gamma \frac{EI}{L^2}$$

As the buckling indicator $\Psi = \sigma L / \sqrt{qEF_{tot}}$ and the total load (self-weight incl.) $F_{tot} = F + \rho V$, the above expression becomes:

$$\frac{\sigma V}{(F + \rho V)L} = \frac{\sigma L}{\sqrt{qE(F + \rho V)}} . W^{(C)}$$

As the total load F is a fraction F = ε(ρV) of the total self-weight:

$$\frac{1}{(1 + \varepsilon)\rho L} = \frac{L}{\sqrt{qE(1 + \varepsilon)\rho V}} . W^{(C)}$$

which can be rewritten:

$$L^2 = \sqrt{\frac{E}{\rho}} \sqrt{\frac{1}{(1 + \varepsilon)}} \frac{1}{W^{(C)}} \sqrt{qV} \tag{6}$$

Fig. 6 shows that the total volume V of the arch with constant section Ω:

$$V = \Omega l_{arc} = \Omega L g^{(L/H)}$$

And as $qZ = h^2 / 16\Omega$, eqn (6) is now:

$$L^4 = \frac{E}{\rho} \frac{1}{(1 + \varepsilon)} \frac{1}{\left(W^{(C)}\right)^2} \frac{h^2}{16Z} L\, g^{(L/H)}$$

One finally gets:

$$\boxed{L_{\max} = \sqrt[3]{\frac{E}{\rho} \frac{1}{(1 + \varepsilon)} \left[\frac{g^{(L/H)}}{16\left(W^{(C)}\right)^2} \right] \frac{1}{Z} h^2}} \tag{7}$$

The term between square brackets only depends on L/H. For L/H = 4, the value is:

- 2,425 for the three hinged arch;
- 6,038 for the clamped arch.

The limit span is found when the arch can only sustain its self-weight, i.e. when $\varepsilon \to 0$. For L/H=4, with the two above mentioned values:

$$L_{\lim} = 1{,}343 \sqrt[3]{\frac{E}{\rho} \frac{1}{Z} h^2} \qquad \text{for the 3 hinged arch;}$$

$$L_{\lim} = 1{,}821 \sqrt[3]{\frac{E}{\rho} \frac{1}{Z} h^2} \qquad \text{for the clamped arch.}$$

$$L_{\max,rés.} = \left(\sqrt[3]{\left(\frac{1}{1+\varepsilon}\right)}\right)(1{,}343 \text{ or } 1{,}821)\sqrt[3]{\left(\frac{E}{\rho}\right)\frac{1}{Z}\,h^2} \quad with \quad \sqrt[3]{\left(\frac{1}{1+\varepsilon}\right)} = 0{,}97 \quad for \quad \varepsilon = 10\%$$

$$= 0{,}94 \quad for \quad \varepsilon = 20\%$$

$$= 0{,}87 \quad for \quad \varepsilon = 50\%$$

$$= 0{,}79 \quad for \quad \varepsilon = 100\%$$

$$= 0{,}69 \quad for \quad \varepsilon = 200\%$$

$$= 0{,}55 \quad for \quad \varepsilon = 500\%$$

$$= 0{,}45 \quad for \quad \varepsilon = 1000\%$$

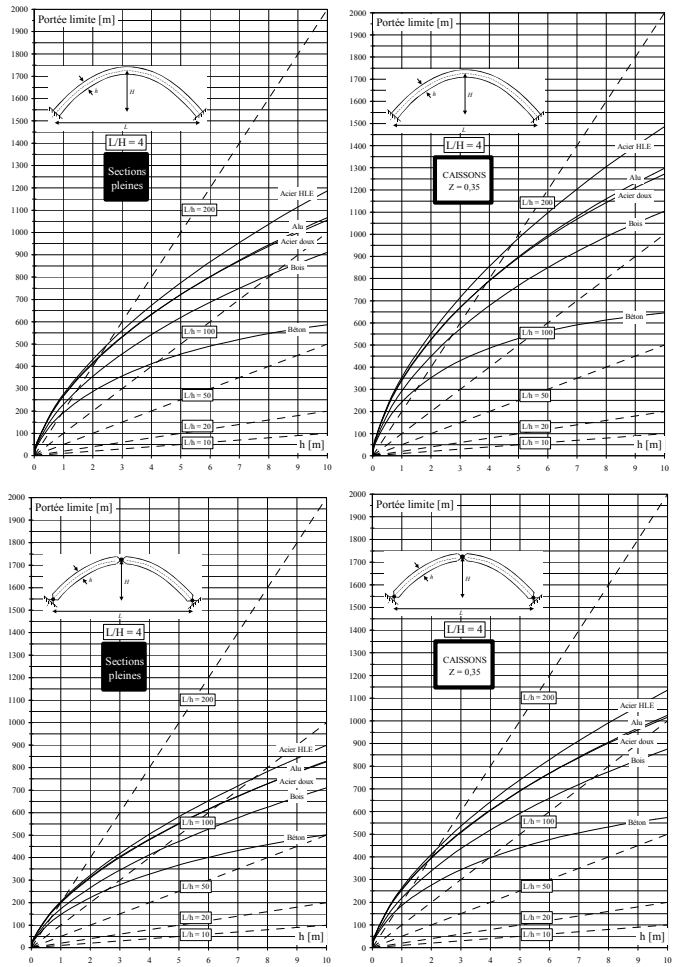

Figure 7: Limit spans of arches with slenderness L/H = 4, in function of h, height of the section (sections pleines = massive sections, caissons = boxes, béton = concrete, bois = timber, portée limite = limit span).

The values of E/ρ for frequently used materials are:

- for steel: $E/\rho = 2727.10^6$ [mm], (E= 210000 Mpa, ρ = 77 kN/m^3);
- for aluminium: $E/\rho = 2592.10^6$ [mm], (E = 70000 Mpa, ρ = 27 kN/m^3);
- for timber: $E/\rho = 1670.10^6$ [mm], (E = 10000 Mpa, ρ = 6 kN/m^3);
- for reinforced or prestressed concrete: E/ρ = 600.10^6 till 1200.10^6 [mm], (E = 15000…30000 Mpa, ρ = 25 kN/m^3).

4 Conclusions

Morphological indicators are tools which are used by designers in the conceptual design stage. They allow for a suboptimal design of structures and give a preliminary indication of the mechanical possibilities of materials, in the context of structural typologies. The theory allowed to establish good approximations of the limit spans of cable (only traction) and arch (essentially compression and thus sensitive to buckling) structures.

An important conclusion concerns the approximation of the deflection curve of a cable structure by a parabola: this approximation has been shown to be safe and sufficient.

The authors have also applied this theory and established limit spans for beams and classical trusses. These are reported in [3] and could be included in a later paper.

Acknowledgement

The authors want to acknowledge continuous support of the Scientific Research Board of Vrije Universiteit Brussel in their research.

References

[1] Latteur P., Samyn Ph., "Optimization of Arches Subjected to Distributed Loads", Proceedings of the IASS International Congress on Shells and Spatial Structures, Vol. I, p. B.3.11-B.3.20, Madrid, Septembre 1999.

[2] Latteur P., Samyn Ph., De Wilde W. P., "Optimisation des arcs paraboliques et en chaînette - aide à la conception sur base d'indicateurs morphologiques", Revue Française de Génie Civil, vol. 5, n°1, 2001, Hermès, Paris.

[3] Latteur P., "Optimisation et prédimensionnement des treillis, arcs, poutres et câbles sur base d'indicateurs morphologiques – Application aux structures soumises en partie ou en totalité au flambement", Thèse de doctorat, Vrije Universiteit Brussel, Belgique, 2000.

Other useful references

- Latteur P., Samyn Ph., "Une méthode globale d'optimisation des treillis", actes du 2ième Congrès Universitaire de Génie Civil, p. 365-372, Poitiers, mai 1999.
- Latteur P., Samyn Ph., De Wilde W. P., "A Search For Efficient Trusses", Proceedings of the International Congress on Shells and Spatial Structures, p. 605-615, Istanbul, Mai 2000.
- Latteur P., Samyn Ph., De Wilde W. P., "Etude du poids et de la raideur des treillis Warren, Pratt et Howe", Revue Française de Génie Civil, vol. 4, n°4, 2000, Hermès, Paris.

Optimization of the underground gas storage in different rock environments

S. Kravanja & B. Žlender
University of Maribor, Faculty of Civil Engineering, Maribor, Slovenia

Abstract

This paper presents the cost optimization of underground gas storage (UGS), designed from lined rock caverns (LRC). The optimization is performed by the non-linear programming (NLP) approach in different rock environments. For this purpose, the NLP optimization model OPTUGS was developed. The model comprises the cost objective function, which is subjected to geomechanical and design constraints. The optimization proposed is to be performed for the phase of the conceptual design. A numerical example at the end of the paper demonstrates the efficiency of the introduced optimization approach.
Keywords: underground gas storage, UGS, lined rock cavern, LRC, rock mass rating, RMR, optimization, non-linear programming, NLP.

1 Introduction

This paper deals with the optimization of the investment and operational costs of the underground gas storage (UGS), designed from lined rock caverns (LRC) [1–3]. The optimization is performed by the non-linear programming (NLP) approach. For this purpose, the NLP optimization model is developed. Since the optimization is proposed to be performed for the phase of the conceptual design, only some basic conditions are defined in the optimization model in order to assure enough strength safety of the rock mass and impermeability of the cavern wall and steel lining. The latter is achieved by the limitation of steel lining and concrete wall stains.

Since there exist various rock masses with enough strength to support the UGS, the optimization of the UGS is proposed to be calculated in different rock environments. For this purpose, a rock mass classification – the so called rock mass rating (RMR) system is used.

WIT Transactions on The Built Environment, Vol 125, © 2012 WIT Press
www.witpress.com, ISSN 1743-3509 (on-line)
doi:10.2495/OP120021

The considered UGS is performed by the construction of one or more LRCs. The structure of the LRC is simple: its reservoir wall is designed from a concrete wall and a steel lining. Although the concrete wall is reinforced, it just transports the gas pressure from the cavern on the surrounding rock. The same holds with the steel lining, which only enables the impermeability (sealing) of the cavern.

The primary objectives of the proposed optimization of the investment and operational costs of the UGS are:

- Minimization of the investment and operational costs of the UGS system in different rock environments (RMR),
- Calculation of the optimal inner gas pressure, the cavern depth, the cavern inner diameter, thickness of the cavern concrete wall and the height of the cavern tube through the optimization for the treated RMR,
- Storing the highest possible quantity of gas under high pressure,
- Ensure the safety of the UGS at the time of construction and service.

In order to achieve the upper objectives, the geotechnical problem is proposed to be solved simultaneously. Geomechanical rock mass parameters are determined from geological conditions of a selected suitable UGS location and a special FE model is generated. Strength stability of the rock mass and safety of the system are then analyzed for various design parameters like the inner gas pressures, cavern depths, cavern diameters and the cavern wall thickness. As a result, geomechanical constraints are proposed to be approximated/defined and put into the optimization model.

2 Underground gas storage designed from LRC

The design of the considered LRC structure is typical, see Figure 1. The LRC consists from the cylindrical wall and the upper and lower spheres. The caverns are typically 50 to 100 m high and are located at depths from 100 to 300 m. Their concept involves relatively large diameters: between 10 and 50 m. The concrete wall is 2 or more meters thick, the thickness of the steel lining amounts from 12 to 15 mm.

It is expected that the gas pressure cyclically increases and decreases during periods of gas supply and discharge between the minimal (3 MPa) and maximal (calculated) value. The internal pressure therefore causes static and cyclic loads. The minimum lifetime of the LRC is limited to be higher than 500 cycles. Since caverns are constructed at the depths between 100 and 300 m, the hydrostatic pressure reaches 1 to 3 MPa. Drainage system is installed on the outer side of the cavern wall. It drainages the water and enables the monitoring, collection and removing of the gas in the case of gas leakage.

The system of tunnels is designed in order to transport material and allow the access for machinery during the construction of the underground chambers. The tunnels also provide a cost-effective mining of caverns. Cross-section of tunnels amounts about 25 m^2 in the flat areas and 40 m^2 in curved areas.

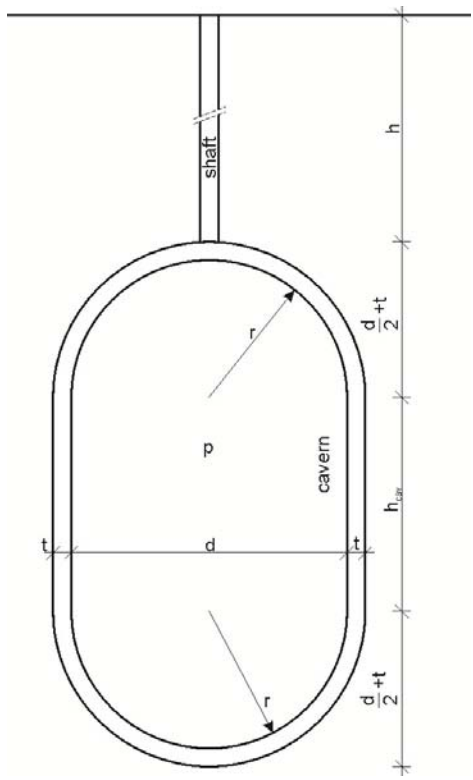

Figure 1: Vertical cross-section of the lined rock cavern (LRC).

The risks which occur during the construction are similar to ones at the construction of tunnels: large scale failure of the rock cover, large deformations of the cavern wall, irruption of the water and impact on water resources in the surrounding area. The risks which may occur during the operation are: failure of the rock mass, uplift of the rock cover, failure of the rock between two caverns, large deformation or destruction of the steel lining, unequally deformation of the LRC structure because of the rock heterogeneity and the draining system does not work. Since the risks during the operation are decisive, the risks during the construction are not considered explicitly in this paper.

The LRC concept should provide a safe and environmentally friendly mode for gas storage. Since the gas should never been in contact with the environment, the gas storage is designed as a closed system. The caverns and the entire gas network are impermeable.

3 Optimization model OPTUGS

The general optimization model OPTUGS was developed for the optimization of the underground gas storage. As the optimization problem of the UGS is non-

linear, the non-linear programming (NLP) optimization approach is used and described in the paper.

3.1 NLP problem formulation

The general NLP optimization problem can be formulated as follows:

$$\min \; z = f(\boldsymbol{x})$$

subjected to:

$$\boldsymbol{h}(\boldsymbol{x}) = \boldsymbol{0} \qquad \textbf{(NLP)}$$

$$\boldsymbol{g}(\boldsymbol{x}) \le \boldsymbol{0}$$

$$\boldsymbol{x} \in X = \{\, \boldsymbol{x} \mid \boldsymbol{x} \in R^n, \boldsymbol{x}^{Lo} \le \boldsymbol{x} \le \boldsymbol{x}^{Up} \,\}$$

where $\boldsymbol{x}$ is a vector of continuous variables, defined within the compact set X. Functions $f(\boldsymbol{x})$, $\boldsymbol{h}(\boldsymbol{x})$ and $\boldsymbol{g}(\boldsymbol{x})$ are nonlinear functions involved in the objective function z, equality and inequality constraints, respectively. All functions $f(\boldsymbol{x})$, $\boldsymbol{h}(\boldsymbol{x})$ and $\boldsymbol{g}(\boldsymbol{x})$ must be continuous and differentiable.

In the context of structural optimization, variables include dimensions, cross-section characteristics, strains, materials, stresses, economic parameters, etc. Equality and inequality constraints and the bounds of the variables represent a rigorous system of the design, loading, stress, resistance and deflections functions taken from structural analysis and the dimensioning.

3.2 NLP optimization model

According to the above NLP problem formulation, an NLP optimization model OPTUGS was developed. As an interface for mathematical modelling and data inputs/outputs GAMS (General Algebraic Modelling System), a high level language [4], was used. The proposed optimization model includes input data (constants), variables and cost objective function of the UGS system, subjected to defined geomechanical and design non-linear and linear constraints.

Input data represent design and economical data (constants) for the optimization. Coefficients involved in the objective function and geomechanical inequality constraints are also defined as input data.

The inner gas pressure p [MPa], the cavern depth h [m], the cavern inner diameter d [m], the cavern concrete wall thickness t [m] and height of the cavern tube h_{cav} [m] are in the optimization model OPTUGS declared as variables, see Figure 1.

3.2.1 Objective function

The objective function comprises the investment and operational costs of the UGS system *COSTS* [EUR], see eqn. (1).

$$COSTS = \left\{ \begin{array}{l} cos\,ts_{up} + cos\,ts_{under} \\ + C_{exc,tun} \cdot V^{sf}_{exc,tun} + C_{prot,tun} \cdot V^{sf}_{exc,tun} \\ + C_{exc,cav} \cdot V^{sf}_{exc,cav} \\ + C_{prot,cav} \cdot A^{sf}_{exc,cav} + C_{drain} \cdot A^{sf}_{exc,cav} \\ + C_{wall} \cdot \left(V^{sf}_{exc,cav} - V^{sf}_{cav}\right) + C_{reinf} \cdot \left(V^{sf}_{exc,cav} - V^{sf}_{cav}\right) \cdot \rho \cdot r_{perc} \\ + C_{steel} \cdot A^{sf}_{cav} \end{array} \right\} \cdot No_{cav} \quad (1)$$

The objective variable *COSTS* includes fixed costs (constant sum) and dimension dependence (variable) costs. The fixed costs amounts upper ground works $costs_{up}$ [EUR] and underground works $costs_{under}$ [EUR].

The dimension dependence costs are dependant on a depth of the tunnel excavation, structure and protection, on a geometry of the cavern excavation, protection and drainage system as well as on used quantities of the cavern concrete, the reinforcement and steel lining. In this way, the tunnel excavation and protection costs are determined by the term $C_{exc,tun} \cdot V^{sf}_{exc,tun} + C_{prot,tun} \cdot V^{sf}_{exc,tun}$, where $C_{exc,tun}$ [EUR/m^3] represents the price of the tunnel excavation, $C_{prot,tun}$ [EUR/m^3] is the price of the tunnel protection and $V^{sf}_{exc,tun}$ [m^3] denotes a volume of vertical and horizontal tunnel excavation. The cavern excavation costs $C_{exc,cav} \cdot V^{sf}_{exc,cav}$ are defined with the price of the cavern excavation $C_{exc,cav}$ [EUR/m^3] and the cavern excavation volume $V^{sf}_{exc,cav}$ [m^3].

In addition, the cavern protection and drainage system costs are expressed by the expression $C_{prot,cav} \cdot A^{sf}_{exc,cav} + C_{drain} \cdot A^{sf}_{exc,cav}$, where $C_{prot,cav}$ [EUR/m^2] represents the price of the cavern protection, C_{drain} [EUR/m^2] stands for the price of the cavern drainage and $A^{sf}_{exc,cav}$ [m^2] is the cavern excavation area. Costs of the concrete for walls are calculated by the expression $C_{wall} \cdot (V^{sf}_{exc,cav} - V^{sf}_{cav})$, where C_{wall} [EUR/m^3] represents the price of the cavern wall concrete, the term $(V^{sf}_{exc,cav} - V^{sf}_{cav})$ denotes the volume of used concrete, V^{sf}_{cav} stands for the inner volume of the cavern. Costs for the reinforcements are defined by the term $C_{reinf} \cdot (V^{sf}_{exc,cav} - V^{sf}_{cav}) \cdot \rho \cdot r_{perc}$, where C_{reinf} [EUR/t] is the price for the wall reinforcement, ρ [t/m^3] represents the unit mass of steel and r_{perc} [-] denotes the percentage of the reinforcement.

Finally, costs of steel lining are determined by the term $C_{steel} \cdot A^{sf}_{cav}$, where C_{steel} [EUR/m^2] represents the price of the steel lining and A^{sf}_{cav} the spread area of the steel lining (inner cavern area). No_{cav} stands for the number of constructed caverns in the UGS system.

3.2.2 Geomechanical constraints

Geomechanical inequality constraints enable the rock mass strength stability and safety. In this way, four conditions have to be defined in a form of four geomechanical inequality constraints:

- Condition 1: Strength of the rock mass is not exceeded, eqn. (2),
- Condition 2: Uplift of the rock cover is prevented, eqn. (3),
- Condition 3: Failure of the rock between two caverns is prevented, eqn. (4),

- Condition 4: Strains of the steel lining need to be limited under the acceptable value, eqn. (5).

Condition 1 is checked by eqn. (2), bay which the design gas pressure p [MPa] must not exceed the limit gas pressure p_{GSI}, calculated by Noren criterion [5]. While parameter *GSI* has to be evaluated for the each UGS system separately by the generalized Hoek-Brown failure criterion [6], parameter a is 0.004 and parameter b is 2.190.

$$p \le p_{GSI}^{sf} \tag{2}$$

where:

$$p_{GSI}^{sf} = a_{\mathrm{N}} \cdot GSI^{b_N} \tag{2.1}$$

Condition 2 is satisfied when the calculated safety factor against the rock cover uplift SF_{up} is greater than a defined minimal value $SF_{up,min}$, see Eq. (3). A typical value for $SF_{up,min}$ is taken 3.

$$SF_{up}^{sf} \ge SF_{up,min} \tag{3}$$

where SF_{up}^{sf} is a following substitution function:

$$SF_{up}^{sf} = SF_{up,0} \cdot c_1 \cdot \left(\frac{p}{p_0}\right)^{f_1} \cdot c_2 \cdot \left(\frac{h}{h_0}\right)^{f_2} \cdot c_3 \cdot \left(\frac{d}{d_0}\right)^{f_3} \tag{3.1}$$

When Condition 3 is considered, the calculated safety factor against the rock failure between two caverns SF_{horiz} must be greater than a defined minimal value $SF_{horiz,min}$, see Eq. (4). A typical value for $SF_{horiz,min}$ is 2.5.

$$SF_{horiz}^{sf} \ge SF_{horiz,min} \tag{4}$$

where SF_{horiz}^{sf} is:

$$SF_{horiz}^{sf} = SF_{horiz,0} \cdot g_1 \cdot \left(\frac{p}{p_0}\right)^{i_1} \cdot g_2 \cdot \left(\frac{h}{h_0}\right)^{i_2} \cdot g_3 \cdot \left(\frac{d}{d_0}\right)^{i_3} \tag{4.1}$$

When Condition 4 is checked, strains of steel lining ε are limited to be smaller than a defined maximal strain ε_{max}, see Eq. (5). For a typical number of 1000 cycles of cavern loading ε_{max} is 3.5 ‰.

$$\varepsilon^{sf} \le \varepsilon_{max} \tag{5}$$

where ε^{sf} is:

$$\varepsilon^{sf} = \varepsilon_0 \cdot j_1 \cdot \left(\frac{p}{p_0}\right)^{k_1} \cdot j_2 \cdot \left(\frac{h}{h_0}\right)^{k_2} \cdot j_3 \cdot e^{k_5 \cdot \left(\frac{t/d}{t_0/d_0}\right)} \tag{5.1}$$

While p [MPa] represents inner gas pressure, h [m] is the cavern depth, d [m] stands for the cavern inner diameter and t [m] is thickness of the concrete wall; constants p_0, h_0, d_0, t_0, and l_0 represent the initial values of mentioned parameters.

It should be noted that the substituted functions, i.e. eqn. (3.1), (4.1) and (5.1), are proposed to be approximated from a series of FEM analyses for the particular UGS system and its geomechanical parameters (see the numerical example at the end of the paper).

3.2.3 Design (in)equality constraints

Design (in)equality constraints determine the UGS cavern geometry and the gas pressure to be calculated inside the defined limits. The reliability of the system depends on several geometrical parameters such as the depth and diameter of the cavern, and its height. Thickness of the cavern wall also plays an important role. Relation between the cavern volume, the design stored gas capacity and gas pressure should also be defined. Gas pressure p is calculated by the constraint (6).

$$10 \le p \le 30 \tag{6}$$

Depth of the cavern h [m] is bounded, see eqn. (7).

$$100 \le h \le 300 \tag{7}$$

The cavern inner diameter d [m] vary between its lower and upper bounds, see eqn. (8).

$$10 \le d \le 30 \tag{8}$$

Constraint (9) defines bounds of the concrete wall thickness t [m].

$$2 \le t \le 5 \tag{9}$$

The height of the cavern tube h_{cav} [m] is defined by eqn. (10).

$$0 \le h_{cav} \le 30 \tag{10}$$

Relation between the cavern volume V^{sf}_{cav}, the stored gas capacity V_{gas} and the gas pressure p is given by eqn. (11).

$$V^{sf}_{cav} = \frac{V_{gas}}{13{,}246 \cdot p - 0{,}073 \cdot p^2} \tag{11}$$

4 Numerical example

In order to interpret the proposed optimization approach, the paper presents a study of the NLP optimization of the investment and operational costs of an underground gas storage, planned in Senovo [7, 8], located in the south-eastern part of Slovenia. The UGS is planned to be constructed from a single lined rock cavern in order to store 5.56 millions m^3 of natural gas. The concrete C 30/37 and structural steel S 235 are used for the construction of tunnels, cavern walls

and steel lining. Steel S 400 was used for the reinforcement. Steel lining is 12 mm thick. The optimization/calculation of the UGS system comprises:

- Optimization of the UGS in seven different rock environments,
- Determination of the rock mass parameters for the location of Senovo,
- Definition of the geomechanical inequality constraints for the treated UGS,
- Optimization of the UGS system Senovo.

4.1 Optimization of the UGS in 7 different rock environments

For the optimization, 7 different rock mass qualities were defined, for which different rock mass parameters are typically determined. We used the rock mass rating (RMR) system. E.g., the unconfined compressive strengths of the intact rock σ_{ci} are 55, 60, 65, 70, 75, 80 and 85 MPa, the geological strength indexes *GSI* are 41, 46, 51, 56, 61, 66 and 71, etc. Consequently, for 7 different rock environments (parameters), 7 optimizations were performed for the data of the UGS Senovo to store 5.56 millions m^3 of natural gas. The developed optimization model OPTUGS was applied. The optimal investment and operational costs per the cavern and per the m^3 of stored gas in Senovo are presented in Table 1.

Table 1: Optimal investment and operational costs of the UGS Senovo in 7 possible different rock environments (RMR).

Rock mass rating RMR	Investment costs per the cavern, EUR	Investment costs per m^3 of the stored gas, EUR/m^3
RMR 1	$36.701 \cdot 10^6$	6.601
RMR 2 (Senovo)	$32.807 \cdot 10^6$	5.901
RMR 3	$31.172 \cdot 10^6$	5.606
RMR 4	$30.193 \cdot 10^6$	5.430
RMR 5	$29.783 \cdot 10^6$	5.357
RMR 6	$29.733 \cdot 10^6$	5.348
RMR 7	$29.625 \cdot 10^6$	5.328

While the highest costs were obtained for the lowest rock strength (RMR 1), the costs of all other RMRs were found to be smaller and similar. Rock masses RMR 2 to RMR 7 can be thus suitable for storing the gas. Since in the neighbourhood of Senovo the rock mass RMR 2 was located, it was selected for the storing the gas. The optimization in this rock environment is presented in the following sections.

4.2 Determination of the rock mass parameters

Data obtained from geological mapping and geological inventory of the core wells, confirming act and limestone dolomites in the eastern area of mine Senovo are presented in reference [7]. After all needed geological data were obtained, rock mass parameters were determined on the basis of the generalized Hoek-

Brown failure criterion [6, 9]. The computer program RocLab was applied [10]. While the unconfined compressive strength of the intact rock σ_{ci} was 60 MPa, the geological strength index *GSI* was 46. The Mohr-Coulomb strength parameters are derived, i.e. the cohesion c was 900 kPa and the friction angle φ was 39°. Finally, calculated were the rock mass parameters: the rock mass tensile strength σ_t was 0.092 MPa, the uniaxial rock mass compressive strength σ_c was 2.29 MPa, the global rock mass compressive strength σ_{cm} was 8.13 MPa and the rock mass deformation modulus E_{rm} was 10.70 GPa.

4.3 Definition of the geomechanical inequality constraints

After the rock mass parameters were determined, the calculation was followed by the development of the geomechanical inequality constraints for the location of Senovo. When Conditions 1, 2 and 3 (strength, uplift and failure of the rock) where checked, the rock mass was treated as discontinuous, having enough shear strength. On the other hand, when strains of the steel lining were calculated (Condition 4), the rock mass was treated as a continuum with uniform conditions over the circumference of LRC. It was assumed that the concrete cracks are small and enable to transfer the load on the rock mass.

While Eq. (2) was in point of fact already defined because the *GSI* parameter was determined as mentioned in Section 4.2, other geomechanical constraints, i.e. eqn. (3)-(5) with all coefficients had still to be evaluated.

For this purpose, a 3-D FE model of the UGS system and the surrounding rock mass area was generated. The FE mesh, consisted from triangle prismatic finite elements, was defined for a space area of 280x280x300 m^3 (x-y-z, with z the axis in depth). The FEM computer program Plaxis Version 3D [11] was used. A series of FEM analyses for the treated UGS of Senovo were performed.

In this way, safety factors against the rock cover uplift SF_{up} and the rock failure between two caverns SF_{horiz} as well as strains of steel lining ε were calculated for various combinations between different inner gas pressures, cavern depths, cavern diameters and the cavern wall thickness.

As a result, geomechanical functions/constraints and their coefficients were finally approximated and put into the optimization model OPTUGS, see Table 2.

Table 2: Evaluated coefficients for geomechanical functions eqn. (3.1), (4.1) and (5.1).

SF^{sf}_{up} eqn. (3.1)	SF^{sf}_{horiz} eqn. (4.1)	ε^{sf} eqn. (5.1)
p_0 = 20 MPa, h_0 = 150 m, d_0 = 25 m, t_0 = 2 m		
$SF_{up,0}$ = 2.5686	$SF_{horiz,0}$ = 2.6190	ε_0 = 4.9300
c_1 = 0.9999	g_1 = 0.9946	j_1 = 1.0084
f_1 = -0.9999	i_1 = -0.9701	k_1 = 1.8511
c_2 = 0.9957	g_2 = 0.9990	j_2 = 1.0050
f_2 = 1.7159	i_2 = 0.8714	k_2 = -0.5540
c_3 = 0.9979	g_3 = 0.9789	j_3 = 1.1619
f_3 = -1.0610	i_3 = -0.9410	k_3 = -0.1481

4.4 Optimization of the UGS system

The optimization of the underground gas storage system in Senovo was performed by the NLP optimization approach. The task of the optimization was to find the minimal possible system's investment and operational costs for the phase of the conceptual design.

The developed optimization model OPTUGS was used. The economic data for the optimization, which were fulfilled into the objective function, are presented in Table 3. The design stored gas capacity per the cavern V_{gas} was planned to be 5.56 millions m^3, number of planned caverns No_{cav} was 1, the volume of tunnel excavation per cavern was 1330 m^3, the unit mass of steel ρ was 7.85 t/m^3 and the percentage of the reinforcement r_{perc} was 0.15%.

Table 3: Economic data for the optimization.

$costs_{up}$	upper ground works	10480000	EUR
$costs_{under}$	underground works	6048025	EUR
$C_{exc,tun}$	price of the tunnel excavation	2440	EUR/m^3
$C_{prot,tun}$	price of the tunnel protection	1340	EUR/m^3
$C_{exc,cav}$	price of the cavern excavation	100	EUR/m^3
$C_{prot,cav}$	price of the cavern protection	90	EUR/m^2
C_{drain}	price of the cavern drainage	60	EUR/m^2
C_{wall}	price of the cavern wall concrete	190	EUR/m^3
C_{reinf}	price for the wall reinforcement	2000	EUR/t
C_{steel}	price of the steel lining	920	EUR/m^2

Since the NLP model OPTUGS is highly non-linear, the optimization was performed by the computer code GAMS/CONOPT2 (the general reduced gradient method) [12]. The optimal result represented the obtained UGS system's minimal investment and operational costs of 32.807 millions EUR or 5.901 EUR per m^3 of stored gas. The solution also comprised the calculated optimal inner gas pressure p = 17.46 MPa, the cavern depth h = 190.12 m, the cavern inner diameter d = 30.00 m, thickness of the cavern concrete wall t = 2.00 m and the height of the cavern tube h_{cav} = 17.63 m, see Figure 2.

Since the investment and operational costs of the primal non-optimized project amounted 9.00 EUR per m^3 of stored gas, the proposed optimization decreased the costs for 34.44%. The optimal solution also enabled the rock mass strength stability and the system's safety.

5 Conclusions

The paper presents the optimization of the investment and operational costs of underground gas storages (UGS) designed from lined rock caverns (LRC). The optimization is performed by the non-linear programming (NLP) approach in

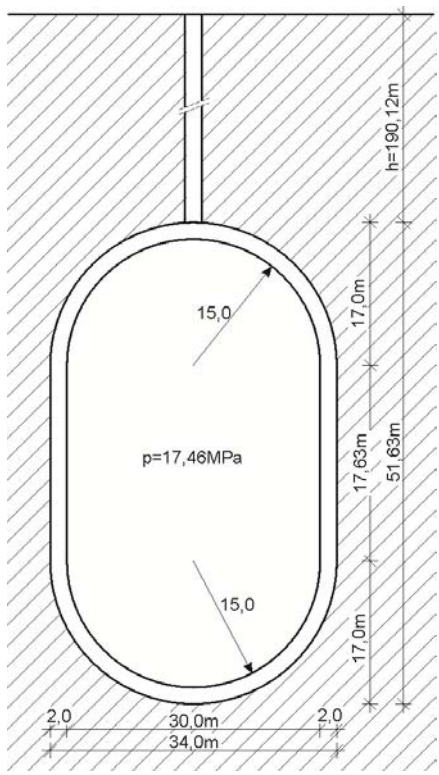

Figure 2: Optimal design of the cavern, UGS Senovo.

different rock mass environments. For this purpose, the NLP optimization model OPTUGS was developed. As the model was developed in a general form, the optimization of the system can be performed for different economic conditions, different number of LRCs, various gas capacities as well as for different rock environments. The optimization is proposed to be performed for the phase of the conceptual design. Since there exist of various rock mass qualities to support the UGS, the optimization of the UGS is proposed to be calculated in different rock environments. For this purpose, a rock mass classification – the so called rock mass rating (RMR) is used.

A study of the optimization of investment and operational costs of underground gas storages is presented at the end of the paper. The optimization enables 34% of savings in investment costs when compared to the design obtained by the classical method. The optimal solution also enables the rock strength stability and the system's safety. The suitable rock mass was selected.

References

[1] Sofregaz, U.S., Commercial potential of natural gas storage in lined rock caverns (LRC), U.S. Department of Energy, 1999.
[2] Brandshaug, T., Christianson, M., Damjanac, B., U.S., Department of Energy: Technical Review of the Lined Rock Cavern (LRC) - Concept and Design Methodology: mechanical Response of Rock Mass, U.S. Department of Energy, 2001.
[3] Chung, I.M, Chob, W., Heob J.H., Stochastic hydraulic safety factor for gas containment in underground storage caverns. *Journal of Hydrology*, **284**, pp. 77-91, 2003.
[4] Brooke, A., Kendrick, D. and Meeraus, A., GAMS - A User's Guide, Scientific Press, Redwood City, CA, 1988.
[5] Noren, C., Underground Storage of Natural Gas in Lined Rock Cavern in Brestanica Area, NCC, Stockholm, 2006.
[6] Hoek, E., Brown, E.T., Practical Estimates of Rock Mass Strength. *International Journal of Rock Mechanics and Mining Sciences*, **34** (8), pp. 1165-1186, 1997.
[7] Vukelič, Ž., Sternad, Ž., Vukadin, V., Čadež, F., Hude, M., Pečovnik, I., High Pressure Storage of Gas in Area of Coal Mine Senovo. *RMZ - Materials and Geoenvironment*, **53** (3), pp. 303-313, 2006.
[8] Trauner, L., Škrabl, S., Vrecl Kojc, H., Žlender, B., Geotechnical opinion on feasible high-pressure natural gas storage Zakov/Senovo, 2007.
[9] Hoek, E. and Diederichs, M.S., Empirical estimation of rock mass modulus. *International Journal of Rock Mechanics and Mining Sciences*, **43**, pp. 203–215, 2006.
[10] Hoek, E., Practical Rock Engineering – An Ongoing Set of Notes, available on the website, www.rocscience.com
[11] Plaxis, http://www.plaxis.nl
[12] Drudd, A.S., CONOPT – A Large-Scale GRG Code. *ORSA Journal on Computing*, **6** (2), pp. 207-216, 1994.

Coupled multi-disciplinary methods for structural reliability and affordability

C. C. Chamis
NASA Glenn Research Center, Cleveland, USA

Abstract

A computational simulation method is presented for Non-Deterministic Multidisciplinary Optimization of engine composite materials and structures. A hypothetical engine duct made with ceramic matrix composites (CMC) is evaluated probabilistically in the presence of combined thermo-mechanical loading. The structure is tailored by quantifying the uncertainties in all relevant design variables such as fabrication, material, and loading parameters. The probabilistic sensitivities are used to select critical design variables for optimization. In this paper, results of the non-deterministic optimization are presented with probabilistic lower bounds of 0.001 and upper bounds of 0.999.
Keywords: applications-aerospace, composite components, thermal analysis, structural analysis, probability, ceramic composites.

1 Introduction

Recent research activities have focused on developing multi-scale, multi-level, multi-disciplinary analysis and optimization methods. Multi-scale refers to formal methods which describe complex material behavior; multi-level refers to integration of participating disciplines to describe a structural response at the scale of interest; multi-disciplinary refers to open-ended for various existing and yet to be developed disciplines. For example, these include but are not limited to: multi-factor models for material behavior, multi-scale composite mechanics, general purpose structural analysis, progressive structural fracture for evaluating durability and integrity, noise and acoustic fatigue, emission requirements, hot fluid mechanics, heat-transfer and probabilistic simulations. Many of these, as well as others, are encompassed in an integrated computer code identified as Engine Structures Technology Benefits Estimator (EST/BEST) [1]. The

WIT Transactions on The Built Environment, Vol 125, © 2012 WIT Press
www.witpress.com, ISSN 1743-3509 (on-line)
doi:10.2495/OP120031

discipline modules integrated in EST/BEST include: engine cycle (thermodynamics), engine weights, internal fluid mechanics, cost, mission and coupled structural\thermal, various composite property simulators and probabilistic methods to evaluate uncertainty effects (scatter ranges) in all the design parameters. The EST/BEST (Engine Structures Technology Benefits Estimator) software, shown in Fig. 1, is used to carry out the investigative study presented in this paper. Component as well as system evaluations are performed within a single software. The modules included are integrated computer codes with multiple functional capabilities. The ones that were used for the results to be presented later are (1) Cosmo for finite element generation; (2) Material Library - for composite mechanics simulation; (3) IPACS [2] for composite structures probabilistic evaluation and (4) CSTEM [3] for coupled structural/thermal analysis and Optimization.

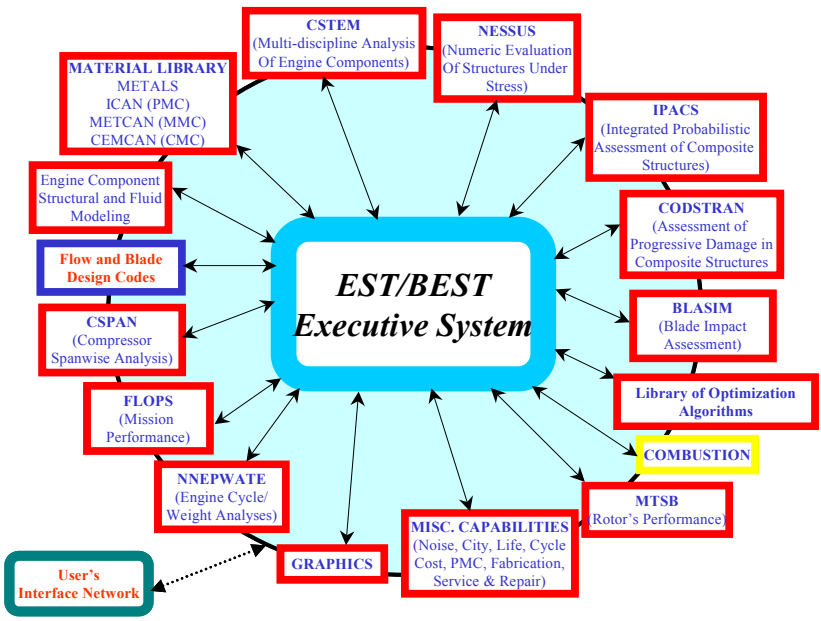

Figure 1: EST/BEST: Engine structures technology benefit estimator.

2 Non-deterministic coupled structural/thermal analysis

In EST/BEST, the IPACS module is used to perform probabilistic assessment of the composite structure. With the direct coupling of composite mechanics, structural analysis and probabilistic methods, IPACS is capable of simulating uncertainties in all inherent scales of the composite, from constituent materials to the composite structure and its loading conditions. The temperature distribution obtained for the composite duct from the coupled structural/thermal analysis is shown in Fig. 2.

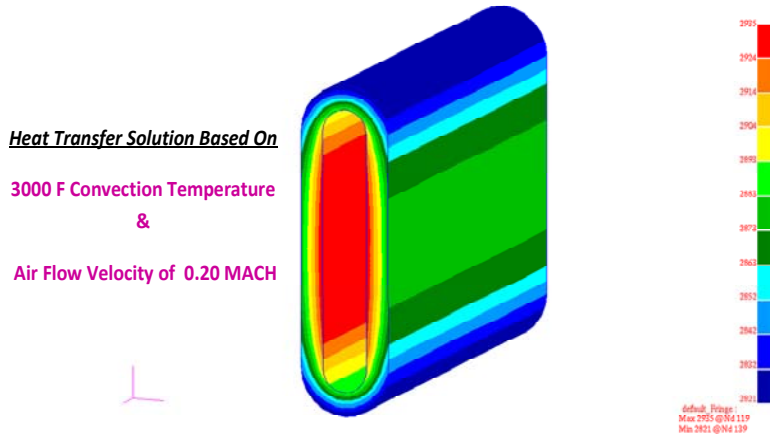

Figure 2: Temperature plot of CMC duct with combined 50 psi internal pressure and internal forced convection.

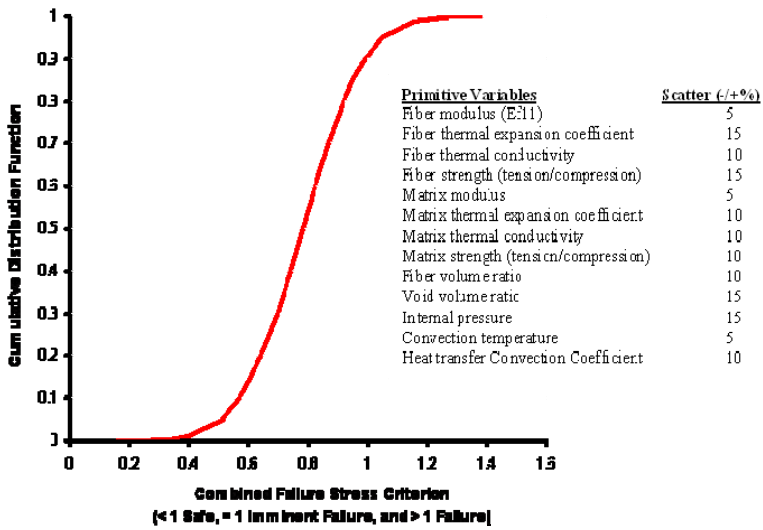

Figure 3: Probabilistic evaluation of combined stress failure criterion of CMC duct with combined internal pressure and forced convection.

The temperature varied from 1633C (2935^0F) on the inner walls of the duct to 1547C (2821^0F) on the outside. In CSTEM, the combined stress failure criterion is evaluated. The combined failure stress criterion is computed by summing various ply stresses to strength ratios. A failure function less than 1 indicates no

failure, equal to 1 indicates failure is imminent and greater than1 indicates failure. Figure 3 shows the probabilistic evaluation of the CMC duct under combined thermo-mechanical loading.

The effects of uncertainties in composite material properties, composite fabrication parameters, and combined thermo-mechanical loading are assessed. The combined stress failure criterion is evaluated probabilistically based on the following scatter in primitive variables: ±5% in fiber and matrix moduli, and convection temperature; ± 10% in fiber and matrix thermal conductivity, matrix thermal expansion coefficient, matrix strength, fiber volume ratio and heat transfer convection coefficient; and ± 15% in fiber thermal expansion coefficient and fiber strength, void volume ratio, and internal pressure, Table 1.

Table 1: Summary of results from probabilistic evaluation followed by optimization.

Design Variables	**0.001 Prob**	**0.50 Prob**	**0.95 Prob**	**Initial Design**	**Optimum Design**
Matrix Modulus (Msi)	4.314	4.4	4.44	4.44	4.314
Matrix Thermal Expansion Coefficient (x 1.0E-06 in/in/F)	3.059	3.25	3.35	3.35	3.059
Matrix Thermal Conductivity (BTU/hr-ft-F)	3.097	3.0	2.94	2.94	3.097
Matrix Tensile Strength (ksi)	15.81	13.0	11.84	11.84	15.81
Fiber Volume Ratio	0.399	0.45	0.479	0.479	0.399
Void Volume Ratio	0.071	0.100	0.116	0.1168	0.071
Objective					
Combined Stress Failure Criterion	0.3577	0.781	1.00	1.058	0.482
Constraint					
1st Natural Frequency (cps)	Limit set between 6517 and 8412			8116	7179

One Msi=6.9GPa; degree ^{0}F=5/9C:ksi=6.9MPa; Btu=1055.1Joules

The scatter ranges considered here are typical for the primitive variables selected in the study. The results from the probabilistic evaluation Fig.3 show that probability higher than 0.92, failure is imminent. The probabilistic sensitivities of the combined stress failure criterion to the scatter range of the primitive variables are presented in Fig. 4.

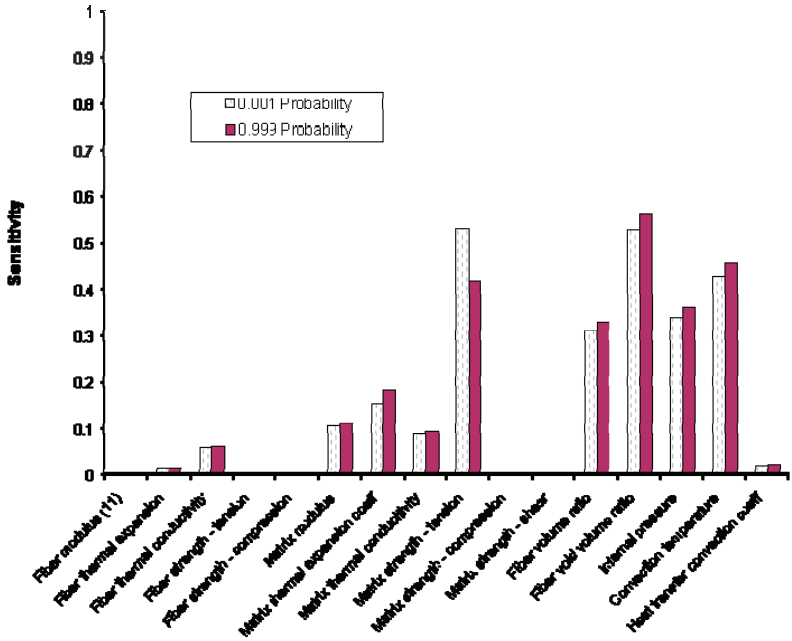

Figure 4: Sensitivity of combined stress failure criterion of CMC duct to the scatter range with combined internal pressure and forced convection.

3 Non-deterministic multi-disciplinary optimization

Non-deterministic optimization may be defined as follows: Find a set of primitive variables (those that describe the physics and can be varied by the designer such that some combined objective (merit) function is simultaneously minimized/maximized subject to probabilistically described variability in the primitive variables and in the constraints of the behavior (response) variables. In equation form the above statement is expressed thus:

$$\text{Optimize:} \quad \mathfrak{I}\ (\text{P.V.}) \ni \max\ (P_d) \min\ (P_c) \max\ (P_s) \min\ (P_f)$$
$$\text{And} \ni P_{lb} \leq (\text{P.V.}) \leq P_{ub} \qquad (1)$$

where $\mathfrak{I}$ is the function to be optimized; P.V. are a set of primitive variables; the symbol $\ni$ denotes such that; P_d is the probability of durability; P_c is the probability of cost; P_s is the probability of survivability and P_f is the probability of failure. Note that the non-deterministic optimization is carried out based on a design (feasible) region that is constrained by the limits that are determined in the probabilistic evaluation, Table 2. As indicated in Fig. 5, the feasible region bounds are represented by the limits set at high and low probability levels.

Table 2: Summary of results from optimization followed by probabilistic evaluation.

Design Variables	**Lower Bound**	**Upper Bound**	Initial Design	**Optimum Design**
Matrix Modulus (Msi)	4.18	4.62	4.62	4.18
Matrix Thermal Expansion Coefficient (x 1.0E-06 in/in/F)	2.925	3.575	3.575	2.925
Matrix Thermal Conductivity (BTU/hr-ft-F)	2.70	3.3	3.30	3.30
Matrix Tensile Strength (ksi)	11.70	14.30	14.30	14.30
Fiber Volume Ratio	0.405	0.495	0.495	0.405
Void Volume Ratio	0.085	0.115	0.115	0.085
Objective				
Combined Stress Failure Criterion	0.712	0.910	0.910	0.563
Constraint				
1st Natural Frequency (cps)	Limit set between 6590 and 8357		8357	7187

Msi=6.9GPa; ^{0}F=%/(C; Ksi=6.9MPa; Btu=1055.1Joules

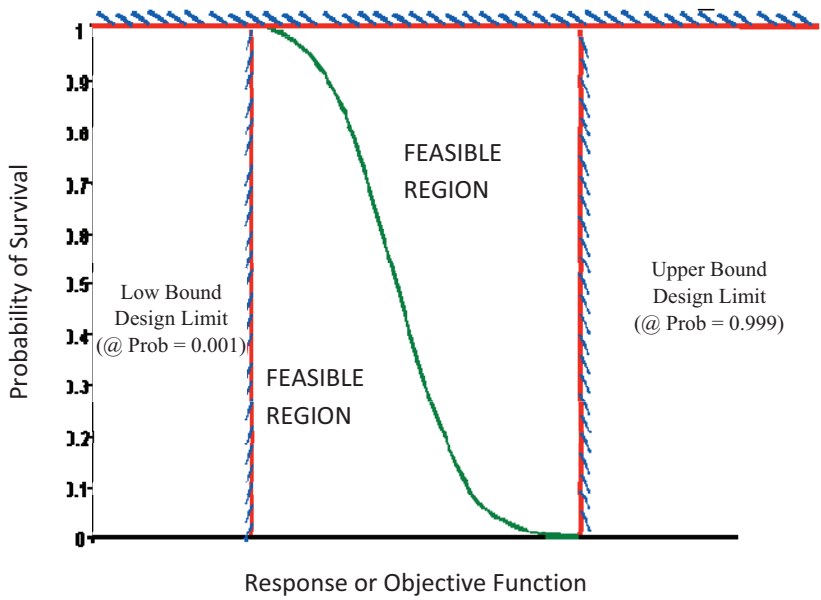

Figure 5: Probabilistic evaluation of combined stress failure criterion followed by optimization (with reduced design variables list).

4 Conclusions

The use of a collective multi-scale, multi-level, multi-disciplinary analysis and optimization and probabilistic methods shows that non-deterministic optimization can be done by performing probabilistic evaluation and optimization. The probabilistic evaluation is computationally more efficient than optimization. If the accuracy of the probabilistic response at extreme probabilities is improved, the use of optimization is not necessary. The probabilistic sensitivities can be used to select a reduced set of design variables for subsequent optimization.

Acknowledgement

This paper is declared a work of the U.S. Government and it is not subject to copyright protection.

References

[1] Abumeri, G.H. and Chamis, C.C.: T/BEST a computer code for assessing the benefits of advanced aerospace technologies, published in the Advances in Engineering Software Journal, pp.231-238, 1997 Elsevier Science Limited, Printed in Great Britain.
[2] Chamis, C.C.; and Shiao, M.C.: IPACS – Integrated Probabilistic Assessment of Composite Structures: Code Development and Applications. Third NASA Advanced Composite Technology Conference, Vol. 1, Pt. 2, NASA CP-3178-VOL-1-PT-2, 1993, pp.987-999.
[3] Hartle, M.; and McKnight, R.L: CSTEM User Manual, NASA CR-2000-209308, January 2000.

This page intentionally left blank

Metamodel-based multi-objective robust design optimization of structures

J. Martínez-Frutos & P. Martí-Montrull
Structural Optimization Group, Technical University of Cartagena, Spain

Abstract

Multi-objective robust optimization (MORO) is a highly demanding computational task because of the direct nesting of the uncertainty quantification within optimization. This work presents an approach based on Kriging models to efficiently include the uncertainty quantification in the optimization procedures. In the proposed approach the metamodels appear both at optimization level as well as at uncertainty quantification level. The proposed methodology allows us to: (1) assess the robustness of each design using a reduced number of simulator runs, as compared with conventional approach procedures; and (2) to decouple the uncertainty quantification of the optimization, allowing us to solve the problem with a lower computational cost compared to the nested approach. A benchmark problem has been considered using different approaches in order to compare their relative merits. The results show that the proposed method has potential to obtain solutions with reasonable accuracy and a considerably lower number of function calls than required by conventional methods.
Keywords: efficient multi-objective robust optimization, evolutionary algorithms, Kriging models.

1 Introduction

In structural engineering, the designer often has to deal with problems that involve conflicting objectives and sources of uncertainty in diverse structural parameters, such as geometric imperfections, material properties or applied loads. The set of optimal solutions obtained using conventional deterministic methods can be very sensitive to perturbations in design variables, leading to a deterioration of the optimal structural performance or even to a set of infeasible designs. Hence, it is desirable to obtain a set of optimal solutions which are less sensitive to variations


WIT Transactions on The Built Environment, Vol 125, © 2012 WIT Press
www.witpress.com, ISSN 1743-3509 (on-line)
doi:10.2495/OP120041

in the structural parameters. The Multi-Objective Robust Optimization (MORO) takes into account the robustness of each design in the optimization process, leading to a set of robust solutions known as Pareto robust solutions [1].

Among the different approaches that address the MORO problem, authors such as Deb and Gupta [2] incorporate the robustness of the objective function within the optimization problem without considering the uncertainty in the constraints. Conversely, Gunawan and Azarm [1] and Li *et al.* [3] take into account both the robustness of the objective functions as well as the robustness of the constraints. Gunawan and Azarm [1] and Li *et al.* [3] propose a double loop optimization approach with interval uncertainty. These approaches can be computationally intractable, especially in high-dimensional problems [4], since two optimization problems need to be resolved for each design. In order to reduce the computational cost, some authors such as Hu *et al.* [4] and Shimoyama *et al.* [5] suggest the use of approximations to assist the multi-objective optimization problem. In this respect, Hu *et al.* [4] propose a two-level optimization with uncertainty intervals assisted by Kriging models. In the work proposed by Shimoyama *et al.* [5], Kriging models are used to obtain mean and standard deviation of the objective functions efficiently. The methodology proposed by Shimoyama *et al.* [5] doubles the number of objective functions compared to the deterministic approach. Said methodology can be inefficient in high-dimensional problems. The former approaches provide a set of robust solutions, but do not identify what the degree of robustness against other design is [6]. Recently, Erfani and Utyuzhnikov [6] presented a methodology suitable for obtaining solutions with different levels of robustness by introducing an additional objective function.

This work presents an approach based on Kriging models to efficiently include the uncertainty quantification in the optimization procedures. The proposed methodology allows: (1) to appraise the robustness of each design using a reduced number of simulator runs compared with conventional approach procedures; (2) to solve the MORO problem in a single-loop optimization assisted by Kriging models; and (3) to obtain multiple solutions to the MORO problem with different levels of robustness of both the objective functions and the constraints, without additional simulator calls.

2 Metamodel-based multi-objective robust optimization

2.1 Multi-objective robust optimization

The conventional multi-objective optimization problem can be formulated as follows:

$$\begin{aligned} &\min_{\mathbf{x}\in\mathbb{R}^n} \{f_1(\mathbf{x},\mathbf{p}),\ldots,f_m(\mathbf{x},\mathbf{p})\} \\ &s.t.\ \ g_j(\mathbf{x},\mathbf{p}) \le 0\ j=1,\cdots,m_i \\ &s.t.\ \ h_k(\mathbf{x},\mathbf{p}) = 0\ k=1,\cdots,m_k \\ &\quad \mathbf{x}^{\text{lower}} \le \mathbf{x} \le \mathbf{x}^{\text{upper}} \end{aligned} \tag{1}$$

where $\mathbf{x} \in \mathbb{R}^{\mathrm{n}}$ is the vector of design variables to be optimized; $\mathbf{p} \in \mathbb{R}^{\mathrm{q}}$ is the vector of non-design parameters; $\mathbf{x}^{\mathrm{lower}}$ and $\mathbf{x}^{\mathrm{upper}}$ are the lower and the upper bounds of the design variables respectively; g_j and h_k are the problem inequality and equality constraints. The solution of the multi-objective problem defined in (1), leads to a set of optimal solutions in the Pareto sense: A vector $\mathbf{x}$ is called a Pareto solution to problem (1) if another design vector $\mathbf{x}^*$ does not exist in the feasible space such that, $f_i(\mathbf{x}^*, \mathbf{p}) \leq f_i(\mathbf{x}, \mathbf{p})$ for any $i = 1, \cdots, m$, and $j \in \{1, \cdots, m\}$: $f_j(\mathbf{x}^*, \mathbf{p}) < f_j(\mathbf{x}, \mathbf{p})$ exists.

The conventional multi-objective optimization problem considers all the variables and parameters involved in the problem as being deterministic. For that reason, the optimal performance of the structure can be dramatically degraded in the presence of sources of uncertainty. The Multi-Objective Robust Optimization (MORO) takes into account the robustness of each design in the optimization process, leading to a set of robust solutions known as Pareto robust solutions [1].

Among the different approaches that address the MORO problem, in this paper the formulation proposed by Mattson and Messac [7] is considered. The mean values of the design metrics plus the standard deviations are minimized as follows:

$$\begin{aligned} &\min_{\mathbf{x},\mathbf{p},\in\mathbb{R}^{\mathrm{n}}} \left\{\mu_{f_1(\mathbf{x},\mathbf{p},\boldsymbol{\xi})} + k\sigma_{f_1(\mathbf{x},\mathbf{p},\boldsymbol{\xi})}, \ldots, \mu_{f_m(\mathbf{x},\mathbf{p},\boldsymbol{\xi})} + k\sigma_{f_m(\mathbf{x},\mathbf{p},\boldsymbol{\xi})}\right\} \\ &s.t.\ \ \mu_{g_j(\mathbf{x},\mathbf{p},\boldsymbol{\xi})} + k\sigma_{g_j(\mathbf{x},\mathbf{p},\boldsymbol{\xi})} \leq 0 \quad j = 1, \cdots, m_i \\ &\quad \mathbf{x}^{\mathrm{lower}} \leq \mathbf{x} \leq \mathbf{x}^{\mathrm{upper}} \end{aligned} \tag{2}$$

where ξ is a random variable vector that represents the uncertainty of the problem (design variables and/or parameters); μ_{f_i} and σ_{f_i} are the mean and the standard deviation of the objective function f_i; and μ_{g_j} and σ_{g_j} are the mean and the standard deviation of the inequality constraints respectively. All the equality constraints are transformed into inequality constraints to obtain multiple solutions to the MORO problem with different levels of robustness of both the objective functions and constraints.

In order to solve the problem formulated in 2, it is necessary to combine optimization techniques with uncertainty quantification techniques. The most straightforward approach is to perform an uncertainty quantification loop for each iteration of the optimization algorithm. However, this can lead to an intractable problem. For this reason, diverse approaches exist in the literature that aim to break the nested relationship between uncertainty quantification and optimization [8]. In this work we investigate the used of Kriging models to efficiently include the uncertainty quantification in the MORO procedures.

2.2 Kriging models

A metamodel replaces a computationally expensive simulation model called a simulator by an emulator which is much faster to evaluate. Among the different metamodeling techniques, the Kriging models [9] have gained increasing popularity in recent years for use in engineering design, owing to the flexibility

in capturing nonlinear behaviours [10], and the ability to provide statistical information on the predicted output [11].

Kriging models assume that the simulator can be approximated by a sample path of a Gaussian stochastic process $\mathscr{G}(\mathbf{x})$ whose prior mean $E[\mathscr{G}(\mathbf{x})] = \mathbf{f}(\mathbf{x})^{\mathrm{T}}\,\boldsymbol{\beta}$ and prior covariance function $Cov[\mathscr{G}(\mathbf{x}), \mathscr{G}(\mathbf{x}')] = \alpha^2 \mathrm{R}(\mathbf{x}, \mathbf{x}', \boldsymbol{\phi})$ are unknown. In the former expressions; $\boldsymbol{\beta} = [\beta_1, \ldots, \beta_{\mathrm{p}}]^{\mathrm{T}}$ is a vector of unknown parameters; $\boldsymbol{f}(\mathbf{x}) = [f_1(\mathbf{x}), \ldots, f_{\mathrm{p}}(\mathbf{x})]^{\mathrm{T}}$ is a set of known functions of $\mathbf{x} \in \mathbb{R}^{\mathrm{n}}$; α^2 is the variance of $\mathscr{G}(\mathbf{x})$; and $R(\mathbf{x}, \mathbf{x}', \boldsymbol{\phi})$ is the autocorrelation function between $\mathbf{x}$ and $\mathbf{x}'$. The stochastic process $\mathscr{G}(\mathbf{x})$ represents the prior knowledge of the simulator, for that reason the choice of the autocorrelation model should be made consistently with the known properties of the simulator. The most widely used class of autocorrelation function is the anisotropic generalized exponential model:

$$\mathrm{R}(\mathbf{x}, \mathbf{x}', \boldsymbol{\phi}) = \exp\left(\sum_{\mathbf{i}=\mathbf{1}}^{\mathbf{n}} -\frac{|\mathbf{x_i} - \mathbf{x_i'}|^s}{\phi_{\mathbf{i}}}\right), \quad \mathbf{1} \leq s \leq 2 \tag{3}$$

The parameters $\boldsymbol{\beta}$, α^2 and ϕ are unknown a priori and are determined from the set of simulator responses $\mathscr{Y} = \{y_1, \ldots, y_m\}$ which are evaluated onto an experimental design $\mathscr{X} = \{\mathbf{x}_1, \ldots, \mathbf{x}_m\}$. Using Bayesian techniques, the posterior distribution of $\mathscr{G}(\mathbf{x})$ conditional on the vector of observations $\mathscr{Y} = \{y_1, \ldots, y_m\}$ is also Gaussian [12] with mean value:

$$\hat{y}(\mathbf{x}) \equiv \mathrm{E}[\mathscr{G}(\mathbf{x})|\mathscr{Y}] = \mathbf{f}(\mathbf{x})^{\mathrm{T}}\hat{\boldsymbol{\beta}} + \mathbf{r}(\mathbf{x})^{\mathrm{T}}\mathbf{R}^{-1}(\mathscr{Y}^{\mathrm{T}} - \mathbf{F}\hat{\boldsymbol{\beta}}) \tag{4}$$

and variance:

$$\begin{aligned} Cov[\mathscr{G}(\mathbf{x}), \mathscr{G}(\mathbf{x}')|\mathscr{Y}] = \alpha^2\{R(\mathbf{x}, \mathbf{x}', \boldsymbol{\phi}) - \mathbf{r}(\mathbf{x})^{\mathrm{T}}\mathbf{R}^{-1}\mathbf{r}(\mathbf{x}') + \\ + \mathbf{u}(\mathbf{x})^{\mathrm{T}}(\mathbf{F}^{\mathrm{T}}\mathbf{R}^{-1}\mathbf{F})^{-1}\mathbf{u}(\mathbf{x}')\} \end{aligned} \tag{5}$$

where we have introduced:

$$\mathbf{u}(\mathbf{x}) = \boldsymbol{f}(\mathbf{x}) - \mathbf{F}^{\mathrm{T}}\mathbf{R}^{-1}\mathbf{r}(\mathbf{x}) \tag{6}$$

$$\hat{\boldsymbol{\beta}} = (\mathbf{F}^{\mathrm{T}}\mathbf{R}^{-1}\mathbf{F})^{-1}\mathbf{F}^{\mathrm{T}}\mathbf{R}^{-1}\mathscr{Y} \tag{7}$$

$$\alpha^2 = \frac{1}{m}(\mathscr{Y} - \mathbf{F}\hat{\boldsymbol{\beta}})^{\mathrm{T}}\mathbf{R}^{-1}(\mathscr{Y} - \mathbf{F}\hat{\boldsymbol{\beta}}) \tag{8}$$

$$F_{\mathrm{ij}} = f_j(\mathbf{x}_{\mathrm{i}}), \quad i = 1, \ldots, m, \; j = 1, \ldots, p \tag{9}$$

$$R_{\mathrm{ij}} = \mathrm{R}(\mathbf{x}_{\mathrm{i}}, \mathbf{x}_{\mathrm{j}}, \boldsymbol{\phi}), \quad i = 1, \ldots, m, \; j = 1, \ldots, m \tag{10}$$

$$r_{\mathrm{ij}}(\mathbf{x}) = \mathrm{R}(\mathbf{x}_{\mathrm{i}}, \mathbf{x}_{\mathrm{j}}, \boldsymbol{\phi}), \quad i = 1, \ldots, m, \; j = 1, \ldots, m \tag{11}$$

$\hat{y}(\mathbf{x})$ represents the best prediction of the simulation model for a point $\mathbf{x}$, and $Cov[\mathscr{G}(\mathbf{x}), \mathscr{G}(\mathbf{x})|\mathscr{Y}]$ is the predicted error variance which provides probabilistic confidence intervals in addition to the prediction.

In (4) and (5) $\hat{\boldsymbol{\beta}}$ and α^2 are derived analytically and only depend on the autocovariance parameters $\boldsymbol{\phi}$. In the present work, the correlation parameters are

determined using *maximum likelihood estimation* (MLE) [12], solving the global optimization problem:

$$\max\left(-\frac{m\ln(\alpha^2)+\ln(|\mathbf{R}|)}{2}\right) \tag{12}$$

In this work, a set of different instances of Kriging are created using different correlation and regression functions. The best model of the set is selected using the mean square errors, in particular the root mean square error ($RMSE$) and the R^2. Both the $RMSE$ and the R^2 are estimated using a global cross-validation errors measure called prediction sum of squares ($PRESS$) [13] without additional simulator calls:

$$\mathrm{PRESS_{RMSE}} = \sqrt{\frac{\sum_{i=1}^{m}(\hat{y}_i-\hat{y}_{-i})^2}{m}},\ \ \mathrm{Pred}\ R^2 = 1-\frac{\sum_{\mathrm{i=1}}^{m}(\hat{\mathrm{y}}_\mathrm{i}-\hat{\mathrm{y}}_{-\mathrm{i}})^2}{\sum_{\mathrm{i=1}}^{m}(\hat{\mathrm{y}}_\mathrm{i}-\bar{\mathrm{y}})^2} \tag{13}$$

$\hat{y}_i$ is the prediction at the design point i, $\bar{y}$ is the mean of the predicted values and $\hat{y}_{-i}$ is calculated by removing each point i from the modeling points, constructing a new Kriging model at the remaining points and obtaining the prediction at the removed point.

2.3 Proposed approach

This work presents an approach based on Kriging models that approximate the statistical moments on the design domain and efficiently include the uncertainty quantification in the optimization loop. The scheme of the proposed approach is depicted in figure 1.

The proposed method consists in a two-stage framework. The first stage aims at constructing a set of Kriging models that approximate the statistical moments of both the objective functions and the constraints on the design domain ($\boldsymbol{\mu}(\mathbf{x}), \boldsymbol{\sigma}(\mathbf{x})$, $\boldsymbol{\gamma}(\mathbf{x}), \boldsymbol{\beta}(\mathbf{x})$). The second stage consists in the resolution of the multi-objective problem using deterministic algorithms. In this work an evolutionary algorithm (NSGA-II) was used to fulfilled this target. The two-stage framework is further detailed below:

Stage 1: setting up Kriging models

1. Create a *design of experiment* (DoE) in the design variable domain $\mathbf{X} = \{\mathbf{x}_1, \cdots, \mathbf{x}_i, \cdots, \mathbf{x}_{m_x}\}$. *Latin Hypercube Sampling* (LHS) was used for this.
   (a) For each design point $\mathbf{x}_i$ a new design of experiments is generated in the random variables domain $\{\boldsymbol{\xi}_1, \cdots, \boldsymbol{\xi}_j, \cdots, \boldsymbol{\xi}_{m_\xi}\}$.
   (b) Each point $\{\mathbf{x}_i, \boldsymbol{\xi}_j\}$ is evaluated with the simulator.
   (c) A Kriging model is constructed using the responses from the above step. This step involves solving the MLE problem (12) and selecting the best model by $PRESS_{RMS}$.

(d) The accuracy of the Kriging model (*Metamodel level 2*, figure 1) is assessed based on the predicted R^2. If the accuracy is not enough, new infill samples ($\boldsymbol{\xi}_{\text{infill}}$) are selected in regions with higher predicted error variance. If sufficient accuracy has been achieved then proceed to the following step.

(e) Statistical moments ($\mathbf{Y} = \boldsymbol{\mu}(\mathbf{x}_i), \boldsymbol{\sigma}(\mathbf{x}_i), \boldsymbol{\gamma}(\mathbf{x}_i), \boldsymbol{\beta}(\mathbf{x}_i)$) are obtained using Monte Carlo simulation assisted by *Metamodel level 2*, figure 1.

2. Using $\mathbf{X}$ e $\mathbf{Y}$, a Kriging model (*Metamodel level 1* , figure 1) is fitted for each statistical moment ($\hat{\boldsymbol{\mu}}(\mathbf{x}_)), \hat{\boldsymbol{\sigma}}(\mathbf{x}), \hat{\boldsymbol{\gamma}}(\mathbf{x}), \hat{\boldsymbol{\beta}}(\mathbf{x})$).
3. The accuracy of the Kriging model (*Metamodel level 1*, figure 1) is assessed based on the predicted R^2. If sufficient accuracy has not been achieved, new infill samples ($\mathbf{x}_{\text{infill}}$) are selected in regions with higher predicted error variance. If sufficient accuracy has been achieved then proceed to stage 2.

Stage 2: Multi-objective optimization

(a) the MORO problem (2) is solved using the evolutionary algorithm (NSGA-II) assisted by the Kriging models obtained in stage 1.

3 Numerical application

In this section the proposed methodology is applied to solve the problem of multi-objective robust design of a two-bar truss structure [14]. Different approaches (figure 2) for surrogate-based optimization under uncertainty [8] are used in order to compare their relative merits:

1. *Nested approach (N)* : the multi-objective optimization is performed on the results of the uncertainty quantification. The statistical moments are obtained using Monte Carlo simulations directly on the simulator. Metamodels are not used at any level. The results obtained by this approach are considered as a reference.
2. *Nested/Layered (N-L)* : the multi-objective optimization is performed on the results of the uncertainty quantification. The statistical moments are obtained using Monte Carlo simulations on a Metamodel. The metamodel approximates the simulator performance $f(\mathbf{x}, \boldsymbol{\xi})$ in the random variables domain (*Metamodel level 2*).
3. *Layered/Nested/Layered (L-N-L) (this work)* : the multi-objective optimization is performed on a Metamodel (*Metamodel level 1*). The statistical moments are obtained using Monte Carlo simulations on a Metamodel. The metamodel approximates the simulator performance $f(\mathbf{x}, \boldsymbol{\xi})$ in the random variables domain (*Metamodel level 2*).

Independently of the approach, the multi-objective optimization was carried out using the following parameters of the NSGA-II algorithm: binary tournament selection, number of generations (100), population size (50), crossover probability (0.9), mutation probability (0.1). The Monte Carlo simulations were carried out using 10,000 points.

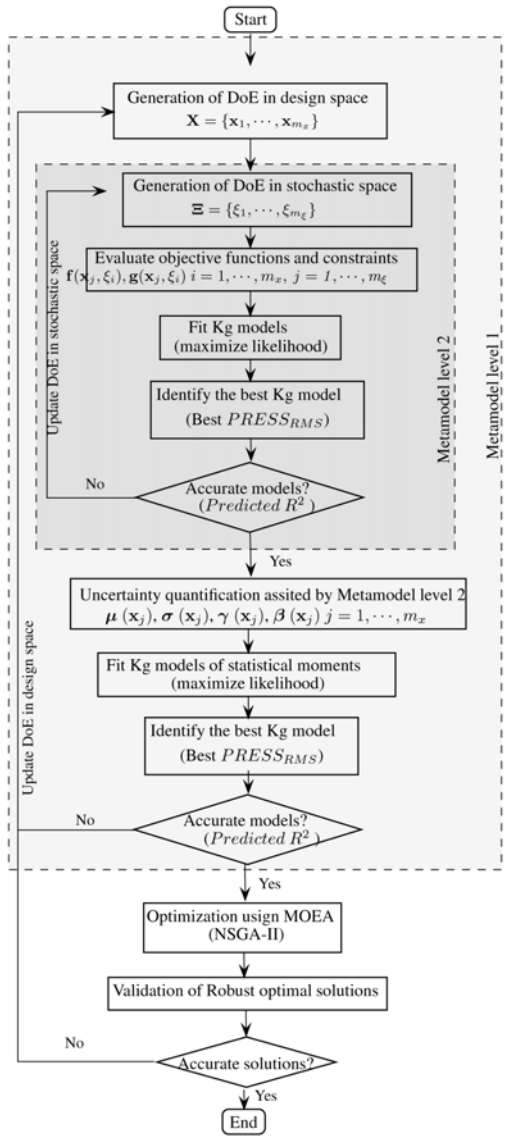

Figure 1: Flowchart of the metamodel-based MORO process.

3.1 Benchmark problem: two-bar truss structure

The popular two-bar truss structure problem (figure 3) is used as a benchmark test in this work for the multi-objective robust optimization. The test case is adapted from [14]. The design variables are the cross section diameter (d) and

the structure height (H). The random parameters of the problem are: the vertical force ($P \sim \mathcal{N}(150, 5)$ kN) , the structure width ($B \sim \mathcal{N}(750, 10)$ mm), the Elastic modulus ($E \sim \mathcal{N}(2.1\text{e}5, 5\text{e}3)$ N/mm^2), and the member thickness ($t \sim \mathcal{N}(2.5, 0.4)$ mm). The optimization problem is to minimize the volume and the vertical displacement of the structure subject to constraints of stress, buckling as well as the bound constraints (14).

$$\begin{aligned} &\min_{d,H} \{\mu_{volume} + k\,\sigma_{volume},\ \mu_{deflection} + k\,\sigma_{deflection}\} \\ &s.t.\ g_1 = \mu_S + k\,\sigma_S \leqslant S_{max} \\ &\quad g_2 = \mu_S + k\,\sigma_S \leqslant S_{crit} \\ &\quad 20 \leq d \leq\ 80,\ \ 200\ \leq H \leq\ 1,000 \end{aligned} \tag{14}$$

where:

$$S_{max} = 400\ MPa,\ S_{crit} = \frac{\pi^2 E(t^2+d^2)}{8(B^2+H^2)},\ S = \frac{P\sqrt{B^2+H^2}}{2\pi tdH}$$

$$volume = 2\pi dt\sqrt{B^2+H^2},\ deflection = \frac{P(B^2H^2)^{3/2}}{(2\pi tEdH)^2}$$

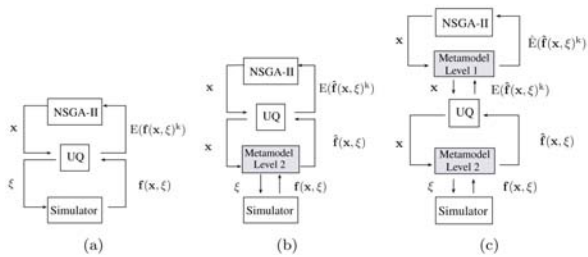

Figure 2: Multiobjective robust optimization approaches. (a) Nested approach, (b) nested/layered, (c) layered/nested/nayered.

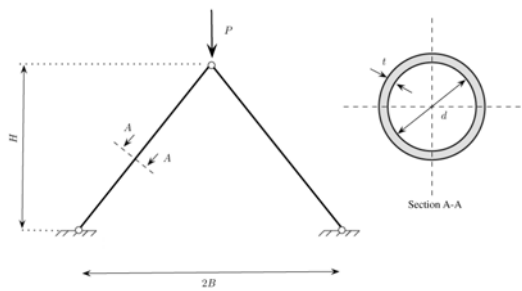

Figure 3: Two-bar truss structure.

3.2 Results and discussion

Twelve Kriging models were constructed. The regression and correlation models are depicted in table 1. Two LHS of 30 points and 20 points were used to fit the metamodels at levels 1 and 2 respectively. The predicted R^2 is shown in table 1 along with the R^2 estimated from Monte Carlo integration at 10,000 points. For this case, the Kriging models have been shown to be highly accurate, with R^2 values above than 0.98. Assisted by the former Kriging models, the MORO problem is solved as a deterministic one using the NSGA-II algorithm. The robust Pareto fronts obtained from different approaches and values of $k = 1, 2 \text{ and } 3$ are depicted in figure 4. The Pareto fronts show a good agreement between all the

Table 1: Kriging models.

	reg. order	corr. func.	$Pred.\ R^2$	R^2
$f_1/\mu_{f_1}/\sigma_{f_1}$	0/3/3	g/e/eg	1/0.999/0.999	1/0.999/0.999
$f_2/\mu_{f_2}/\sigma_{f_2}$	2/3/2	g/s/s	0.999/0.969/0.986	0.999/0.998/0.993
$g_1/\mu_{g_1}/\sigma_{g_1}$	3/3/3	g/g/g	0.992/0.989/0.994	0.994/0.994/0.993
$g_2/\mu_{g_2}/\sigma_{g_2}$	3/3/3	g/g/g	0.995/0.986/0.999	0.999/0.999/0.991

R^2 evaluated by Monte Carlo integration at 10,000 points

correlation: g (gauss), e (exponential), ge (general exponential), s (spline)

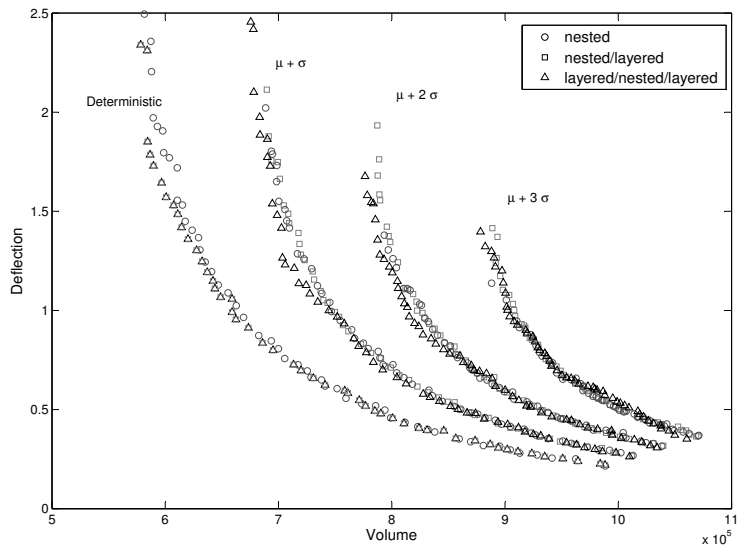

Figure 4: Robust Pareto fronts.

different approaches. As the volume increases the robust Pareto fronts are closer to the deterministic one, hence the designs are less sensitive to variations in the random parameters. The computational costs of each approach in terms of the number of simulator calls are discussed below:

$$N_n = N_{pop} N_{gen} N_{MC} N_k = 50 \times 100 \times 10,000 \times 3 = 1.5e8 \quad (15)$$

$$N_{n/l} = N_{pop} N_{gen} N_{DOE_{M2}} = 50 \times 100 \times 20 \times 3 = 3.0e5 \quad (16)$$

$$N_{l/n/l} = N_{DOE_{M1}} N_{DOE_{M2}} = 30 \times 20 = 600 \quad (17)$$

where N_{pop} is the population size; N_{gen} is the number of generations; N_{MC} is the Monte Carlo size; N_k is the number of parameter k values; $N_{DOE_{M1}}$ is the DoE size used in metamodel level 1; and $N_{DOE_{M2}}$ is the DoE size used in metamodel level 2. The proposed approach allows one to reduce the number of simulator calls by six and three orders of magnitude respectively in comparison to the nested and the nested/layered approaches. It is also worth noting that the proposed approach does not require further simulator runs to obtain Pareto fronts with different levels of robustness.

4 Conclusion and future prospects

An approach based on Kriging models to efficiently include the uncertainty quantification in the optimization procedures has been proposed. The proposed methodology allows one: (1) to appraise the robustness of each design using a reduced number of simulator runs compared with conventional methods; (2) to solve the MORO problem in a single-loop optimization assisted by Kriging models; and (3) to obtain multiple solutions to the MORO problem with different levels of robustness of both the objective functions and the constraints, without additional simulator calls.

The results show that the proposed method has the potential to obtain solutions with reasonable accuracy and a considerably lower number of function calls than conventional methods. For the studied case, Kriging models have been shown to be suitable for surrogating the simulator, allowing to estimate the statistical moments efficiently compared with conventional methods. It is also worth noting that the metamodels created during the optimization can be employed in new optimization processes or computationally demanding applications.

The proposed approach is well suited for the multi-objective robust optimization of problems that involve computationally demanding objective functions and/or implicit constraints (FEA). In future works this approach will be applied to higher dimensionality structural problems and different formulations of the MORO problem.

Acknowledgement

The work presented in this paper was carried out with the support of the Spanish Ministry of Economy and Competitiveness under DPI2011-26394 research project. Its support is greatly appreciated.

References

[1] Gunawan, S. and Azarm, S., Multi-objective robust optimization using a sensitivity region concept. *Structural and Multidisciplinary Optimization*, **29**, pp. 50–60, 2005. 10.1007/s00158-004-0450-8.

[2] Deb, K. and Gupta, H., Introducing robustness in multi-objective optimization. *Evol Comput*, **14**, pp. 463–494, 2006.

[3] Li, M., Azarm, S. and Aute, V., A multi-objective genetic algorithm for robust design optimization. *Proceedings of the 2005 conference on Genetic and evolutionary computation*, ACM: New York, NY, USA, GECCO '05, pp. 771–778, 2005.

[4] Hu, W., Li, M., Azarm, S. and Almansoori, A., Multi-objective robust optimization under interval uncertainty using online approximation and constraint cuts. *Journal of Mechanical Design*, **133(6)**, p. 061002, 2011.

[5] Shimoyama, K., Lim, J.N., Jeong, S., Obayashi, S. and Koishi, M., Practical implementation of robust design assisted by response surface approximation and visual data-mining. *Journal of Mechanical Design*, **131(6)**, p. 061007, 2009.

[6] Erfani, T. and Utyuzhnikov, S.V., Control of robust design in multiobjective optimization under uncertainties. *Structural and Multidisciplinary Optimization*, **45**, pp. 247–256, 2012.

[7] Mattson, C.A. and Messac, A., Pareto frontier based concept selection under uncertainty, with visualization. *Optimization and Engineering*, **6**, pp. 85–115, 2005.

[8] Eldred, M.S., Giunta, A.A., S. F. Wojtkiewicz, J. and Trucano, T.G., Formulations for Surrogate-Based Optimization Under Uncertainty. *Proceedings of the 9th AIAA/ISSMO Symposium on Multidisciplinary Analysis and Optimization*, Atlanta, 2002.

[9] Krige, D.G., A statistical approach to some basic mine valuation problems on the witwatersrand. *Journal of the Chemical, Metallurgical and Mining Society of South Africa*, **52(6)**, pp. 119–139, 1951.

[10] Kleijnen, J.P., Kriging metamodeling in simulation: A review. *European Journal of Operational Research*, **192**, pp. 707–716, 2009.

[11] Jones, D.R., A taxonomy of global optimization methods based on response surfaces. *Journal of Global Optimization*, **21**, pp. 345–383, 2001.

[12] Sacks, J., Welch, W.J., Mitchell, T.J. and Wynn, H.P., Design and analysis of computer experiments. *Statistical Science*, **4(4)**, pp. 409–435, 1989.

[13] Meckesheimer, M., Booker, A.J., Barton, R.R. and Simpson, T.W., Computationally inexpensive metamodel assessment strategies. *AIAA Journal*, **40**, pp. 2053–2060, 2002.

[14] Messac, A. and Ismail-Yahaya, A., Multiobjective robust design using physical programming. *Structural and Multidisciplinary Optimization*, **23**, pp. 357–371, 2002. 10.1007/s00158-002-0196-0.

This page intentionally left blank

Simplified structural analysis of steel portal frames developed from structural optimization

H. K. Issa
Faculty of Engineering Soran University, Kurdistan Region of Iraq

Abstract

A parametric study, based on design optimization using distributed genetic algorithm, is conducted to develop a reliable design procedure for steel portal frames. The efforts are made to modify distributed genetic algorithm in order to enhance the quality of performance and accelerate the convergence to possible optimum solutions. The modification includes defining a state-of-art mutation scheme and a reproduction procedure. Software called DO-DGA has been developed to handle the design optimization.

The study can help structural designers to work out the member forces required to design the elements of steel portal frames without referring to the complicated structural analysis. Implementing the results of structural optimization by DO-DGA, graphs and tables are developed from which the designers can determine the member forces. The main variables in the parametric study of steel portal frame are the slope of pitched rafter, the applied load to the rafter, the length and height of the haunch and the span of the frame. The procedure is promising since it can bring the design optimization into a daily-use tool in design offices.
Keywords: distributed genetic algorithm, steel portal frame, structural optimisation.

1 Introduction

It has been witnessed that considerable developments have occurred in the Kurdistan region of Iraq during the past few years. Along with the developments many single storey buildings in the form of factories, workshops and showrooms have been constructed. Because of its economy and versatility for large spans in construction of pitched-roofs such as shopping centres, warehouses, retail shops,

WIT Transactions on The Built Environment, Vol 125, © 2012 WIT Press
www.witpress.com, ISSN 1743-3509 (on-line)
doi:10.2495/OP120051

pools, factories, etc, the steel portal frame (SPF) has become the most often used structure within this sector.

Any structural designer attempts to conduct an economical design. This can be achieved by formulating a design problem and solving it by an optimization technique while meeting the requirements of a code of practice to control the safety of the structure [1]. However, large number of iterations in implementing the optimization technique, it cannot be achieved by using the designer's experiences and intuition. As it is believed that the major cost of structural steelwork is its own weight, approaches to minimizing the weight have become increasingly interesting for the researchers.

Any structural system needs to be analyzed before stepping into the design process. Structural optimization techniques offer a sophisticated procedure including several iterations of structural analysis and design until an optimum design solution is achieved. The whole process is time consuming and complicated so that it makes the designers hesitant to apply the techniques to the design of real life structures. Hence, developing a simplified yet comprehensive technique will encourage designers to apply optimization techniques as a daily-use tool in design offices.

In this paper, a modified distributed genetic algorithm (DGA) is implemented to conduct the weight minimization of SPF. Through the design optimization applied to different sizes of SPFs, the author develops a number of graphs and tables from which the structural designers can figure out the member forces and assign sections to the structural components of SPFs. The main privilege of the method is that the designers do not need to carry out the complicated analysis procedure.

2 Distributed genetic algorithm

The basic mechanism of the genetic algorithm (GA) is based on randomised procedures of selecting and reproduction of the population of individuals and copying the fittest individuals into the next generation. A GA moves from one generation to another until either a certain individual dominates over population or a predetermined maximum number of generations is reached. A basic GA consists of three main operators; reproduction, crossover and mutation. In the reproduction stage, a set of population is selected for mating depending on their fitness values which represent the objective function. If any constraint is violated, a penalty is applied to the objective function. The value of the penalty is related to the degree in which the constraints are violated. Then each individual undergoes crossover and mutation based on the predetermined probability values.

Many researchers have examined GA and have yielded satisfied results. They have applied different genetic operators to enhance the performance quality of GA. Toropov and Mahfouz [1] modified GA to improve its rate of convergence. The modified GA was linked to a system of structural design rules, interacting with a finite element package in order to obtain minimum weight designs of plane structural steel frames. Camp *et al*. [2] used three crossover schemes;

fixed, flexible, and uniform to minimize the weight of the structure. Kameshki and Saka [3] applied a GA for optimum design of unbraced multi-storey frames with semi-rigid beam-to-column connection. Saka [4] studied optimum design of pitched roof SPFs using GA. Degertekin *et al*. [5] implemented GA to investigate the optimal load and resistance factor design. These researchers have applied simple GA to minimize the weight of steel structures.

Another form of modification in GA is DGA. In DGA, the performance of the conventional GA is improved by some minor modifications in its main algorithm that leads to quicker convergence and higher searching capability compared to conventional GA [6]. Adopting the migration idea of the population, DGA uses a number of population groups and implements genetic operations in parallel for all populations existing in different groups. Then the best populations of each group migrate to another group, making them possible to contribute in quicker converge than GA into an optimum solution.

In this study, a DGA has been modified for the purpose of improving the algorithm performance and saving the computation time in convergence into an optimum solution. For this purpose software coded by Visual Basic 6.0, called design optimization with distributed genetic algorithm (DO-DGA) has been developed to conduct the optimization process. The main aspects of modification are introducing twin analogy and a state-of-art mutation scheme [7] as follows:

- Although twin is not meaningful in genetic algorithm, DO-DGA had adopted this idea to produce more offspring. As the best parents in the population can give better offspring, a probability has been assigned to the parents that allow them to undergo crossover operation twice resulting in producing more offspring. This will make it possible to increase the number of better individuals among the population of the group.
- In contrast to the literatures which have addressed a constant value for mutation probability, DO-DGA uses a variable mutation probability. This assists the algorithms to make more diversity among population and consequently more feasible design spaces can be employed to reach the fittest individuals. Reaching to global optimum requires best diversity among population. The mutation probability can be formulated as follows:

$$P_m^{G_C} = P_m^{\max} - \frac{e^{-1/20} - e^{-G_C/20}}{e^{-1/20} - e^{-N_G/20}}(P_m^{\max} - P_m^{\min}) \tag{1}$$

  where P_m^{Gc}= mutation probability of the current generation; P_m^{max} and P_m^{min}= maximum and minimum mutation probabilities; G_C = number of current generation; and N_G = number of predetermined generations.
- The algorithm uses a DO-DGA penalty function when the aim is to minimize the weight as below:

$$C = \begin{array}{l} \text{If } g_i \le 0 \\ \text{If } 0 < g_i \le 1 \\ \text{If } g_i > 1 \end{array} \tag{2}$$

whereby the fitness function is defined as follows:

$$F = W(1 + C) \tag{3}$$

where g_i = value of constraint i; F = fitness value; W = total weight of frame; and C = penalty value.

In addition to those modifications, DO-DGA uses a general stiffness matrix for both prismatic and non-prismatic developed by Issa and Mohammad [8].

3 Optimum design to Eurocode 3

Eurocode 3 states that when an elastic analysis is used for the design of steel frames such as the one shown in fig. 1, the section capacity and buckling resistance should be calculated. The interaction effect of axial compressive and bending moment stresses should be verified to make sure the capacity of section required to withstand the compressive stress which may end up with lateral torsional buckling and overall buckling failures in beam-column members. It is required to use the effective length equal to that between two intermediate restraints to check the buckling resistance.

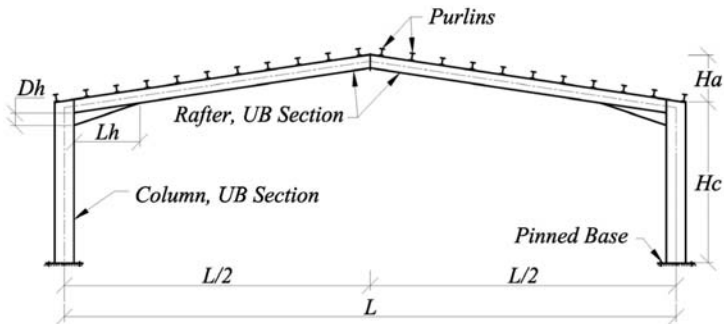

Figure 1: Typical pitched roof steel portal frame.

In the design of pitched roof SPF, it is common to have the same universal beam section for rafters and a different universal beam sections for the columns. For the reason of economy, the same section of rafter is used to produce the haunch. Therefore, the optimum design of the pitched roof steel portal frame necessitates using two design variables; one for rafter and its haunch and another for the columns. However, if it is necessary to use different section for the haunched part, the number of design variables increases to three.

The design of pitched roof SPF with haunched eaves, when the objective is obtaining minimum weight and the constraints are implemented according to Eurocode 3 has the following form of formula:

$$\text{Minimize } W = \sum_{i=1}^{ng} \gamma_{im} \sum_{j=1}^{nm} V_j \tag{4}$$

Subjected to:

- Displacement and deflection

$$\delta_i \le \delta_{iu} \quad i=1, 2, 3 \ldots, nj \tag{5}$$

$$\Delta_j \le \Delta_{ju} \; j=1,2, \quad nm \tag{6}$$

- Strength

$$M_{xj} \le M_{cxj} \; j=1,2, \ldots nm \tag{7}$$

$$M_{xj} \le M_{bj} \; j=1,2, \ldots nm \tag{8}$$

$$\frac{P_j}{P_{bxj}} + k_{xx} \frac{M_{xj}}{M_{cxj}} \le 1 \; j=1, \ldots nm \tag{9}$$

$$\frac{P_j}{P_{bxj}} + k_{xx} \frac{M_{xj}}{M_{bj}} \le 1 \; j=1, \ldots nm \tag{10}$$

$$\frac{P_j}{P_{byj}} + k_{yx} \frac{M_{xj}}{M_{bj}} \le 1 \; j=1, \ldots nm \tag{11}$$

- Dimension

$$B_{fbk} \le B_{fck} \; k=1, 2, 3 \ldots nj \tag{12}$$

Where, W = total weight of frame; ng = number of member groups; γ_m = unit weigh of the member group; nm = number of members in a group; V_j = volume of member j; nj = total number of joints; δ_i = horizontal and vertical displacements of joint i, δ_{iu} = upper limit of displacements; Δ_j = maximum deflection of member j; Δ_j = maximum allowable deflection; M_{xj} = maximum bending moment about major axis; M_{cxj} = bending moment capacity of member j; M_{bj} = lateral torsional buckling resistance moment; P_j = axial member force of member j; P_{bxj} and P_{byj} = buckling capacity of member j about major and minor axes respectively; k_{xx} and k_{yx} = interaction factors depend on equivalent moment factor; B_{fbk} and B_{fck} = width of the beam and column at the intersection joint respectively.

Eqn. (5) verifies the displacement of the joints. Eqn. (6) verifies the deflection of members. Eqn. (7) checks the moment capacity of the member section-section and Eqn. (8) makes sure that the lateral torsional buckling does not take place. Eqns. (9 - 11) verify the interaction of axial compressive and bending moment stresses. Eqn. (12) should be applied to the joint of beam-column connection to keep the width of beam not greater than the width of column.

As the nature of the structural optimization variables is discrete, the solution of the optimum design problem given in Eqn. (4) necessitates selecting universal beam section from the table of standard section for rafters, columns and haunched section.

4 Parametric studies

In this section, the relationships between structural parameters of SPF, such as span length, haunch length, loads and member forces are illustrated. A SPF with varied span, angle of pitched-roof, and applied loads is employed to conduct the other parametric studies such as the pitch angle-weight relationships and coefficients of bending moments, shear forces, and axial forces. As shown in fig. 2, the frame is assumed to experience a uniform factored load, w. The reason for the parametric study is to have an insight for the structural engineers to calculate bending moments, shear forces and axial forces induced in SPFs' members.

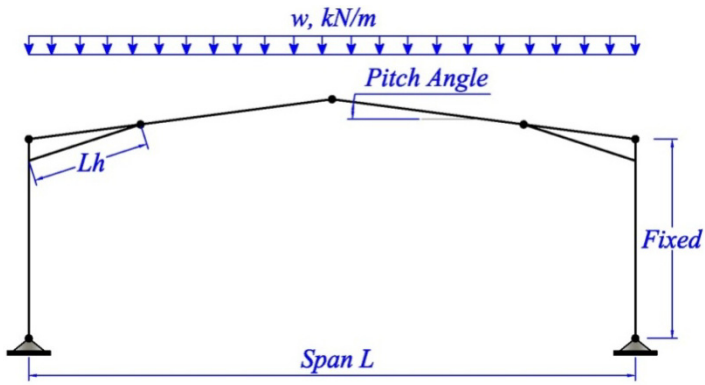

Figure 2: The SPF for the parametric studies.

4.1 Role of haunch

A number of optimum solutions with similar column and rafter cross-sections were selected to investigate the effect of haunch on the lateral displacement and the average strength ratio of SPFs. Lateral displacement ratio is joint's displacement/allowable displacement and strength ratio is member's strength/induced stress. The surface area of haunch that is taken into account involves a product of the depth and the length of haunch. Fig. 3 shows that there is a proportional relationship between the surface area of haunch and the average displacement ratio, i.e. the optimum solution with smaller average displacement ratio has smaller haunch length and depth and vice versa. In contrast, there is an inverse relationship between the surface area of haunch and the average strength ratio as shown in fig. 4, i.e. the optimum solution that possesses higher strength ratio has smaller haunch length and depth. This demonstrates the influential role of the haunch in controlling the displacement rather than strength. This implies that the construction of the haunch depends much more on displacement rather than the large bending moment.

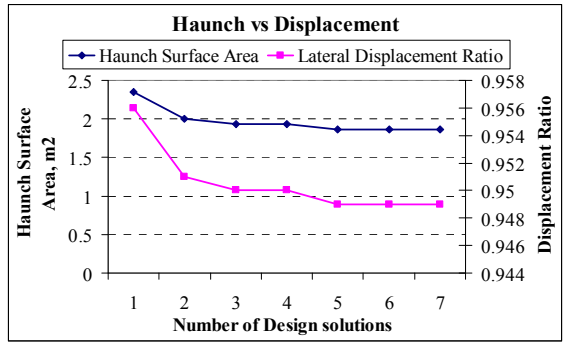

Figure 3: Surface triangular area of haunch versus lateral displacement of SPF.

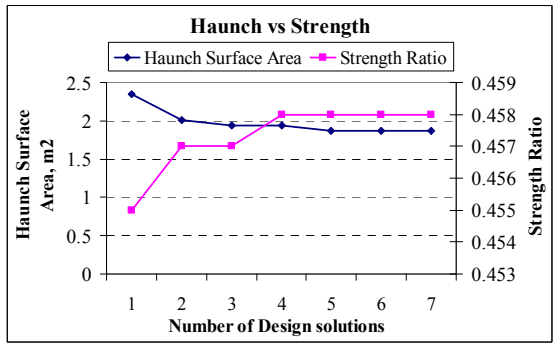

Figure 4: Surface triangular area of haunch versus strength ratio of SPF.

4.2 Weight-pitch angle relationships

The study investigated the relationship between weight of optimum solution and the pitch angle of SPF with different spans and applied loads. In general, the results show that increasing pitch angle decreases the weight of SPF. Although the same steel sections are assigned to the member cross-sections, the dimensions of haunch are reduced due to a decrease in displacement made by increasing the pitch angle. This is why the weight is slightly reduced.

4.3 Members forces coefficients

Fig. 5 depicts the relationship between the span of SPF and the ratio of positive to negative bending moments at the rafter. It can be seen that as the span increases the positive to negative bending moment ratio drops. It can be pointed out that for smaller span the positive moment is critical, whereas for the larger span the negative bending moment will control the design, as clearly shown in figs. 6 and 7. The coefficient has to be multiplied by wL^2, where w is the factored applied load and L is the span of SPF, in order to find the bending moments.

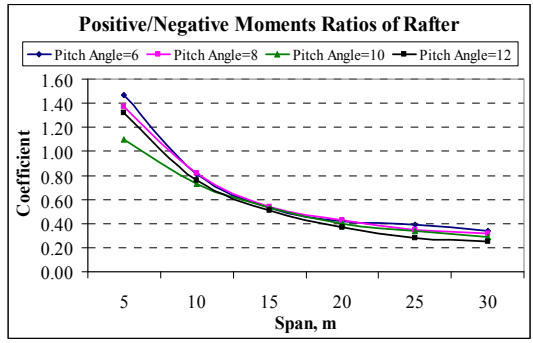

Figure 5: Relationships between the rafter positive/negative moments ratio and span.

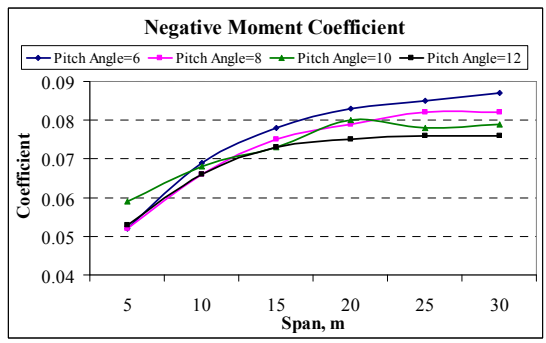

Figure 6: Relationships between the coefficient of negative moment and span.

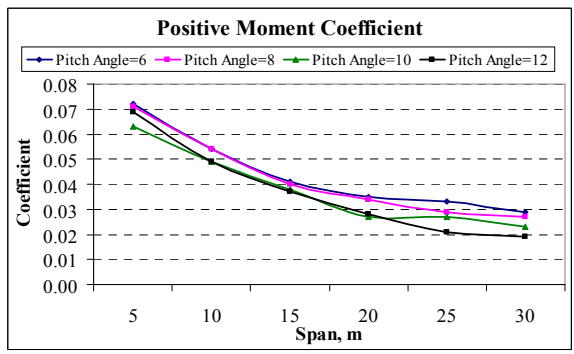

Figure 7: Relationships between the coefficient of positive moment and span.

Including the frame's self weight, the relationship between the span and coefficients of maximum axial and shear forces at column and rafter are illustrated in fig. 8 through fig. 10 with different pitch angle. There are sharp increases in axial force at column and rafter as length of span increases, whereas this change is smoother for the maximum shear coefficient at the rafter. The pitch angle does not have significant effects on the maximum axial force at column and rafter, but it does affect the value of shear force at the rafter. The coefficient must be multiplied by wL, in order to find the shear and axial forces in structural members.

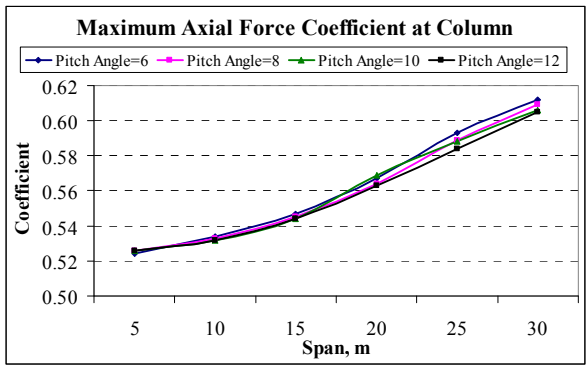

Figure 8: Relationships between the coefficient of column axial force and span.

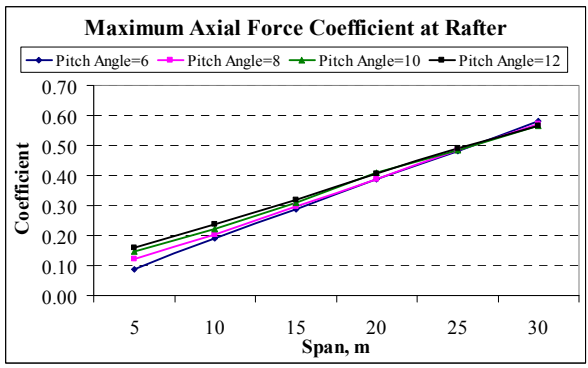

Figure 9: Relationships between the coefficient of rafter axial force and span.

4.4 Haunch length

Fig. 11 shows that the role of haunch is substantial when the span of SPF is between 10m and 20m. The role of haunch is less effective for the SPF with the span of less than 10m or greater than 20m. This is because the frame is controlled by strength when the span of SFP is less than 10m or greater than 20m.

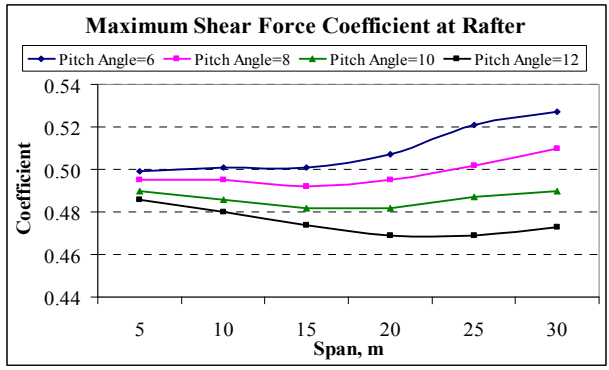

Figure 10: Relationships between the coefficients of rafter shear force and span.

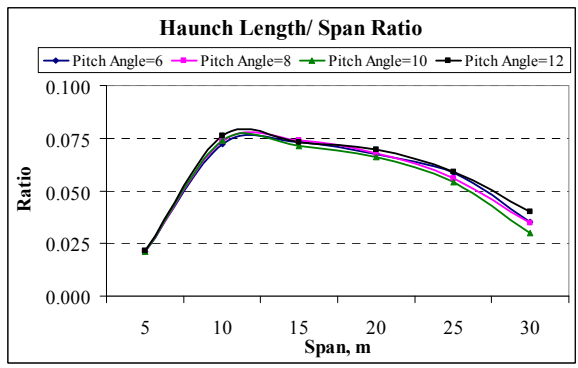

Figure 11: Relationships between the span and the haunch length/span ratio.

5 Numerical example

A numerical example is conducted to demonstrate the effectiveness of the simplified method of analysis. The frame shown in fig. 12 is used for the analysis with a uniform factored gravity load of 15kN/m. The SPF of the example has a 20m span. The length of haunch is 1.4m as calculated from fig. 11. The slope of the pitched roof is assumed to be 10˚.

The results of the simplified method of analysis and the actual analysis using matrix analysis method are tabulated in table 1.

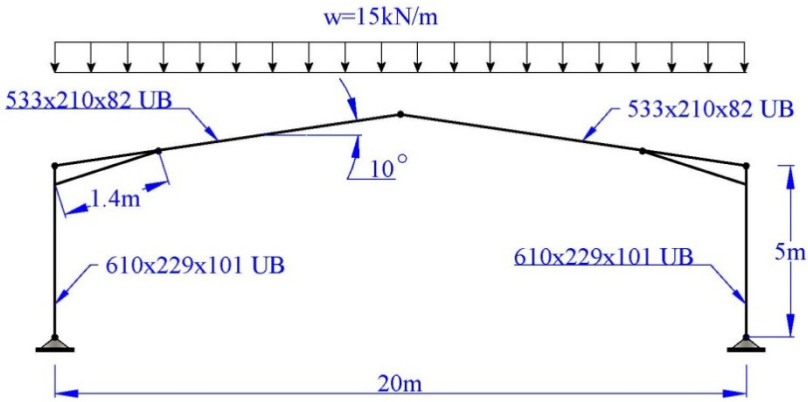

Figure 12: The SPF used in the numerical example.

As can be seen in table 1, there is a small difference between the results obtained by the simplified method of analysis and the analysis that has been conducted by matrix method of analysis. The maximum difference yielded does not exceed from 3%.

Table 1: The results yielded from the analysis of SPF in the numerical example.

Method of Analysis	Axial Force, Column	Axial Force, Rafter	Shear Force, Rafter	Negative Moment, Rafter	Positive Moment, Rafter
Simplified Method	171 kN	120 kN	145 kN	468 kN.m	174 kN.m
Matrix Method	167 kN	120 kN	142 kN	466 kN.m	178 kN.m

6 Conclusion

A parametric study was conducted to develop a simplified method of structural analysis for SPF through generated graphs used to determine the member forces. The graphs were constructed based on the solutions offered by a structural optimization technique. The developed graphs are easy to use and seem totally practical.

A modified DGA was used to perform the structural optimization process on SPFs. The modification includes using a variable mutation probability and twin analogy to bring the elite individuals into the genetic operations twice while they are already secured to be dropped into the next generation. DO-DGA software handles the structural optimization using modified DGA. It can obtain the optimum solutions of SPFs within a few minutes.

Applying DO-DGA to develop graphs will make it possible for an engineer to determine all member forces of SPFs required for design of cross-sections without carrying out the structural analysis procedures provided that the applied loads, pitch angle and span length are given. Consequently, it can save the time of calculations.

Applying a numerical example, it is demonstrated that there is no considerable difference between the simplified method of analysis using graphs and the conventional matrix method of analysis. This proves that the graphs are valid and promising since they can expedite bringing the usage of optimization technique into daily office-use by structural engineers.

References

[1] Toropov, V.V., and Mahfouz, S.Y., Design optimization of structural steelwork using a genetic algorithm, FEM and a system of design rules. *Engineering Computations,* **18 (3/4)**, pp. 437–459, 2001.

[2] Camp, C., Pezeshk, S., and Cao G., Optimum design of two-dimensional structures using a genetic algorithm. *ASCE Journal of Structural Engineering*, **124 (5)**, pp. 551–559, 1998.

[3] Kameshki, E.S., and Saka, M.P., Optimum design of non-linear steel frames with semi-rigid connection using a genetic algorithm. *Computer and Structures*, **79**, pp. 1593–1604, 2001.

[4] Saka, M.P., Optimum design of pitched roof steel frames with haunched rafter by genetic algorithms. *Computers and Structures*, **81**, pp. 1967–1978, 2003.

[5] Degertekin, S.O., Saka, M.P., and Hayalioglu, M.S., Optimal load and resistance factor design of geometrically nonlinear steel space frames via tabu search and genetic algorithm. Engineering Structures, 30, pp. 197–205, 2008.

[6] Mühlenbein, H., Schomisch, M., and Born, J., The parallel genetic algorithms as a function optimizer. *Parallel Computing*, **17**, pp. 619–632, 1991.

[7] Issa, H.K, and Mohammad, F.A. Effect of mutation schemes on convergence to optimum design of steel frames. *Journal of Constructional Steel Research*. **66**, pp. 954–961, 2010.

[8] Issa, H.K, and Mohammad, F.A Practical non-prismatic stiffness matrix for haunched-rafter pitched-roof steel portal frames. (Book Chapter) *Challenges, Opportunities and Solutions in Structural Engineering and Construction*. ed. N. Ghafoori, CRC Press: Las Vegas, pp. 167–171, 2010.

Structural optimization of high voltage transmission line towers considering continuum and discrete design variables

J. París, S. Martínez, F. Navarrina, I. Colominas & M. Casteleiro
GMNI — Group of Numerical Methods in Engineering,
Civil Engineering School, University of A Coruña, Spain

Abstract

Structural optimization has been usually applied to singular projects (e.g. a dam) and/or to common designs largely repeated (e.g. automotive components), and high voltage transmission towers can be included in both groups since they are expensive and a large number of them is required.

In this paper, the authors propose a general formulation for obtaining the structural optimum design of latticed high voltage towers. The formulation is devoted to obtaining the most common objective in engineering (minimum cost) considering the limitations imposed in actual norms for this kind of structure. According to this idea, real applications are studied and modeled under real conditions (e.g. loads, constraints, building process). Constructive aspects like the specific geometry, the structural elements or the building process are specifically considered. The optimization model proposed also deals with continuum design variables (global geometry variables) and discrete design variables (area, inertia and/or cross section dimensions, for example) both together. The use of both types of design variables is crucial for defining a realistic model that can be used in practical applications in engineering. The optimum design formulation proposed is general and can be easily applied to other different types of 3D latticed structures.

Finally, a real application example of a high voltage tower under real conditions and requirements is analyzed.

Keywords: structural optimization, high voltage towers, discrete design variables, continuum design variables.

WIT Transactions on The Built Environment, Vol 125,
www.witpress.com, ISSN 1743-3509 (on-line)
doi:10.2495/OP120061

1 Introduction

Structural design is a crucial topic in engineering since it allows to propose solutions to multiple challenges in modern societies. Design process has been continuously studied and applied in real problems in engineering and many other disciplines. However, this kind of procedures to propose adequate designs has become insufficient nowadays. Design methods need to be reformulated by including optimization techniques since traditional designs are usually effective but they are not the most efficient, in general.

In this paper the authors propose an optimization methodology that allows to obtain more efficient solutions than conventional designs of high voltage transmission line towers. The optimization model proposed was developed by taking into account specific aspects related to this kind of structures in order to give a realistic approach of the problem. In addition, these practical considerations facilitate the transference of optimized designs from numerical models to industrial applications. According to this idea, the proposed formulation tries to keep the main considerations related to the building process and includes all the design specifications established in the current norms and standards for this kind of structures in Spain. The model proposed includes all the design constraints proposed in the Spanish and European Standards [1, 2], but other similar constraints that could appear in other norms and laws can be easily included [3, 4].

The formulation proposed allows to deal with continuum design variables (related to global geometric properties of the structure) and with discrete design variables (related to cross-section properties of the bars that define the structure) both together. According to this, the methodology proposed deals with the discrete set of commercially available steel rolled sections which are generally used to define the structure of high voltage transmission line towers. In addition, the proposed methodology gives an optimized solution with conventional computing resources in adequate, and perfectly affordable, CPU time.

Finally, a real application example is analyzed in order to test the complete methodology developed and to verify the validity of the results in practical application cases.

2 Structural model

In the introduction section the authors present the main characteristics of the optimization methodology developed for the design of high voltage towers and the practical considerations required to obtain adequate solutions. In real applications, most of this kind of structures correspond to three dimensional latticed structures assembled by joining a set of rolled steel sections. These steel bars usually correspond to symmetric L-shaped cross-sections according to a commercial catalog. In addition, the steel sections are usually bolted in real designs due to practical considerations during the building process. Nowadays there exist rare specific designs with welded joints but they are not commonly used in practice. Consequently, the structural model for this kind of towers corresponds

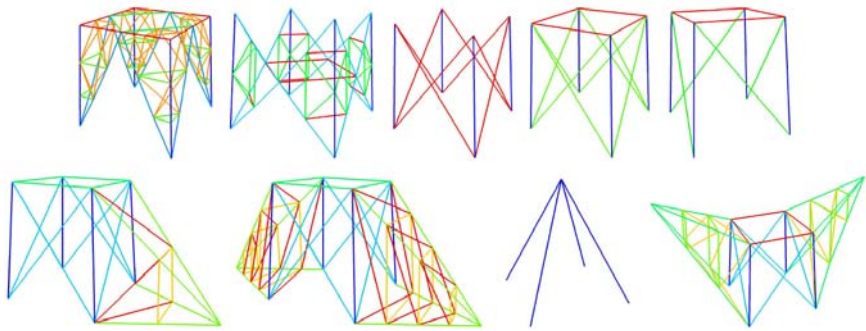

Figure 1: Examples of blocks commonly used in Spanish designs of high voltage towers.

to a 3D lattice of symmetric L-shaped cross-section bars with bolted joints. From a practical point of view, most of the joints of the structure correspond to articulations but there are some of them that correspond to semi-rigid articulations (specially in the vertical bars). From a mathematical point of view the numerical model used to develop the structural analysis corresponds to a 3D articulated bars formulation, since it adequately approximates the structural response. In addition, some important standards like the ones proposed by the ASCE [3, 4] also recommend this kind of numerical models.

Furthermore, high voltage transmission line towers usually have large dimensions (tens of meters high and some meters wide) and are built in practice by assembling a set of smaller blocks with predefined geometric and structural properties. Some of the most frequent blocks used in the Spanish and European towers can be observed in figure 1.

The combination of some of these blocks, with adequate shape and dimensions, produces the final designs which are used in practice (figure 2).

In addition, it is important to take into account that for practical considerations the number of different rolled steel sections per block must be small. In practice, the symmetry of the design and the external forces applied suggest that the cross-section of a number of elements in a block (the vertical bars for instance) must be equal. Thus, each block is usually defined by adequately combining a small number of different rolled steel sections, depending on the complexity of the block. The distribution of different steel rolled sections can be also observed in figure 1.

3 Structural analysis

The structural analysis model proposed in this paper corresponds to an articulated latticed structure made of predefined blocks and normalized steel rolled sections. Consequently, the numerical analysis model under the conventional hypotheses of small displacements, small displacements gradients and linear elasticity

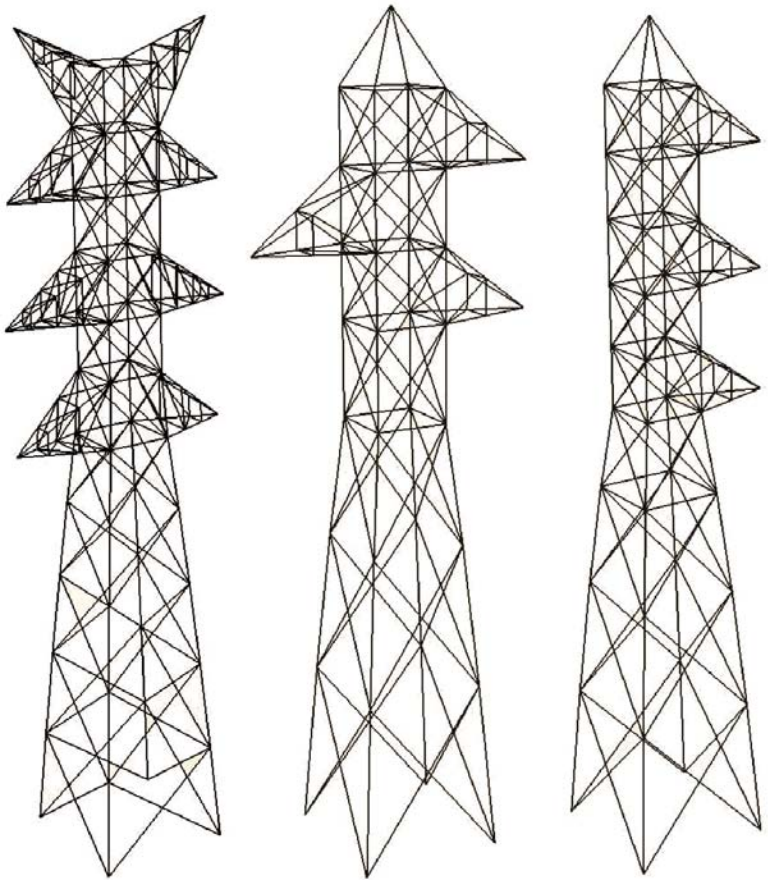

Figure 2: Examples of real designs of high voltage towers.

corresponds to a 3D analysis of articulated latticed structures. Furthermore, the Spanish and European Standards and Norms corresponding to this kind of structures [1, 2] impose a set of load cases and additional design constraints. The Spanish Standard [2] states that five different loads must be considered:

- Self weight of the tower and the conductors
- Ice load on the full length of the conductors
- Wind load on the tower and on the conductors
- Tension imbalance of the conductors connected to the tower on both sides along the line.
- Collapse of one conductor.

Figure 3 shows the displacements of a general design of a high voltage transmission line tower for the loads indicated in the actual Spanish Norm [2].

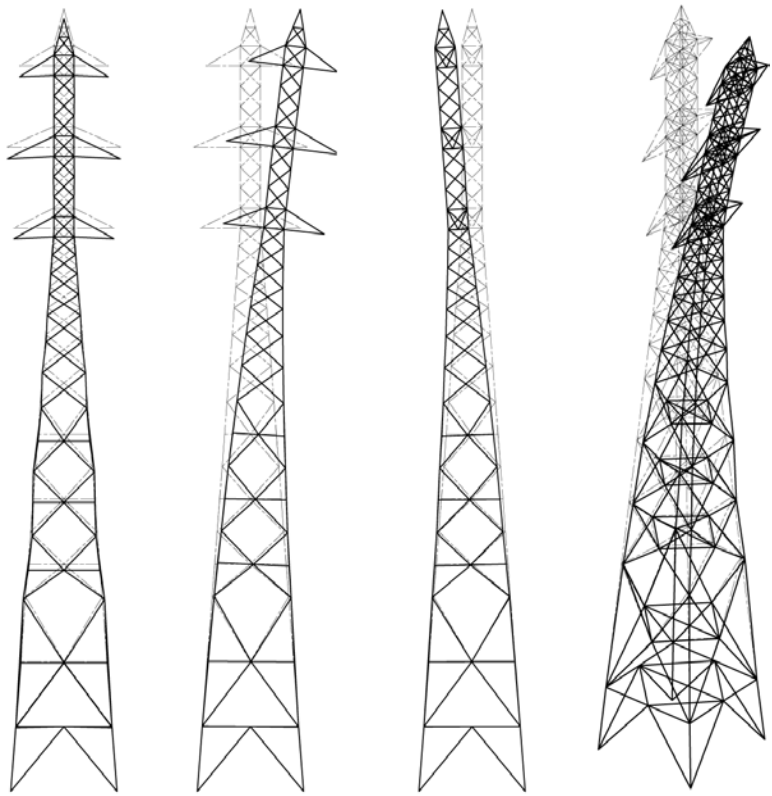

Figure 3: Displacements of a high voltage transmission line tower for (from left to right): ice load, wind load, tension imbalance of the conductors and collapse of one conductor.

The combination of these loads produces more than 7 different load cases. For each one of the indicated load cases, the structure must satisfy design constraints on:

- Elemental shape-section ratio: The section of the bars that define the structure corresponds to symmetric L-shaped sections. This kind of sections can be identified by the thickness and the length of their legs. The Spanish and European Standards [1, 2] impose a maximum value for the ratio between the length and the thickness of the cross-section legs in order to avoid local buckling.
- Elemental section-length ratio: The ratio between the radius of gyration of the cross-section and its length must satisfy a minimum value. This constraint is also related to buckling phenomena and it will be used further in the definition of other additional constraints.

- Elemental tension limits: Each bar of the structure must satisfy the maximum tension stress of the material for each load case. Otherwise the structure will collapse.
- Elemental compression limits: Each bar of the structure must satisfy the minimum compression stress of the material being used for each load case. In addition, this constraint must guarantee that global buckling of bars do not appear. This buckling constraint is considered by taking into account the value of the section-length ratio proposed in the second item.

In practice, the proposed problem involves at least 7 load cases and each load case requires the verification of tension stress, compression stress and buckling constraints for each bar of the structure. In addition, geometrical constraints related to shape and dimensions of the bars need to be considered.

4 Design model

The structural model proposed in the previous section deals with realistic considerations that must be satisfied in order to accomplish with the Spanish and European Standards. The design model must allow to verify all these constraints and to improve the design without loosing any of the main properties of the conventional designs used in practice. Thus, the design model proposed must keep the modular construction by assembling blocks of predefined typologies vertically. In addition, the sections of the bars that define the structure must correspond to one of the normalized steel rolled sections defined in Spanish and European Standards and Norms due to economic and practical considerations. In addition, the multiple sections of the bars that define a block must be treated in groups according to their structural properties, as it can be observed in figure 1. Thus, the bars of each group present identical cross-sectional properties and dimensions.

According to these ideas the design model must include discrete design variables related to the cross-section properties of the groups of bars defined. These design variables can only take a set of predefined values established on normalized steel rolled sections catalogs. On the other hand, it is also important to allow the modification of the external geometry of the high voltage tower in order to improve the design. Consequently, the main dimensions of the blocks of the structure can be also included as design variables in the optimization problem. The formulation proposed includes the dimensions (width and length) of the upper and lower bases of the blocks as design variables. The heights of the blocks are treated as design constants in this paper. However, the inclusion of the heights of the blocks as design variables should not increase substantially the complexity of the underlying optimization problem. The geometrical design variables proposed can be included in the model as continuum variables since the length of each bar can be easily adjusted during the constructive process.

Thus, the design model proposed to optimize the structure of high voltage transmission line towers includes both continuum and discrete design variables. This fact introduces even much more complexity in the model than the large number of constraints and load cases presented in section 3. The use of both

types of variables in one optimization model is a challenging problem nowadays, specially when realistic studies with a large number of design variables and constraints needs to be addressed. Conventional algorithms can not deal with discrete design variables and special algorithms that consider discrete variables are not efficient enough to manage a large number of discrete design variables and constraints. Specific algorithms like evolutionary methods or genetic algorithms have been used in the literature [5] but most of the practical considerations proposed in this paper were not stated. In practice most of the works related to this topic only study the discrete or the continuum problem. As far as the authors know both types of design variables (continuum and discrete) have not been previously treated in real applications related to the main objective of this paper.

5 Optimization algorithm

The optimization problem stated in the design model section presents crucial aspects that can not be treated with conventional optimization algorithms. According to that and considering previous works related to this topic [5–7], the authors propose an optimization methodology based on heuristic approaches. More specifically, the authors have developed a numerical model based on Simulated Annealing [8–13] since this formulation can include natively continuum and discrete design variables and it obtains optimal solutions for real cases in an acceptable computing time.

This algorithm is based on heuristic rules that allows to simulate the minimization problem defined in the previous sections by assuming that the optimization process is analogous to the cooling and annealing of metals in metallurgy. Furthermore, this formulation also allows to include design constraints. However, this optimization algorithm requires to compute and verify a large number of designs. The analysis of the structural problem and the verification of all the stress constraints is not critical from a computational point of view. However, the large number of designs to be analyzed turns the CPU time a critical aspect. Consequently, the authors have developed a numerical approximation of the objective function and the constraints based on first order Taylor expansions in order to reduce the required computing time. These Taylor expansions of the objective function and the design constraints allow to verify a large number of modified designs with a relatively small computing effort. On the other hand, first order derivatives of the objective function and the constraints needs to be computed. These derivatives are obtained analytically by using direct differentiation techniques [6, 7, 14, 15] in order to avoid propagation of rounding errors and to reduce the computing time required.

Design constraints are included in the optimization methodology by using penalty functions to define the objective function. In addition, normalized values of the objective function and the constraints are used in practice in order to avoid scale problems due to different natures of the objective function (the weight of the structure) and the design constraints (geometrical dimensions, stresses, ...). The objective function is normalized by dividing the current weight over the initial

weight, and design constraints are normalized by dividing its value (computed as the difference between the computed values and a established maximum) over the maximum value allowed. This formulation allows to obtain adequate sensitivities for applying Taylor expansions at each global iteration of the simulated annealing process. The use of Taylor expansions allows to drastically reduce the computing effort devoted to explore and study neighbor designs of a previous solution. In practice the computing time devoted to this exploration of the neighborhood can be reduced two orders of magnitude without loosing suitable precision in the computations.

However, it is obvious that first order Taylor expansions introduce considerable error if great modifications are applied. To avoid this effect, the modification of continuum variables is limited by using moving limits around the design solution previously obtained. The values for the discrete design variables are stated by searching adequate solutions on the neighborhood of the current design. This exploration is performed by considering increasing levels of neighborhood. First exploration tries to find an improved solution in the first set of contiguous values for each discrete design variable. If no adequate solution is found then a second level of neighborhood is also explored for the discrete design variables and so on. Moving limits of continuum design variables are also amplified. If no improvements are achieved after increasing the level of neighborhood up to a certain predefined limit, the search on discrete design variables stops since no better solution can be achieved.

6 Application example

The validity of the formulation presented in previous sections is developed by solving a real application example. In this paper, the authors present the solution obtained for the structural optimization of a 400 kV transmission line tower with double circuit and two ground conductors on top. These towers are 41.20 m tall and present 7 different types of blocks, 66 groups of bars defined with normalized steel rolled sections and 32 continuum geometrical variables. In this case, the current Spanish Norm [2] imposes more than ten thousand design constraints that need to be considered during the optimization process.

Figure 4 (left) shows the initial geometry and materials for one of the actual designs commonly used in Spain in this kind of high voltage transmission lines. Figure 4 (right) shows the final optimized design obtained by using the methodology proposed in this paper. The use of the optimization formulation allows to reduce 25.7 % of the initial weight of an actual design without modifying neither the topology nor the constructive process.

7 Conclusions

In this paper the authors develop an entire optimization methodology that allows to minimize the weight of high voltage transmission line towers by satisfying all

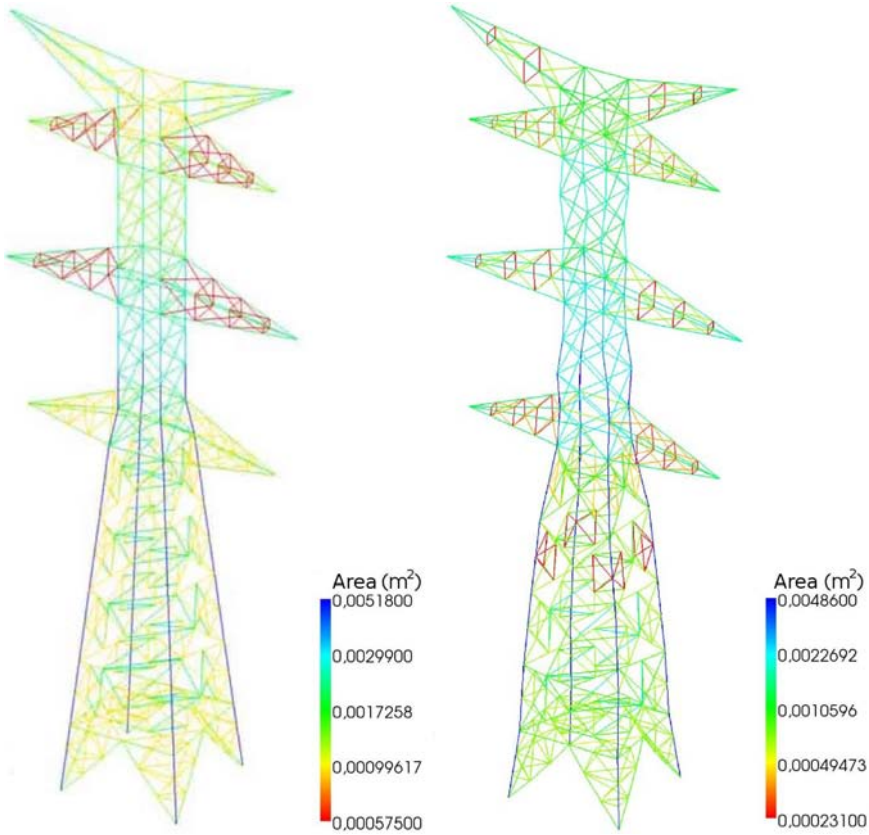

Figure 4: Initial design of the high voltage tower (left) and final optimized design (right).

the requirements imposed in the European and Spanish Standards and Norms [1, 2]. The formulation proposed is realistic and it considers all the practical specifications required during the constructive process. The optimal designs obtained satisfy all the specifications included in the actual norms and can be directly applied in practice since they satisfy all the safety conditions imposed. According to this idea, real structural models are analyzed by using 3D articulated latticed structure models. These models are defined by assembling a set of predefined blocks according to the conventional constructive process.

In addition, the optimization model allows to deal with continuum design variables that define the global geometry of the structure and discrete design variables that correspond to the set of commercially available rolled steel sections. Consequently, the optimization problem can not be treated with conventional optimization algorithms.

The proposed formulation allows to obtain important material savings in real application examples in an acceptable computing time.

Acknowledgements

This research work has been partially supported by the "Ministerio de Ciencia e Innovación" of the Spanish Government (DPI2009-14546-C02-01 and DPI2010-16496), by the Autonomous Government of the "Xunta de Galicia" (Grants CEOU 2007/09, PGDIT09MDS00718PR and PGDIT09REM005118PR) cofinanced with FEDER funds, by the "Universidade da Coruña" and by the "Fundación de la Ingeniería Civil de Galicia".

References

[1] European Committee for Standardization, EN 1993 - Eurocode 3: Design of steel structures, 1994.
[2] *Ministerio de Industria, Turismo y Comercio* (Spanish Ministry of industry, tourism and trade), *Reglamento sobre condiciones técnicas y garantías de seguridad en líneas eléctricas de alta tensión y sus instrucciones técnicas complementarias ITC-LAT 01 a 09* (Spanish Standard about high voltage transmission lines), *Boletín Oficial del Estado del 15 de Febrero de 2008*, pp. 16436-16554, 2008.
[3] American Society of Civil Engineers, ASCE 1097: Design of Latticed Steel Transmission Structures, 1997.
[4] American Society of Civil Engineers, ASCE Manual 52: Design of Steel Transmission Towers, 1988.
[5] Vieswara Rao G., Optimum Design for Transmission Line Towers, Computers and Structures, Vol. 57(1): 81–91, 1995.
[6] Navarrina F., Valera A., París J., Colominas I., Casteleiro M., Optimization of High Tension Towers by Sequential Linear Programming with Quadratic Line Search, Proceedings of the Ninth International Conference on Computer Aided Optimum Design in Engineering, Skiathos, Grecia, 2005.
[7] París J., Martínez S., Navarrina F., Colominas I., Casteleiro M., Structural Optimization of High Tension Towers, Proceedings of the 2^{nd} International Conference on Engineering Optimization, Lisbon, Portugal, September 6-9, 2010.
[8] Kirkpatrick S., Gelat C. D., Vecchi M.P., Optimization by Simulated Annealing, Science, New Series, Vol. 220(4598):671–680, 1983.
[9] Ledesma S., Aviña G., Sánchez R., Practical Considerations for Simulated Annealing Implementation, Simulated Annealing, Vol. 20:401–420, 2008.
[10] Lundy M., Mees A., Convergence of an Annealing Algorithm, Mathematical Programming, Vol. 34:111–124, 1986.
[11] Wah B. W., Chen Y., Wang T., Theory and Applications of Simulated Annealing for Nonlinear Constrained Optimization, Simulated Annealing, 9:155–187, 2008.

[12] White S. R., Concepts of Scale in Simulated Annealing, Proceedings of the IEEE International Conference on Computer Design, Port Chester, USA, pp. 646-651, 1984.
[13] Cruz J. R., Dorea C. C. Y., Simple Conditions for the Convergence of Simulated Annealing Type Algorithms, Journal of Applied Probability, Vol. 35(4): 885-892, 1998.
[14] Schmit L. A., Structural design by systematic synthesis, Second Conference on Electronic Computation, Pittsburg, USA, pp. 105-132, 1960.
[15] Choi K. K., Kim N., Structural Sensitivity Analysis and Optimization, Mechanical Engineering Series, Springer, 2004.

This page intentionally left blank

Heuristic optimization of short corbels by smeared cracking finite element analysis

G. Rojas[1], P. Rojas[1], F. González-Vidosa[2] & V. Yepes[2]
[1]*Department of Construction Eng., Universidad de Alicante, Spain*
[2]*Department of Construction Eng., Universitat Politècnica de València, Spain*

Abstract

This paper deals with the economic optimization of reinforced concrete short corbels typically used in construction. The study shows the efficiency of heuristic optimization by the random search, the descent local search and the Simulated Annealing (SA) algorithms. The evaluation of solutions follows a nonlinear finite element analysis with smeared cracking up to failure. Designs are considered feasible when they withstand a prescribed reference load. The algorithms are applied to a typical short corbel of 0.350m of total depth for which there is available data about the mode of failure and ultimate loads. The distance of the applied load to the built-in section is 0.150m. This example has seven discrete design variables for the geometry of the corbel, material and passive reinforcement. The application of the SA algorithm requires the calibration of the initial temperature and threshold, the number of variables modified in each iteration, the length of the Markov chains and the reducing coefficient. Each heuristic is run nine times so as to obtain statistical information about the minimum, average and deviation of the results. The best result has a cost of 10.4770€ for the SA algorithm. Finally, solutions and run times indicate that heuristic optimization is a forthcoming option for the design of real non-linear finite element analysed structures.
Keywords: economic optimization, heuristics, concrete structures, structural design, smeared cracking.

WIT Transactions on The Built Environment, Vol 125,
www.witpress.com, ISSN 1743-3509 (on-line)
doi:10.2495/OP120071

1 Introduction

The emergence of heuristic optimization techniques was a consequence of artificial intelligence procedures. These approximate techniques are appropriate for optimizing realistic structures because they often find a fast and near global optimal solution. Heuristic approaches include several algorithms such as genetic algorithms, simulated annealing, particle swarm optimization, and ant colony optimization, inter alia. A recent review of heuristics for project and construction management can be found in the study by Liao *et al*. [1]. Cohn and Dinovitzer [2] provided an extensive state-of-the-practice in structural optimization noting that most of the research studies focused mainly on steel structures, whereas only few dealt with concrete structures. The history of heuristic optimization in RC structures can be traced back to the late 1990s. From them on, many studies based on evolutionary computation have been applied for optimizing structural concrete problems, especially genetic algorithms. The present authors' research group has recently reported on non-evolutionary algorithms to the fully automated structural design and cost optimization of realistic three-dimensional structures such as walls [3–9].

Building on this research line, this paper proposes an automatic design method for reinforced concrete short corbels using heuristic optimization techniques as well as a smeared cracking model for concrete fracture. This method requires two basic tools: (i) a numerical analysis module capable of evaluating the ultimate failure load of the structure in different load states considering progress smeared cracking criteria, and (ii) an optimization module capable of performing an iterative variation of the current design and evaluating the objective function to accept or reject the modified design.

A realistic short corbel is analyzed to validate the numerical analysis module. The realistic structures have been tested in the laboratory so the real deformation and ultimate failure loads results results are available. The calculation module is based on a finite element program called FINEL, where several sub-modules to analyze the concrete smeared cracking have been coded. On the other hand, the optimization module is based on four heuristic algorithms.

2 Numerical analysis module

The numerical analysis module is validated using the experimental ultimate failure load of eight short corbels performed by Montenegro [10]. This work analyzed the failure mechanisms depending on the amount of reinforcing steel as well as the onset of cracking load level. In addition, relations between applied load and reinforcement deformation for the corbels tested are established. Figs. 1 and 2 show the dimensions and the reinforcement setup of the corbels tested. The concrete mix design, the curing process and the instrumentation used during the test can be found in the mentioned reference. Note that the loading process has been gradual, starting with 20kN loading steps until the appearance of the first cracks and then stepped up to 50kN load, until the corbel ruin.

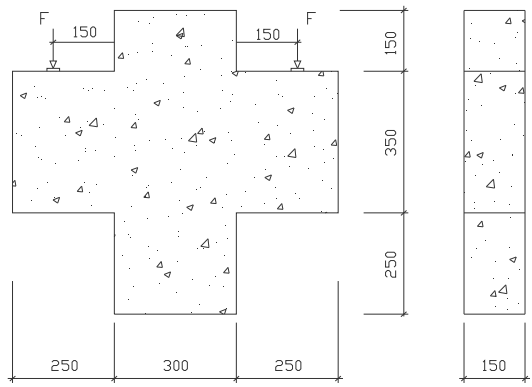

Figure 1: Short corbel geometry.

Table 1 includes the reinforcement setup of the corbels tested. The nomenclature of the corbels has been adopted in the form "CHϕVϕ", where C stands for "*Consolo*" (corbel in Portuguese), Hϕ and Vϕ represents the vertical and horizontal stirrups, respectively. Table 2 summarizes the onset of cracking load results and the ultimate failure load for the different tests. As noted above, the software used to check the ultimate failure load was FINEL which modular structure has allowed to use some of its calculation modules and adapt them to the smeared cracking scheme, particularly altering aspects of the material non-linearity. The original FINEL modules used were the mesh generation, the nodal renumbering, the boundary conditions and the Choleski method to solve equations. Issues related to non-linearity was reflected in the rigidity matrix, non-linear relationships, residual stresses, cracking, etc. Two auxiliary modules, which were made by the third author [11], were also used to process and obtain graphs representing a section of mesh reference plane parallel to the XZ and contains Gauss point closest to the plane XZ.

Table 1: Number and diameter of the reinforcement setup.

Corbel	Reinforcement setup (mm)					
	N1	N2	N3	N4	N5	N6
CH0V0	6 ϕ 12.5	11 ϕ 5	4 ϕ 12.5	4 ϕ 12.5	-	-
CH5V5	"	"	"	"	4 ϕ 5.0	8 ϕ 5.0
CH5V0	"	"	"	"	4 ϕ 5.0	-
CH0V5	"	"	"	"	-	8 ϕ 5.0
CH4V0	"	"	"	"	4 ϕ 4.2	-
CH4V4	"	"	"	"	4 ϕ 4.2	8 ϕ 4.2
CH6V0	"	"	"	"	4 ϕ 6.3	-
CH4V4*	"	"	"	"	4 ϕ 4.2	4 ϕ 4.2

Table 2: FINEL model prediction versus laboratory test results.

TEST	Laboratory test results [10]			FINEL model prediction (kN)			
	Cracking load (kN)		Ultimate failure load (kN)				
	Onset of cracking	Onset of strut		First crack rising	Strut cracking rising	Ultimate failure load (kN)	F_r/F_c
CH0V0	200	400	1000	240	480	1080	0.93
CH5V5	160	400	1250	180	448	1080	1.16
CH5V0	160	400	1070	180	480	1050	1.02
CH0V5	200	400	965	180	450	1065	0.91
CH4V4	180	320	1080	180	420	1080	1.00
CH4V0	180	400	1160	180	480	1035	1.12
CH6V0	200	350	1195	240	540	1150	1.04
CH4V4*	160	250	790	120	360	915	0.86

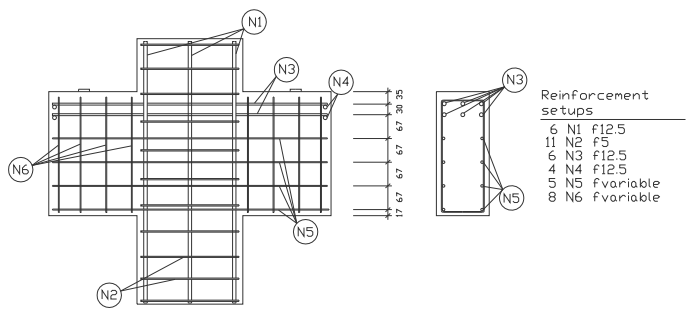

Figure 2: Reinforcement setup.

Figure 3 shows the finite element modeling of a corbel of 250mm long, 150mm wide and 350mm height tested in the laboratory. The total mesh consists of 25 elements for concrete and 79 elements for steel. The reinforcing steel is arranged in the edges of the concrete elements that surrounds them. Half of the corbel has been analyzed given the existence of a symmetry plane of both geometry and loading. Steps were applied using a 15kN load uniformly distributed applied in the 23 and 24 finite elements of the top face.

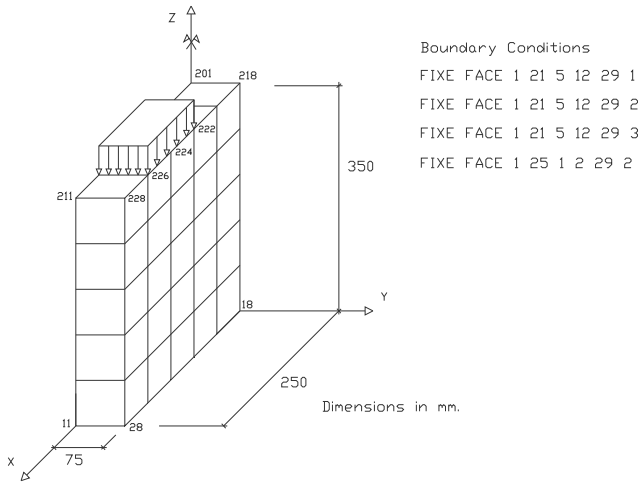

Figure 3: Finite element modelling and boundary conditions.

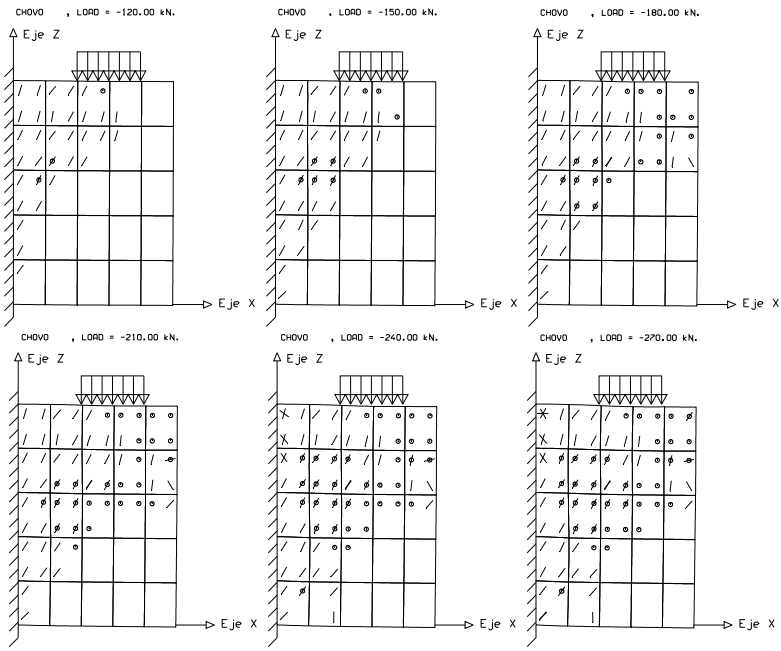

Figure 4: Graphical representation of the cracking development using the numerical analysis modulus. Case: CH0V0, ultimate failure load: 2 x 270kN.

Table 2 summarizes the results obtained using FINEL for predicting the ultimate failure loads as well as the values for which the first crack and the strut

cracking appear. The calculated ultimate failure load according to the last converged load step has been included as well. The results obtained with FINEL are of high quality both in regard to obtaining the ultimate failure load as determining the cracking development.

shows a graphic example of the output results of the numerical analysis modulus for a specific case.

One of the main disadvantages of FINEL is the computation time required for each iteration, which normally has hovered around three minutes. This drawback has been forced to limit the maximum number of iterations to be run rather than imposing improving conditions on the objective function for a specified number of iterations.

3 Optimization problem definition

The structural optimization problem deals with the minimization of the objective function F of expression (1), satisfying also the restrictions of expressions (2).

$$F(x_1, x_2, ...x_n) = \sum_{i=1,r} p_i * m_i(x_1, x_2, ..., x_n) \tag{1}$$

$$g_j(x_1, x_2, ...x_n) \leq 0 \tag{2}$$

$$x_i \in (d_{i1}, d_{i2}, ..., d_{iq}) \tag{3}$$

Note that F in expression (1) is the sum of unit prizes multiplied by the measurements of construction units (concrete, steel, formwork, etc.), and that the restrictions on expression (2) are all the structural constraints. The design variables, x_1, x_2,..., x_n, take the discrete values in a list in expression (3). The analysis includes seven discrete variables: the corbel width (B), the characteristic strength of concrete (f_{ck}), and the longitudinal and transverse reinforcement (A_{s1}, A_{s2}, A_{s3}, A_{s4} and A_{s5}) as shown in Fig. 5.

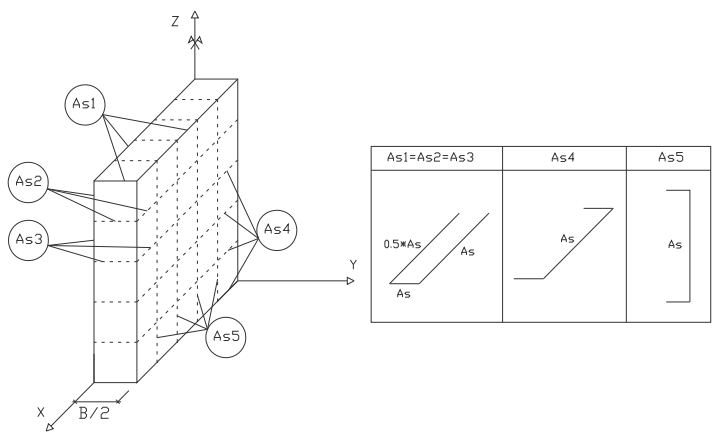

Figure 5: Corbels reinforcement setup.

The parameters of the analysis are all fixed quantities and therefore they are not subject to optimization. Tables 3 and 4 provide details of those parameters for the corbels analyzed. The ultimate failure load is the only restriction imposed on the structure which has to be equal or greater than 500kN. Note that for calculating the failure load provided by FINEL no material safety factor has been considered. Thus, the failure load is the actual resistance load of the corbel.

Table 3: Main parameters of the analysis.

Parameter	Notation	Description	Value
Geometric parameters	L	Corbel length	250 mm
	C	Corbel depth	350 mm
	a	Load application distance	150 mm
Mechanical parameters	f_{yk}	Modulus of elasticity of steel	479 MPa
Loading parameters	P	Loading step	2.0 N/mm^2

Table 4: Basic prizes of the cost function.

Unit	Cost (€)
kg of steel (B-500S)	1.25
m^2 of shuttering and stripping formwork	22.75
m^3 of concrete HA-25	77.80
m^3 of concrete HA-30	82.34
m^3 of concrete HA-35	98.03
m^3 of concrete HA-40	105.17
m^3 of concrete HA-45	111.72
m^3 of concrete HA-50	118.26

4 Optimization module

The optimization module used in this study is based on four heuristic search algorithms: the random search (RS), the directional movement greedy best-first search (DGLS), the descent local search (DLS) and the simulated annealing (SA) method. The algorithms were coded in Visual Basic 6.0 and computer runs were performed in a conventional PC computer with an Intel Pentium of 2.80GHz.

RS consists of generation solutions by random choice of the optimization problem variables. The cost function is evaluated for each solution and then it is checked if the solution satisfies the structural constraints. The computation time has limited the number of iterations performed, which has been 200. Among the feasible solutions found, the lowest cost solution is chosen. Figure 6 shows the results for 200 iterations of RS. The best result found has a cost of 13.5737€ with a computation time of 10 hours.

DGLS involves the progressive reduction of the cost of the objective function from an initial maximum cost solution. The initial solution is modified

iteratively. If the change produces a better solution and fulfills the condition of minimum ultimate failure load, then the new solution replaces the previous one. The local changes of the current solution are performed by varying one (D1), three (D3) or five variables (D5) simultaneously in order to determine the most efficient movement. The mechanism that modifies a solution defines the neighborhood of this solution. The movements of each variable always move in the direction of decreasing costs so that no variables are allowed to increase its value at any time. 120 iterations have been executed, storing all lower cost solutions found by this algorithm. Figure 7 shows the comparative results of cost trends for D1, D3 and D5.

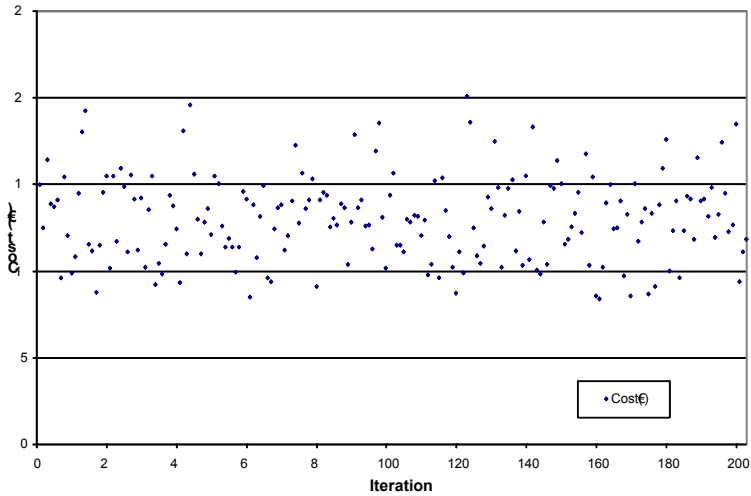

Figure 6: Cost results for a standard RS for 200 iterations.

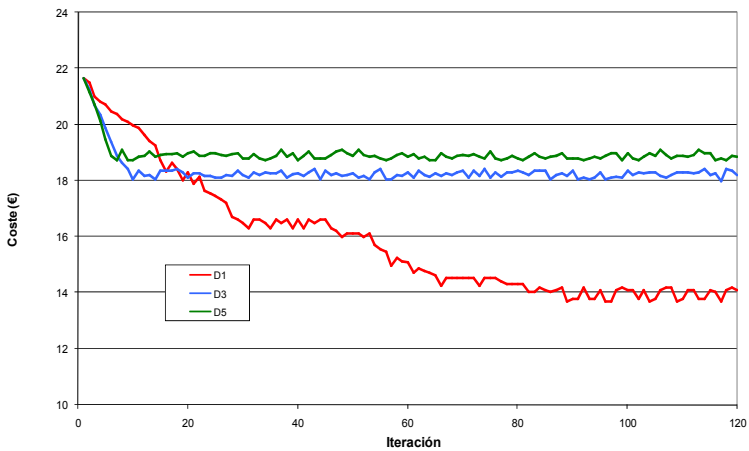

Figure 7: Cost variation for DGLS.

DLS is a greedy best-first search, but unlike the previous method, DLS starts with a random feasible solution and the movements of each variable are allowed to move in any the direction. Unlike DGLS, DLS is a non-directional movement greedy best-first search is an iterative algorithm that starts with a random feasible solution and then attempts to find a better solution by changing some variables of the current solution. If the change produces a better solution, this new solution replaces the previous one, repeating the movements until no further improvements can be found. DLS involve modifying a starting feasible solution iteratively through an appropriate mechanism. From this solution, a random change is applied to the values of the variables. The local changes of the current solution are performed by varying one (G1), three (G3) or five variables (G5) simultaneously, but now allowing random non-directional changes in each chosen variable. The new solution is evaluated and, if this solution reduces the cost and is feasible then this solution replaces the previous one. The starting solution selected to begin with DLS was the best solution found in the RS. A usual stopping criterion used in these iterative local search methods is to finish the movements until a maximum number of iterations without improvement. Here, the number of iterations without improvement is limited to 120 due to the high computation time required. Figure 8 shows the evolution of the cost for each of the movements G1, G3 and G5 applied to DLS. The best solution found with DLS has a cost of 11.9775€ with 7 hours of computation time, being D5 the most effective movement.

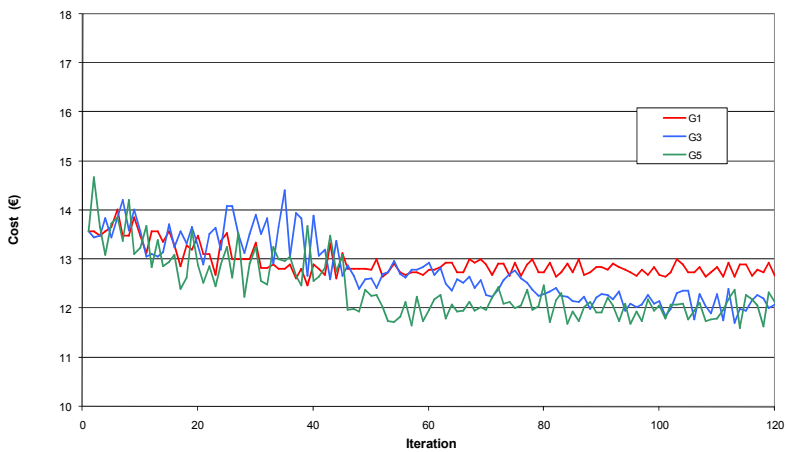

Figure 8: Cost variation for DLS.

The fourth algorithm used in this work was the well-known SA algorithm, that was originally proposed by Kirkpatrick *et al.* [12]. SA is used in global optimization problems to find a good approximation solution in a large search space. SA is based on the analogy of crystal formation from masses melted at high temperature and let cool slowly. The process is governed by Boltzmann

expression *exp(-ΔE/T)*, where *ΔE* is the increment of energy of the new configuration and *T* is the temperature. The algorithm starts with a feasible solution randomly generated and a high initial temperature. The initial working solution is changed by a small random move of the values of the variables. The new current solution is evaluated in terms of cost. Greater cost solutions are accepted when a 0 to 1 random number is smaller than the expression *exp(-ΔE/T)*, where *ΔE* is the cost increment and *T* is the current temperature. The current solution is then checked against structural restrictions and if it is feasible, it is adopted as the new working solution. The initial temperature is decreased geometrically (*T=kT*) by means of a coefficient of cooling *k*. A number of iterations called Markov chains is allowed at each step of temperature. The algorithm stops when the temperature is a small percentage of the initial temperature (typically 1%). The SA method is capable of surpassing local optima at high-medium temperatures and gradually converges as the temperature reduces to zero. The SA method requires calibration of the initial temperature, the length of the Markov chains and the cooling coefficient. The initial temperature was adjusted following the method proposed by Medina [13], which consists in choosing an initial value and checking whether the percentage of acceptances of higher energy solutions is between 20-40 percent. If the

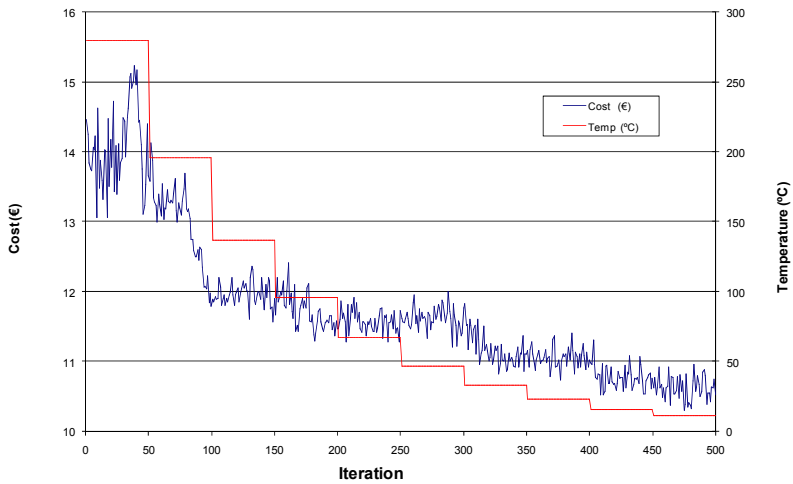

Figure 9: Typical cost variation and temperature reduction for SA.

percentage is greater than 40%, the initial temperature is halved; and if it is smaller than 20%, the initial temperature is doubled. The movement selected for SA was G3. The initial temperature calibrated was 280, the Markov chain length was 50 and the cooling rate was 0.7. These calibration data provide 500 iterations with a computer time of 20 hours. Computer runs were performed 9 times so as to obtain minimum, mean and standard deviation of the random

results. The best solution found with SA has a cost of 10,4770€ with 25 hours of computation time Figure 4.6 shows a typical cost evolution for the SA.

5 Results from numerical experiments

Table 5 summarizes the results of best cost and computer running times of the four heuristics used in the research. It can be seen that the lowest cost solution found by SA improves by 22.81%, 27.28% and 12.53% the best results of RS, DGLS and DLS, respectively.

Table 5: Best solutions found by the heuristics.

Algorithm	Cost (€)	Computation time (hours)
RS	13.5737	10.00
DGLS	14.4072	8.25
DLS	11.9775	7.40
SA	10.4770	25.60

The optimized corbel uses concrete with the highest permitted characteristic resistance (50MPa). Its width is very strict, 180mm and the reinforcing steel setup at the top of the corbel works as a tie. The optimized-cost corbel does not require longitudinal (A_{s5}) nor transverse reinforcement (A_{s4}). The ultimate failure load is 504kN.

6 Conclusions

In this paper we describe an automatic method for the design of real nonlinear finite element analysed reinforced concrete short corbels using heuristic optimization techniques as well as a smeared cracking model for concrete fracture. The results obtained are very close to those obtained experimentally both in regard to obtaining the ultimate failure load as determining the cracking development The analysis reveals that SA is an efficient algorithm for the optimal design of real corbels. In addition, a computer time reduction for the calculation module is required in order to apply other stopping criteria for the heuristics rather than a predetermined number of iterations. The optimized-cost corbel has a very strict width, use concrete with the highest permitted characteristic resistance (50MPa) and does not require longitudinal nor transversal reinforcing steel. Nevertheless, future studies should include additional structures, such as bridge braces and pile plates; and a restatement of the calculation modules to apply the methodology to other more complex structures such as prestressed concrete.

Acknowledgements

This study was funded by the Spanish Ministry of Science and Innovation (Research Project BIA2011-23602) and the European Community with the FEDER funds.

References

[1] Liao T.W., Egbelu P.J., Sarker B.R. and Leu S.S., Metaheuristics for project and construction management –A state-of-the-art review, *Automation in Construction*, **20**(5), pp.491-505, 2011.
[2] Cohn M.Z. and Dinovitzer A.S. (1994), Application of structural optimization, *Journal of Structural Engineering*, **120**(2), pp.617-649, 1994.
[3] Yepes V., Alcala J., Perea C. and Gonzalez-Vidosa F., A parametric study of earth-retaining walls by simulated annealing, *Engineering Structures*, **30**(3), pp.821-830, 2008.
[4] Perea C., Alcala J., Yepes V., Gonzalez-Vidosa F. and Hospitaler A., Design of reinforced concrete bridge frames by heuristic optimization, *Advances in Engineering Software*, **39**(8), pp.676-688, 2008.
[5] Paya I., Yepes V., Gonzalez-Vidosa F. and Hospitaler A., Multiobjective optimization of concrete frames by simulated annealing, *Computer-Aided Civil and Infrastructure Engineering*, **23**(8), pp.596-610, 2008.
[6] Martí J.V. and Gonzalez-Vidosa F., Design of prestressed concrete precast pedestrian bridges by heuristic optimization, *Advances in Engineering Software*, **41**(7-8), pp.916-922, 2010.
[7] Martinez F.J., Gonzalez-Vidosa F., Hospitaler A. and Yepes V., Heuristic optimization of RC bridge piers with rectangular hollow sections, *Computers & Structures*, **88**(5-6), pp.375-386, 2010.
[8] Martinez F.J., Gonzalez-Vidosa F., Hospitaler A. and Alcala J., Design of tall bridge piers by ant colony optimization, *Engineering Structures*, **33**(8), pp.2320-2329, 2011.
[9] Carbonell A., Gonzalez-Vidosa F. and Yepes V., Design of reinforced concrete road vault underpasses by heuristic optimization, *Advances in Engineering Software*, **42**(4), pp.151-159, 2011.
[10] Montenegro F., Análise-teórico-experimental de consolos de concreto armado, Escola de Engenharia de São Carlos. Universidade de São Paulo, São Carlos, 1998.
[11] González-Vidosa F., Análisis triaxial de estructuras de hormigón bajo carga estática creciente por elementos finitos con fisuración distribuida, Tesis Doctoral, Universidad Politécnica de Valencia, 1988.
[12] Kirkpatrick S., Gelatt C.D. and Vecchi M.P., Optimization by simulated annealing, *Science*, **220**(4598), pp.671-680, 1983.
[13] Medina J.R.., Estimation of incident and reflected waves using simulated annealing, *ASCE Journal of Waterway, Port, Coastal and Ocean Engineering*, **127**(4), pp.213-221, 2001.

Optimal design of full disks with respect to mixed creep rupture time

K. Szuwalski & A. Ustrzycka
Cracow University of Technology, Poland

Abstract

The mixed rupture theory to the optimization problem for the complex stress state is used. The problem of optimal shape for the rotating full disk with respect to mixed rupture time is investigated. The mathematical model of mixed creep rupture is described by the system of five partial differential equations. Difficulty of the problem results from two types of nonlinearities: geometrical connected with the use of the finite strain theory and physical - the material is described by the Norton's creep law, here generalized for true stresses and logarithmic strains. Additional time factor leads to subsequent complications. The parametric optimization describing the initial shape of the disk is applied. The obtained results are compared with the optimal disks with respect to ductile creep rupture time.
Keywords: mixed creep rupture, structural optimization, full disk.

1 Introduction

Structural elements working under creep conditions belong to the relatively new branches of structural optimisation, started in the seventieth years of the last century. The problem of time to rupture evaluation is of obvious relevance for various machine parts working under high temperature conditions. Theoretical modelling of long time strength appears to be important. A broad presentation of various objective functions with division on time-dependent and time-independent, was given by Życzkowski [1]. To the latter group belong criteria connected with creep rupture. Most papers on optimal structural design are based on the brittle creep rupture theory proposed by Kachanov (small strain theory). It was due to its relative simplicity - possibility of rigidification theorem


WIT Transactions on The Built Environment, Vol 125, © 2012 WIT Press
www.witpress.com, ISSN 1743-3509 (on-line)
doi:10.2495/OP120081

application. Optimal solutions with respect to brittle creep rupture often coincide with uniform strength structures.

In the work published by Hoff [2], the moment of failure of a bar under tension is defined as the one at which the cross-sectional area becomes zero as a result of quasiviscous flow. It was shown that the calculated results are in good agreement with the experimental data (Mentl [3]).

Applications of the ductile rupture theory, proposed by Hoff in optimization problems are rather scarce as it requires finite strain theory. For the first time it was used by Szuwalski for optimization of bars under nonuniform tension [4] and for optimisation of Mises truss [5]. Some problems of prismatic tension rods were discussed by Pedersen [6]. Such an approach introduces not only physical nonlinearities, connected with creep law (usually Norton's law), but geometrical, resulting from the finite strain theory, as well. Additional time factor leads to such complication, that till now, only few papers were devoted to optimization with respect to ductile rupture time. The optimal full disks with respect to ductile creep rupture time were found by Szuwalski [7], and first attempts for annular disks were made by Szuwalski and Ustrzycka [8].

The Hoff's concept has certain limitations. It predicts contrary to observations that creep does not result in damage of material. Also, his scheme does not explain fractures at small strains (brittle ruptures) and the change of character of rupture (from ductile to brittle).

Here, we suggest a theoretical model for creep deformation of the disk, which takes into account ductility and embrittlement of the material. We emphasize that the physics of such phenomena is very complex. Application of mixed rupture theory proposed by Kachanov [9] takes into account both: geometrical changes - diminishing of transversal dimensions resulting from large strains (as in ductile rupture) and growth of microcracks (as in brittle rupture). Straight line b (Figure 1) corresponds to the purely brittle fracture and d to the ductile fracture according to experimental data. The curve m showing relations for the mixed rupture, asymptotically approaches straight lines b and d.

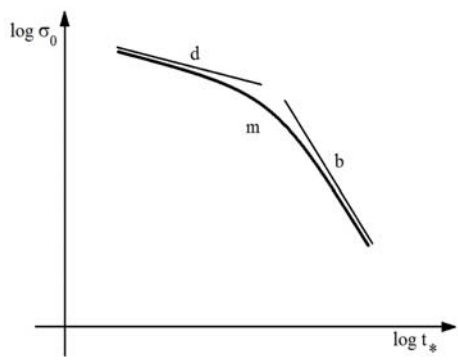

Figure 1: m- mixed rupture, d- Hoff's ductile creep rupture, b- Katchanov's brittle rupture.

The first attempt of application the mixed rupture theory to shape optimization was made by Szuwalski and Ustrzycka [10] for bars under nonuniform tension.

In present paper the problem of optimal shape with respect to mixed creep rupture time for the complex stress state - rotating full disk is investigated. We assume that microcracking and diminishing of transversal dimensions start from the very beginning of creep process. Such an approach introduces not only physical nonlinearities, connected with creep law (usually Norton's law), but geometrical, resulting from finite strain theory, as well. Additional time factor leads to subsequent complications. The whole creep process must be analyzed from its beginning up to rupture.

2 Governing equations

The concept of the mathematical description of mixed creep rupture requires an examination of the entire process, taking into account geometrical changes occurring in the course of it. The problem is solved in material (Lagrangean) coordinates and all parameters in initial state, for time equal zero, are denoted by capital letters, while current values of these parameters by the same small letters. Due to axial symmetry all quantities will be functions of two independent variables: radius R and time t. The disk rotates with constant angular velocity ω and body forces connected with own mass of the disk are taken into account (Figure 2).

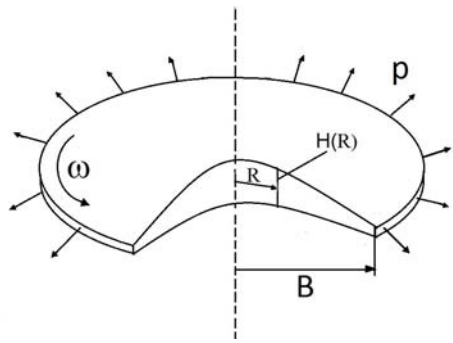

Figure 2: Model of the rotating full disk.

The material of the disk fulfills the Norton's creep low:

$$\dot{\varepsilon}_e = k\sigma_e^n \tag{1}$$

where σ_e denotes the effective stress, according to the Huber-Mises-Hencky hypothesis generalized to true stresses:

$$\sigma_e = \left(\sigma_r^2 + \sigma_\vartheta^2 - \sigma_r \sigma_\vartheta\right)^{\frac{1}{2}} \tag{2}$$

and respectively, $\dot{\varepsilon}_e$ is the effective strain rate, k and n are material constants.

The internal equilibrium condition for plane stress state, with body force, takes form:

$$\frac{1}{hr'}\frac{\partial}{\partial R}(h\sigma_r)+\frac{\sigma_r-\sigma_\vartheta}{r}+\frac{\gamma}{g}\omega^2 r=0 \tag{3}$$

where σ_r stands for current value of radial stress and σ_ϑ of circumferential one, h – for current thickness, γ – specific weight of material and g – acceleration of gravity.

Assumption of incompressibility leads to:

$$HRdR = hrdr \tag{4}$$

where R stands for material coordinate of the discussed point, while r for spatial one.

Finite strains require logarithmic strains:

$$\varepsilon_r=\ln\frac{\partial r}{\partial R}=\ln r';\ \varepsilon_\vartheta=\ln\frac{r}{R};\ \varepsilon_z=\ln\frac{h}{H} \tag{5}$$

The shape change law, assumed in form of similarity of true stresses and velocities of logarithmic strains deviators according to Szuwalski [7] leads to:

$$\frac{\dot{r}}{r}=\frac{1}{2}k\sigma_e^{n-1}(2\sigma_\vartheta-\sigma_r) \tag{6}$$

Compatibility condition, after some rearrangements, presented by Szuwalski [7], takes form:

$$\sigma_r'[(n-1)(2\sigma_r-\sigma_\vartheta)(2\sigma_\vartheta-\sigma_r)-2\sigma_e^2]+\sigma_\vartheta'[(n-1)(2\sigma_\vartheta-\sigma_r)^2+4\sigma_e^4]=$$
$$=6\sigma_e^2\frac{r'}{r}(\sigma_r-\sigma_\vartheta)\cdot \tag{7}$$

To find the mixed rupture time, the evolution equation proposed by Kachanov [9] will be applied:

$$\frac{\partial\Psi}{\partial t}=-D\left[\frac{\sigma_e}{\Psi}\right]^m \tag{8}$$

in which D and m are material constants.

Continuity function Ψ is defined by the ratio of effective cross - sectional area a_{ef} to undamaged area a:

$$\Psi=\frac{a_{ef}}{a} \tag{9}$$

In contrast with brittle rupture theory σ denotes here the true stress - related to the current cross – section a (geometrical changes are taken into account).

We characterize damage by the continuity function $0 \le \Psi \le 1$. At the initial moment (no damage): $\Psi = 1$, as time goes on, it decreases. The moment of rupture corresponds to a value $\Psi = 0$ at which fracture localizes.

We define the rupture criterion in the following form:

$$\exists R : (R \in \langle 0, l \rangle \wedge \Psi \in \langle 1,0 \rangle \wedge \Psi(\sigma)\Big|_{t_*^{(m)}} \to 0) \tag{10}$$

Time after which the continuity function will diminish to zero will be the time of mixed rupture $t_*^{(m)}$.

For the sake of numerical calculations, dimensionless quantities are introduced. Both material and spatial coordinates are related to the initial external radius B:

$$\hat{R} = \frac{R}{B}\ ;\ \hat{r} = \frac{r}{B} \tag{11}$$

The thickness of the disk is related to the mean thickness h_m of the full disk of volume V and radius B:

$$\hat{H} = \frac{\pi B^2}{V} \cdot H\ ;\ \hat{h} = \frac{\pi B^2}{V} \cdot h \tag{12}$$

Radial loading at radius b of the rotating disk is resulting from mass M uniformly distributed on the outer edge.

$$\sigma_r(b) = p = \frac{M\omega^2}{2\pi h(B)} \tag{13}$$

Dimensionless stresses are referred to stresses calculated using a rigidification theorem in the motionless full plane disk subject to tension with uniform pressure p (13):

$$\hat{\sigma}_i = \frac{2V}{M\omega^2 B^2}\sigma_i\ ;\ \ i = r, \vartheta \tag{14}$$

Consequently dimensionless time is defined:

$$\bar{t} = \frac{t}{t^{(d)}} \tag{15}$$

where: $t^{(d)}$ stands for the time of ductile rupture for full plane disk (Szuwalski [7]). To avoid the large number of material constants in numerical calculations we introduce the new parameter Θ. This parameter is equal to the radio of the brittle rupture time to the ductile rupture time for the prismatic bar subject to tension with the initial stress σ_s:

$$\Theta = \frac{t_{pr}^{(K)}}{t_{pr}^{(H)}} = \frac{nk\sigma_s^n}{(m+1)D\sigma_s^m} \tag{16}$$

where σ_s is equal:

$$\sigma_s = \frac{M\omega^2 R_0^2}{2V} \tag{17}$$

The parameter Θ contains four material constants: n and k from Norton's law (1) and m and D from evolution equation (8). In some way it describes sensitivity of material on type of damage: brittle or ductile.

The mathematical model of mixed creep rupture is described by the system of five partial differential equations in dimensionless form:

$$\hat{\sigma}_r' = \frac{\hat{r}'}{\hat{r}}(\hat{\sigma}_r - \hat{\sigma}_\vartheta) - 2\cdot\hat{r}\hat{r}'\mu - \frac{\hat{h}'}{\hat{h}}\hat{\sigma}_r$$

$$\hat{\sigma}_\vartheta' = \frac{6\hat{\sigma}_e^2(\hat{\sigma}_r - \hat{\sigma}_\vartheta)\frac{\hat{r}'}{\hat{r}} - \hat{\sigma}_r'\left[(n-1)\left(5\hat{\sigma}_r\hat{\sigma}_\vartheta - 2\hat{\sigma}_r^2 - 2\hat{\sigma}_\vartheta^2\right) - 2\hat{\sigma}_e^2\right]}{(n-1)(2\hat{\sigma}_\vartheta - \hat{\sigma}_r)^2 + 4\hat{\sigma}_e^2}$$

$$\frac{d\hat{r}}{d\hat{t}} = \frac{\hat{r}}{2\cdot n}\left(\hat{\sigma}_r^2 + \hat{\sigma}_\vartheta^2 - \hat{\sigma}_r\hat{\sigma}_\vartheta\right)^{\frac{n-1}{2}}\left(2\hat{\sigma}_\vartheta - \hat{\sigma}_r\right) \tag{18}$$

$$\hat{h} = \frac{\hat{H}\hat{R}}{\hat{r}'\hat{r}}$$

$$\frac{\partial\Psi}{\partial\hat{t}} = \frac{-1}{(m+1)\Theta}\left[\frac{\hat{\sigma}_e}{\Psi}\right]^m.$$

In presented above equations we have five unknowns: true stresses σ_r and σ_ϑ, current thickness – h, spatial radial coordinate – r and continuity function – Ψ.

At the initial moment $(t = 0)$ disk remains undeformed, therefore the initial conditions take form:

$$\hat{r}(\hat{R},0) = \hat{R}\,;\quad \hat{h}(\hat{R},0) = \hat{H}(\hat{R}) \tag{19}$$

The boundary conditions are described in this form:

$$\hat{r}(0,\hat{t}) = 0\,;\quad \dot{\hat{r}}(0,\hat{t}) = 0$$

$$\hat{\sigma}_r(0,\hat{t}) = \hat{\sigma}_\vartheta(0,\hat{t}) \tag{20}$$

The condition at external radius, where the mass M is distributed, in dimensionless form may be written:

$$\hat{\sigma}_r(1,t) = \frac{1}{\hat{h}(1,t)} \tag{21}$$

In the fourth of equations (16) and in the second of initial conditions (17), we have the function $\hat{H}(\hat{R})$ describing the initial profile of the disk. It is necessary to know this function in order to solve the set (16). Because this function is being sought in the optimisation process, we shall apply parametric optimisation. We shall look for the best possible function $\hat{H}(\hat{R})$, leading to the longest lifetime to mixed rupture in assumed class of polynomial functions.

Let's consider an optimality criterion in the form:

$$\left(\exists! \, \hat{H}(\hat{R}) \in f\right) \quad t_*^{(m)} \xrightarrow[V=const]{} \max \tag{22}$$

where functions $f : \mathrm{R} \to \mathrm{R}$, $R \to b_0 + b_1 R + b_2 R^2 + ... + b_l R^i$, for all arguments $R \in \langle 0,1 \rangle$, where $i \in \mathrm{N} \subset \{0\}$ (i is a non-negative integer) and $b_l \in \mathrm{R}$ are constant coefficients, where $l = 0, 1, 2, \ldots, i$, and $b_l \neq 0$.

3 Numerical algorithm

In order to perform an optimisation procedure, the rupture and optimality criterion to the mathematical model is introduced. The numerical algorithm is proposed for the complex stress state. We must follow step by step the whole creep process for each new geometry of the deformed disk up to the moment of fulfilling of rupture criterion in order to establish the mixed creep rupture time. The numerical algorithm consists of two blocks, which are sequentially activated.

The algorithm begins by defining the initial geometry, constant parameters and the boundary conditions for the stresses (20). In the first block, for given geometry of the disk, the true stresses distribution is established by integration of the first and the second equations of the set (18) with respect material coordinate $\hat{R}$. The Runge – Kutta fourth order method is applied. We do not know values of stresses in the centre of the disk, so they are assumed arbitrarily, but they must satisfy the boundary condition at the outer edge of the disk (21). Therefore, the recurrential procedure must be applied. Found distribution of true stresses, with help of the evolution equation (the last from the set (18) makes it possible to establish the distribution of continuity function Ψ. If it's minimal value satisfies the rupture criterion, the creep process finishing – the time to mixed rupture was found.

When values of continuity function are sufficiently large, the new changed geometry of the disk is calculated. The integration of the third of equation (18) with respect to time is performed using Euler's method. The time dependent solutions have high sensitivity on time step dimension, so we choose the varying time step, depending on current creep velocity. In this way new spatial coordinates are calculated. Finally incompressibility condition (fourth of set (18)) makes it possible to find changed shape (thickness) of the disk. From the results obtained for many initial shapes of the disk, described by assumed polynomial function, the best leading to the longest time to mixed creep rupture

is chosen – this is the optimal disk. Consequently, for the new geometry of the disk, the full cycle of the above mentioned calculations are repeated.

4 Discussion of results

At the beginning optimal solutions for the problem of rotating full disk with respect to mixed creep rupture time are sought in the class of linear functions:

$$\hat{H}(\hat{R};u_0,u_1) = u_0 + u_1\hat{R} \tag{23}$$

Parameters u_0 and u_1 (uniparametric optimisation), which optimal values are sought, are linked together by the condition of given volume V:

$$u_1 = \frac{3}{2}\frac{u_0(\beta^2-1)+1}{\left(1-\beta^3\right)} \tag{24}$$

The influence of parameter μ as the ratio of own mass of the disk to mass uniformly distributed at the outer edge and the parameter Θ ratio of the brittle rupture time and ductile rupture time of the prismatic bar, rotating with the constant angular velocity ω, loaded by mass M distributed at the external edge, with the bar's own mass neglected is investigated. Profiles of optimal disks for uniparametric optimization are shown in Figure 3 as a function of the parameter μ for three different values of parameter Θ

Obtained solutions strongly depend on ratio Θ and μ. When the mass M is very large in comparison with own mass of the disk (small values of μ) optimal disks are close to flat ones. For the larger values of parameter Θ (ductile materials) the thickness of optimal disks in the vicinity of outer edge grows. For larger values of parameters μ (small mass M at the outer radius), the mass of the disk is distributed as close to the rotation axis as possible.

Better results may be obtained for disks, which initial shape is defined by quadratic function:

$$\hat{H}(\hat{R};b_0,b_1,b_2) = b_0 + b_1\hat{R} + b_2\hat{R}^2, \quad b_2 \neq 0 \tag{25}$$

Because now we have three parameters, finding of their optimal values takes much more time than for uniparametric optimization. From three parameters in this function, only two may be treated as free ones, the third results from given volume of disk:

$$\hat{V} = \int_0^1 2\pi\left(b_0 + b_1\hat{R} + b_2\hat{R}^2\right)\hat{R}d\hat{R} = \pi \tag{26}$$

from which:

$$b_2 = 2 - 2b_0 - \frac{4}{3}b_1 . \tag{27}$$

Profiles of optimal disks for biparametric optimization are shown in Figure 4.

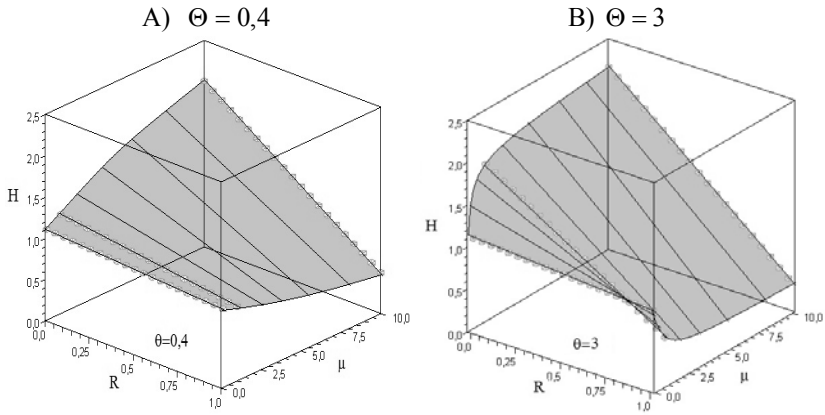

Figure 3: Optimal shapes of the disks for uniparametric optimisation.

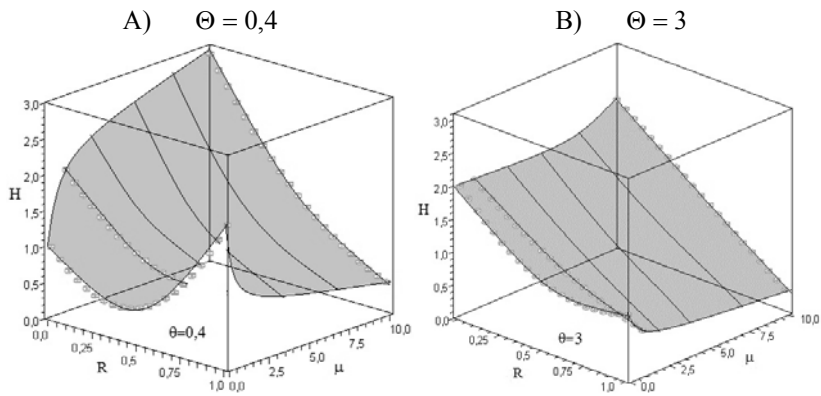

Figure 4: Optimal shapes of the disks for biparametric optimisation.

For smaller values of parameters μ (the own mass almost neglected), the growth of thickness at the outer edge was observed, optimal solutions have minimum inside the disk width. The larger thickness at the outer edge works as some kind of reinforcement and thanks to it time to mixed rupture may be longer. For larger values of parameters Θ (brittle materials), this effect is smaller.

In Figure 5A) the changed profiles of the optimal disk and in Figure 5B) the corresponding distribution of continuity function at the same time moments are shown. The results are presented for optimal disk for parameters: $\mu = 0.1,\ n = 3, m = 2, \Theta = 3$, which initial shape is described by function $H(R) = 2 - 3R + 2R^2$.

We observed that despite the strengthening of the outer edge of the disk, the rupture criterion for the continuity function Ψ is fulfilled there. Inside the disk the values of function Ψ are quite large. This effect is due to limitation only to the disks of initial profile described by quadratic function (23).

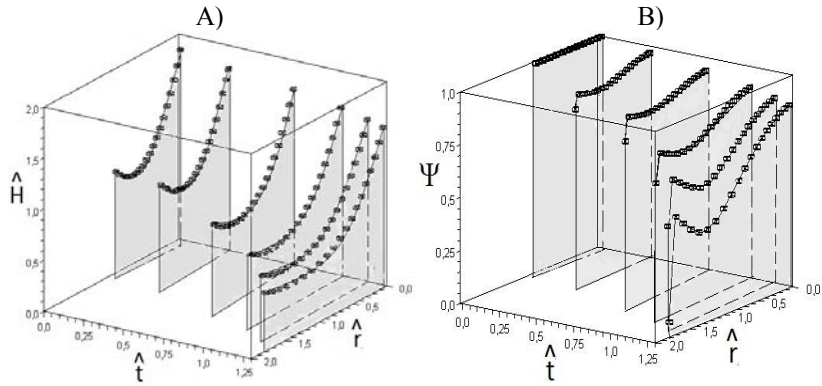

Figure 5: Time cross-section of creep process.

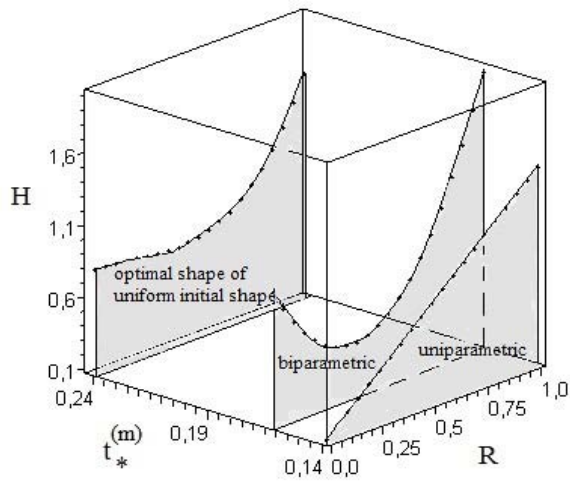

Figure 6: Optimal shape of the uniform initial strength disks compared with uni- and biparametric optimisation.

We may expect that disks of uniform initial strength, in which both radial and circumferential stresses are the same for $0 \le R \le B$ are close to optimal with respect to mixed rupture time.

Such disks described by formula:

$$\hat{H}_{us}\left(\hat{R}\right) = \frac{1}{\hat{\Sigma}} \exp\left[\frac{\mu}{\hat{\Sigma}}\left(1 - \hat{R}^2\right)\right], \tag{28}$$

where: $\hat{\Sigma}$ - dimensionless equalized initial stress, calculated from the condition of constant volume:

$$\hat{\Sigma} = \frac{\mu}{\ln(1+\mu)}, \tag{29}$$

may be slightly corrected, to obtain the longest life – time to creep rupture. Correction is adopted in form of the third degree polynomial function:

$$\hat{H}_{cor} = p_0 + p_2 \hat{R}^2 + p_3 \hat{R}^3, \tag{30}$$

without the linear element, so as to the thickness derivative in the middle of the disk was equal to zero.

As the correction cannot change the total volume of the bar, only two coefficients of eq. (30) may be treated as free parameters, while the third results from the constant volume condition:

$$p_3 = -\frac{5}{2} p_0 - \frac{5}{4} p_2 . \tag{31}$$

For different values of these parameters we designated the initial shape of the disk,

$$\hat{H}\left(\hat{R}\right) = \hat{H}_{us}\left(\hat{R}\right) + \hat{H}_{cor}\left(\hat{R}\right) \tag{32}$$

then we integrate the system of equations (16)

Calculations were carried for $\mu = 0{,}1$, $\Theta = 3$, exponent in Norton's law $n = 3$ and exponent in Kachanov's law $m = 2$. Optimal shapes of the corrected shape of uniform initial strength the disk compared with obtained earlier for parametric optimization are presented in Figure 6.

The optimal shapes of different disks are placed on the time axis at the points corresponding to obtained times m of mixed rupture. As expected, the corrected shape of uniform initial strength disk provides the longest time to mixed creep rupture. Introduction of parabolic disk enlarges this time a for about 14%, while for corrected disk of uniform strength the gain in comparison with conical disk is about 70%.

5 Conclusions

In conclusion, it is worth pointing out that the mathematical model of mixed creep rupture discussed in this paper addresses one of the fundamental phenomena that occur at high temperatures in the materials. The theoretical model for creep deformation of the disk with the account of ductility and embrittlement of the material is described. Application of mixed rupture theory proposed by Kachanov in this model takes into account: geometrical changes - diminishing of transversal dimensions resulting from large strains (as in ductile rupture) and growth of microcracks (as in brittle rupture). The time to rupture is defined as a time when continuity function Ψ diminishes to zero.

The paper is embedded in the branch of research dedicated to optimum design of structures under creep conditions with the objective function in the form of mixed creep rupture time. The problem of optimal shape with respect to mixed creep rupture time for the complex stress state - rotating full disk is investigated. Both the own mass of the disk and a mass uniformly distributed on the outer

radius are taken into account. The Norton creep law has been applied. The problem has been solved in the framework of large strains – true stresses approach. The logarithmic measure of strains has been adopted. The optimal profiles of disks, satisfying the condition of maximum time to rupture, were found for full disks and for the constant volume of material. The best profile of the disk, leading to the longest lifetime to mixed rupture in assumed class of polynomial functions was sought.

The corrected shape of uniform initial strength disk provides the longest time to mixed creep rupture. Correction is adopted in form of the third degree polynomial function. In comparison of conical disk enlarges the time to mixed rupture for about 70%.

The results presented in the paper have fundamental meaning for possible applications in different technologies. Both the power plants or the automobile industry and ship or aircraft technologies can profit from decent analysis presented in the submitted manuscript. Also, this domain of research looks promising for the future studies in view of multi-scale modeling applied to creep rupture mechanisms.

References

[1] Życzkowski M., Optimal structural design under creep conditions, Appl. Mech. Rev. 12, 453 – 461, 1988.
[2] Hoff N.J., The necking and rupture of rods subjected to constant tensile loads, J. Appl. Mech. Trans. ASME 20 105–112, 1953.
[3] Mentl V., An application of a phenomenological theory of creep damage, Materials at High Temperatures, 23, 195-200, 2006.
[4] Szuwalski K., Optimal design of bars under nonuniform tension with respect to ductile creep rupture, Mech. Struct. Mach. 3, 303–319, 1989.
[5] Szuwalski K., Optimal design of Mises truss with respect to time to creep rupture, Engng. Trans. 42, 145–155, 1994.
[6] Pedersen, P., On the influence of boundary conditions, Poisson's ratio and material non-linearity on the optimal shape, Int. J. of Solids and Structures 38(3), 465–477, 2001.
[7] Szuwalski K., Optimal design of disks with respect to ductile creep rupture time, Strict. Opt. 10, 54–60, 1995.
[8] Szuwalski K., Ustrzycka A., The Influence of Boundary Conditions on Optimal Shape of Annular Disk With Respect to Ductile Creep Rupture Time, European Journal of Mechanics, (2012), (in print).
[9] Kachanov L.M., Creep theory, Fizmatgiz, Moskwa, 1960.
[10] Szuwalski K., Ustrzycka A., Optimal Design of Bars Under Nonuniform Tension With Respect to Mixed Creep Rupture Time, International Journal of non-linear mechanics, 2012, (in print).

High performance mortar may help to reduce damages in masonry constructions for seismic areas in Mexico

J. Gomez-Dominguez & L. A. Badillo
Monterrey TEC, Monterrey Campus, Mexico

Abstract

Seismicity is a great concern in Mexico and other Latin-American countries, particularly low income construction houses and small masonry buildings suffer considerable damages under earthquakes. This work describes a practical research for developing and testing at the laboratory stage an optimal high performance mortar in small masonry sections under loads. Results showed that masonry sections made with the high performance mortar were 34.65% stronger in compression than sections made with conventional mortar; on the other hand masonry sections tested under diagonal compression were 11.91% stronger. A simplified seismic analysis carried out on three story buildings located in Mexico City showed that the lower story for the conventional masonry building would not comply with its code, while the building with high performance mortar was considered satisfactory. Using high performance mortar to make masonry walls would cost 11% more than using conventional mortar.
Keywords: high performance mortar, masonry houses, brick walls in buildings.

1 Introduction

On March 20, 2012 an earthquake 7.4 on the Richter scale was felt in Mexico City with many aftershocks, fortunately no major damages were suffer, this reminded us of the devastation left by the 8.0 earthquake that occurred in 1985. This work describes an initial effort to do some research on the development of a better performance masonry, the need exists to alleviate in some way the damages produced by earthquakes on conventional constructions, were little attention is given to the mortars used. Low income houses and small buildings

WIT Transactions on The Built Environment, Vol 125, © 2012 WIT Press
www.witpress.com, ISSN 1743-3509 (on-line)
doi:10.2495/OP120091

are abundant in seismic areas and become in many cases seriously damaged when earthquakes strike.

2 Materials

Two types of mortars were used in this work, one designated as conventional mortar (CM) and one designated as high performance mortar (HPM), both included a Portland cement designated as CPC30R that complies with a Mexican standard, this is basically cement with 50 to 90% clinker plus gypsum and the rest includes other proper additions. The sand used in all the mixes was a crushed limestone that complies with ASTM C33 and its fineness modulus was 2.72.
The high performance mortar also included silica fume, polypropylene fibres and a superplasticizer admixture.

The type of brick used for making small masonry sections in this work is shown in figure 1, this is a common piece for construction and complies with the Mexican standard for such application, table 1 shows its physical characteristics.

Figure 1: Typical clay brick.

Table 1: Physical brick characteristics.

Characteristic	Measure
Depth	60 mm
Width	90 mm
Length	200 mm
Weight per unit	1.40 kg
Units per m^2	68
Water absorption	9.4 %

It was necessary to set a group of basic performance requirements for the high performance mortar, in order to distinguish it from the usual requirements specified by the Complementary Technical Norms for Design and Construction of Masonry Structures in Mexico City (CTNM) [1]. Consideration was given to literature review and common practices in setting up table 2. CTNM does not specify any requirement on consistency of the mortar but indicates that the amount of water should be enough to get a workable mix, it suggests that the mortar should include one part of cement and not less than 2.25 parts of sand but no more than 3 parts of sand by volume.

Table 2: Performance requirements for high performance mortar.

Characteristic	Performance requirement	Norm requirement CTNM
Compressive strength	≥49 MPa	≥3.93MPa
Flexural strength	≥9.81 MPa	none
% Flow	110 ± 5 %	none

3 Experimental work to obtain HPM

The methodology to obtain the best high performance mortar is based on research carried out by the Transportation Research Board as part of the National Cooperative Highway Research Program (NCHRP), particularly "NCHRP Project 18-08A, Supplementary Cementitious Materials to Enhance Durability of Concrete Bridge Decks" [2].

3.1 Statistical design of the experiment

The experiment considers the basic requirements from table 2 as responses, they are: compressive strength obtained from cubes (ASTM C109-08), flexural strength obtained from beams (ASTM C348-08) and flow of mortar (ASTM C1437-07). Valuable help was obtained from the software Statistical Experimental Design for Optimizing Concrete (SEDOC) [3], in setting up a fractional orthogonal design of the experiment and a final selection of the best HPM with basis on an overall function of "Desirability".

3.1.1 Factors and levels

With base on initial trials, personal experience and recommendations from literature review the factors and levels chosen are shown in table 3. It should be mentioned that the amount of fibres considered in al mixes was fixed to 3000 grams per cubic meter of mortar.

Table 3: Factors and levels of the statistical design of experiment.

Factor number	Factor name	Factor type	Level 1	Level 2	Level 3
1	Amount of water (dm^3/m^3)	Quantitative	230	250	270
2	Silica Fume (%)	Quantitative	0	5	10
3	Superplasticizer (%)	Quantitative	0	0.5	1
4	w/cm	Quantitative	0.35	0.40	-

3.1.2 Design matrix suggested by SEDOC

Factors and levels of table 3 were introduced to SEDOC analysis program which handled the unbalanced arrangement of the experiment, table 4 indicates what is called the correspondent matrix of design.

Table 4: Design matrix obtained from SEDOC analysis.

Mixture	Factor1 Amount of water (dm^3/m^3)	Factor 2 Silica fume (%)	Factor 3 Superplasticizer (%)	Factor 4 w/cm
Control Mixture	270	0	0.0	0.35
Mixture #1	230	0	0.0	0.40
Mixture #2	230	5	0.5	0.35
Mixture #3	230	10	1.0	0.35
Mixture #4	250	0	0.5	0.35
Mixture #5	250	5	1.0	0.40
Mixture #6	250	10	0.0	0.35
Mixture #7	270	0	1.0	0.35
Mixture #8	270	5	0.0	0.35
Mixture #9	270	10	0.5	0.40

3.1.3 Mix proportions

Mix proportions for all of the mortar ingredients were obtained with a method by absolute volumes suggested by Aïtcin [4]. Table 5 shows the proportions for each of the ten mortar mixes.

3.1.4 Testing the mortars designed

All the mixes designed were subject to three basic tests, namely flow, compressive strength and flexural strength, strength was checked at different ages. The results are presented in figures 2, 3 and 4.

Table 5: Mix proportions for mortars, kg/m^3 (except dm^3/m^3 for water).

Mixture	Water	Cement	Silica fume	Fine aggregate	Superplaticizer	Fibres
Control	287.60	771.43	0.00	1204.46	0.00	0.00
M1	251.56	575.00	0.00	1475.56	0.00	3.00
M2	248.37	624.29	32.86	1392.01	3.04	3.00
M3	246.19	591.43	65.71	1378.30	6.08	3.00
M4	266.88	714.29	0.00	1302.06	3.31	3.00
M5	266.20	593.75	31.25	1365.32	5.79	3.00
M6	268.72	642.86	71.43	1281.34	0.00	3.00
M7	282.87	771.43	0.00	1197.91	7.14	3.00
M8	287.41	732.86	38.57	1191.64	0.00	3.00
M9	286.40	607.50	67.50	1261.15	3.13	3.00

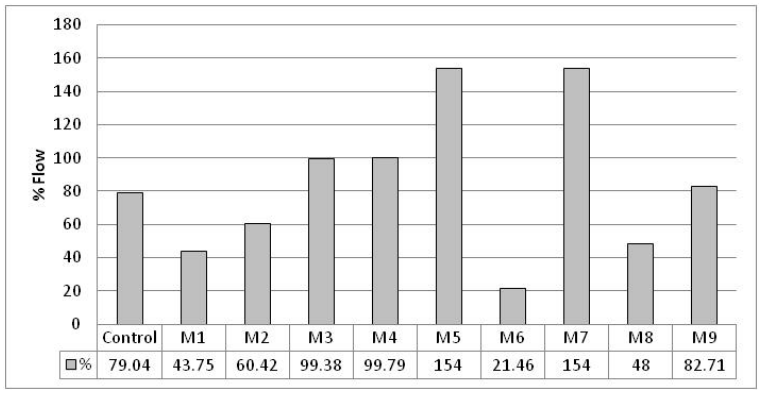

Figure 2: Fresh mortar consistency.

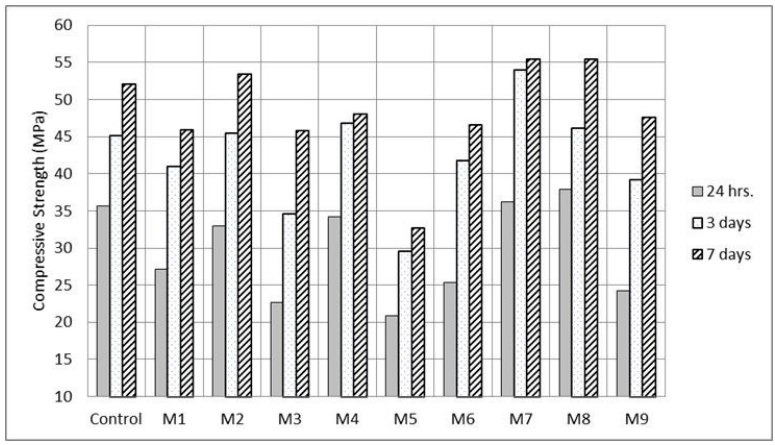

Figure 3: Compressive strength.

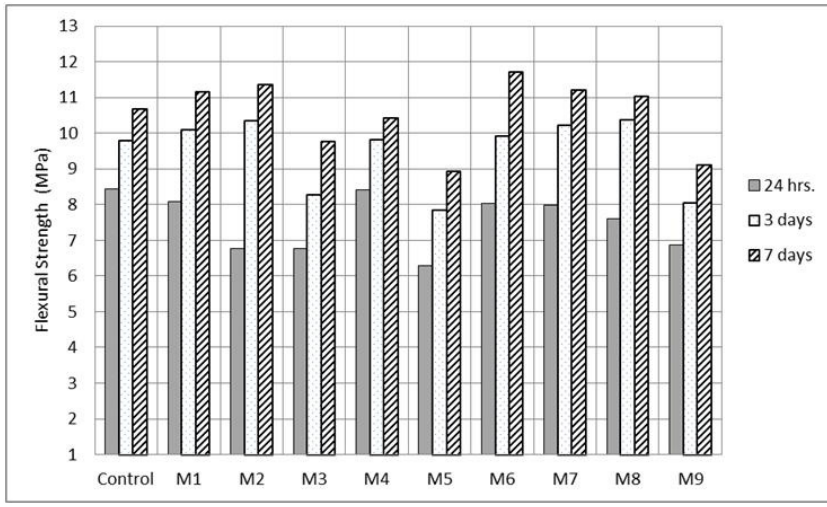

Figure 4: Flexural strength.

Table 6: Best mixture obtained from SEDOC analysis.

	Water (dm^3/m^3)	Silica fume (%)	Superplasticizer (%)	w/cm	Global desirability
BTM	250	0	0.5	0.35	0.911
BPM	270	0	0.5	0.35	0.992

Table 7: Confirmation tests results (average).

Mixture	% Flow	Compressive strength (MPa)	Flexural strength (MPa)	Global desirability
BTM	101.25	47.14	10.44	
Desirability	0.900	0.908	0.955	0.920
BPM	120	52.12	10.48	
Desirability	0.980	0.975	0.956	0.971

Table 7 also shows the best predicted mortar as BPM out of 5184 different possible mixes, the global desirability for this mix is 0.992. Notice that no silica fume was included in the final mix, this influenced most likely for the time constraint in the experiment.

3.1.5 Confirmation analysis

The final step in finding the high performance mortar for the study consists in making and testing the mixes indicated in table 7, namely BTM and BPM. Hence new sets of 3 cubes 50x50x50 cm and 3 beams 40x40x160 cm were casted and tested for each mix at 7 days of age. Table 8 shows the results, from here it can

be confirmed that the best mix and therefore selected as HPM is the mix designated as BPM because its higher overall desirability value of 0.971.

Table 8: Compressive strength of masonry prisms constructed with CM.

Prism	Area (mm^2)	Pu (N)	Height/Width	Slenderness correction	*fm* (MPa)
1	17,836	155,750	3.54	0.954	8.35
2	17,745	58,418	3.52	0.952	3.12
3	17,940	88,711	3.43	0.943	4.67
4	18,032	164,272	3.49	0.949	8.70
5	17,940	112,110	3.49	0.94	5.91
6	17,940	197,242	3.51	0.951	10.47

3.2 Testing masonry sections

Small masonry sections were fabricated considering two different mortar mixes, one designated as conventional (CM, proportions 1:3 by volume) and the other designated as HPM which comes from previous analysis. It was decided that both mortars should have the same consistency, so in order to compensate for brick absorption flow was set at 126.3%. Tables 9 and 10 show results in compression of masonry prisms for each type of mortar indicated.

Table 9: Compressive strength of masonry prisms constructed with HPM.

Prism	Area (mm^2)	Pu (N)	Height/Width	Slenderness correction	*fm* (MPa)
7	17,940	176,814	3.44	0.944	9.36
8	17,836	120,642	3.57	0.957	6.45
9	18,032	86,730	3.45	0.945	4.56
10	17,940	139,818	3.58	0.958	7.44
11	17,836	174,461	3.56	0.956	9.30
12	17,745	129,497	3.56	0.956	6.93

Table 10: Shear strength for masonry assemblages with CM.

Prism	Area (mm^2)	Pu (N)	Height/Width	Slenderness correction	*fm* (MPa)
7	17,940	176,814	3.44	0.944	9.36
8	17,836	120,642	3.57	0.957	6.45
9	18,032	86,730	3.45	0.945	4.56
10	17,940	139,818	3.58	0.958	7.44
11	17,836	174,461	3.56	0.956	9.30
12	17,745	129,497	3.56	0.956	6.93

Figure 5 shows a typical failure of conventional masonry while figure 6 shows a failure of HPM masonry.

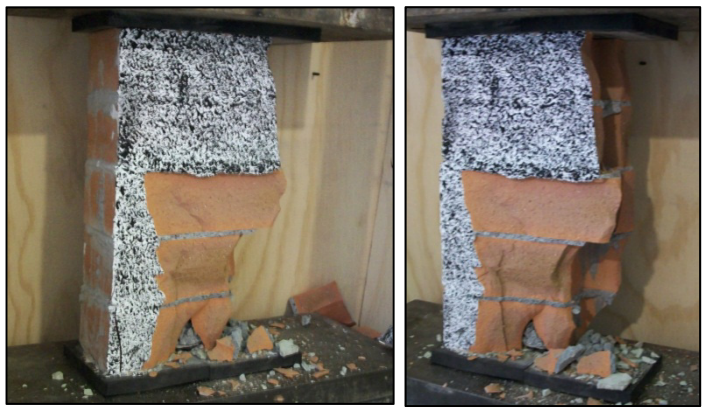

Figure 5: Failure of masonry prism constructed with conventional mortar.

Figure 6: Failure of masonry prism constructed with high performance mortar.

Table 11 shows shear strength results of conventional masonry assemblages subjected to diagonal compression. Table 12 shows shear strength results of HPM assemblages under diagonal compression.

Table 11: Shear strength for masonry assemblages with HPM.

Assemblages	Average (mm.)		Coefficient	Area (mm^2)	Pu (N)	V (MPa)
	Height	Width				
1	327	296	0.91	40,358	40,462	1.00
2	325	295	0.91	40,161	38,521	0.96
3	325.5	296	0.91	40,256	42,826	1.06
4	326	296	0.91	40,290	39,295	0.98
5	326	297	0.91	40,352	49,798	1.23
6	326	296	0.91	40,290	37,138	0.92
					Average	1.00

Table 12: Shear strength for masonry assemblages with HPM.

Assemblages	Average (mm.)		Coefficient	Area (mm^2)	Pu (N)	V (MPa)
	Height	Width				
7	322	294	0.91	39,896	43,198	1.08
8	320	295	0.92	39,824	43,296	1.09
9	320	295	0.92	39,824	47,611	1.19
10	321	295	0.92	39,891	44,443	1.11
11	319	295	0.92	39,756	47,111	1.18
12	320	295	0.92	39,824	41,963	1.05
					Average	1.12

Figure 7 shows a typical failure of conventional masonry assemblage on the left and assemblage with HPM on the right.

Figure 7: Failure of masonry assemblages, conventional mortar on the left, HPM used on the right.

As it can be seen from the pictures of the masonry sections tested, specimens were painted to obtain during testing correlated digital images with the software Vic-2D [5], images were valuable in helping to register a history of deformations and mode of failure. This technique was used also in calculating the modulus of elasticity and the modulus of rigidity of the masonry.

4 Discussion

Results obtained when comparing the performance of conventional mortar against the high performance mortar, as well as comparing their participation in masonry evaluation can be summarized in table 13.

Table 13: Summary of findings.

Material	Characteristic	Improvement with HPM
Mortar	Compressive Strength	62.5 %
	Flexural Strength	26.9 %
Masonry	Compressive Strength	34.7 %
	Modulus of elasticity	7.80 %
	Shear Strength	12.5 %
	Modulus of Rigidity	78.6 %

As it can be seen from table 13, HPM contributes to develop superior mechanical properties as compared to conventional mortar, in this case a typical mortar suggested by a norm that applies to masonry constructions in Mexico City. However because HPM includes a superplasticizer caution in handling this mortar should be encouraged since this mortar tends to flow more in time, therefore timing in building the masonry is important.

What can we expect from seismic demand on masonry made with HPM? Initially and as a result of static testing on the small masonry sections, it was observed that most of the masonry sections made with conventional mortar tend to show an explosive mode of failure, while HPM masonries tend to show an implosive mode of failure. This suggests that adding fibers helped to hold longer before failing.

In order to check theoretically about the differences in behavior considering both the HPM masonry and conventional masonry, a three story building was subjected to seismic forces. A basic architectural design for masonry walls with hollow bricks and monolithic slabs on top of them was considered, and then a simplified seismic analysis was carried out for each case as per the Complementary Technical Norms for Design under seism in Mexico City (CTNM). From the results shown in Table 14, it can be concluded that resistant forces on directions x and y are better than acting forces due to seism only if HPM is used on the masonry walls of the first floor.

Table 14: Acting and resistant forces for a first floor of a small building.

Direction	Acting force Due to seism, kN	Resistant force Conventional mortar, kN	Resistant force HPM, kN
X	447.18	431.88	469.54
Y	437.37	457.18	508.82

As far as cost is concern, a straightforward analysis considering basic and non specialized labour yielded an 11% higher cost for masonry walls using HPM, however the benefits are still to be accounted for when using this alternative in construction.

5 Conclusion

Building houses and small buildings with brick masonries is and will be a very common way of construction in Mexico City and many other cities elsewhere, and it is believed that using HPM in this kind of construction may help to reduce the damages that people may suffer when earthquakes strike in seismic areas.

References

[1] NTC. NTC-Normas Técnicas Complementarias para Diseño y Construcción de Estructuras de Mampostería. México: Gaceta Oficial del Distrito Federal, 2004.
[2] NCHRP. Report 566: Guidelines for Concrete Mixtures Containing Supplementary Cementitious Materials to Enhance Durability of Bridge Decks. Washington D. C.: Transportation Research Board, 2007.
[3] The Statistical Experimental Design for Optimizing Concrete (SEDOC), www.trb.org/Main/Public/Blurbs/158851.aspx
[4] Aïtsin, P-C. *High-Performance Concrete*. London: E&FN SPON, 2004.
[5] Cintrón, R. and Saouma, V. Strain Measurements with the Digital Image Correlation System Vic-2D. Department of Civil Environmental and Architectural Engineering, University of Colorado. Boulder: s. n., 2008.

Section 2
Shape and topology optimization

This page intentionally left blank

Aerodynamic shape optimization of axial flow fan nose cones

R. W. Derksen[1] & J. R. Bender[2]
[1]*Department of Mechanical and Manufacturing Engineering, University of Manitoba, Canada*
[2]*Airline Analysis, Boeing Commercial Airplanes, USA*

Abstract

The purpose of this work is to improve the efficiency of large scale axial flow fans through the introduction of a more uniform velocity distribution over the fan blades. This improved velocity distribution being realized through the use of an aerodynamically optimized inlet cone. The procedure for optimizing the inlet cone uses existing aerodynamic optimization methods programmed into a completely self contained FORTRAN program. The type of optimization algorithm used here is the use of design optimization to solve an inverse design problem. The different modules of the program include a surface vorticity panel method flow solver, a Bezier curve surface definition routine and a minimization method. Three different minimization methods were tested to determine the most appropriate one, this being the downhill simplex method in multidimensions. Many different sized fans and inlet cones were tested, with two different types of optimized inlet cones being discovered. Short inlet cones typically make use of a very blunt inlet cone with a slight hump or rise above the hub radius. Longer inlet cones make use of a more curved inlet cone with no hump. It was also found from this work that the relatively simple methods used can provide an adequate modeling of the problem and a reasonable solution.
Keywords: axial flow fans, aerodynamic shape optimization, inverse design.

WIT Transactions on The Built Environment, Vol 125,
www.witpress.com, ISSN 1743-3509 (on-line)
doi:10.2495/OP120101

1 Introduction

The main objective for this work is to increase the efficiency of industrial and commercial fans and turbines by introducing a more uniform flow at the inlet plane to the blading than normally exists. An example of an axial flow fan and its components is shown in Figure 1 below.

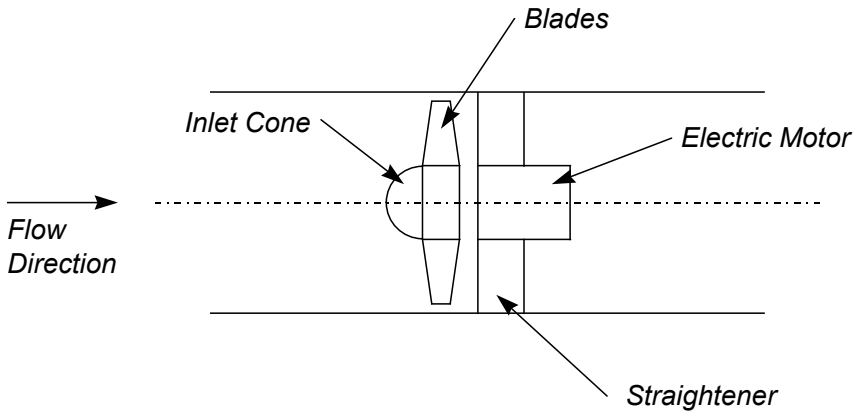

Figure 1: An example of an axial flow fan.

One of the more useful methods is the use of design optimization to solve an inverse design problem. This method makes use of a prescribed final condition such as an optimal velocity distribution or pressure distribution and uses one of the many minimization or maximization methods to search for the proper geometry to provide the desired distribution.

1.1 The flow optimization process

Three main program modules are required for an aerodynamic shape optimization program. The modules are: the flow solver, shape definition and minimization algorithms. A full discussion of the program details and issues that form its development are given in Bender [1].

The flow solver used in this research was an inviscid potential flow model, a surface vorticity model based on Martensen method, to model the flow in the duct and around the inlet cone. The problem is axisymmetric, as all objects involved will be either bodies of revolution, ducts or annuli. The equations used to model axisymmetric flow are different from the standard 2-dimensional equations. This work is based on the work of Lewis [2] who provides a derivation and explanation of the necessary equations and programming issues that arise.

The shape of the inlet cone was parameterized using Bezier curves which are specified by a set of control points that "steer" the curve towards them. The curve only passes through the two end points, however it does remain in the

convex hull (the polygon defined by the control points) of the control points. The function of each control point is to bend the curve towards it as the curve gets near. The use and theory of Bezier curves is thoroughly discussed in Newman and Sproull [3] and Paulidis [4] and will not be elaborated on here.

Three separate minimization techniques were used to solve the current problem: successive iteration of Brent's method in one-dimension, the downhill simplex method in multidimensions and simulated annealing. The first two methods are known as "hill climbing" techniques. That is, they simply follow the local landscape until they reach a minimum. Simulated annealing is a more complicated method that searches the solution domain for the global minimum.

One-dimensional minimization, in particular Brent's method, is very well understood and the theory can be found in most introductory numerical analysis text books such as Press *et al.* [5]. Brent's method is one of the simplest types of minimization methods, a "hill climbing" technique. One of the drawbacks of Brent's method is that the algorithm must have a minimum bracketed before it is started. This can be accomplished through the use of a bracketing routine such as the one found in Press *et al.* [5] and used in this project. Brent's method can be used to solve a multidimensional minimization problem through the use of successive iterations. Each design variable is in turn used as the variable in the function to be minimized while all other design variables are held constant.

The downhill simplex method in multidimensions was introduced by Nelder and Mead [6]. The algorithm is set up to locate a minimum of a function of more than one independent variable. This method is still a "hill climbing" method and therefore does not guarantee that a global minimum will be found. The downhill simplex method makes use of a simplex to find its way "downhill" to a minimum. A simplex in N dimensions consists of N+1 points or vertices and the lines that connect these vertices. For example, in two dimensions (two independent variables) the simplex is a triangle. Once the initial simplex is defined the algorithm continuously modifies it in such a way as to allow it to "crawl" downhill to a minimum where the program is terminated. The simplex is moved downhill through the use of three basic steps: reflection, expansion and contraction of the simplex. The most common step is the reflection, where the "highest point" is moved through the opposite face of the simplex to a lower point. The simplex is also allowed to expand in one direction to allow it to move more quickly down a valley floor. The simplex can also contract itself around one point or a minimum.

Simulated annealing is a technique that uses an analogy with thermodynamics to solve minimization problems. Simulated annealing has the attractive feature that it can search out a global minimum even when it is located amongst many local minimums. The thermodynamic analogy uses the way in which a metal cools and anneals to its lowest energy level. There are four basic elements that must be present for the algorithm to work: an objective function E (analogous to energy) that is to be minimized, a control parameter T (analogous to temperature), an annealing schedule for the reduction of T and a random number generator to provide a random search of the design space. There are several different variations of simulated annealing in the literature, but the variation

chosen was found in Press *et al.* [5] and works as follows. The system state is described by a simplex of N+1 points as in the downhill simplex method in multidimensions, and the simplex moves are the same as those described previously. At any temperature T the simplex scales itself to the approximate size of the region that can be searched at that temperature. The region is then randomly searched. The routine will always accept a downhill step but will also sometimes accept an uphill step. This is known as the Metropolis procedure and is what allows the algorithm to escape from a local minimum in favour of a global minimum. Therefore, if the temperature is reduced sufficiently slowly it is likely that the simplex will shrink into the global minimum.

Several different objective functions were considered for use in the program. For the sake of simplicity the following function was chosen:

$$F(x) = \left| \frac{U_{\max}}{U_{\min}} - 1 \right|$$

U_{max} and U_{min} are the maximum and minimum velocities on the blade inlet velocity distribution. It is easily shown that as the velocity distribution approaches uniformity this function will approach zero, and the more uniform the velocity distribution the lower the objective function value will be.

2 Problem definition

The tests used to compare the three different minimization methods were done using a single hub-to-tip ratio, $h/R_T = 0.25$, fan, with non-dimensional hub lengths, L/R_T, of: *0.125*, *0.25*, *0.50 0.75*, and *1.0*.

Tests were undertaken to determine the effect of hub-to-tip ratio on the solution.

In order to determine the effect of the hub-to-tip ratio a number of tests were run using three different h/R_T: *0.25, 0.5*, and *0.75*. For each hub-to-tip ratio five different inlet cone lengths were tested. These lengths were the same as used for the tests on the minimization methods

Table 1: Number of function calls required for stopping criteria of 0.001.

Method	*0.25* L/R_T	0.50 L/R_T	1.0 L/R_T	1.5 L/R_T	2.0 L/R_T
Original 1-D	147	153	146	288	147
Multi - D	43	33	97	91	160
Simulated Annealing	100	118	151	211	212

3 Results

The tests on the minimization methods were done with a very fine stopping condition of *0.001*. This value corresponds to the smallest change in the objective function that will not terminate the optimization process. Table 1 gives the number of flow solver function calls required by each method.

The most important result that can be determined is that the downhill simplex method in multidimensions is significantly better than the other two methods. Therefore the downhill simplex method is considered to be the most efficient minimization method for this problem.

The objective function value was observed to be significantly higher for large hub-to-tip ratio fans with short inlet cone lengths. The general trend for inlet cone length is that as the cone length is increased the objective function is decreased. These two results were expected from performance data on industrial fans. As the h/R_T is increased the efficiency of the fan unit generally decreases. Due to the fact that some fan manufacturers use an arbitrarily shaped inlet cone with a length of $0.125\ R_T$ or less there is no efficiency data for different inlet cone lengths. However, it is an intuitive assumption that the value of the objective function used would decrease with increasing inlet cone length.

The most surprising observation was that the $0.75\ h/R_T$ fan actually provided a lower objective function than the other two for an inlet cone length of $0.25\ R_T$. Also, for an inlet cone length of $0.50\ R_T$ or longer there is almost no difference in final objective function value among the three different hub-to-tip ratios. This would suggest that there is an optimum inlet cone length for each $h/\ R_T$. This optimum inlet cone length would then correspond to a point of diminishing returns where any subsequent increase in inlet cone length would not significantly decrease the final objective function value or increase the efficiency of the fan.

Figure 2 gives the final designs and streamlines for the $0.25\ h/R_T$ fans, Figure 3 gives the final designs and streamlines for the $0.5\ h/R_T$ fans, and Figure 4 gives the final designs and streamlines of the $0.75\ h/R_T$ fans. There are two different classes of final shapes; the first type of shape has a distinctive hump or rise near the front of the inlet cone, while the second type is just a slight variation of the initial parabolic shape.

These figures provide examples of the first type of inlet cone shape with a distinctive hump. This type of inlet cone is characterized by a very blunt face with a distinctive hump that rises above the hub radius. This class of inlet cone shape was found mainly on the shorter inlet cones. Typically, inlet cone lengths of less than $0.75\ L/R_T$ demonstrated this type of shape. The one exception to this is the inlet cone for the $0.75\ h/R_T$ fan with an inlet cone length of $0.125\ R_T$. It is unknown why this case demonstrates the second class of inlet cone shape.

The second class of inlet cone shape is classified by a very smooth curved inlet cone with a relatively large radius of curvature and by the lack of a blunt face and hump. This parabolic shape was originally expected for all inlet cone lengths. However, this type of shape was typically found on inlet cones of length $0.75\ R_T$ and longer. The above mentioned exception is for a $0.75\ h/R_T$ with a $0.125\ R_T$ inlet cone length. This case however provides significantly poorer performance than all other tests.

It should be noted that there does seem to be a natural transition from a very sharp hump shape to the curved parabolic shaped inlet cone. This is generally affected by inlet cone length. The hub-to-tip ratio seems to have little effect on the type of shape found except for the single exception at $0.75\ h/R_T$.

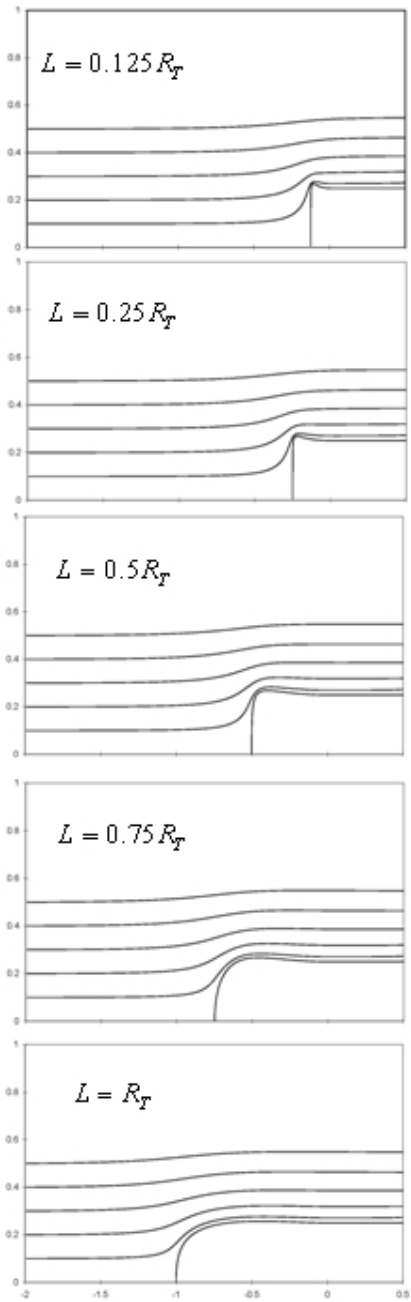

Figure 2: The effect of hub length for a *h/t=0.25* on hub shape and streamlines.

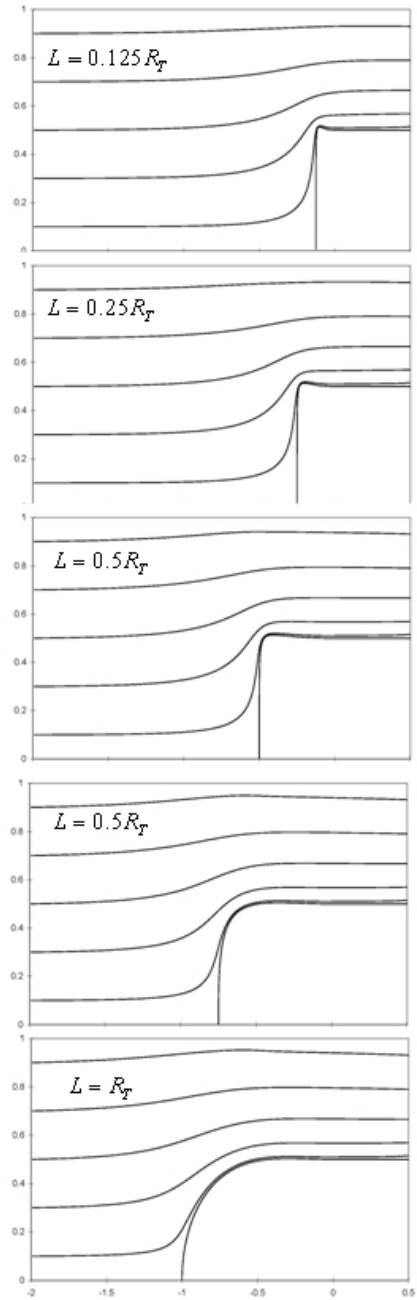

Figure 3: The effect of hub length for a *h/t=0.5* on hub shape and streamlines.

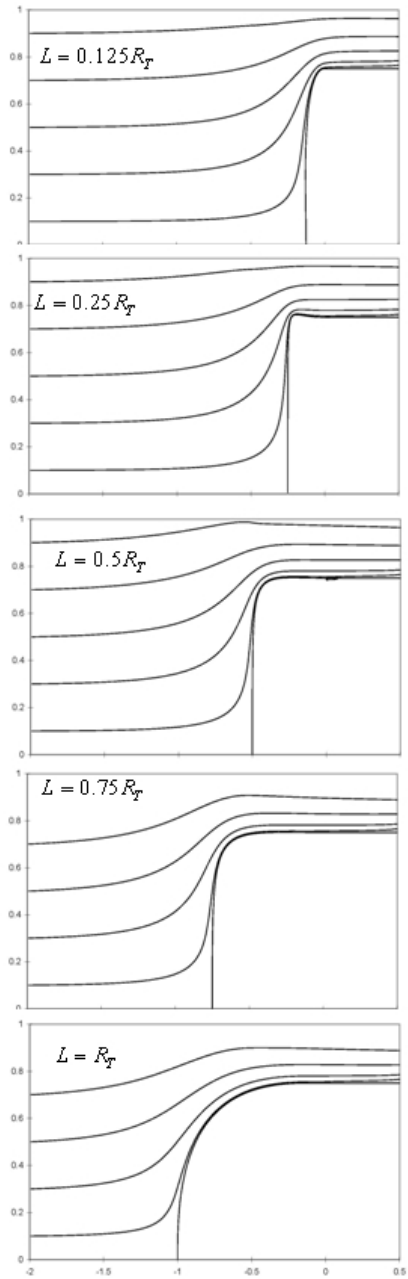

Figure 4: The effect of hub length for a *h/t=0.75* on hub shape and streamlines.

4 Conclusions and recommendations

The most obvious conclusion is that the use of Bezier curves to model the surface provides an exceptional design tool. Not only is the surface controlled by only a few control points that can be used as design variables but the generated surface is guaranteed to be smooth and not oscillate away from the defining points.

In comparison to the other minimization methods tested, the downhill simplex method in multidimensions is far superior in terms of efficiency. There is still a small concern regarding the minimization to a local minimum instead of a global minimum. However, due to the geometrical constraints placed on the design variables and the extensive testing with this problem it is reasonable to assume that the downhill simplex method is locating the global minimum. The very simple objective function used in this problem was developed to force the velocity distribution towards a uniform profile. Subsequent testing proved the objective function to be highly successful in this capacity.

The main question regarding the optimization program is whether or not the surface vorticity panel method is adequate or not. From the numerous tests done using this method the panel method is shown to produce reasonable qualitative results for problems that do not exhibit extreme geometries such as regions of obvious separation and discontinuous surfaces.

Two main types of inlet cones were found using the optimization code. Fans with short inlet cones, less than $0.75\ h/R_T$, typically displayed the first type. Fans with longer inlet cones generally made use of the second type of inlet cone. The first type of inlet cone has a characteristic hump near the front of the inlet cone and a very blunt face. The second type of inlet cone is generally a parabolic shaped inlet cone. There does seem to be a natural transition between the two types as the inlet cone length is increased.

Two important conclusions can be made regarding the effects of cone length and hub-to-tip ratio on the velocity distribution. First, the length of the inlet cone has a significant effect on the velocity distribution for inlet cones shorter than $0.75\ h/R_T$ m for the test case. For lengths greater than this the effect is limited and therefore there is no reason to attempt to improve the efficiency by drastically increasing the length of the inlet cone.

There are many possibilities for further work involving improvements to the program and further testing and verification of the program. The main areas that could possibly be improved upon are the flow solver and the minimization method.

One of the most important improvements that could be made to this program is the addition of a boundary layer solver. This would provide a more realistic approximation to the flow and the necessary corrections for the case of separated flow. While the inclusion of a boundary layer solver would increase the accuracy of the flow solver, and hence the final solution, it would significantly increase the complexity of the computer code and the computational effort required to produce a solution.

One important step in the development of this program remains to be done, experimental verification. The results from this program should be tested experimentally before the program is used for practical applications in order to increase the confidence in the final solution.

One final improvement that may be of practical interest is the addition of an efficiency calculation before and after the optimization is performed. This would provide an estimate for the overall improvement in the total fan efficiency. This improvement, while being of practical interest would require substantial development work due to the need to model the three-dimensional effects of the fan blades.

References

[1] Bender, J.R., *Aerodynamic Shape Optimization of Axial Flow Fans*, M.Sc. Thesis, University of Manitoba, Winnipeg, Canada, 1997.
[2] Lewis, R.I., *Vortex Element Methods For Fluid Dynamic Analysis of Engineering Systems*, Cambridge University Press, Cambridge, pp.1-43, 146-176, 1991.
[3] Newman, W.M., and Sproull, R.F., *Principles of Interactive Computer Graphics*" McGraw-Hill, Tokyo, Japan, pp.315-318, 1981.
[4] Paulidis, T., Algorithms *For Graphics and Image Processing*, Computer Science Press, Rockville, MD., pp.221-230, 1982.
[5] Press, W.H., Vetterling, W.T., Teukolsky, S.A., and Flannery, B.P., *Numerical Recipes in FORTRAN: the art of scientific computing*, 2nd ed., Cambridge University Press, Cambridge, pp.34-40, 51-63, 124-133, 206-209, 254-261, 387-448, 1992.
[6] Nelder, J.A. and Mead, R., "A Simplex Method for Function Minimization," *Computer Journal*, Vol. 7, pp.308-313, 1965.

Isogeometric shape sensitivity analysis

F. Navarrina, H. Gómez, J. París, I. Colominas,
X. Nogueira & M. Casteleiro
GMNI — Group of Numerical Methods in Engineering,
Civil Engineering School, University of A Coruña, Spain

Abstract

On a regular basis, engineering analysis requires stating and solving systems of partial differential equations (PDEs). The most powerful and widely extended techniques for solving PDEs are the so-called Weighted Residuals Methods. To this group belong, among others, the Finite Element Method (FEM), the Boundary Element Method (BEM), the Finite Volume Method (FVM) and the Mesh-Free Method (MFM), as well as the many different formulations included in each of these categories. The new Isogeometric Analysis (IGA) methods were proposed by Hughes *et al.* in 2005, and it is our belief that they really deserve special attention. The key idea of IGA is to use a previously generated CAD model for discretizing both the geometry and the solution to the problem being analyzed. In return for some minor drawbacks, IGA offers a number of major advantages that make the technique specially attractive and promising in comparison with standard FEM, BEM, FVM and MFM formulations.

In this presentation we will state a general formulation for the sensitivity analysis of Weighted Residual Methods, both for linear and non-linear problems with constant or varying geometry. The effects due to variation of geometry are addressed by defining a generic procedure for integration in manifolds on the basis of the metric tensor concept. The proposed approach leads to compact and relatively simple expressions to obtain directional derivatives of arbitrarily high order. The resulting scheme can be easily applied to IGA formulations, its implementation being quite a straightforward task. Finally, one application example is presented.

Keywords: IGA, isogeometric analysis, high order shape sensitivity analysis.

WIT Transactions on The Built Environment, Vol 125,
www.witpress.com, ISSN 1743-3509 (on-line)
doi:10.2495/OP120111

1 Introduction

As a general rule, engineers are required to state and manipulate quite complicated computational models in order to make proper decisions regarding the design and the operation of structures, devices or systems of any kind.

We can think of the actual computational model being used for analyzing a certain case as a black box (that will be called analysis module from here on) type

$$\xrightarrow{\boldsymbol{\alpha}} \boxed{\text{ANALYSIS MODULE}} \xrightarrow{\boldsymbol{\omega}} \tag{1}$$

where $\boldsymbol{\alpha}$ represents the set of input data that are provided by the user, and $\boldsymbol{\omega}$ represents the corresponding set of output results that are provided by the computational model for each given case. We will say that a direct problem is being solved when the value of the outputs $\boldsymbol{\omega}$ are to be obtained for given values of the inputs $\boldsymbol{\alpha}$. This is what the analysis module is originally made for, and this might be all what was needed in certain real cases. But not always, indeed.

If we were dealing with a so-called calibration problem, our aim would be to set up the values of some (or all) of the adjustable parameters $\boldsymbol{\alpha}$ for the results $\boldsymbol{\omega}$ to reach a desired target value. On the other hand, if we were dealing with a so-called parameter estimation problem (also called inverse problem, as opposed to the concept of direct problem), our aim would be to find out the values of some (or all) of the hidden parameters $\boldsymbol{\alpha}$ for the computed outputs $\boldsymbol{\omega}$ to fit some real measures (taken from the real structure, device or system under consideration). Finally, if we were dealing with a so-called optimum design problem, our aim would be to choose the optimum values of some (or all) of the inputs $\boldsymbol{\alpha}$ for the results $\boldsymbol{\omega}$ to minimize a suitable objective function with some additional constraints.

The solution to a problem in any of the above mentioned categories (calibration, parameter estimation and optimum design) could be tackled by trial and error or by means of some heuristics. If we proceed in this way, the analysis module will be simply used (as a black box) for solving a sequence of direct problems. This is what we call a zeroth-order approach. Zeroth-order approaches are conceptually simple and easy to implement. But the price to pay for these advantages is a very poor rate of convergence (kind of 1st-order). For this reason, an extremely large (if not completely out of range) number of iterations is expected as a general rule. This effect strongly limits the accuracy and the efficiency of zeroth-order methods for solving many real problems, what precludes their use in a number of cases. Other more sophisticated (but still zeroth-order) techniques of this type would be the bisection method (in the case of one-dimensional calibration problems) and the golden search method (in the case of one-dimensional optimum design problems.

The above discussion makes clear why higher order approaches (type Newton-Raphson, with a better rate of convergence) are called for solving calibration, parameter estimation and optimum design problems. But the price to pay for a higher rate of convergence (2nd-order) is the need for computing the derivatives of the outputs $\boldsymbol{\omega}$ with respect to the inputs $\boldsymbol{\alpha}$, what is called the sensitivity analysis.

2 Sensitivity analysis

For a given analysis module (1), our aim is to compute the derivatives

$$\frac{d\boldsymbol{\omega}}{d\boldsymbol{\alpha}}, \frac{d^2\boldsymbol{\omega}}{d\boldsymbol{\alpha}^2}, \cdots \frac{d^i\boldsymbol{\omega}}{d\boldsymbol{\alpha}^i}, \cdots \frac{d^n\boldsymbol{\omega}}{d\boldsymbol{\alpha}^n}, \tag{2}$$

up to a certain order n. In real engineering problems both the number of inputs $\dim(\boldsymbol{\alpha})$ and the number of outputs $\dim(\boldsymbol{\omega})$ are expected do be quite large. On the other hand, the number of derivatives (2) increases exponentially with the order of derivation n. Thus, both the computational cost and the amount of memory storage needed for performing a complete nth order sensitivity analysis must be considered unaffordable in most real cases.

However, not all derivatives (2) will be needed as a general rule, since part of the inputs $\boldsymbol{\alpha}$ are expected to be constant and part of the outputs $\boldsymbol{\omega}$ are expected to be irrelevant for the particular case being considered. On the other hand, the derivatives of a function and the function itself belong to a different class (both from the mathematical and from the computer science point of view). Thus, the ith order derivative of $\boldsymbol{\omega}$ with respect to $\boldsymbol{\alpha}$ in (2) is a multidimensional array with $i+1$ indices. This effect poses additional difficulties at the time of implementing the sensitivity analysis in a computer code. We conclude that the sensitivity analysis procedure will be more suitable for each particular case if it allows to select which derivatives are to be computed. Moreover, the implementation of the procedure will be definitely easier if the results $\boldsymbol{\omega}$ and the selected derivatives to be computed are unidimensional arrays of the same size.

The answer for achieving both objectives lies with directional derivatives. For a known value of the first order directional derivative of the inputs $\boldsymbol{\alpha}$ along a certain vector $\boldsymbol{s}$, the first order directional derivative of the outputs $\boldsymbol{\omega}$ along the same vector is given by

$$D_s\ \boldsymbol{\omega} = \left[\frac{\partial \boldsymbol{\omega}}{\partial \boldsymbol{\alpha}}\right]\ D_s\ \boldsymbol{\alpha}. \tag{3}$$

The concept can be extended for higher order derivatives. Thus, the nth order directional derivative of the outputs $\boldsymbol{\omega}$ along vectors $\{\boldsymbol{s}_1, \boldsymbol{s}_2, \ldots, \boldsymbol{s}_n\}$ is given by

$$D^n_{s_1,s_2,\ldots,s_n}\ \boldsymbol{\omega} = D_{s_n}\ \left(\ldots D_{s_2}\ \left(D_{s_1}\ \boldsymbol{\omega}\right)\right). \tag{4}$$

Now it seems clear that the information provided by the high order sensitivity analysis allows for computing approximations to the outputs $\boldsymbol{\omega}$ without the need to repeat the analysis when the inputs $\boldsymbol{\alpha}$ are modified. Thus, if the inputs $\boldsymbol{\alpha}$ are modified as

$$\widetilde{\alpha}(\theta) = \boldsymbol{\alpha} + \sum_{k=1}^{n}\ \frac{1}{k!}\ \left(D^k_{s^k}\ \boldsymbol{\alpha}\right)\ \theta^k + \mathcal{O}(\theta^{n+1}), \tag{5}$$

in terms of a parameter θ, then the corresponding outputs $\boldsymbol{\omega}$ take the values

$$\widetilde{\omega}(\theta) = \boldsymbol{\omega} + \sum_{k=1}^{n}\ \frac{1}{k!}\ \left(D^k_{s^k}\ \boldsymbol{\omega}\right)\ \theta^k + \mathcal{O}(\theta^{n+1}). \tag{6}$$

This is what Lucien Schmidt [1] called "Structural Synthesis Concept" in his pioneering works on structural optimization. And this is the essential point for understanding why sensitivity analysis plays a key role for solving calibration, parameter estimation and optimum design problems in engineering (as well as control problems, that are basically time-dependent problems of any of the former three categories).

Finally, it seems also clear that numerical differentiation should be avoided for at least two reasons: the lack of accuracy and the high computational cost. To illustrate this point, let's suppose that the following procedure is used for approximating the first order derivative of a scalar function of one variable $f(x)$:

$$f'(x) = \frac{f(x+h) - f(x)}{h} + \mathcal{O}(h). \tag{7}$$

It is obvious that the correct balance between round-off and truncation errors is difficult to achieve in practice, since it depends on the value of the increment h. On the other hand, for computing the single derivative $f'(x)$ by means of approximation (5) the original function must be evaluated twice. These effects are more noticeable indeed in the case of multiple variables.

3 Linear and non-linear analysis

For the sake of simplicity, we can think of the analysis module (1) as a computer implementation of a numerical method that states and solves the so-called state equation

$$\boldsymbol{\psi}(\boldsymbol{\alpha}, \boldsymbol{\omega}) = \mathbf{0}. \tag{8}$$

However, the forthcoming concepts can be also quite easily extended to time-dependent and eigenvalue problems.

If the state function $\boldsymbol{\psi}(\boldsymbol{\alpha}, \boldsymbol{\omega})$ is linear

$$\boldsymbol{\psi}(\boldsymbol{\alpha}, \boldsymbol{\omega}) = \boldsymbol{K}(\boldsymbol{\alpha})\,\boldsymbol{\omega} - \boldsymbol{b}(\boldsymbol{\alpha}) = \mathbf{0}, \tag{9}$$

then the analysis module is prepared for solving linear systems type

$$\boldsymbol{K}(\boldsymbol{\alpha})\,\boldsymbol{\omega} = \boldsymbol{b}(\boldsymbol{\alpha}) \tag{10}$$

by means of a direct solver (very likely a sparse matrix factorization solver type Cholesky or Crout) or an iterative solver (type PCG o GMRES).

On the other hand, if the state function $\boldsymbol{\psi}(\boldsymbol{\alpha}, \boldsymbol{\omega})$ is non-linear the analysis module is prepared for performing iterations until convergence type Newton-Raphson's method

$$\begin{cases} \text{solve} & \boldsymbol{K}(\boldsymbol{\alpha},\boldsymbol{\omega}_\kappa)\ \Delta\boldsymbol{\omega}_\kappa = \boldsymbol{b}(\boldsymbol{\alpha},\boldsymbol{\omega}_\kappa), \\ \text{update} & \boldsymbol{\omega}_{\kappa+1} = \boldsymbol{\omega}_\kappa + \Delta\boldsymbol{\omega}_\kappa, \end{cases} \tag{11}$$

where

$$\begin{cases} \boldsymbol{K}(\boldsymbol{\alpha},\boldsymbol{\omega}) = \left[\dfrac{\partial\boldsymbol{\psi}}{\partial\boldsymbol{\omega}}\right], \\ \boldsymbol{b}(\boldsymbol{\alpha},\boldsymbol{\omega}) = -\boldsymbol{\psi}(\boldsymbol{\alpha},\boldsymbol{\omega}). \end{cases} \tag{12}$$

Therefore, each non linear step (iteration) is roughly equivalent to a full linear analysis.

4 Sensitivity analysis master techniques

Direct differentiation of the state equation (8) yields the linear system

$$\left[\frac{\partial\boldsymbol{\psi}}{\partial\boldsymbol{\omega}}\right]\ D_s\ \boldsymbol{\omega} = -\left(\frac{\partial\boldsymbol{\psi}}{\partial\boldsymbol{\alpha}}\ D_s\ \boldsymbol{\alpha}\right). \tag{13}$$

If the state function $\boldsymbol{\psi}(\boldsymbol{\alpha},\boldsymbol{\omega})$ is linear as in (9) then

$$\left[\frac{\partial\boldsymbol{\psi}}{\partial\boldsymbol{\omega}}\right] = \boldsymbol{K}(\boldsymbol{\alpha}), \quad \frac{\partial\boldsymbol{\psi}}{\partial\boldsymbol{\alpha}}\ D_s\ \boldsymbol{\alpha} = D_s\ \boldsymbol{b} - (D_s\ \boldsymbol{K})\ \boldsymbol{\omega}. \tag{14}$$

Hence, the sensitivity analysis consists in solving the linear system

$$\boldsymbol{K}(\boldsymbol{\alpha})\ D_s\ \boldsymbol{\omega} = D_s\ \boldsymbol{b} - (D_s\ \boldsymbol{K})\ \boldsymbol{\omega} \tag{15}$$

which coefficient matrix is the same as in (10). Therefore, if the analysis module is based on a direct solver, the computing overload associated to the sensitivity analysis is expected to be small in comparison with the analysis itself (about the cost of calling for one additional load case).

On the other hand, if the state function $\boldsymbol{\psi}(\boldsymbol{\alpha},\boldsymbol{\omega})$ is non-linear, we notice that (13) is still a linear system with the same coefficients matrix that was used in the last iteration of Newton-Raphson's method (11). Therefore, if the analysis module is based on a direct solver, the computing overload associated to the sensitivity analysis is expected to be also small in comparison with the analysis itself (about the cost of performing one more Newton-Raphson iteration in the analysis).

The first order sensitivity analysis procedure above explained is known as the Direct Differentiation Method. Depending on other considerations (see [1, 2] for more details), the operations involved can be conveniently rearranged. This leads to the so-called Adjoint State Method [3, 4].

Finally, deriving a high order sensitivity analysis procedure by means of the same principles above outlined is just a matter of algebra. Thus, if the state function $\boldsymbol{\psi}(\boldsymbol{\alpha},\boldsymbol{\omega})$ is linear as in (9) recursive differentiation of the state equation (8) yields

linear systems type

$$\boldsymbol{K}(\boldsymbol{\alpha})\ D^n_{s^n}\ \boldsymbol{\omega} = D^n_{s^n}\ \boldsymbol{b} - (D^n_{s^n}\ \boldsymbol{K})\ \boldsymbol{\omega} - \sum_{i=1}^{n-1} \binom{n}{i}\ \left(D^i_{s^i}\ \boldsymbol{K}\right)\ D^{n-i}_{s^{n-i}}\ \boldsymbol{\omega}. \quad (16)$$

A similar (but more cumbersome) expression can be derived for the non-linear case. One again, we notice that the coefficient matrix is the same as in (10) and in (15). Therefore, if the analysis module is based on a direct solver, the computing overload associated to the high order sensitivity analysis is still expected to be small in comparison with the analysis itself.

We conclude that in practice it will be realistic to ask for the first directional derivative (or the full gradient, if necessary) of the outputs $\boldsymbol{\omega}$. And it will also be realistic to ask for their second (or higher) order directional derivative. But it will not be realistic, as a general rule, to call for the full hessian (or higher order full set of derivatives) of the outputs $\boldsymbol{\omega}$ due to the large number of items to be computed and to the associated amount of memory storage that would be required.

5 Isogeometric analysis (IGA)

Very likely, the Analysis Module (1) will consist on a FEM, BEM, FVM, MFM or IGA code. Hence, we are talking about a quite sophisticated intensive CPU time consuming tool.

All these formulations belong to the group of the so-called Weighted Residuals Methods. Describing and enumerating the similarities and the differences between all of them is far beyond the scope of this paper. But, as far as we are concerned in this section, the aim of the Weighted Residual Methods is to obtain an approximate numerical solution for a given partial differential equation in a given domain. For achieving this objective, the weighted residuals principle (and other techniques, such as the Divergence Theorem) are used to convert the original partial differential equation into a suitable variational weak form. Then, the solution to the problem is discretized in order to convert the above mentioned variational weak form into an algebraic system of linear or non-linear equations type (8). Finally, the geometry of the domain is discretized in order to compute the integral terms that are introduced by the weighted residuals principle. Quite frequently both, the solution to the problem and the geometry of the domain, are discretized by means of the same interpolation techniques (isoparametric interpolation), what contributes some computational advantages.

FEM, BEM, FVM and MFM formulations are based on classic interpolation techniques (type Lagrangian interpolation, least squares, etc.). On the contrary, IGA formulations are based on the much more powerful and versatile CAD interpolation techniques, namely B-Splines, NURBS and (more recently) T-Splines. The IGA concept was first introduced in 2005 by Hughes *et al.* [5]. The original aim of IGA was to avoid the need for producing the coarse and non smooth FEM type discretizations that were needed for the analysis, while the much more sophisticated and smooth discretizations that were generated by CAD systems

had to be systematically discarded. The key idea is quite simple: just import the discretization generated by the CAD system into the analysis module, and use it for discretizing both, the geometry and the solution to the problem.

B-Splines, NURBS and T-Splines belong to the same family of interpolation methods. Again, describing and enumerating the similarities and the differences between all of them is far beyond the scope of this paper. Essentially NURBS are B-Splines in homogeneous coordinates [6]. Although this slight difference gratefully improves the power of the interpolation technique, the underlying concepts are essentially identical. On the other hand, the aim of the T-Splines formulation is to provide local h-refinement in bi-dimensional and three-dimensional discretizations. The T-Spline formulation is more complicated (and also more versatile and powerful) than the B-Spline formulations, but the underlying concepts regarding IGA are basically the same. For these reasons we will focus on B-Splines.

Let the definition domain of a certain problem be a curve embedded in the three-dimensional material space. The IGA B-Spline one-dimensional interpolation for this case can be written as

$$\begin{cases} \boldsymbol{r}^h(\xi) = \sum_{i=1}^{n} N_{i,p}(\xi)\, \boldsymbol{r}_i, \\ \\ u^h(\xi) = \sum_{i=1}^{n} N_{i,p}(\xi)\, u_i, \end{cases} \qquad \xi \in [0,1]. \tag{17}$$

For each value of the so-called reference coordinate ξ, the above expressions give the interpolated position of each point $\boldsymbol{r}^h(\xi)$ within the domain and the interpolated value of the solution $u^h(\xi)$ to the problem at that point. The so-called control points $\{\boldsymbol{r}_i\}_{i=1,\ldots,n}$ will be provided by the CAD system and define the geometry of the domain (the curve itself) of the problem being solved. On the other hand, the unknowns $\{u_i\}_{i=1,\ldots,n}$ must be computed by the analysis module in order to approximate the solution to the problem.

The base of shape functions $N_{i,p}(\xi)$ in the above expression are given by the Cox-De Boor recursion formula [7]

$$\begin{cases} N_{i,q}(\xi) = \begin{cases} 1 & \text{if } \xi \le \xi_{i+1}, \\ \\ 0 & \text{otherwise}, \end{cases} & \begin{cases} q = 0, \\ \\ i = 1, \ldots, n + (p-q). \end{cases} \\ \\ N_{i,q}(\xi) = \left(\dfrac{\xi - \xi_i}{\xi_{i+q} - \xi_i} \right) N_{i,q-1}(\xi) \\ \qquad + \left(\dfrac{\xi_{i+q+1} - \xi}{\xi_{i+q+1} - \xi_{i+1}} \right) N_{i+1,q-1}(\xi), & \begin{cases} q = 1, \ldots, p, \\ \\ i = 1, \ldots, n + (p-q). \end{cases} \end{cases} \tag{18}$$

The above computations are normally implemented by means of the Piegl and Tiller Algorithms [8], that are considered as the best numerically stable and fully

optimized routines to perform the Cox-De Boor recursion. Functions $N_{i,p}(\xi)$ generated by this procedure are piecewise polynomials in terms of the variable ξ. We also notice that for $\xi_1 \leq \xi \leq \xi_{n+p+1}$, the following assertions hold [7]:

$$\begin{cases} \displaystyle\sum_{i=1}^{n} N_{i,p}(\xi) = 1 & \text{(partition of unity)}, \\ N_{i,p}(\xi) \geq 0, & \\ N_{i,p}(\xi) \in \mathcal{C}^{p-1} & \text{(if knots are not repeated)}, \\ N_{i,p}(\xi) \neq 0 & \text{in } (p+1) \text{ knot spans at most.} \end{cases} \tag{19}$$

The partition of unity assertion in (19) guarantees that the IGA approximation type (17) for $u^h(\xi)$ is able to represent (exactly) a constant function (what happens when u_i takes the same value for all i). This is an essential requirement for an interpolation technique to be acceptable in computational mechanics as a general rule. On the other hand, the last assertion in (19) is quite surprising, but also important and beneficial, since it guarantees that the bandwidth of the final system type (8) will not be too large.

The degree and the continuity of the piecewise polynomials $N_{i,p}(\xi)$ are controlled by the so called knot vector [7]

$$\begin{aligned} &\Xi = [\xi_1, \ldots, \xi_i, \xi_{i+1}, \ldots, \xi_{n+p+1}], \\ &\text{with } \xi_j \in \mathbb{R} \ \forall j, \text{ and } \xi_i \leq \xi_{i+1} \text{ for } 1 \leq i \leq n+p. \end{aligned} \tag{20}$$

where the ξ_j are called knots, $[\xi_i, \xi_{i+1}]$ is a so-called knot span, n is the number of basis functions and p is the polynomial order. We notice that knots must form a non decreasing sequence, although multiplicity is allowed (and has some important effects). As a general rule, the thus defined IGA approximation (17) is not guaranteed to be "interpolatory" in the strict sense, since it is possible that $\boldsymbol{r}^h(\xi)$ and $u^h(\xi)$ will not match the values of $\boldsymbol{r}_i$ and u_i (respectively) for any value of the reference coordinate ξ. However, if a knot is repeated, the approximation looses one order of continuity for each repetition of the knot at the corresponding value of ξ . Therefore, the approximation becomes discontinuous if the knot is repeated exactly $p+1$ times. Furthermore, it becomes interpolatory if the knot is repeated exactly p times. In many practical applications the knot vector is said to be open and uniform. This means that $\xi_1 = \xi_2 = \ldots = \xi_{p+1} = 0$, $\xi_{n+1} = \xi_{n+2} = \ldots = \xi_{n+p+1} = 1$ and knots $\{\xi_{p+1}, \ldots, \xi_{n+1}\}$ are uniformly distributed in the interval $[0, 1]$. The thus defined IGA approximation is interpolatory only at the first and at the last control point [7].

Another important issue in favor of IGA is the fact that the so-called Oslo Knot Insertion procedure [7] allows for creating new knots while the domain geometry remains unchanged. Therefore, the functional interpolation can be improved as much as desired without affecting the geometry of the problem. This makes h-refinement a trivial automatic task that can be done on the fly by the analysis code, without the need for a mesh refinement preprocessor. However, knot insertion

in bi-dimensional and three-dimensional problems makes h-refinement non-local (and this is one of the reasons why there is so much interest and research on T-Splines at present)

Finally, bi-dimensional and three-dimensional B-Spline interpolations can be easily generated by means of a tensor product of several one-dimensional B-Spline interpolations type (17), thus giving [7]

$$\begin{cases} \boldsymbol{r}^h(\xi,\eta,\chi) = \displaystyle\sum_{i=1}^{n}\sum_{j=1}^{m}\sum_{k=1}^{\ell} N^{\xi}_{i,p_\xi}(\xi)\, N^{\eta}_{j,p_\eta}(\eta)\, N^{\chi}_{k,p_\chi}(\chi)\, \boldsymbol{r}_{i,j,k}, \\ \qquad\qquad\qquad\qquad\qquad\qquad\qquad\qquad (\xi,\eta,\chi) \in [0,1]^3. \\ u^h(\xi,\eta,\chi) = \displaystyle\sum_{i=1}^{n}\sum_{j=1}^{m}\sum_{k=1}^{\ell} N^{\xi}_{i,p_\xi}(\xi)\, N^{\eta}_{j,p_\eta}(\eta)\, N^{\chi}_{k,p_\chi}(\chi)\, u_{i,j,k} \end{cases} \tag{21}$$

IGA can be quite easily implemented within an existing FEM code. The rules to do so are quite simple:

1. ELEMENTS are substituted by KNOT SPANS.
2. NODES are substituted by CONTROL POINTS.
3. SHAPE FUNCTIONS are substituted by the PIEGL AND TILLER ALGORITHMS.
4. The rest remain unchanged (same weak form, same general organization of the code, same integration formulas, etc.).

It is true that IGA has some drawbacks in comparison with FEM, BEM, FVM, MFM formulations since unknowns no longer represent nodal values, essential boundary conditions may become non-trivial and geometric modelling is much less intuitive. But IGA also offers a number of major advantages, namely: CAD models are expected to be analyzed without the need for mesh generation (although this has not been fully accomplished because CAD systems are designed to model surfaces mainly, instead of solids); mesh refinement becomes (almost) trivial, and geometry is not modified in the process; continuity can be arbitrarily raised without heavy tolls to pay for in return; the capacity of the formulation for approximating complex behaviors is dramatically increased; and higher order problems can be addressed (such as Phase-Field models type Cahn-Hilliard and Navier-Stokes-Korteweg equations, and many others).

6 Sensitivity analysis specifics for IGA

In Weighted Residuals based formulations (such as IGA) state equation (8) takes the general form

$$\boldsymbol{\psi}(\boldsymbol{\alpha},\boldsymbol{\omega}) = \int_{\boldsymbol{r}\in\Omega(\boldsymbol{\alpha})} \boldsymbol{\mathcal{P}}(\boldsymbol{r},\boldsymbol{\alpha},\boldsymbol{\omega})\, d\Omega, \tag{22}$$

where $\boldsymbol{\alpha}$ are the input data to the IGA analysis module (geometry, physical properties, loads, etc.), $\boldsymbol{\omega}$ are the so called state variables or output results (deformation–stress, velocity-pressure, etc.), Ω is the definition domain of the problem embedded in the material space (normally $\mathbb{R}^3$) and $\boldsymbol{r}$ are the coordinates

of an arbitrary point in Ω. For the sake of simplicity, we assume that geometry (and hence, domain Ω) does not depend on $\boldsymbol{\omega}$. Otherwise, the suitable corrections should be included.

Therefore, the sensitivity analysis of this kind of formulations requires taking derivatives of functions that are defined by integration in arbitrary domains. If the geometry of the problem being solved is constant, so will be the integration domains. In these conditions it is fairly straightforward to state the sensitivity analysis by means of fully analytical techniques. On the contrary, if the geometry of the problem being solved is not constant (i.e. in shape optimization or shape parameter estimation problems, non-confined flow problems, etc.) stating the sensitivity analysis is not immediate. For this reason, the sensitivity analysis for varying-geometry problems has been mainly addressed by means of low order finite difference approximations, that are known to be inaccurate and difficult to calibrate. In an attempt to overcome this drawbacks, a number of analytical approaches have been proposed to address the sensitivity of 1) the numerical implementation, 2) the analytical model in weak form, and 3) the discretized formulation corresponding to the numerical method being used [1, 3]. The latter approach is in perfect agreement with the analysis model being used, and gives rise to a most compact and flexible formulation than the other options. For those reasons, this will be the approach that we will follow in this paper.

As shown in (13) we need to compute sensitivity terms type

$$\left[\frac{\partial \boldsymbol{\psi}}{\partial \boldsymbol{\omega}}\right] = \frac{\partial}{\partial \boldsymbol{\omega}} \int_{\boldsymbol{r}\in\Omega(\boldsymbol{\alpha})} \boldsymbol{\mathcal{P}}(\boldsymbol{r},\boldsymbol{\alpha},\boldsymbol{\omega})\, d\Omega \tag{23}$$

and

$$D_s^{\alpha}\ \boldsymbol{\psi} = D_s^{\alpha} \int_{\boldsymbol{r}\in\Omega(\boldsymbol{\alpha})} \boldsymbol{\mathcal{P}}(\boldsymbol{r},\boldsymbol{\alpha},\boldsymbol{\omega})\, d\Omega, \quad \text{being } D_s^{\alpha}\ \square = \frac{\partial \square}{\partial \boldsymbol{\alpha}}\, D_{\mathrm{s}}\boldsymbol{\alpha}. \tag{24}$$

Terms type (23) can be considered immediate, since integration domain $\Omega(\boldsymbol{\alpha})$ does not vary with $\boldsymbol{\omega}$. Thus,

$$\left[\frac{\partial \boldsymbol{\psi}}{\partial \boldsymbol{\omega}}\right] = \int_{\boldsymbol{r}\in\Omega(\boldsymbol{\alpha})} \frac{\partial}{\partial \boldsymbol{\omega}}\ \boldsymbol{\mathcal{P}}(\boldsymbol{r},\boldsymbol{\alpha},\boldsymbol{\omega})\ d\Omega \tag{25}$$

On the other hand, terms type (24) can not be considered immediate, since integration domain $\Omega(\boldsymbol{\alpha})$ does vary with $\boldsymbol{\omega}$. This is the reason why a traditional distinction is made between sizing optimization (when $\Omega(\boldsymbol{\alpha})$ is constant) and shape optimization (when $\Omega(\boldsymbol{\alpha})$ is variable). However, it can be proved [3] that

$$D_s^{\alpha}\ \boldsymbol{\psi} = \int_{\boldsymbol{r}\in\Omega(\boldsymbol{\alpha})} \mathcal{D}_{\mathrm{s}}\ \boldsymbol{\mathcal{P}}(\boldsymbol{r},\boldsymbol{\alpha},\boldsymbol{\omega})\ d\Omega \tag{26}$$

where,

$$\mathcal{D}_{\mathrm{s}}\ \square = D_s^{\alpha}\ \square\ +\ \square\ \frac{1}{2}\ \mathrm{Tr}\left[\boldsymbol{G}^{-1}\ D_s\ \boldsymbol{G}\right], \tag{27}$$

being $\boldsymbol{G}$ the so-called metric tensor of the IGA mapping type (21). The details on how to compute and manipulate the metric tensor can be found in [3].

We notice that expressions (25) and (26) are analogous to the previous expression (22). Therefore, the same integration techniques can be used for the three of them. Furthermore, the corresponding high order sensitivity terms can be generated by recurrence.

7 Application example

In this section we will present some results obtained for a concrete roof spanning over a square room and built-in at its four vertices. Because of symmetry, only one quarter of the structure is analyzed. The complete specifications of the structure are given in [3]. In particular, the height of the mid-surface at the keystone is 1:839920 m. The analysis is performed by means of a linear elastic three-dimensional isogeometric model with uniform open knot vectors, B-Spline interpolating functions (p = 2) null displacements at the built-in supports, symmetry conditions where applicable, and integration by means of 3-point Gauss quadratures.

The geometry of the roof is defined by a total of 27 control points (see left side of Fig. 1). An h-refined mesh is automatically generated for the analysis by knot insertion, giving a total of $32 \times 32 \times 4 = 4,096$ control points (nodes) and $30 \times 30 \times 2 = 1,800$ knot spans (elements). We notice that this IGA model reproduces the exact geometry of the roof (as defined in [3]) for all and any level of h-refinement being applied.

Fig. 1 (right side) shows how the 1st principal stress in the vicinity of control point # 1 changes when the design in modified. In this figure we compare the IGA computed results with the IGA 3rd order predicted values. The former were obtained by recalculating the structure each time. The latter were obtained by approximating the structural response in terms of a Taylor expansion, taking into account the information given by a 3rd order directional sensitivity analysis of the unmodified design.

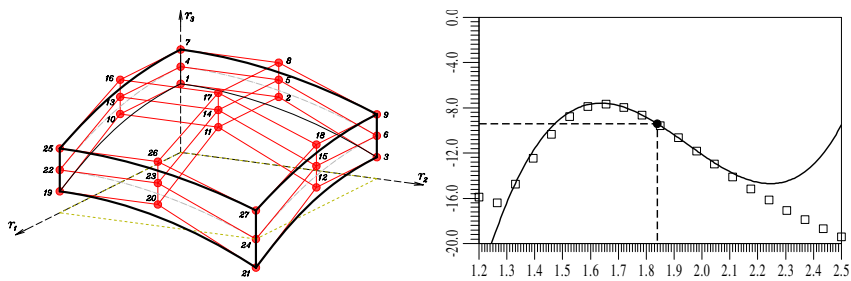

Figure 1: Left: IGA model. Right: 1st principal stress [Pa] at a given point for different heights [m] of the mid-surface at the keystone; 3rd order predicted (line) vs. computed results (squares).

8 Conclusions

A unified approach for the high order sensitivity analysis of IGA formulations has been presented. The technique is based on the IGA mapping that links material and reference coordinates. High order directional sensitivity derivatives are given by a single, unified and compact expression. The 1st order sensitivity analysis is cheap in terms of computing time, and may contribute essential information for decision-making. The 2nd order sensitivity analysis is relatively cheap in terms of computing time, and may contribute important information for improving algorithms. Higher order information is more expensive in terms of computing time, although it contributes to improve the quality of the approximations being used. The scope of future versions of IGA-based codes will be gratefully expanded if support for high order directional sensitivity analysis is provided as a standard feature.

Acknowledgements

This research work has been partially supported by FEDER funds of the European Union, by Grants # DPI2009-14546-C02-01 and # DPI2010-16496 of the *"Ministerio de Ciencia e Innovación"* of the Spanish Government, by Grants #CEOU 2007/09, # PGDIT09MDS00718PR and # PGDIT09REM005118PR of the *"Subdirección Xeral de I+D"* of the *"Xunta de Galicia"* and by research fellowships of *"Universidad de A Coruña"* and *"Fundación de la Ingeniería Civil de Galicia"*.

References

[1] Navarrina F. and Casteleiro M., A General Methodologycal Analysis for Optimum Design, *International Journal for Numerical Methods in Engineering*, **31(1)**, pp. 85–111, 1991.
[2] Haug J.E., Choi K.K. and Komkov V., *Design Sensitivity Analysis of Structural Systems*, Academic Press: Orlando, 1986.
[3] Navarrina F., López S., Colominas I., Bendito E. and Casteleiro M., High Order Shape Design Sensitivity: A Unified Approach, *Computer Methods in Applied Mechanics and Engineering*, **188(4)**, pp. 681–696, 2000.
[4] Choi K.K. and Kim N.H., *Structural Sensitivity Analysis and Optimization (Vol. 1 & 2)*, Springer Mechanical Engineering Series: New York, 2005.
[5] Hughes T.J.R., Cottrell J.A. and Bazilevs Y., Isogeometric analysis: CAD, finite elements, NURBS, exact geometry and mesh refinement, *Computer Methods in Applied Mechanics and Engineering*, **194**, pp. 4135–4195, 2005.
[6] Rogers D.F., *An Introduction to NURBS*, Academic Press: San Diego, 2001.
[7] Cottrell J.A., Hughes T.J.R. and Bazilevs Y., *ISOGEOMETRIC ANALYSIS. Towards Integration of CAD and FEA*, John Wiley & Sons Ltd.: Chichester, 2009.
[8] Piegl L., Tiller W., *The NURBS Book*, Monographs in Visual Communication, Springer-Verlag: Berlin, 1997.

Free-form optimization of thin-walled structures for achieving a desired deformed shape

M. Shimoda
Department of Advanced Science and Technology,
Toyota Technological Institute, Japan

Abstract

Thin-walled structures such as shells and folded plates are extensively used in various industrial products. In this paper, a free-form optimization method is presented that is aimed at giving a function to thin-walled structures. As a concrete target, a method to achieve a desired deformation, or to control a static deformed shape to a desired one, is proposed for the design of linear elastic shell structures. As an objective functional, we introduce a squared error norm of a deformed shape on its prescribed surface. It is assumed that the shell is varied in the normal direction to the surface and that the thickness is constant. A distributed-parameter shape optimization problem is formulated, and the shape gradient function for this problem is theoretically derived. The non-parametric free-form optimization method for shells, which was developed by the author, is applied to solve this problem. With this method, an optimal arbitrarily formed shell with smoothness can be obtained while minimizing the objective functional. The calculated results show the effectiveness of the proposed method for the optimal free-form design of thin-walled structures with a desired deformed shape.
Keywords: optimum design, shape optimization, shell, shape identification, inverse problem, deformation control, traction method.

1 Introduction

Thin-walled or shell structures have high load-carrying capacity in spite of their thinness and lightness. A smart and simple thin-walled structure may be created by adding a function to them without using any actuators. As such a function, a

WIT Transactions on The Built Environment, Vol 125, © 2012 WIT Press
www.witpress.com, ISSN 1743-3509 (on-line)
doi:10.2495/OP120121

desired deformation, i.e., obtaining a given displacement distribution, against an external force is considered in this study. An optimization technique is necessary for designing such a structure. For executing the shape design of a thin-walled structure with a high level performance yet using the minimum amount of material, it is especially necessary to optimize its curvature distribution while satisfying the design purposes.

The author and colleagues have been developing a free-form optimization method, called the "H^1 gradient method for shells" for designing the optimal smooth free-form surface of thin-walled structures with curvatures. In our previous studies, we proposed solutions to stiffness problems [1] and vibration problems [2] of shell structures. Focusing on shape optimization of shell structures, the methods can be categorized into parametric and non-parametric methods in terms of design variables. Although most previously proposed shape optimization methods for shells [3, 4] are parametric methods, which require parameterization of the shape in advance and the obtained shape is strongly dominated by the parameterization process, our method is classified as a non-parametric method. The proposed method and its features will be described in the following sections. Another non-parametric method with a filter for smoothing was presented by Bletzinger *et al*. [5].

In this study, a shape identification problem for linear elastic thin-walled structures is newly solved with the H^1 gradient method for shells for the purpose of achieving a desired deformed shape under an external force. Controlling the displacement distribution to a given desired one can contribute to solving stiffness design and compliant design problems of thin-walled structures, which means that the solution described here can impart a function to structures by simply changing their shapes. This design problem is a so-called compliant mechanism design or a homology design, and many related papers proposing topology or shape optimization methods have been published [6–10]. However, few papers have discussed the use of a non-parametric shape optimization method to control the deformation design of thin-walled structures. In this study, the desired deformed shape is identified by introducing a squared error norm of a deformed shape on its prescribed surface as the objective functional. With the free-form optimization method, an optimum thin-walled structure with a smooth free-form surface and a desired deformed shape as its function can be obtained without any shape parameterization.

2 Governing equation for a shell as a set of infinitesimal flat surfaces

As shown in Fig. 1(a) and Eqs. (1–3), consider a shell having an initial bounded domain $\Omega \subset \mathbf{R}^3$ with the boundary $\partial\Omega$, mid-area A with the boundary ∂A, side surface S and thickness h. It is assumed for simplicity that a shell structure occupying a bounded domain is a set of infinitesimal flat surfaces as shown in Fig. 1(b).

$$\Omega = \left\{(x_1, x_2, x_3) \in \mathbf{R}^3 \mid (x_1, x_2) \in A \subset \mathbf{R}^2, x_3 \in (-h/2, h/2)\right\}, \tag{1}$$

$$\Omega = A \times (-\frac{h}{2}, \frac{h}{2}), \tag{2}$$

$$S = \partial A \times (-\frac{h}{2}, \frac{h}{2}) \tag{3}$$

It is assumed that the mapping of the local coordinate system $(x_1, x_2, 0)$, which gives the position of the mid-area of the shell, to the global coordinate system (X_1, X_2, X_3), i.e., $\phi : (x_1, x_2, 0) \in \mathbf{R}^3 \mapsto (X_1, X_2, X_3) \in \mathbf{R}^3$, is piecewise smooth. The Mindlin-Reissner plate theory is applied concerning plate bending, and the coupling of the membrane stiffness and bending stiffness is ignored. Using the sign convention in Fig. 1(b), the displacements expressed by the local coordinates $\boldsymbol{u} = \{u_i\}_{i=1,2,3}$ can be divided into the displacements in the in-plane direction $\{u_\alpha\}_{\alpha=1,2}$ and the displacement in the out-of-plane direction u_3. In this paper, the subscripts of the Greek letters are expressed as $\alpha = 1, 2$, and the tensor subscript notation uses Einstein's summation convention and a partial differential notation with respect to the spatial coordinates $(\cdot)_{,i} = \partial(\cdot)/\partial x_i$.

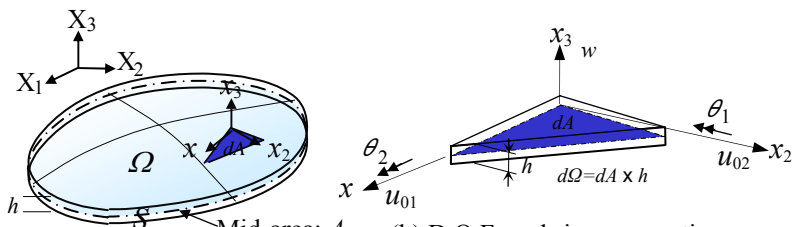

(a) Geometry of a shell (b) D.O.F. and sign convention

Figure 1: Shell geometry as a set of infinitesimal flat surfaces.

The Mindlin-Reissner plate theory posits that

$$\sigma_{33} = 0, \tag{4}$$

$$u_\alpha(x_1, x_2, x_3) \equiv u_{0\alpha}(x_1, x_2) - x_3 \theta_\alpha(x_1, x_2), \tag{5}$$

$$u_3(x_1, x_2, x_3) \equiv w(x_1, x_2), \tag{6}$$

where $\{u_{0\alpha}\}_{\alpha=1,2}$, w and $\{\theta_\alpha\}_{\alpha=1,2}$ express the in-plane displacements, out-of-plane displacement and rotational angles of the mid-area of the shell, respectively.

Then, the weak form state equation relative to $(\boldsymbol{u}_0, w, \boldsymbol{\theta}) \in U$ can be expressed as Eq. (7) by substituting Eqs. (4–6) into the variational equation for the three-dimensional linear elastic body, eliminating ε_{33}. Forces acting relative to the local coordinate system $(x_1, x_2, 0)$ on the domain A and the sub-boundary

$\partial A_g (\subset \partial A)$ are defined as follows: an out-of-plane load q per unit area, an in-plane loads $\boldsymbol{f} = \{f_\alpha\}_{\alpha=1,2}$ and an out-of-plane moments $\boldsymbol{m} = \{m_\alpha\}_{\alpha=1,2}$ per unit area, an in-plane loads $\boldsymbol{N} = \{N_\alpha\}_{\alpha=1,2}$ per unit length, a shearing force Q per unit length and a bending moments $\boldsymbol{M} = \{M_\alpha\}_{\alpha=1,2}$ per unit length.

$$a((\boldsymbol{u}_0, w, \boldsymbol{\theta}), (\bar{\boldsymbol{u}}_0, \bar{w}, \bar{\boldsymbol{\theta}})) = l((\bar{\boldsymbol{u}}_0, \bar{w}, \bar{\boldsymbol{\theta}})), \ \ (\boldsymbol{u}_0, w, \boldsymbol{\theta}) \in U, \ \ \forall (\bar{\boldsymbol{u}}_0, \bar{w}, \bar{\boldsymbol{\theta}}) \in U \ , \qquad (7)$$

where $\bar{(\ )}$ expresses a variation. In addition, the bilinear form $a(\cdot\ ,\ \cdot)$ and the linear form $l(\cdot)$ are defined respectively as shown below.

$$a((\boldsymbol{u}_0, w, \boldsymbol{\theta}), (\bar{\boldsymbol{u}}_0, \bar{w}, \bar{\boldsymbol{\theta}})) = \int_\Omega \{C_{\alpha\beta\gamma\delta}(u_{0\alpha,\beta} - x_3\theta_{\alpha,\beta})(\bar{u}_{0\gamma,\delta} - x_3\bar{\theta}_{\gamma,\delta})$$

$$+ C^S_{\alpha\beta}(w_{,\alpha} - \theta_\alpha)(\bar{w}_{,\beta} - \bar{\theta}_\beta)\} d\Omega \ ,$$

$$(= \int_A \{c^B_{\alpha\beta\gamma\delta}\kappa_{\gamma\delta}\bar{\kappa}_{\alpha\beta} + c^M_{\alpha\beta\gamma\delta}u_{0\gamma,\delta}\bar{u}_{0\alpha,\beta} + kc^S_{\alpha\beta}\gamma_\alpha\bar{\gamma}_\beta\} dA) \qquad (8)$$

$$l((\bar{\boldsymbol{u}}_0, \bar{w}, \bar{\boldsymbol{\theta}})) = \int_A (f_\alpha\bar{u}_{0\alpha} - m_\alpha\bar{\theta}_\alpha + q\bar{w}) dA + \int_{\partial A_g} (N_\alpha\bar{u}_{0\alpha} ds - M_\alpha\bar{\theta}_\alpha + Q\bar{w}) ds \ , \quad (9)$$

where $\{C_{\alpha\beta\gamma\delta}\}_{\alpha,\beta,\gamma,\delta=1,2}$ and $\{C^S_{\alpha\beta}\}_{\alpha,\beta=1,2}$ express an elastic tensor including bending and membrane stresses, and an elastic tensor with respect to the shearing stress, respectively. $\{c^B_{\alpha\beta\gamma\delta}\}_{\alpha,\beta,\gamma,\delta=1,2}$, $\{c^S_{\alpha\beta}\}_{\alpha,\beta=1,2}$ and $\{c^M_{\alpha\beta\gamma\delta}\}_{\alpha,\beta,\gamma,\delta=1,2}$ express an elastic tensor with respect to bending, shearing and membrane component in case of considering the relationship $\int_\Omega (\cdot)\, d\Omega = \int_A \int_{-h/2}^{h/2} (\cdot)\, dz dA$, respectively. In addition, $\{\kappa_{\alpha\beta}\}_{\alpha,\beta=1,2}$ and $\{\gamma_\alpha\}_{\alpha=1,2}$ express the curvatures and the transverse shear strains which are defined by the following equations. The constant k denotes a shear correction factor (assuming k=5/6).

$$\kappa_{\alpha\beta} \equiv \frac{1}{2}(\theta_{\alpha,\beta} + \theta_{\beta,\alpha}) \ , \qquad (10)$$

$$\gamma_\alpha \equiv w_{,\alpha} - \theta_\alpha \ . \qquad (11)$$

It will be noted that U in Eq. (7) is given by the following equation.

$$U = \{(u_{01}, u_{02}, w, \theta_1, \theta_2) \in (H^1(A))^5 \mid \text{satisfy the given Dirichlet condition on each subboundary}\}, \qquad (12)$$

where H^1 is the Sobolev space of order 1.

3 Free-form optimization problem of shell structure

3.1 Domain variation

Consider that a linear elastic shell structure having an initial domain Ω, mid-area A, boundary ∂A and side surface S undergoes domain variation $\boldsymbol{V}$ (design velocity field) in the out-of-plane direction such that its domain, mid-area, boundary and side surface become Ω_s, A_s, ∂A_s and S_s, respectively as shown in Fig. 2. It is assumed that the plate thickness h remains constant under the domain variation. The domain variation at this time can be expressed by a mapping from Ω to Ω_s, which is denoted as $T_S : \boldsymbol{X} \in \Omega \mapsto \boldsymbol{X}_s(\boldsymbol{X}) \in \Omega_s,\ 0 \le s \le \varepsilon$ (ε is a small integer) given by $\boldsymbol{X}_s = T_s(\boldsymbol{X}),\ \Omega_s = T_s(\Omega)$. The subscript s expresses the iteration history of the domain variation. Assuming a shape constraint is acting on the variation in the domain, the infinitesimal variation of the domain can be expressed by

$$T_{s+\Delta s}(\boldsymbol{X}) = T_s(\boldsymbol{X}) + \Delta s \boldsymbol{V}\ , \tag{13}$$

where the design velocity field is given as $\boldsymbol{V}(\boldsymbol{X}_s) = \partial T_s(\boldsymbol{X}) / \partial s$. The free-form optimization method explained later is a method for determining the optimal domain variation $\boldsymbol{V}$ of shell structures.

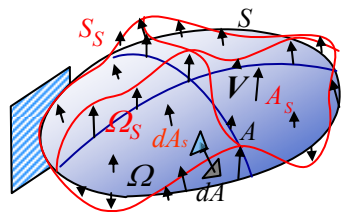

Figure 2: Out-of-plane shape variation $\boldsymbol{V}$.

3.2 Shape identification problem for achieving a desired deformed shape

Let us consider a free-form optimization problem for achieving a given desired deformed shape of a thin-walled structure. This problem is formulated in a function space, and the shape gradient function is theoretically derived using the material derivative method as described below.

As an objective functional, we introduce a squared deformed shape error norm on a prescribed surface. Letting the state equation in Eq. (7) be the constraint condition, a distributed-parameter shape identification problem for finding the optimal design velocity field $\boldsymbol{V}$, or $A_s (= A + \Delta s \boldsymbol{V})$ can be formulated as shown below:

$$\text{Given} \quad A \tag{14}$$

$$\text{Find} \quad A_s \text{ or } \boldsymbol{V} \tag{15}$$

$$\text{that mimimizes} \quad d(((\boldsymbol{x}_0+\boldsymbol{u})-\hat{\boldsymbol{z}}),((\boldsymbol{x}_0+\boldsymbol{u})-\hat{\boldsymbol{z}})) \tag{16}$$

$$\text{subject to} \quad \text{Eq. (7)}, \tag{17}$$

where $d(\bullet,\bullet)$ is the inner product defined as shown in the following equation.

$$d(\boldsymbol{u},\boldsymbol{v})=\int_{A_D} u_i v_i dA \tag{18}$$

The notations $\boldsymbol{x}_0+\boldsymbol{u}$ and $\hat{\boldsymbol{z}}$ indicate the position vector of the deformed shape and that of a given desired deformed shape, respectively, which are given on the prescribed surface A_D.

Letting $(\overline{\boldsymbol{u}}_0,\overline{w},\overline{\boldsymbol{\theta}})$ denote the Lagrange multipliers for the state equation, the Lagrange functional L for this problem can be expressed as

$$\begin{aligned} L(A,(\boldsymbol{u}_0,w,\boldsymbol{\theta}),(\overline{\boldsymbol{u}}_0,\overline{w},\overline{\boldsymbol{\theta}})) &= d((\boldsymbol{x}_0+\boldsymbol{u}-\hat{\boldsymbol{z}}),(\boldsymbol{x}_0+\boldsymbol{u}-\hat{\boldsymbol{z}})) \\ &+l(\overline{\boldsymbol{u}}_0,\overline{w},\overline{\boldsymbol{\theta}})-a((\boldsymbol{u}_0,w,\boldsymbol{\theta}),(\overline{\boldsymbol{u}}_0,\overline{w},\overline{\boldsymbol{\theta}})) \end{aligned} \tag{19}$$

For the sake of simplicity, it is assumed that the sub-boundaries acted on by the non-zero external forces $\boldsymbol{N}$, $\boldsymbol{Q}$ and $\boldsymbol{M}$ do not vary (i.e., $\boldsymbol{V}$=0), and that the forces acting on the shell surface $\boldsymbol{f},\boldsymbol{m},q$ do not vary with regard to the space and the iteration history s (i.e., $(\dot{f}=\dot{m}=\dot{q}=0)$. Then, the material derivative $\dot{L}$ of the Lagrange functional can be derived as shown in Eq. (20) below using the formula of material derivative [12].

Letting $\boldsymbol{n}^{mid}(\equiv\boldsymbol{n})=\boldsymbol{n}^{top}=-\boldsymbol{n}^{btm}$ represent a unit normal vector of the mid-area, the relationship $(\boldsymbol{V}\cdot\boldsymbol{n}^{top})\boldsymbol{n}^{top}=-(\boldsymbol{V}\cdot\boldsymbol{n}^{btm})\boldsymbol{n}^{btm}$ is assumed. The notations $\boldsymbol{n}^{top}$ and $\boldsymbol{n}^{btm}$ denote unit normal vectors that make the outward top and bottom surfaces of the shell positive. The notations $(\cdot)'$ and $\dot{(\cdot)}$ are the shape derivative and the material derivative with respect to the domain variation, respectively [12].

$$\begin{aligned} \dot{L} &= 2d(\boldsymbol{x}_0+\boldsymbol{u}-\hat{\boldsymbol{z}},\boldsymbol{u}')-a((\boldsymbol{u}_0',w',\boldsymbol{\theta}'),(\overline{\boldsymbol{u}}_0,\overline{w},\overline{\boldsymbol{\theta}})) \\ &+l(\overline{\boldsymbol{u}}_0',\overline{w}',\overline{\boldsymbol{\theta}}')-a((\boldsymbol{u}_0,w,\boldsymbol{\theta}),(\overline{\boldsymbol{u}}_0',\overline{w}',\overline{\boldsymbol{\theta}}'))+\langle G\boldsymbol{n},\boldsymbol{V}\rangle, \quad \boldsymbol{V}\in C_\Theta \end{aligned} \tag{20}$$

$$\langle G\boldsymbol{n},\boldsymbol{V}\rangle \equiv \int_A G\boldsymbol{n}\cdot\boldsymbol{V}dA+\int_{A_D} G_D\boldsymbol{n}\cdot\boldsymbol{V}dA=\int_A \boldsymbol{G}\cdot\boldsymbol{V}dA+\int_{A_D}\boldsymbol{G_D}\cdot\boldsymbol{V}dA \tag{21}$$

$$\begin{aligned} G=-\{C_{\alpha\beta\gamma\delta}(u_{0\alpha,\beta}+\frac{h}{2}\theta_{\alpha,\beta})(\overline{u}_{0\gamma,\delta}+\frac{h}{2}\overline{\theta}_{\gamma,\delta})-C_{\alpha\beta\gamma\delta}(u_{0\alpha,\beta}-\frac{h}{2}\theta_{\alpha,\beta})(\overline{u}_{0\gamma,\delta}-\frac{h}{2}\overline{\theta}_{\gamma,\delta}) \\ +Hf_\alpha\overline{u}_{0\alpha}-Hm_\alpha\overline{\theta}_\alpha+Hq\overline{w} \end{aligned} \tag{22}$$

$$G_D=H(x_{0_i}+u_i-\hat{z}_i)(x_{0_i}+u_i-\hat{z}_i)+2(x_{0_i}+u_i-\hat{z}_i)(x_{0_i}+u_i-\hat{z}_i)_{,j}\,n_j \tag{23}$$

Equations (22) and (23) express the shape gradient functions, i.e., the sensitivity functions, for this problem. The notation H denotes twice the mean

curvature of the surface. C_Θ expresses the kinematically admissible function space that satisfies the constraints of shape variation. When the optimality conditions with respect to the state variable $(\boldsymbol{u}_0, w, \boldsymbol{\theta})$, the adjoint variable $(\overline{\boldsymbol{u}}_0, \overline{w}, \overline{\boldsymbol{\theta}})$ of the Lagrange functional L expressed by Eqs. (24) and (25), are satisfied,

$$a((\boldsymbol{u}_0, w, \boldsymbol{\theta}), (\overline{\boldsymbol{u}}_0', \overline{w}', \overline{\boldsymbol{\theta}}')) = l((\overline{\boldsymbol{u}}_0', \overline{w}', \overline{\boldsymbol{\theta}}')), \quad \forall (\overline{\boldsymbol{u}}_0', \overline{w}', \overline{\boldsymbol{\theta}}') \in U \tag{24}$$

$$a((\boldsymbol{u}_0', w', \boldsymbol{\theta}'), (\overline{\boldsymbol{u}}_0, \overline{w}, \overline{\boldsymbol{\theta}})) = 2d(\boldsymbol{x}_0 + \boldsymbol{u} - \hat{\boldsymbol{z}}, \boldsymbol{u}'), \quad \forall (\boldsymbol{u}_0', w', \boldsymbol{\theta}') \in U \tag{25}$$

Eq. (20) becomes

$$\dot{L} \equiv \langle G\boldsymbol{n}, \boldsymbol{V} \rangle, \quad \boldsymbol{V} \in C_\Theta. \tag{26}$$

Equation (24) is the governing equation for the state variable $(\boldsymbol{u}_0, w, \boldsymbol{\theta})$ that coincides with Eq. (7), and Eq. (25) is the governing equation for the adjoint variable $(\overline{\boldsymbol{u}}_0, \overline{w}, \overline{\boldsymbol{\theta}})$.

The shape gradient function derived is applied to the free-form optimization method for shells.

4 Free-form optimization method (H^1 gradient method for shells) for designing the optimal surface of thin-walled structures

The free-form optimization method developed by the author is based on the traction method (often called the H^1 gradient method), which is a gradient method in a Hilbert space. The original H^1 gradient method was proposed by Azegami in 1994 [11]. It is a non-parametric shape optimization method that can treat all nodes as design variables and does not require any design variable parameterization. The original method has been modified for shells by the author, and called the free-form optimization method or the H^1 gradient method for shells. This method varies a shell in the normal direction to the surface, making it possible to obtain the optimal free-form shape of shell structures.

As shown in Fig. 3, a distributed force proportional to the shape gradient function $-\boldsymbol{G}$ is applied in the normal direction to the surface in order to vary the surface. The Robin boundary condition (spring constant α>0) is defined for the pseudo-elastic shell. This analysis for shape variation is called a velocity analysis. As the shape gradient function is not used directly to vary the shape but rather is replaced to a distributed force, this makes it possible both to reduce the objective functional and to maintain the smoothness, i.e., mesh regularity, which is the most distinctive feature of this method. The displacements obtained as the optimum shape variation in the velocity analysis are added to the original shape to update iteratively the shape. Considering the design velocity $\boldsymbol{V} = \{V_i\}_{i=1,2,3}$ as a combination of the in-plane velocity $\{\boldsymbol{V}_{0\beta}\}_{\beta=1,2}$ and the out-of-plane velocity V_3, which are defined in local coordinate systems, the governing equation of the

velocity analysis for $\boldsymbol{V} = (V_{0_1}, V_{0_2}, V_3)$ is expressed as Eq. (27) with the definition of C_Θ, Eq. (28). Equation (27) can be solved using a standard finite element code.

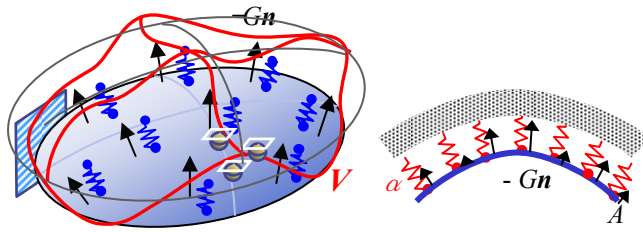

Figure 3: Schematic of free-form optimization method ("H^1 gradient method for shell" with Robin condition).

$$a((\boldsymbol{V}_{0\alpha}, V_3, \boldsymbol{\theta}), (\bar{\boldsymbol{u}}_0, \bar{w}, \bar{\boldsymbol{\theta}})) + \alpha \left\langle (\boldsymbol{V}\cdot\boldsymbol{n})\boldsymbol{n}, (\bar{\boldsymbol{u}}_0, \bar{w}, \bar{\boldsymbol{\theta}}) \right\rangle = -\left\langle G\boldsymbol{n}, (\bar{\boldsymbol{u}}_0, \bar{w}, \bar{\boldsymbol{\theta}}) \right\rangle,$$
$$(\boldsymbol{V}_{0\alpha}, V_3, \boldsymbol{\theta}) \in C_\Theta, \quad \forall (\bar{\boldsymbol{u}}_0, \bar{w}, \bar{\boldsymbol{\theta}}) \in C_\Theta, \tag{27}$$

$$C_\Theta = \{(V_{0_1}, V_{0_2}, V_3, \theta_1, \theta_2) \in (H^1(A))^5 \mid$$
$$\textit{satisfy Dirichlet condition for shape variation on } S\} \tag{28}$$

It is confirmed that this gradient method in a Hilbert spaces reduces the Lagrange functional L as follows. When the state equation and the adjoint equation are satisfied, the perturbation expansion of the Lagrange functional L can be written as

$$\Delta L = \left\langle G\boldsymbol{n}, \Delta s(\boldsymbol{V}, \boldsymbol{\theta}) \right\rangle + O(|\Delta s|). \tag{29}$$

Substituting Eq. (27) into Eq. (29) and taking into account the positive definitiveness of $a((\boldsymbol{V}_{0\alpha}, V_3, \boldsymbol{\theta}), (\bar{\boldsymbol{u}}_0, \bar{w}, \bar{\boldsymbol{\theta}}))$ and $\alpha \left\langle (\boldsymbol{V}\cdot\boldsymbol{n})\boldsymbol{n}, (\bar{\boldsymbol{u}}_0, \bar{w}, \bar{\boldsymbol{\theta}}) \right\rangle$, based on the positive definitiveness of the elastic tensors $C_{\alpha\beta\gamma\delta}$ and $C^S_{\alpha\beta}$, the following relationship is obtained when Δs is sufficiently small:

$$\Delta L = -a(\Delta s(\boldsymbol{V}, \boldsymbol{\theta}), \Delta s(\boldsymbol{V}, \boldsymbol{\theta})) - \alpha \left\langle (\Delta s \boldsymbol{V}\cdot\boldsymbol{n})\boldsymbol{n}, \Delta s(\boldsymbol{V}, \boldsymbol{\theta}) \right\rangle < 0 \tag{30}$$

In problems where convexity is assured, this relationship definitely reduces the Lagrange functional in the process of updating the shell shape using the design velocity field $\boldsymbol{V}$ determined by Eq. (27).

The advantages offered by this method are summarized as follows: (1) a smooth and natural surface without any jaggedness can be obtained because the elastic tensor in the velocity analysis serves as a mapping function and as a smoother for maintaining mesh smoothness, and its positive definitiveness is the

necessary condition for minimizing the objective functional. (2) An optimal free-form surface is created because the number of the design degrees of freedom is not limited. (3) It does not require shape design parameterization unlike the basis vector method or the parametric surface method because all the nodes can be moved as the design variable. (4) Mesh smoothing is simultaneously implemented in the shape changing process. (5) It can be easily implemented in combination with a commercial FEA code, which means it has generality and practical utility for actual design work. (6) It is not necessary to refine the mesh.

5 Calculated results obtained with free-form optimization method

The proposed method was applied to three fundamental design examples in order to verify its validity for controlling the deformed shape of a thin-walled structure to a desired shape.

5.1 Roof problem 1

Problem definition 1 for a cylindrical roof model is shown in Fig. 4. In the stiffness analysis Fig. 4(a), the bottom edges of the roof were simply supported and the downward nodal forces were applied along the line on the top. The deformed shape region was prescribed in the portion around the loaded line on the top as shown in Fig. 4(a). The desired deformed shape was defined as one in which the prescribed region was uniformly deformed downward as shown in Fig. 4(c). In the velocity analysis, the bottom edges were simply supported as shown in Fig. 4(b).

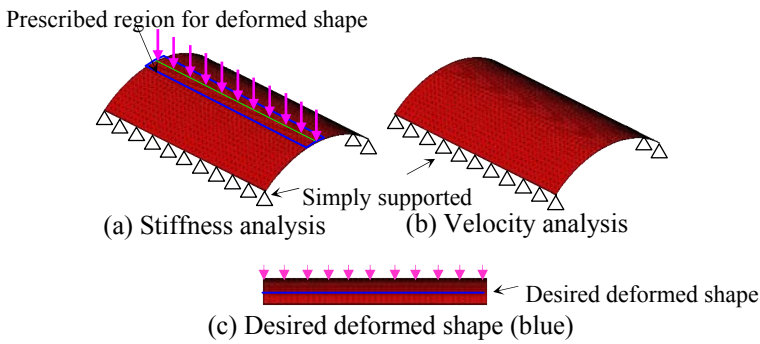

Figure 4: Problem definition for roof problem 1.

The optimal shape obtained and the iteration convergence histories are shown in Fig. 5(a) and (b), respectively. It is seen in Fig. 5(a) that both edges on the top were folded upward for stiffening the edges. The results in Fig. 5(b) indicate that the objective functional converged almost to zero. As a volume constraint was not defined in this study, the calculated results show that the initial volume was

kept almost constant. Figure 6 compares the deformed shapes between (a) the initial and (b) the final. The figures show that although the region of the initial shape was not deformed uniformly, the region of the final shape was deformed downward uniformly as desired.

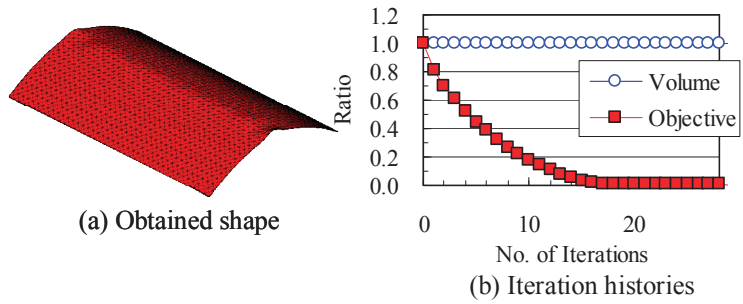

Figure 5: Calculated results for roof problem 1.

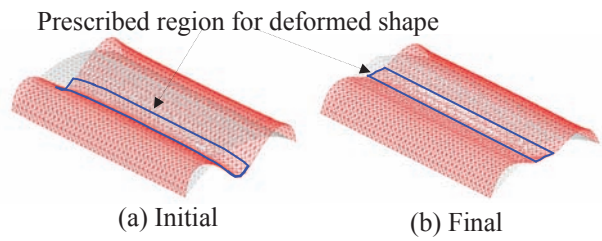

Figure 6: Comparison of deformed shapes of roof problem 1.

5.2 Roof problem 2

The problem definition of roof problem 2 is shown in Fig. 7 using the same model as in roof problem 1 except for the prescription of the deformed shape. The loaded line on the top was defined as the prescribed positions of the deformed shape as shown in Fig. 7(a). The desired deformed shape was defined as one in which the line around half of the top maintained the position and was folded downward linearly at the three-quarters point from the top edges as shown in Fig. 7(c).

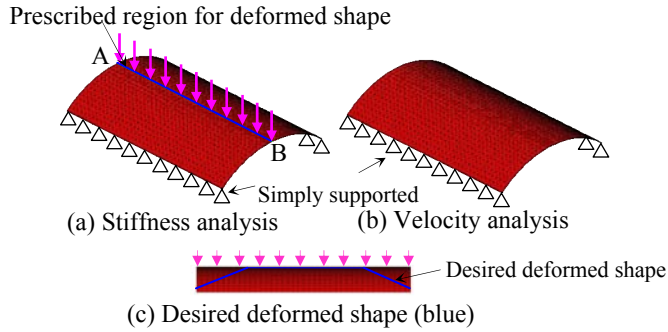

Figure 7: Problem definition for roof problem 2.

Figure 8(a) shows the optimal shape obtained. It is seen that the portions around the edges of the top were linearly varied downward according to the desired deformed shape, which is reasonable for the prescription. Figure 8(b) compares the deformed positions along the prescribed line for the initial, desired and final shapes. The graph indicates that the deformed positions of the final shape coincided well with the desired positions as intended.

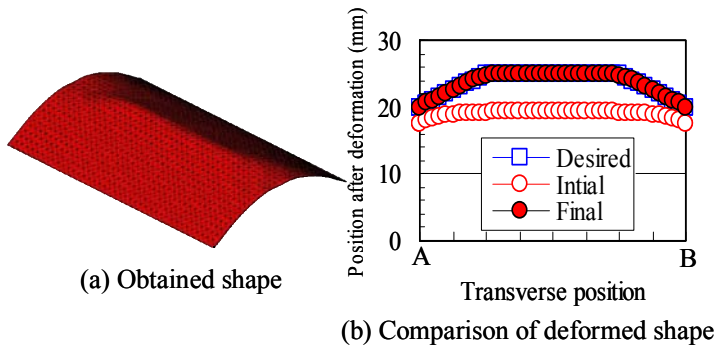

Figure 8: Calculated results of roof problem 2.

5.3 Table problem

A table problem is defined in Fig. 9. The initial shape and the boundary condition of the stiffness analysis are shown in (a). The bottom edges were simply supported and the top surface was uniformly loaded downward in the stiffness analysis. The bottom edges were also simply supported in the velocity analysis. As shown in Fig. 9(b), the prescribed square regions of the deformed shape were defined in the centres of both side surfaces, and the target shape was defined as one in which the initial positions were kept.

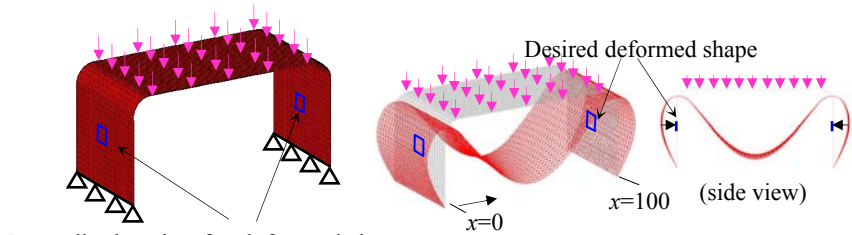

Figure 9: Problem definition for table problem.

Figure 10(a) shows the optimal shape obtained. Several beads were created on both side surfaces to increase the stiffness. Figure 10(b) shows the deformed shapes of the obtained shape. It was confirmed that the prescribed regions of the final shape kept their positions, although those of the initial shape largely deformed outward.

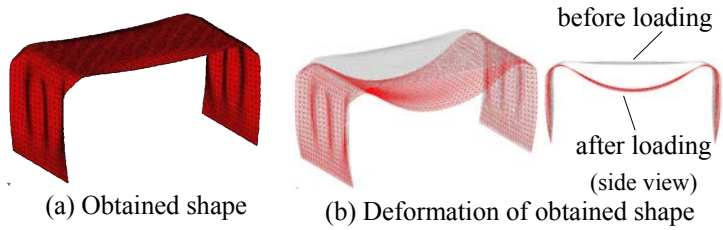

Figure 10: Obtained shape and deformation of table problem.

6 Conclusion

This paper has presented a shell free-form optimization method for controlling a static deformed shape to a desired shape. A shape identification problem, in which the squared error norm of the deformed shape was defined as the objective functional, was formulated as a distributed-parameter shape optimization problem. The shape gradient function with respect to the shape variation in the normal direction to the shell surface was derived theoretically and applied to the H^1 gradient method for shells. With this method, the objective functional converged almost to zero in all the design examples, and shell shapes with beads coinciding with the prescribed deformed shape were obtained. It was confirmed that the use of this method makes it possible to control the deformed shape to a desired shape and imparts a function to thin-walled structures, while creating .an optimal arbitrarily formed surface.

Acknowledgements

This research was supported by grants-in-aid from the Sustainable Mechanical Systems R&D Centre at the Toyota Technological Institute.

References

[1] M. Shimoda, K. Iwasa and H. Azegami, A Shape optimization method for the optimal free-form design of shell structures, in *Proceedings of 8th World Congress on Structural and Multidisciplinary Optimization* (WCSMO-8), H.C. Rodrigues, J. M. Guedes, *et al*. (eds), (2009, Lisbon).
[2] M. Shimoda, Optimal free-form design of shell structures involving a natural frequency problem, in *Proceedings of EUROGEN2011 Conference (Evolutionary And Deterministic Methods For Design, Optimization And Control),* C. Poloni, D. Quagliarella, *et al*. (eds.), (2011, Capua).
[3] E. Ramm, K.–U. Bletzinger and R. Reitiger, Shape optimization of shell structures, *Int. J. Shell and Spatial Structures*, 34 (2), pp.103-121, 1993.
[4] T. Lindby and J. L. T. Santos, Shape Optimization of three-dimensional shell structures with the shape parameterization of a CAD system, *Structural Optimization*, 18, pp.126-133, 1999.
[5] K. U. Bletzinger, M. Firl, *et al*., Optimal shapes of mechanically motivated surfaces, *Comput. Methods Appl. Mech. Engrg*., 199, pp. 324-333, 2010.
[6] N. Yoshikawa and S. Nakagiri, Homology design to maintain quadratic curves, *Proc. 5-th Int. Conf. on Adaptive Structures*, pp.1-9, (1994, Sendai).
[7] S. Nishiwaki, M. I. Frecker, *et al*., Topology optimization of compliant mechanisms using the homogenization method, *Int. J. of Num. Meth. Engrg*., 42 (3), pp.535-560, 1998.
[8] L. Saggere and S. Kota, Static shape control of smart structures using compliant mechanisms, AIAA J. 37 (5), pp.572-579, 1999.
[9] K. J. Lu and S. Kota, Design of compliant mechanisms for morphing structural shapes, *J. of Intelligent Material Systems and Structures*, 14 (6), pp.379-391, 2003.
[10] M. Shimoda, H. Azegami and T. Sakurai, Traction method approach to optimal shape design problems, *SAE Transactions, Journal of Passenger Cars*, 6 (106), pp.2355-2365, 1998.
[11] H. Azegami, A Solution to domain optimization problems, *Trans. of Jpn. Soc. of Mech. Engs*., Ser. A, 60, pp.1479-1486, 1994 (in Japanese).
[12] K. K. Choi and N. H. Kim, Structural *Sensitivity Analysis and Optimization*, 1, Springer, New York, 2005.

This page intentionally left blank

A systems approach to shape and topology optimisation of mechanical structures

K. Fiedler, B. F. Rolfe, A. Asgari & T. de Souza
Institute for Frontier Materials, Deakin University, Australia

Abstract

Optimisation techniques have become more and more important as the possibility of simulating complex mechanical structures has become a reality. A common tool in the layout design of structural parts is the topology optimisation method, which finds an optimum material distribution within a given geometrical design space to best meet loading conditions and constraints.

Another important method is shape optimisation, which optimises weight given parametric geometric constraints. In the case of complex shaped parts or elaborate assemblies, for example automobile body structures, shape optimisation is still hard to do; mainly due to the difficulty in translating shape design parameters into meaningful analysis models. Tools like the parametric geometry package SFE CONCEPT are designed to mitigate these issues.

Nevertheless, shape methods usually cannot suggest new load path configurations, while topology methods are often confined to single parts. To overcome these limitations the authors have developed a method that combines both approaches into an Integral Shape/Topology Method (IST) that is capable of finding new optimal solutions.

This is achieved by an automated optimisation loop and can be applied for both thin walled structures as well as solid 3D geometries. When optimising structures by applying IST, global optimum solutions can be determined that may not be obtained with isolated shape- or topology-optimisation methods.
Keywords: topology optimisation, shape optimisation, simultaneous shape and topology optimisation, structural optimisation, IST.

WIT Transactions on The Built Environment, Vol 125,
www.witpress.com, ISSN 1743-3509 (on-line)
doi:10.2495/OP120131

1 Introduction

In structural mechanics, the requirements for structural parts are highly complex. And yet, in a highly competitive environment, engineers are expected to shorten development and test time, while also cutting material and production costs. Moreover, energy efficiency plays an increasingly important role in the life cycle of any product. One way to achieve this is light-weighting of structures, where the engineers aim to minimize material usage and simultaneously maximize performance. In the transportation industry, light-weighting is a key enabler for reducing fuel consumption and CO_2 emission. In this context, simulation and optimisation methods are of crucial importance.

Today, in designing load bearing parts, the engineer often develops a structural layout using topology optimisation (Bendsøe and Kikuchi [1], Suzuki and Kikuchi [2]). The necessary next step is then to either fine-tune the resulting shape or else translate it into multiple manufacturable parts.

In this context, shape optimisation is limited to fine-tuning the topology optimisation result with respect to local details, e.g. curvature and local stresses.

Put simply, topology optimisation and shape optimisation today are still two distinct fields. While shape optimisation approaches in general are incapable of varying topological layouts, topology methods either use shape design for fine-tuning only, or else cannot account for specific characteristics of the parts. For example, thin walled structures or complex relationships between members. On the other hand, it may be beneficial to simultaneously do large scale shape variation to find an optimum shape with corresponding optimum load path layout.

The authors have developed a method that can tackle both of these aspects at the same time.

Figure 1 illustrates a traditional process flow whereas Figure 2 shows the IST approach where shape variation is an integral part of a combined optimisation process.

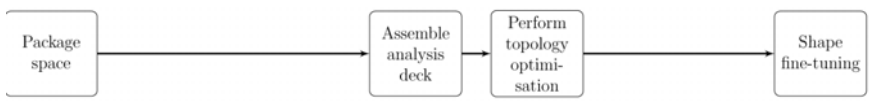

Figure 1: Traditional topology optimisation method.

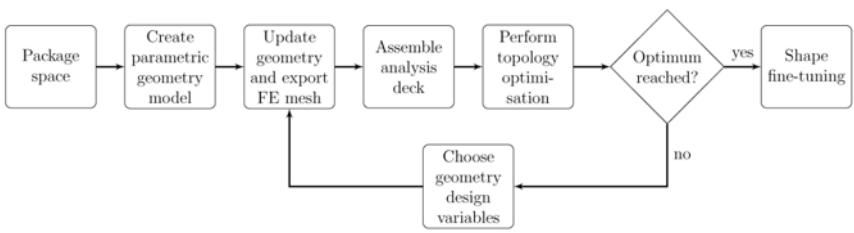

Figure 2: Integral Shape/Topology Method (IST).

1.1 Review of existing approaches

A number of combined shape and topology methods have been proposed and published, and will be briefly discussed in this section.

In the method described by Balamurugan *et al.* [3], shape modifications are implicitly applied using B-splines and essentially accelerate the topology optimisation algorithm without delivering qualitatively different results compared to a pure topology optimisation approach. A similar idea has been described by Cappello and Mancuso [4], where shape modification is applied on the topology optimisation result in order to smooth rough boundaries. Their approach is limited to two dimensions, and does not allow the definition of geometric design variables.

Ansola *et al.* [5] adopts a unique approach by starting with a plane finite element mesh in two dimensions. The mesh-topology stays constant (i.e. the connectivity of elements relative to each other cannot change), but grids are allowed to move perpendicular to a fixed plane. Simultaneously, a density distribution for the finite element is determined. The algorithm is limited to sheet structures consisting of a single part, and can deliver only limited out of plane shapes.

In some ways IST is similar to the application of large scale variation as described by Volz *et al.* [6]. Here the authors employ SFE CONCEPT as the tool of choice to create parametric geometry for an automobile body structure. However, the topology optimisation described is not based on a density method. Rather, predefined structural members are either added or subtracted from the structure.

IST is novel in the sense that large scale shape variation can be described explicitly using intuitive structurally meaningful geometry parameters combined with the established topology optimisation algorithms. This allows for a much wider range of applications than existing hybrid methods.

1.2 Aim

In this paper we introduce the basic principles of IST, point out a number of issues that arise with variable geometry combined with a topology optimisation procedure, and provide an example of a combined shape/topology optimisation of a mechanical component.

2 Process description

In order for an automated optimisation loop to work, variation in geometric characteristics need to be created in an automated batch process. Here the parametric CAD tool SFE CONCEPT v4.2 was chosen. SFE CONCEPT enables the creation of parametric geometry with the capacity to do large scale shape modification that can be controlled in a batch loop (Zimmer *et al.* [7]). Hereby, intuitive shape design variables can be defined and result in consistent complex geometrical variation (Duddeck *et al.* [8]), while the integrated meshing tool generates a finite element (FE) model.

For the topology optimisation, the Solid Isotropic Material with Penalty (SIMP) method (Rozvany [9]) both for shell and solid elements was used, as provided by the Altair Hyperworks software package Optistruct v11 (Schramm and Zhou [10]).

A number of scripts and tools developed in C++ and Perl combine the commercial software packages into a closed process loop, as shown in Figure 2.

For a set of geometric design variables $dv_1, \ldots, dv_n$, the parametric model is updated and a FE mesh generated. Loads and constraints are then applied, and a topology optimisation is performed. A subsequent topology optimisation finds optimum load path layouts.

2.1 Flexible and dynamic analysis model setup

IST performs these steps in an automated batch loop with a highly flexible control mechanism. For example, boundary conditions can be created dynamically, and check functions can be defined via plug-ins. Also, the handling and extraction of analysis results is managed.

In the example provided in Section 3 later in the paper we utilize IST to vary the initial package space for a subsequent topology optimisation procedure. This adds an additional dimension to the search space for a minimum mass solution and allows us to consider an additional manufacturing constraint.

2.2 Problems associated with varying geometry

Performing optimisation of any system requires a structured approach. Design variables need to be selected and a single real-valued objective function must be defined. When using a SIMP algorithm to generate load path concepts, two main approaches to establish an objective function prevail:

1. Minimize mass under some performance constraint (typically displacements, stresses, Eigenfrequencies, and manufacturing considerations)
2. Maximize performance for a fixed volume or mass fraction δ, allowing the SIMP algorithm to take away a defined volume/mass of material equal to $1 - \delta$ times the initial volume/mass.

In the first case, the algorithm will determine a material distribution with minimum mass, whereby the amount of remaining material is a priori unknown. In the second case, the amount of material (mass or volume) to be used is fixed, and a load path distribution is generated such that the performance of the structure is maximized.

Using IST, a problem associated with varying initial geometries needs to be addressed: When we generate a number of different geometries, and subsequently take away material by applying topology optimisation, the resulting structures may have different masses and different performance results, which makes it difficult to compare one sample with another. In this section we explore a number of possibilities to solve this problem.

2.3 Topology optimisation minimizing mass under performance constraints

For structures where the mass is minimized under some performance constraints, we have a single-objective problem, and topology optimisation results for different initial geometries are comparable. The optimisation of the shape and load paths of a brake pedal in Section 3 is an example of this approach.

2.4 Topology optimisation maximizing performance under volume fraction constraint

For structures where the objective function is some performance figure, we need to find a solution that allows us to directly compare topology optimisation results for varying initial geometries. Let's consider a structure that consists of non-designable parts (i.e. regions that are not subject to SIMP), and a single designable component, with some volume fraction constraint δ. With the naming conventions

$$\begin{aligned} m_{\text{nd}} &= \text{Mass of the non-designable region} \\ m_{\text{d}} &= \text{Mass of the designable region} \\ m_{\text{init}} &= m_{\text{nd}} + m_{\text{d}} = \text{Initial mass before topology optimisation} \\ \delta &= \text{Mass fraction for the topology optimisation} \end{aligned}$$

the resulting mass after a topology optimisation run will be

$$m_{\text{res}} = m_{\text{nd}} + \delta\, m_{\text{d}}.$$

Since the initial geometry is allowed to change, masses $m_{\text{init},i}, m_{\text{init},j}$ for two geometrically different designs $i \neq j$ vary, such that in general

$$m_{\text{res},i} \neq m_{\text{res},j}.$$

Performance results for these two designs in general will be different, and the two designs are not directly comparable anymore. There are three ways to solve this issue:

The first approach is to do a multi-objective optimisation, where mass and performance are simultaneously assessed. This leads to a Pareto frontier of feasible designs, that need to be interpreted and evaluated by a human operator.

The second approach is to make sure that the resulting mass for the different initial geometries is constant by adjusting the volume fraction for the SIMP algorithm accordingly: Choose δ_i for each initial geometry such that

$$m_{\text{res}} = m_{\text{nd},i} + \delta_i\, m_{\text{d},i} = \text{constant}, \qquad \text{or} \qquad \delta_i = \frac{m_{\text{res}} - m_{\text{nd},i}}{m_{\text{d},i}}.$$

Thus, for a lighter initial geometry with mass $m_{\text{init},i}$ the volume fraction value δ_i needs to be bigger than for a geometry with more mass $m_{\text{init},j}$. After topology

optimisation this leads to structures with identical mass. The problem with this is that varying mass fractions can lead to qualitatively different results.

Finally, we can constrain the shape design parameters to assure that the resulting masses are constant. Assuming a fixed volume fraction δ, choose the shape design variables $dv_1, \ldots, dv_n$ such that

$$m_{\mathrm{nd},i} + \delta\, m_{\mathrm{d},i} = m_{\mathrm{nd},j} + \delta\, m_{\mathrm{d},j}$$

for all geometrically different designs i, j, resulting in $m_{\mathrm{res},i} = m_{\mathrm{res},j}$.

In this paper these options will not be discussed in detail; here we only show examples where topology optimisation is performed under a displacement constraint.

3 Example: variable initial package space for topology optimisation

In this section we apply IST to a simple problem, where a brake pedal is to be designed using the least amount of material necessary. As an additional constraint we require the component be constructed from a light weight aluminium extruded profile in order to reduce manufacturing costs compared to a cast structure.

3.1 Problem setup

Figure 3(a) shows the basic geometry and loads in side view. The rotation axis **R** is fixed, allowing for rotation around the y–axis only. The attachment point for the brake cylinder **A** is constrained in x–direction. A force **F** of 1000N is applied at

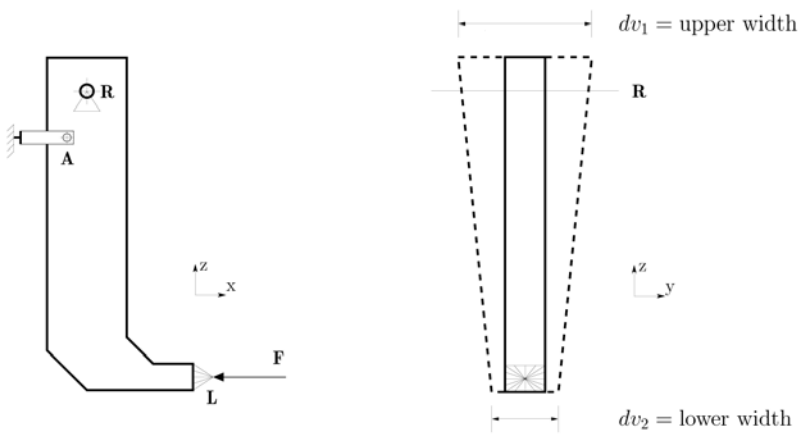

(a) Schematic layout in side view with boundary conditions

(b) Geometry design variables in front view

Figure 3: Brake pedal: layout and variable geometry.

point **L** in negative x–direction, while the contact point **L** is allowed a maximum displacement of 0.5 mm.

3.2 Variable geometrical design space

By varying the upper and lower width of the blank, the initial package space is allowed to change, as indicated in the front view in Figure 3(b). This variability results in a wedge shaped initial geometry which is then subjected to SIMP.

The operation sequence is as described in Figure 2. Values for the two geometry design variables (upper and lower width) are chosen, then the parametric SFE CONCEPT geometry model is updated and a finite element mesh created. Then boundary conditions are applied, and a topology optimisation is performed.

3.3 Design of experiments

The objective of the topology optimisations is to minimize mass given two constraints: a displacement constraint, and an extrusion constraint in y–direction. A design of experiments (DOE) with a coarse mesh (6 mm HEXA voxel mesh) has been conducted with:

$$dv_1 = \text{upper width} = 6, 8, \ldots, 20\,\text{mm}$$
$$dv_2 = \text{lower width} = 6, 8, \ldots, 12\,\text{mm},$$

which results in the response surface shown in Figure 4(a). For different initial geometries we get distinct structural load path layouts, and it can be seen that the best results (meaning lowest mass results) are achieved when the lower width is at its lower limit of $dv_2 = 6\,\text{mm}$.

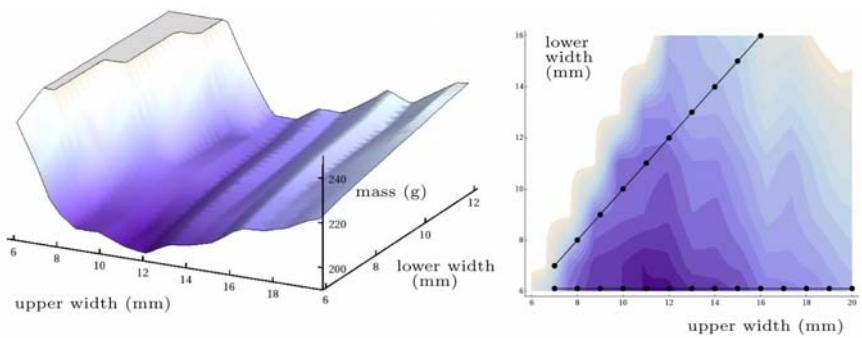

(a) 3D plot (b) Contour plot

Figure 4: Resulting mass after topology optimisation.

3.4 Results

For a refined DOE study we therefore assume dv_2 = constant = 6 mm, while varying dv_1 between 6 mm and 20 mm. For this study a finer mesh size for the voxel elements of 2 mm was used. Figure 5(a) shows the resulting masses, with the lowest mass being 192 g for the design at $dv_1 = 12$. The graph corresponds to the horizontal dotted line in Figure 4(b). The corresponding wedge-shaped structure is shown in Figure 6(a) at a mass fraction cut-off value of 0.3.

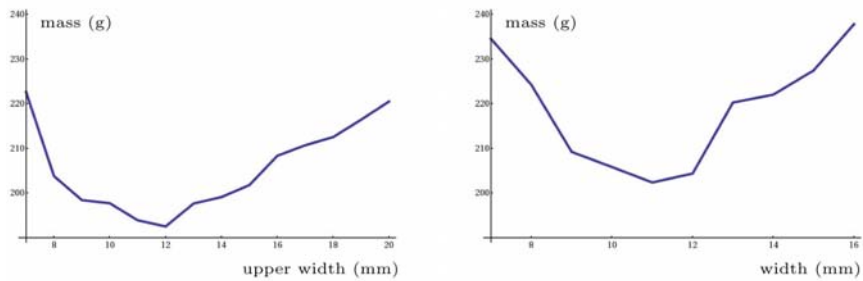

(a) Lower width = constant = 6 mm (b) Upper width = lower width

Figure 5: Resulting mass for refined DOE.

3.5 Comparison with a traditional approach

For validation purposes it is necessary to compare the combined shape/topology (IST) technique to a conventional approach where the designer would start with a flat blank and perform a topology optimisation to find a suitable load path concept.

It is by no means evident that the engineer would choose the 'right' width to start with. For an initial blank thickness of 12 mm, topology optimisation returns a structure weighing 206 g, while the minimum mass for a constant width blank is at 11 mm width (202 g). Figure 6(b) shows the topology optimisation result for a constant blank width of 11 mm. The masses after topology optimisation for different material thicknesses are shown in Figure 5(b), corresponding with the diagonal dotted line in Figure 4(b).

Therefore, even if the optimum width was chosen, the resulting design would still be 5% heavier than the results achieved when applying IST.

In this example, the IST approach essentially added an additional manufacturing constraint to the topology optimisation method: Where traditionally the package space for a topology optimisation would be fixed, the manufacturing restriction to extruded profiles made it beneficial to incorporate variable initial design space characteristics. Thus it was possible to derive an optimum angle for the wedge shaped brake pedal.

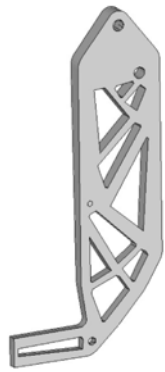

(a) Wedge shaped; upper width = 12 mm, lower width = 6 mm

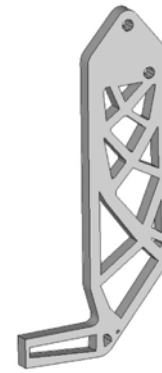

(b) Constant thickness; width = 11 mm

Figure 6: Topology optimisation results.

4 Conclusion

We have introduced the novel Integral Shape and Topology (IST) optimisation method which allows simultaneous large scale shape variation and load path layout optimisation. This method has been shown to be useful for a voxel-based solid structure, where it:

- leads to lower mass structures
- adds additional manufacturing constraints to topology optimisation algorithms

In the example discussed, the optimum found by IST could not have been found by traditional topology optimisation methods alone, and IST allowed us to cater for the specific manufacturing requirement, i.e. the part being made from an extruded profile. A mass saving of 5% over a conventional topology optimisation approach was achieved.

Acknowledgements

The authors would like to thank SFE GmbH, Berlin, for providing the software package SFE CONCEPT, and the Automotive Technology Cooperative Research Centre (AutoCRC) project C2-23 for their financial support.

References

[1] Bendsøe, M. and Kikuchi, N., Generating optimal topologies in structural design using a homogenization method. *Computer Methods in Applied Mechanics and Engineering*, **71(2)**, pp. 197–224, 1988.

[2] Suzuki, K. and Kikuchi, N., A homogenization method for shape and topology optimization. *Computer Methods in Applied Mechanics and Engineering*, **93(3)**, pp. 291–318, 1991.
[3] Balamurugan, R., Ramakrishnan, C.V. and Swaminathan, N., Integrated optimal design of structures under multiple loads for topology and shape using genetic algorithm. *Engineering Computations*, **23(1/2)**, pp. 57–83, 2006.
[4] Cappello, F. and Mancuso, A., A genetic algorithm for combined topology and shape optimisations. *Computer-Aided Design*, **35(8)**, pp. 761–769, 2003.
[5] Ansola, R., Canales, J., Tarrago, J.A. and Rasmussen, J., An integrated approach for shape and topology optimization of shell structures. *Computers & Structures*, **80(5-6)**, pp. 449–458, 2002.
[6] Volz, K., Frodl, B., Dirschmid, F., Stryczek, R. and Zimmer, H., Optimizing topology and shape for crashworthiness in vehicle product development. *International Automotive Body Congress (IABC)*, 2007.
[7] Zimmer, H., Prabhuwaingankar, M. and Duddeck, F., Topology & geometry based structure optimization using implicit parametric models and ls-opt. 7^{th} *European LS-DYNA Conference*, 2009.
[8] Duddeck, F., Hunkeler, S., Zimmer, H., Rota, L. and Zarroug, M., Shape optimization for crashworthiness. *Weimar Optimization and Stochastic Days*, 2009.
[9] Rozvany, G.I.N., Aims, scope, methods, history and unified terminology of computer-aided topology optimization in structural mechanics. *Structural and Multidisciplinary Optimization*, **21(2)**, pp. 90–108, 2001.
[10] Schramm, U. and Zhou, M., *Recent Developments in the Commercial Implementation of Topology Optimization*, Springer Netherlands, volume 137 of *Solid Mechanics and Its Applications*, pp. 239–248, 2006.

Optimization of damping unit

J. Kolář & K. Adámek
VÚTS Liberec, Czech Republic

Abstract

This paper reports the numerical investigation and optimization of a damping unit where oil flow interacts with an elastic chocking plate. Chocking of flow from a by-pass valve is the basic principle of hydraulic shock absorbers. However, cavitation phenomenon caused by strong shocking occurs at high frequencies of an actuating movement and the original damping unit characteristic is being distorted. We used the computational fluid dynamic to minimize the distortion of characteristic as much as possible. To satisfy the high number of unsteady simulations, the involved fluid-structure interaction needs to be coupled in a different way than the routine is. The plate deformation is coupled with an average hydrodynamic loading pressure by a single afore-computed third polynomial equation being predicted by FEM. Numerical simulations of flow by the use of FVM exploiting dynamic mesh in Fluent commercial code then provides a flow field pattern and loading pressure within the unit itself. A User Defined Function (UDF) enables the deformation of the domain boundaries in a coupled way. Finally, the time dependency of the plate position and its dynamic behaviour is obtained. Highly dynamic manners appeared and numerous techniques providing a better stability of computations had to be investigated and developed. The state where the most cavity bubbles are being induced is further applied to shape optimization at the steady state. The shape-based similarity optimization of by-pass geometry is then carried out to minimize the formation of cavitation bubbles.
Keywords: damping unit, shape optimization, computational fluid dynamics, chocking plate, cavitation, user defined functions, shape based similarity.

1 Introduction

The movement of a thin spring-steel plate induced by the impact of oil flow is an example of fluid-structure interaction. This interaction can be found in many engineering devices. The mentioned case is a typical one in the field of chocking

WIT Transactions on The Built Environment, Vol 125, © 2012 WIT Press
www.witpress.com, ISSN 1743-3509 (on-line)
doi:10.2495/OP120141

fluids. The originally stiff plate is loaded and deformed by the surrounding flow. Consequently, the chocking plate truckles to loading and gets deformed. In computational fluid dynamics (CFD), the number of iterative steps is needed to solve the steady state of oil flow and the resulting plate shape which corresponds one to another. In our case, oil flow is induced by the sinusoidal movement of the unit walls with respect to the relation that follows

$$y^{+-} = y_0 \pm A \cdot \sin(2 \cdot \pi \cdot f \cdot t) \tag{1}$$

For the device scheme, see Figure 1. Finally the task is necessarily unsteady with a frequency of f=2 Hz.

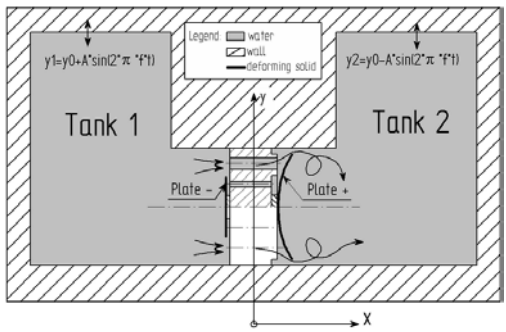

Figure 1: Scheme of damping unit with unsteady movement relations.

We decided to apply the simplified, but more efficient approach to get into the solved problem because the conventional approach with intercommunication and data transfers between FVM and FEM solvers gains unacceptable time cost for unsteady simulations. The non-conventional approach of the mentioned task includes the number of applied techniques and requirements such as dynamic domains, self-guarding routines, and deforming functions.

2 Unsteady fluid-structure interaction and cavity identification

2.1 Fluid-structure coupling

The dynamic computational domain feature allows the computational domain to change its shape with conserved topology with respect to the prescribed relation which relates the surface loading and structure stiffness. As a result, unsteady simulations are not composed from the set of solutions of segregated domains being solved from initialization. Instead, the dynamic solution of the initial domain which underlies the deformation is performed. The computational grid changes upon the predicted shape which results from pressure load at the deformed boundary. More detailed view can be taken in [1] and [2]. The predicted shape, shown in Figure 2(a) is afore-computed by FEM analysis in Mark 3D software package. The surface of the observed plate is one-sidedly loaded by substitutive pressure. This approach presumes minimal or even

negligible twist deformation. This condition is being met as tested in numerous cases. The plate is made of spring steel 12 090 with R_m=950Mpa and E=2.171·10^{11} Pa and fully fixed all-around the inner diameter-r. The shape-substitutive cubic polynomial is derived from the predicted deformation by the method of least squares employing Gauss elimination. The local deformation of the boundary node at the radial coordinate $\varphi_j = R - r_j$, is then given by an average loading pressure given as

$$p_{avg} = \frac{\sum_{i=0}^{i=N^+} F_i^+ + \sum_{i=0}^{i=N^-} F_i^-}{(\sum_{i=0}^{i=N^+} - A[0]_i^+ + \sum_{i=0}^{i=N^-} - A[0]_i^-)/2} \qquad 2)$$

and as a relation which follows

$$\Delta x_j(r_j, p_{load}) = \frac{-0.0032 \cdot r_j{}^3 + 0.066 \cdot r_j{}^2 + 0.0654 \cdot r_j - 0.0163}{16 \cdot 10^5} \cdot p_{load} \qquad (3)$$

Due to the fluid-structure interaction, the plate position always affects the surrounding flow field. This has an effect of overestimated plate position predicted. We have tested and applied absorber coefficient k which corrects the increase of the actual plate position defined as

$$\Delta x'_j = \Delta x_j * k \text{ where } k \in R \mid 0 < k < 1 . \qquad (4)$$

The influence of absorption coefficients may be studied in Figure 2(b).

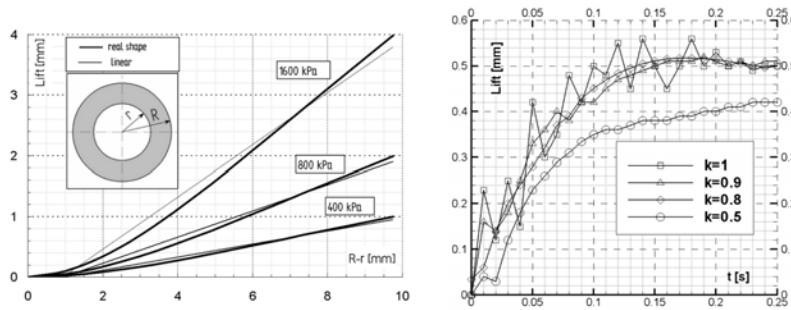

Figure 2: Deformed plate shape predicted by FEM (a) and the overestimation of plate position with various absorption coefficients (b).

The underestimation of the total plate position by coefficient k is limited by the differential approach. A new plate position is based on the actual position and computed increase of coordinate corrected by k. The dynamic movement of the plate was observed even when the nonsensical movements were smoothed out. This led to a large deformation of grid elements or even to a formation of negative cell volume. To avoid this, the self-guarding routine was implemented into the source code. The routine of the source code supervises the maximal increase of coordinate available at the base of the quality of boundary adjacent

cells. The ultimate angular node displacement is established from the equation (5). For the scheme of approach, see Figure 3. More detailed expression can be found in [3].

$$tg(d\alpha_{\max}) \cong \min\{\frac{3\cdot\vec{dr}[0]_i}{r_{\max,c}},...,\frac{3\cdot\vec{dr}[0]_N}{r_{\max,N}}\}\ . \tag{5}$$

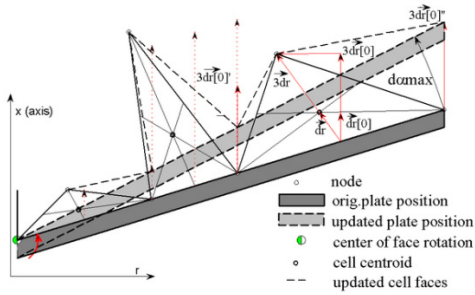

Figure 3: Scheme of ultimate angular displacement based on equation (5).

2.2 CFD simulations

We have used the commercial CFD package Fluent version 6.3 to solve the 3D RANS equations for the incompressible oil phase, with a time step 1E-5s by the final volume technique. The model of the domain consists only from a period of one twelfth of the real device. The turbulence model k-ε Standard completes the system of governing equations [4]. For all equations, convective terms are discretized using a second-order upwind scheme except the linear one for pressure. The discretized system is solved in a simple way. A pressure based, first order implicit solver has been used for unsteady formulation when dynamic mesh applied. A cavitation phenomenon is enabled by the secondary phase defined as incompressible oil vapour with a saturated pressure of 6 kPa [4]. The criterion for assessing convergence was based on the root mean square of the density residues expressed by

$$R(\xi) = \left[\sum_{i=1}^{M}\left(\frac{\partial\xi}{\partial t}\right)_i^2\right]^{\frac{1}{2}} \tag{6}$$

where M is the number of grid points and ξ is the variable considered to check (mass, energy, momentum, etc.). Generally, the next time step is taken when residuals fall below 1E-4.

2.3 Results of unsteady fluid-structure interaction

For brief examples of results, see Figures 4 and 5. Axial and radial coordinate x, r and angular coordinate fi_y define the positions of pressure minima responsible for cavitation within time period. See Figure 4(a). To get easier in the task, see Figure 4(b).

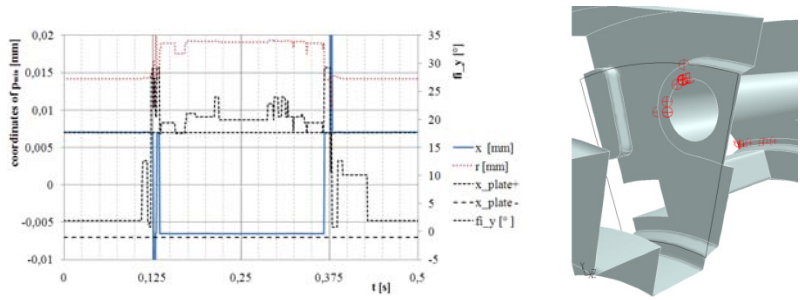

Figure 4: Spatial localization of pressure minima p_min(x, r, fi_y) (a) and its 3D visualization in various time steps for f=2Hz (b).

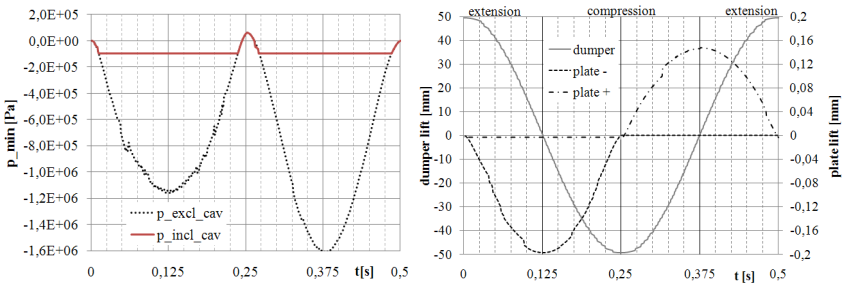

Figure 5: Temporal localization of pressure minima (a). Affected plates lift (b).

There is no temporal point during the damper lift significantly more responsible for the formation of cavitation bubbles as can be seen in Figure 5 a). The level of minimum pressure follows the actual oil flow velocity until the saturation pressure is achieved. From the case with cavitation excluded, the consequent smooth tendency of pressure minima can be observed (even if the result is not fully physically meaningful). Plate lift at the outer diameter R is recorded and is to be seen in Figure 5b).

3 Steady optimization

3.1 Method of by-pass channel and chocking plate optimization

We tried to find the combination of by-pass channel shape and plate stiffness with conserved pressure jump to minimize the production of cavity bubbles and we have decided to apply the optimization procedure to the stationary state adequate to t=0.05 s from the bottom dead centre. This state is of fully developed cavitation flow with an acceptable mass flow rate through the valve, not very threatening for the numerical stability of simulations itself. For the optimization itself, the shape based similarity optimization developed and described in [1] was applied. The shape of the by-pass nozzle is given by the cubic spline,

computed simultaneously from the set of three given parameters y_1, $y_2=y_0$ and α_2, see Figure 6. We have applied the ordinary Gauss's elimination method to find out the spline coefficients. The fourth parameter is the plate lift, used to adjust the oil mass flow rate to the value being equal to the real mass flow at 0.05s. The iterative adjustment of plate lift is provided by simple Newton's gradient method with maximum six steps. An average error of the plate position after six steps does not exceed 1e-5 m in test cases, which is sufficient for the solved case. We have applied the dynamic mesh model update to derive the most benefits of the minimal deformation path given by the shape-based similarity. A User Defined Functions (UDF) described in [3] and applied by Kolář and Dvořák in [2] is compiled to drive the wall boundary deformation over the whole sequence of nozzle shapes (vectors). The original domain that underlies the deformation has a simple linear shape. UDF updates the y-coordinate (y_{node}) of each node at time *t+1* (new shape) according to the spring based deformation defined as follows

$$y_{node}^{t+1} = \frac{y_{node}^{t}}{y_{wall}^{t}} y_{wall}^{t+1}. \tag{7}$$

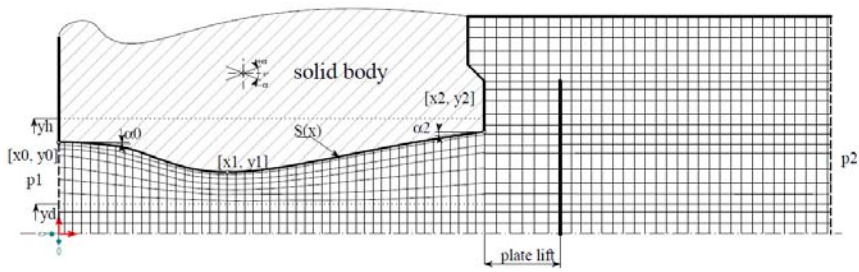

Figure 6: Scheme of domain for optimization of channel shape and chocking plate stiffness. Driving parameters of spline: y1, y0=y2, α2 and boundary conditions.

Optimization of the nozzle passes over two separate procedures. The first part includes the selection of location vectors from the parametric space and consequential optimization of vector sequence in order to minimize the overall deformation defined as follows

$$D_{tot} = \sum_{i=1}^{i=N} D(c_i, c_{i+1}) \tag{8}$$

where *N*= no. of shapes and *i=1,2,…,N,*

$$D_{tot} \sum_{i=1}^{i=N} D(c_i, c_{i+1})$$

where $D(c_i, c_{i+1})$ is the Euclidean distance between vectors (shapes) in R^2 defined as follows

$$D(c,c') = \sqrt{(w_1 - w'_1)^2 + \cdots (w_n - w'_n)^2} \tag{9}$$

and c, c' are two data series (series of y-coordinate vectors) as follows

$$c = \langle w_1, w_2, \ldots, w_n \rangle \quad c' = \langle w'_1, w'_2, \ldots, w'_n \rangle \tag{10}$$

$w,\ w'$ represent y-coordinate of nozzle shape consistently sampled by defined Δx. Flow, turbulence, and status variables in control volume and their fluxes are preserved for the newly formed mesh from the previous shape. With the acceptably small boundary deformation, the complete converging process takes only an incomparable small number of steps when comparing to "zero" initialization. To satisfy the condition of acceptable small boundary deformation, the shortest distance D_{tot} needs to be found out. This problem can be associated as a well-known Travelling Salesman Problem. The decision version of TSP belongs to NP-complete problems. The only approach able to improve the objective is a heuristic algorithm. One of the most sufficient is the Genetic algorithm presented firstly by Holand in [5]. We decided to use the parameter based coding of individuals where the chromosome gets a value of parameters as a real number. The selection of individuals for further evolution is based on the fitness proportionate selection with its modification: stochastic universal sampling. The recombination of individuals is provided by Edge recombination crossover (ERX). The operator of mutation is randomly applied to a selected pair of parameters by bilateral exchange. A more detailed view can be taken in Breitkopf and Coelho [6] and Hynek [7].

A shape-based similarity approach is originally developed by Yanagisawa *et al*. in [8] for the optimization of the mobile object trajectory although applicable even in the shape - based similarity query.

The second part of the optimization procedure includes CFD simulation of flow over the whole shape sequence of designed nozzles. The actual shape mutates towards the subsequent geometry until the final shape is met.

3.2 Results of optimization at steady state

As a first, the seeking for optimized sequence of shape deformation was performed. Evolution of overal deformation from the origanate to finalized shape sampled by Δx=0.1mm are in the Figure 7. The optimization of the shape sequence permutation led to the sequence gaining half of origal value. The best chanel shape sequence found with D_{tot}=3383 mm is used to explore the optimization space. The best variant achieves about 9% les of vapour volume fraction at the exit of domain than the originally cylindrical channel. Despite an achieved improvement, possible limitations of the approach are found because the best variant comes with the highest exit diameter (coordinate y_2) available from limited optimization space. For further optimization, at least the upper boundary of coordinate y_2 should be increased. There are contours of phase volume rate in the Figure 8 for best variant found. The location of pressure minima corresponds to originate shape, but the pressure jump is distributed within larger area of channel exit and channel throat. Consequently the local pressure minimum is restricted.

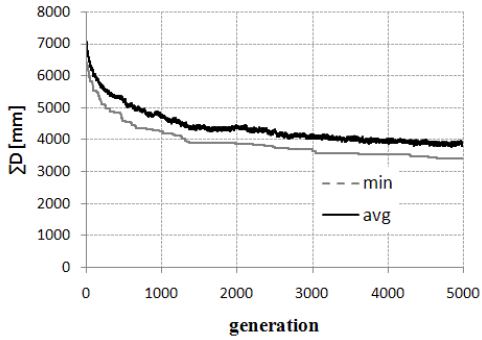

Figure 7: Evolution of average and minimal deformational path of shape sequences in the course of evolutionary algorithm.

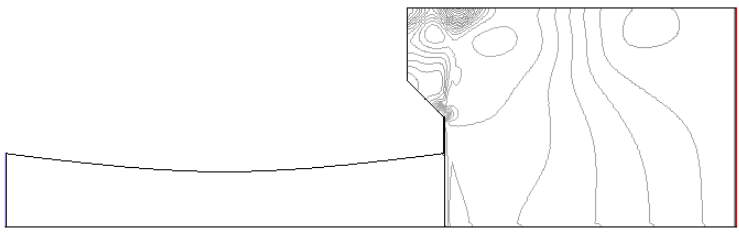

Figure 8: Isolines of vapour volume fraction in the best variant found by optimization. 0-0.5 m^3_{vapour}/m^3_{oil}.

4 Conclusions

The simplified method which enables the unsteady simulation of oil – chocking plate interaction is developed and tested. This method was implemented into commercial FVM code to expand its abilities beyond standards. Numerous techniques used to stabilize the coupled simulations are exposed. Dynamic behaviour of plate lift is than solved and cavitation phenomenon observed. We have applied the shape-similarity-based optimization procedure to reduce the cavitation within the damping unite at steady state previously defined. The best by-pass channel shape and plate stiffness combination comes with the vapour volume rate limited by 15% when compare to original value.

Nomenclature

$d\vec{r}, d\vec{r}[0]$	vector from boundary face centroids to wall adjacent cell centroids
k	absorber coefficient [-]
f	frequency of movement [Hz]
r_j	radial coordinate of node j [mm]

$r_{max,c}$	max. radial coord. of node within cell c [mm]
t	time [s], time step [-]
p_{avg}	fluid substitutive pressure on plate [Pa]
p_{load}	one-sided loading pressure in FEM [Pa]
y_1, y_2	y-coordinate of moving tank wall, coordinate of by-pass channel [mm]
y_0	initial position of tank wall (y-coord.) [mm]
A	amplitude of lift [mm]
F_i^-, F_i^+	face force located ad the plate + and - [N]
D_{tot}	overall deformation of shape [mm]
$Lift_{max}$	lift of plate at the outer radius R [mm]
N	overall number of plate face adjacent cell [-]
$\Delta x_j^{'}$	damped relative node displacement x-coordinate in node j [mm]
Δx_j	relative node displacement x-coordinate in node j [mm]

References

[1] Fluent Inc. *Fluent user documentation.* Lebanon : s.n., 2006.

[2] Kolář J., Dvořák V. *Aerodynamic optimization of supersonic nozzle exploiting dynamic meshes and sentivity analysis,* In the 2nd International Conference On Engineerig Optimization 2010 Lisboa, Portugal, Istituto Superio Técnico, 2010. ISBN 978-989-96264-3-0.

[3] Dvořák V., Kolář J**.** *Shape optimization of supersonic ejectors with several primary nozzles.* Lisboa, Portugal : In the 2nd International Conference on Engineering Optimization, 6.-9. september 2010. ISBN 978-989-96264-3-0.

[4] Versteeg H. K., Malalasekera W. *An introduction to fluid dynamics.* Harlow : Pearsons education limited, 2007. ISBN-978-0-13-127498-3.

[5] Holand, H J. *Adaption in natural and artificial systems.* Ann Arbor, Michigan : The University of Michigan Press, 1975.

[6] Breitkopf P., Coelho R. F. *Multidisciplinary design optimization in computational mechanics.* s.l. : Wiley-ISTE, 2010. ISBN-10 1848211384.

[7] Hynek J. *Genetic algorithms and genetic programing (in Czech).* Prague : Grada Publishing ,a. s., 2008. ISBN 978-80-247-2695-3.

[8] Yanagisawa Y., Akahani J., Satoh T. *Shape-based similarity query for trajectories of mobile objects.* Taipei : Mobile Data Management p. 63-77, 2003. ISSN 0302-9743.

This page intentionally left blank

Optimization of underground excavation in rock masses using ESO techniques

G. Ren & Y. M. Xie
School of Civil, Environmental and Chemical Engineering, RMIT University, Australia

Abstract

Excavation in rock masses induces complex stress redistribution around the opening. Inter alia, the stability of the opening is principally dependent on the stresses around the opening. The most influential factor attributing to the stress distribution is the geometrical shape of the opening. As such, finding the optimal shape for an underground excavation has practical significance in increasing stability and lowering support costs. This paper describes an approach to the shape optimization of underground excavation using Evolutionary Structural Optimization (ESO) techniques. Through illustrated examples, it is demonstrated that ESO method can be used to explore the excavation shapes that give optimized performance in terms of stress distribution and stability. The method is validated and compared with theoretical solutions. An example of a three dimensional case is presented in comparison with a well-known application case.
Keywords: excavation, cavern, finite element, optimization, evolutionary structural optimization, numerical analysis.

1 Introduction

Stability is one of the primary considerations in an underground excavation design in rock masses. The stability of a rock structure is usually dependant on a number of factors, including the rock mass strength, supporting system and the shape of the excavation. In underground rock structure construction, the rock is used as a structural material which is subjected to massive stress regime change due to exaction. The shape of the excavation influences the stress distribution around the excavation, which in turn affects the stability of the excavation. In addition to satisfying the intended functional requirements of the excavation, it is important to select a propitiate excavation shape that gives the maximum

WIT Transactions on The Built Environment, Vol 125, © 2012 WIT Press
www.witpress.com, ISSN 1743-3509 (on-line)
doi:10.2495/OP120151

stability. The shape optimization for an underground excavation in rock masses seeks to achieve the best performance based on stress regime change and the rock structural stiffness in a design domain.

The evolutionary structural optimization (ESO) techniques were originally developed by Xie and Steven in the 1990s [1], and recently were further developed into a Bi-directional evolutionary structural optimization (BESO) by Huang and Xie [2]. The original ESO method was based on the assumption that an optimal structure can be obtained by gradually removing all "inefficient materials" from the design domain. The "inefficient materials" are defined as those possess the least influence on either stress distribution or stiffness of the design domain. The design domain can be modelled by a finite element mesh with given boundary conditions and constraints. An example of such a finite element model is shown in Figure 1. The more recent bi-directional evolutionary structural optimization (BESO) method allows inefficient materials to be removed and at the same time to add new materials to the model. The BESO techniques significantly improve the efficiency of the optimization process. Both 2 or 3 dimensional models can be built for the optimization process using the ESO or BESO methods.

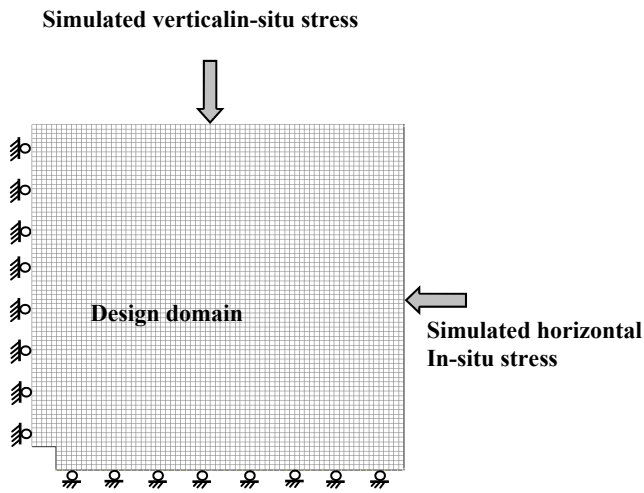

Figure 1: Two dimensional finite element mesh.

In the optimization process, an optimization criterion has to be used for determining the level of efficiency of each element. Both stress and stiffness can be used as criteria for the evolutionary optimization process. In the initial stage of the ESO/BESO procedure, a conventional finite element mesh is established to model the design domain. When stress is used as the optimization criterion, the ESO/BESO will evoke a routine to exam the stress levels of each element in the design domain. Elements with stresses below the predetermined stress level are recorded as inefficient elements and subsequently removed from the finite element mesh. As this evolutionary procedure is repeated for each updated mesh,

more and more inefficient elements are removed from the mesh, so the remaining shape of the finite mesh evolves towards optimum. Full details of the ESO procedure using the stress criterion approach are described by Xie and Steven [1] and Ren *et al*. [3]. When stiffness is used as the optimization criterion, the ESO/BESO examines the effect of each element on the global stiffness. Elements in the design domain with low influence on the stiffness are deemed to be inefficient elements and are subsequently removed from the design domain (Huang and Xie [2]).

In 2004, Ren *et al.* [3] applied the ESO techniques to underground excavation and achieved interesting results. In an attempt to seek the optimal shape of an underground excavation, Ren *et al.* [3] adopted a full stress design strategy, i.e. the whole design domain is fully stressed. This is simulated in the finite element model by applying confined stresses equivalent to the vertical and horizontal in-situ earth pressures (see Figure 1).

2 Rock mass material model and optimization based on stresses around excavation

Unlike manufactured materials, rocks are natural materials which can be highly variable. It is often practically difficult to adopt an appropriate constitutive material model for rock analysis, as the stress-train behaviour of rock is affected by its inherent geological discontinuities, such as beddings and faults. A number of material models for rock analysis have been developed over the years, the most commonly adopted material models include the conventional Mohr–Coulomb and Hoek-Brown models for the civil and mining industries. The earlier work on the shape optimization for underground excavation by Ren *et al.* [3] was limited to linear elastic model due to the limitation of computing power and ESO techniques available at the time. Recent advancement in PC computing power and the development in the BESO analytical efficiency have allowed for non-linear analysis to be carried out for better simulation of the rock mass behaviour.

In a traditional excavation design, a simple shape with an arched roof is usually adopted. It is always desirable to obtain a fully optimized shape within given constraints that would lead to stable excavation. Hoek and Brown [4] provided useful guidelines for underground excavation design based on stress distribution around certain excavation shapes.

Ren *et al.* [3] used the Von Mises stress as optimization criterion. At the initial stage of the optimization procedure, the finite element model was analyzed with an initiation void in the centre of the design mesh (Figure 1). The initiation void created initial stress change in the design domain so that the ESO routines could screen the stress levels in each element and apply an optimization criterion to eliminate those inefficient elements based on Von Mises stress:

$$\sigma_{vm} = \sqrt{0.5 * [(\sigma_1 - \sigma_2)^2 + (\sigma_2 - \sigma_3)^2 + (\sigma_3 - \sigma_1)^2]} \quad (1)$$

where σ_1, σ_2 and σ_3 are principal stresses.

The Von Mises stress (σ_{vm}) was used in the optimization process as the optimization criterion. Elements which sustained a lower level of Von Mises stresses are regarded as inefficient in contributing to the global strength of the structure and hence were eliminated from the design domain. Some interesting shapes were produced using the Von Mises stress criterion approach. Figure 2 shows an example of optimized shape at an underground tunnel intersection. Figures 2(a), 2(b) and 2(c) illustrates the evolutionary process at iteration 15, 30 and 50 respectively.

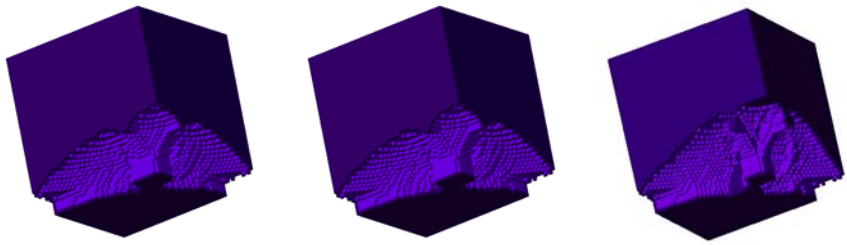

(a) Iteration 15 (b) Iteration 30 (c) Iteration 50

Figure 2: Example of evolution optimization process for a 3D finite element model.

3 Optimization based on stiffness criterion

When an excavation and its surrounding rock mass is considered as the design domain (Figure 3), the stiffness of the design domain is dependant of the shape of the excavation under the given constrains. The rationale behind the stiffness based optimization is that the higher global stiffness indicates a stable design domain, i.e. a stable rock structure. The optimization process aims to create a shape of excavation that would give the highest possible rock structure stiffness. Normally, the overall stiffness of a structure K is inverse measure of the mean compliance C, which is defined by the total strain energy of the structure or the external work done by applied loads [2]:

$$Ku = f \tag{1}$$

where K is the global stiffness matrix; f is the force vector and u is the displacement vector.

If element i is removed from the design domain, the stiffness matrix change is:

$$\Delta K = K^* - K = K_i \tag{2}$$

where K^* is the stiffness matrix of the resulting structure after the element is removed and K_i is the stiffness matrix of element i. The change in global stiffness as a result of the removal of element i can be indexed by:

$$\Delta C = \frac{1}{2} u_i^T K_i u_i \tag{3}$$

where u_i is the displacement vector of the element i.

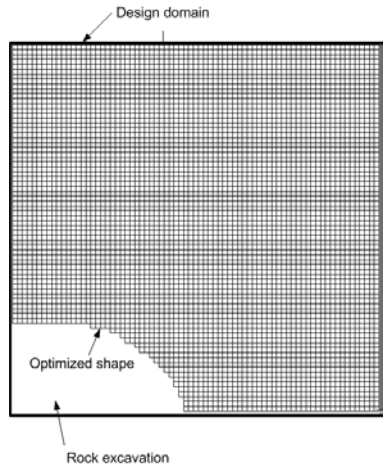

Figure 3: Stiffness optimization in rock mass excavation design domain (quarter model).

The equation (3) indicates the sensitivity of the mean compliance as a result of the removal of the element *i,* which equals to its elemental strain energy.

The evolutionary procedure for stiffness optimization is performed by checking the sensitivity of each element in the following way: elements in the close vicinity of the excavation with lower sensitivity as determined by Equation (3) would imply less efficiency in terms of contributing to the global stiffness; whereas, elements with higher sensitivity could be regarded as efficient elements for the rock structure. The optimization routines are designed to remove the lower efficiency elements in the finite element model in accordance with the predefined optimization criterion defined by Equation (3).

The process of removing elements in a finite element mesh is reminiscent of the underground excavation activity (see Figure 2), although the sequence of removal may be different. The optimized shape of the excavation is obtained when the pre-determined control parameter such as dimension of excavation or prescribed volume of removal is reached.

The full description and details of the ESO/BESO methodology are given in [1] and [5]. The following discussion will mainly focus on the application to underground excavation through illustrated examples.

4 Boundary conditions for underground excavation model

For an underground excavation at depth of z, the vertical stress σ_v is given by:

$$\sigma_v = \gamma z \tag{4}$$

where γ is the unit weight of overlying stratum.

The simulated vertical stress as shown in Figure 1 can be defined using equation (4). The horizontal boundary stress σ_h can be estimated from:

$$\sigma_h = k \sigma_v = k \gamma z \tag{5}$$

where k is the ratio of horizontal stress to the vertical stress.

The value of k is affected by local geological conditions. Hoek *et al.* [6] suggested that the k value for rock mass can be estimated by equation:

$$k = 0.25+7E_h (0.001+1/z) \tag{6}$$

where E_h in GPa is the average deformation modulus of the rock mass.

Equation (4) to (6) can be used to generate boundary stress conditions for the finite element models.

For a simple 2-D case, due to symmetry, only a quarter of the finite element is required to be analyzed as shown in Figure 1.

5 Optimization model validation

Under a conventional stress conditions such as the one shown in Figure 4, it is not hard to find a theoretical solution for the optimal shape of an excavation under vertical and horizontal stresses.

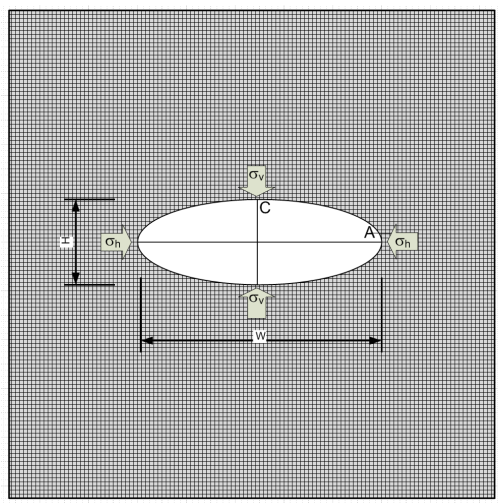

Figure 4: Optimal shape of an underground excavation is an elliptical opening with axial lengths matching the in situ stress ratio.

In a biaxial stress field, the tangential boundary stresses (σ_A and σ_C) at the end of the axes of an elliptical opening (see Figure 4, where "W" denotes the length of the horizontal axis, "H" is the length of the vertical axis of the elliptical void) are given by equations:

$$\sigma_A = \sigma_y + 2\sigma_y(\frac{W}{H}) - \sigma_h$$

$$\sigma_C = \sigma_h + 2\sigma_h(\frac{H}{W}) - \sigma_y$$

when $\sigma_A = \sigma_C$, we have:

$$\frac{\sigma_h}{\sigma_v} = \frac{W}{H} \tag{7}$$

It can be seen from equation (7) that the tangential boundary stresses are identical when the axis length ratio (aspect ratio) of an elliptical opening is matched to the in-situ stress ratio.

Figure 5 shows the optimized excavation shapes under various vertical and horizontal stress ratios, and Figure 6 illustrates the resulting optimized excavation for a 3 dimensional finite element model using the ESO procedure.

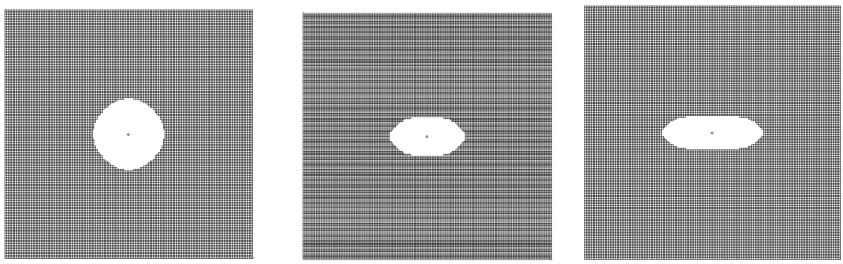

(a) Optimal shape for in-situ stress ratio 1:1

(b) Optimal shape for in-situ stress ratio σ_y / σ_h =1/2

(c) Optimal shape for in-situ stress ratio σ_y / σ_h =1/3

Figure 5: Optimal shapes obtained from ESO procedure under various stress ratios, indicating that the optimal shape for a given stress condition is elliptical opening with axial lengths matching the in-situ stress ratio.

From Figures 5 and 6, it is evident that the ESO derived shape gives identical answer to theoretical solutions, where the optimal shape of an excavation is in the shape of an oval with axis length ratio matching the in-situ stress ratio.

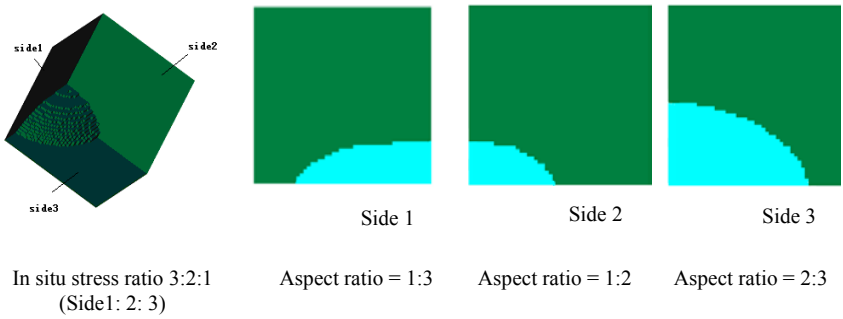

Figure 6: Optimized shape in 3 dimensional finite element models.

6 Application examples and discussions

To illustrate the applicability of the ESO/BESO techniques to underground excavation shape optimization, a model involving two excavations adjoining at a right angle are considered. This model can simulate tunnel intersection in rock masses. The 3-D model is subjected to vertical and horizontal confined stresses which can be represented by underground in-situ stresses. Figure 7 shows a processed image of the optimized shape of the excavation using Von Mises stress criterion. It is interesting to note that ESO/BESO method can generate rather practical configurations for an underground rock structure, which has close resemblance to one of the well-known Swedish Stockholm metro stations as shown in Figure 8. The similarity between the model in Figure 7 and the Stockholm metro station as photographed in Figure 8 suggests that the rock structure design for the Stockholm metro station is not only aesthetically pleasing but also structurally optimal in terms of stress distribution and stability.

The ESO/BESO method is a useful tool in providing optimization solutions to real engineering problems with complex geometries and stress constrains. From the above discussion and demonstration, the following observations are made:

- The shape of excavation in rock mass can be optimized based on stress or stiffness of the rock structure.
- Optimized rock structures are theoretically more stable and require less support, and consequently lead to economical design.
- The ESO/BESO techniques are capable of handling complex rock structures and in-situ stress regimes.
- The ESO/BESO provides an alternative ways of forming an underground cavity based on prescribed constrains, such as vertical and horizontal stresses, function requirements, optimization criteria and material properties.

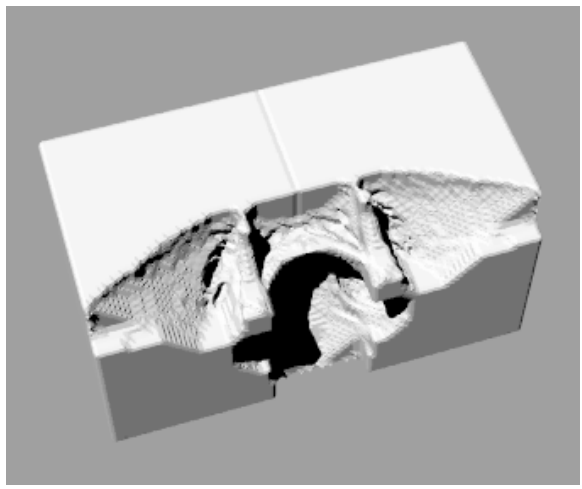

Figure 7: Optimized shape of an excavation at a tunnel intersection based on Von Mises stress criterion.

Figure 8: Stockholm metro system, Sweden is constructed in solid rock, a fine example of excavation in rock mass (photo courtesy of R. P. Young).

From a number of experiments, it is apparent that optimized shapes derived from the ESO/BESO method are optimization criterion dependent. The shape obtained using the Von Mises criterion is different from that using stiffness criterion. The meaning of "optimum shape" in the context of ESO/BESO may not be truly "the optimum" in strict mathematical sense; rather, it should be taken as the shape optimized to stress or stiffness according to the adopted

criterion. More research is required as to which optimization criterion should be used for a specific design problem.

The significance of the ESO/BESO method applying to rock exaction lies in the fact that it is able to derive a geometrical shape that has been subjected to a filtering process eliminating inefficient elements in terms of stress or stiffness. The resulting shape of the excavation can be taken as the optimized one that gives better stability and consequently economical and safe underground rock structure.

References

[1] Xie, Y. M. and Steven, G. P., *A simple evolutionary procedure for structural optimization,* Springer, Berlin, 1997.
[2] Huang, X. and Xie, Y. M., *Bi-directional evolutionary topology optimization of continuum structures with one or multiple materials,* Computational Mechanics, Vol. 43, No. No. 3, 2008, pp.393-401.
[3] Ren, G., Smith, J. V., Tang, J. W., and Xie, Y. M., *Underground excavation shape optimization using an evolutionary procedure,* Computers and Geotechnics, Vol. 32, No. No. 2, 2005, pp.122-132.
[4] Hoek, E. and Brown, E. T.*, Underground excavations in rock*, The Institute of Mining and Metallurgy London, 1980.
[5] Huang, X. and Xie, Y. M., *Evolutionary Topology Optimization of Continuum Structures - Methods and Applications,* John Wiley and Sons 2010.
[6] Hoek, E., Kaiser, P. K., and Bawden, W. F., *Support of underground excavations in hard rock*, Rotterdam: Balkema 1998.

Section 3
Optimization in civil engineering

This page intentionally left blank

Software with a graphical interface for design optimization of prestressed concrete launched bridges

A. N. Fontán, S. Hernández & F. J. Tsao
School of Civil Engineering, University of A Coruña, Spain

Abstract

A computer code aimed to produce optimum design of prestressed concrete launched bridges during construction phase is presented in this paper. The software provides the least cost design for a prestressed concrete bridge constructed by incrementally launching procedures, searching simultaneously for the optimum cross-section dimensions and the prestressing forces of the concrete deck, as well as the most adequate characteristics of the launching nose. The code incorporates the complete set of constraints considered in the Spanish code of practice for this type of structure. The software features an advanced graphical interface to provide a user friendly communication. This graphical environment allows managing multiple projects simultaneously. The benefit of considering the numerical optimization instead of design rules, established by well known bridge designers that can be found in the literature, has been demonstrated by authors in previous publications. In this paper an application example is presented to make clear the capabilities of the code.
Keywords: structural optimization, structural design, incrementally launched bridges, concrete bridges, launching nose.

1 Introduction

The Incrementally Launching Method (ILM) is a common construction procedure for medium span prestressed concrete bridges that consist of building a deck by segments on the ground and advancing the already-built deck portion periodically over the piers until reaching its final position in a similar way to an extrusion [1–4].

WIT Transactions on The Built Environment, Vol 125,
www.witpress.com, ISSN 1743-3509 (on-line)
doi:10.2495/OP120161

Incrementally launched bridges base their economical advantages on not requiring falsework to support the deck during their construction, although a series of auxiliary elements are required: a casting yard, launching devices and a launching nose, which is a light structure normally made of steel, attached ahead of the front part of the deck as an extension allowing to reduce the stresses produced in the cantilever configuration of the concrete girder during launch.

Also, during the construction of a concrete launched bridge it is necessary to consider a prestressing force without eccentricity, known as centric prestressing. The objective of this active reinforcement is to limit at the same time the tensile stresses at the top and bottom extreme fibres of the deck, since due to the launching process, any cross-section will have to support both positive and negative bending moments during launch, while passing over a support or the middle of a span.

Surprisingly, the design of launched bridges is usually carried out by trial and error.

2 Optimization of launched bridges

Several strategies can be followed to improve the construction process of an incrementally launched prestressed concrete bridge. The first alternative is to use traditional methods to design the launching nose, but does not guarantee the best possible solution. Another possibility is to use more sophisticated and powerful methods, using mathematical optimization tools to determine the best dimensions of the launching nose, the deck cross-section and the centric prestressing forces.

The conventional design method basically consists of modifying an initial design by trial and error until a final design is satisfying enough. This process of trial and error does not guarantee achieving the best possible solution and is necessarily limited to a low number of trials. The conventional methods have been used by several authors [5–8] to improve the design of the launching nose and obtain the minimum bending moment in the deck.

A first approach to optimize the launching nose of a launched bridge is to use a parametric model and assume as the optimal length of the launching nose that minimizes the maximum stresses in the deck [9, 10]. Using this approach shows that certain assumptions for the conventional design procedure are not justified. Furthermore, the use of trial and error methods may lead sometimes to error and produce inaccurate results. In any case, it is necessary to consider adequate relations between nose and deck for the results of a parametric optimization of the launching nose to be feasible.

To avoid the limitations of the conventional method or parametric models it is necessary to consider a more general methodology to optimize the construction of a prestressed concrete launched bridge.

This research work proposes a global optimization strategy, solving a structural model for both the nose and deck that simulates the entire launching process and considers the actual geometrical and mechanical characteristics of

the deck and the launching nose, using practical design criteria and taking into account the real problems that engineers usually find.

With this new formulation, the optimization of a launched bridge is not limited to improve the launching nose design, but extended to obtain at the same time the more appropriate values of the dimensions of the deck cross-section, the launching nose and centric prestressing forces to minimize the total cost of the nose and deck. This paper presents the computer application vPULO so that this approach is feasible in terms of time and resources consumption.

This code allows us to generate the structural models of the continuous beam (nose-deck set) for each instant during launch, to analyze the worst internal forces during the construction using matrix analysis and to perform the iterations needed by the optimization algorithms to obtain the optimum launched bridge in terms of construction costs. The code is managed through a friendly graphical user interface to input data and output results.

3 Description of the software vPULO

vPULO code is organized into blocks shown in the flowchart of Figure 1, which in turn are divided into other modules, responsible for solving specific tasks.

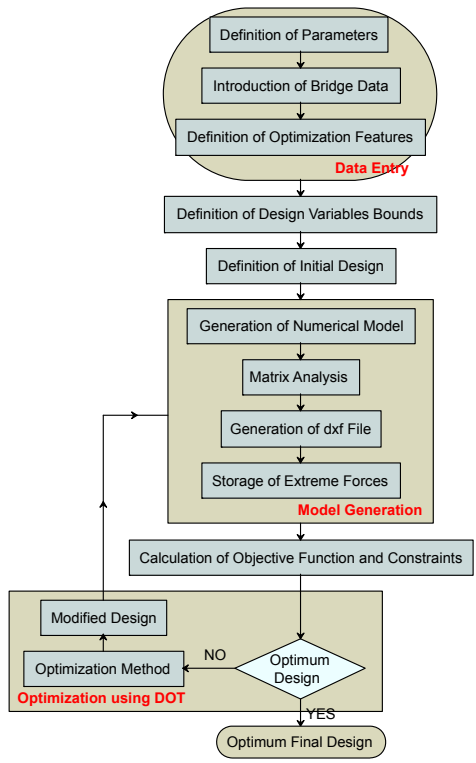

Figure 1: Flowchart of the program vPULO.

The general characteristics and the initial design of the prestressed concrete launched bridge are defined in the first block. The second block is responsible for generating and analyzing all structural models to be considered during the launching process. Finally, the third block deals with optimization tasks using the commercial code DOT [11].

The calculation engine has been developed in Fortran 77, by calling the DOT functions for the optimization process. The graphical environment for pre and post-processing has been made by an object-oriented development in C++ with free programming libraries, Qt for window management, and Qwt for insertion and manipulation of graphics post-processing.

3.1 Model definition

The distribution of bridge spans is constant with length L, except for the end spans with $k \cdot L$.

The bridge deck has a constant height H and hollow box cross-section with flanges, where top and bottom slabs and two inclined webs have constant thickness, respectively e_s, e_i, e_a (Figure 2).

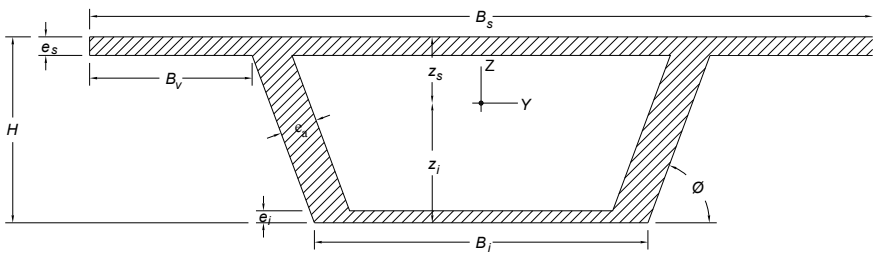

Figure 2: Box cross-section with flanges.

In order to control the stresses in the front end of the deck, a launching nose is considered to be made up with a pair of reinforced beams with solid web and variable height (Figure 3). Both of them are I-beams with constant thickness and linearly variable web height. At the joint with the deck, the launching nose has the same height as that of the deck H, while at the front end, its height es h_N. The two beams of the launching nose must be strongly stiffened and braced between them to avoid any instability. Neither stayed front system nor temporally piers are considered.

For the launching of the concrete girder, a centred straight constant prestressing is needed, that produces only axial compression on the beam. Because bending forces are bigger at the front end of the deck than the rest, a larger centric prestressing (P_f, frontal centric prestressing) is used for the first segments than for the rest of the bridge (P_d, dorsal centric prestressing). The designer must define the number of the foremost segments with larger prestressing.

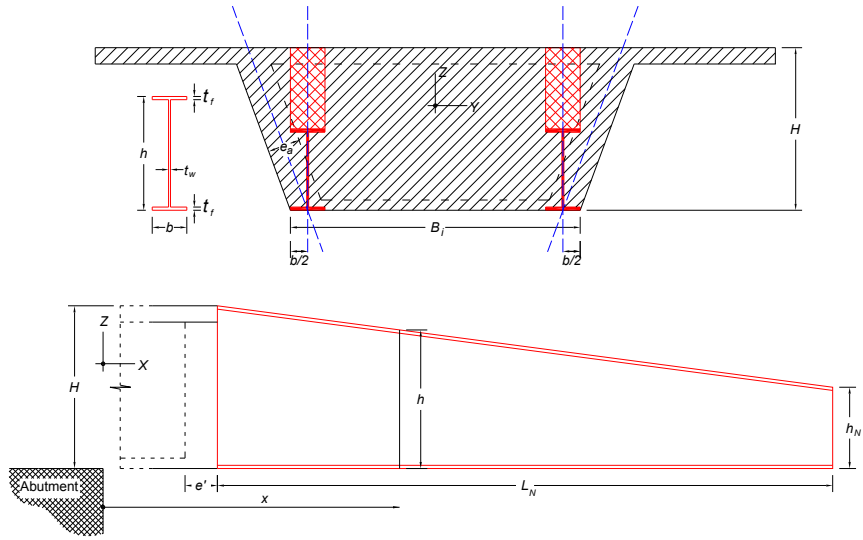

Figure 3: Cross-section and side view of a generic launching nose.

The most appropriate segment length is one half of the regular span (Figure 4). The segments of the end spans have different length.

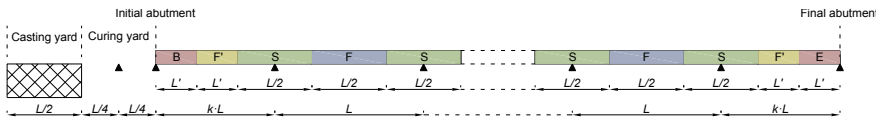

Figure 4: Supports of the structural model.

After defining all the supports and segment sizes for the deck, all the intermediate configurations and sectional forces for the nose-deck system during launch can be determined precisely.

In the model, the considered loads during the construction phase are the self-weight of the deck and the diaphragm of the nose-deck joint, the centric prestressing, thermal gradients and a possible overload acting uniformly on the full length of the girder. According to the Spanish construction codes [12], the following criteria must be satisfied for the calculation of the prestressed concrete bridge deck:

- dimensioning the deck for limit state of decompression,
- dimensioning the web for limit state of shear,
- checking the cross-section for limit state of bending and longitudinal forces,
- checking the deck for serviceability limit state of deformation.

Therefore, the limit states of decompression and shear are taken into account for dimensioning. For a later study, it will be necessary to define passive reinforcement and parabolic prestressing to suit the above requirements.

Taking into account an intense level of execution control, due to a semi-industrial production, and considering the partial safety factors for the loads during transitory stage (construction phase), it is possible to calculate all the required load combinations. Only eight load combinations are necessary to obtain the worst sectional forces for the previously mentioned limit states.

3.2 Numerical model generation and analysis

During the construction process, from the time when the launching nose is placed on the sliding area and the first deck segment is concreted, until the complete girder reaches its final position and the launching nose is removed, the nose-deck system goes through an infinite number of different static configurations.

In order to obtain the maximum forces that the deck experiences during this process, it is necessary to solve a numerical model of the nose-deck system in the worst configurations. To simulate the complete constructive process of a launched bridge, a specific computer code was created, which generates numerical models for all the representative situations during the launching phase.

Later, these models are calculated with an original matrix structural analysis module based in linear elastic theory and that considers variable cross-section. This software solves sectional forces adequately considering the contribution of the launching nose to the behaviour of the nose-deck system by evaluating correctly the inertial variation of the nose.

3.3 Formulation of the optimization problem

The proposed formulation considers that the objective function is the sum of the total construction cost of the concrete deck, the cost of launching nose, and the cost of the centric prestressing.

The design variables, characteristics of the problem that can be varied during the optimization process, are the dimensions of cross-section of the concrete deck, the size of the launching nose, and the value of centric prestressing forces in the front and back part of the girder, namely:

1. H: height of the concrete deck.
2. e_s: thickness of the top slab of the deck cross-section.
3. e_i: thickness of the bottom slab of the deck cross-section.
4. e_a: thickness of the inclined webs of the deck cross-section.
5. h_N: height of the launching nose at its fore end.
6. L_N: length of the launching nose.
7. t_f: thickness of the flanges of the launching nose.
8. t_w: thickness of the webs of the launching nose.
9. P_D: prestressing force in the rear part of the deck.
10. P_F: prestressing force in the front part of the deck.

The limits of validity and a starting value of each design variable can be established using technical criteria and experience from similar previous works [1–3].

The optimization constraints limit the stresses in the deck and the launching nose.

To satisfy the serviceability limit state (SLS) of decompression in the concrete deck, tensile stresses cannot be produced neither in the topmost or bottommost fibre of the cross-section for the maximum and minimum bending moment of SLS. Moreover, the compressive stresses should be limited in order to avoid cracks by excessive compression in concrete.

To fulfil the ultimate limit state (ULS) of shear in the webs of the concrete deck cross-section, it is necessary to check if the maximum shear force will not exceed the shear strength of the webs by both oblique compression and tension.

The steel launching nose is dimensioned according to Eurocode 3 [13] by limiting the worst normal and shear stresses for ULS. Notice that the cross-section is variable.

The worst case forces are calculated for the 8 load combinations, distinguishing between the front and back segments of the deck. Similarly, the worst section forces are obtained for the launching nose. Considering all of the above, 14 different optimization constraints are generated.

Thus, the optimization of a launched bridge results in a problem with 10 design variables and 14 constraints, which can be considered to be a medium-size problem, however, it is highly nonlinear for its objective function as well as constraints. Therefore, it should be resolved by numerical methods [14, 15] and computer applications [11]. Three different optimization algorithms were employed:

- Method 1: modified method of feasible directions.
- Method 2: sequence of linear problems.
- Method 3: sequence of quadratic problems.

The internal parameters of DOT are totally configurable such as the tolerances to satisfy the constraints, the maximum absolute or relative change of the objective function between a certain number of successive iterations to show convergence, or the maximum step for the derivates calculations for finite difference method. Gradients can be calculated by first forward or central finite difference, which is more accurate, but the number of function evaluations is almost doubled.

3.4 Graphical user interface

A graphical user interface (GUI) has been developed to interact friendly with the calculation core. This graphical environment controls the entire program, both pre and post-processing, i.e. for data entry and presentation of results.

An important feature of the code is that it can process several independent models at the same time. This is necessary because the calculation process can be long depending on the size of the model and the hardware. It is possible to run several problems at once, to compare results of models already solved or simply to display results of an example while the program calculates a different one. The user is informed when the optimization algorithm reaches the convergence.

This GUI has all the usual functionalities in a computer program with windows and menus. In the main window are two tabs: “Projects” and “Results”. For multiple projects running at a given time, the first tab manages the data entry and the second the obtained results.

4 Application example

An example of a launched bridge is solved to demonstrate the operation and benefits of the program. The model has total length of *510.4 m* divided into 12 spans as the distribution shown in Figure 5. The rest of the parameters are:

- cross-section: $B_s = 12\ m$, $B_i = 5\ m$, $B_v = 3\ m$,
- number of deck segments with front prestressing: 4,
- launching nose: steel *S275*, 15% additional weight due to bracing and stiffening,
- materials: reinforced concrete *HA50*, passive steel *B500S*, active steel *Y1770*,
- thermal loads: $\Delta T^- = -3\ ºC$, $\Delta T^+ = 7\ ºC$,
- prices: $P_{steel} = 2\ €/kg$, $P_{prestressed\ steel} = 3.1\ €/kg$, $P_{concrete} = 90\ €/m^3$.

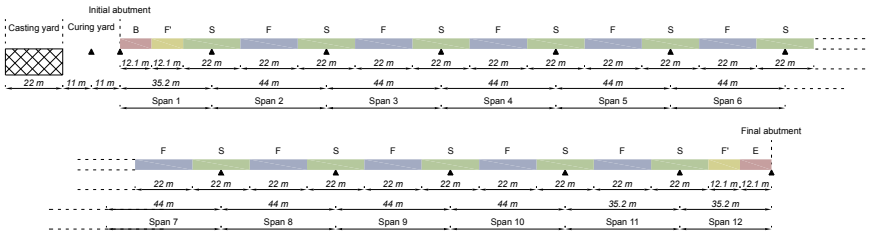

Figure 5: Span distribution of the bridge model.

The initial values of the design variables are: H = 3.2 m, e_s = 25 cm, e_i = 25 cm, e_a = 47 cm, L_N = 26.4 m, h_N = 1 m, t_f = 2 cm, t_w = 1.5 cm, P_F = 45 MN, P_D = 35 MN.

The first step is create a new model from the File menu, and then, in the main form the model data are inserted in different windows: “Viaduct geometry, longitudinal and transversal” (Figure 6), “Launching nose geometry” (Figure 7), “Features of reinforcement”, “Features of materials”, “Loads and construction procedure”, “Materials prices”.

After entering the model data it is possible to start the analysis. First of all, the code checks data for errors. Then, a form is shown for entering the optimization parameters of DOT code and finally the calculation is started (Figure 8).

To view and analyze the results of the optimization process, the user must open the tab “Results” in the main window, from where are available the following forms:

- Main results (Figure 9). The optimum design and the achieved construction cost improvement during the optimization are shown.

- Optimization process (Figure 10). Graphics of the evolution of the objective function, design variables and constraints during the optimization process are drawn.
- Original project. Initial values of the model before optimization are listed.
- Optimization parameters. Parameters used by optimization algorithms are showed.

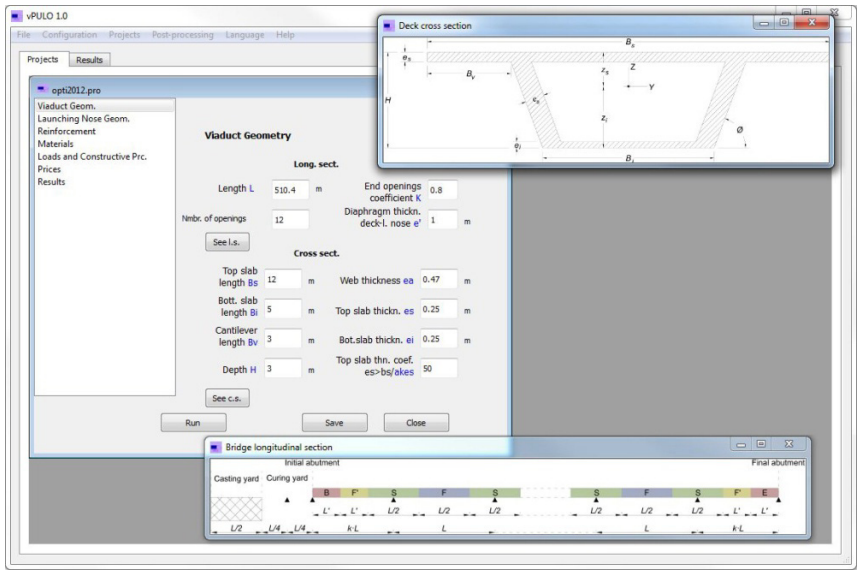

Figure 6: Form of viaduct geometry, longitudinal and transversal.

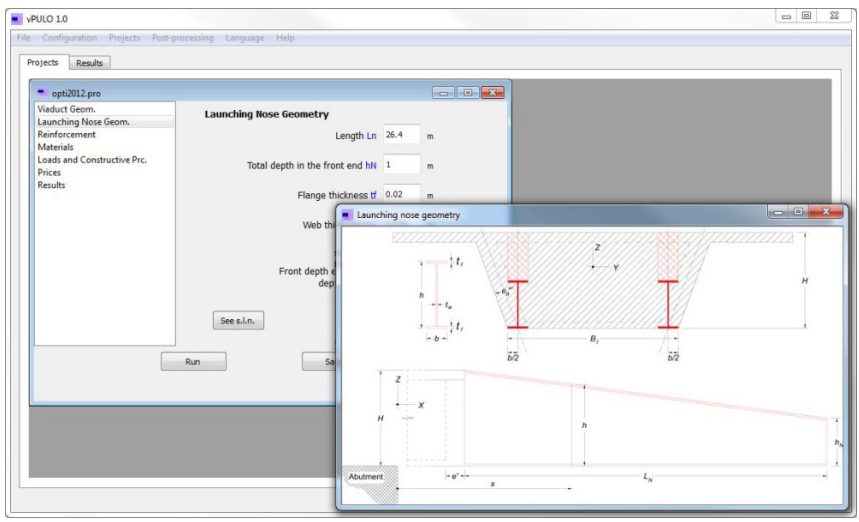

Figure 7: Launching nose geometry form.

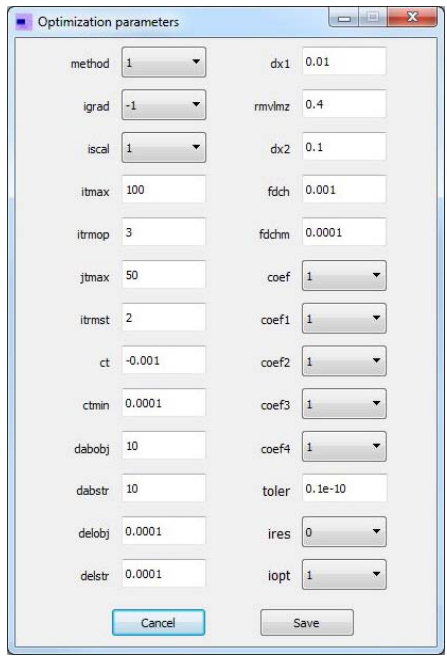

Figure 8: Window of optimization parameters.

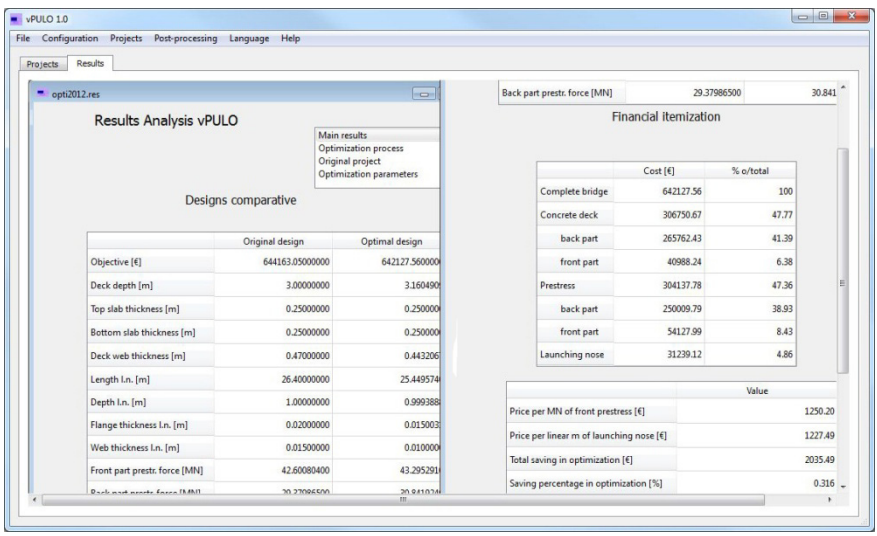

Figure 9: Main results.

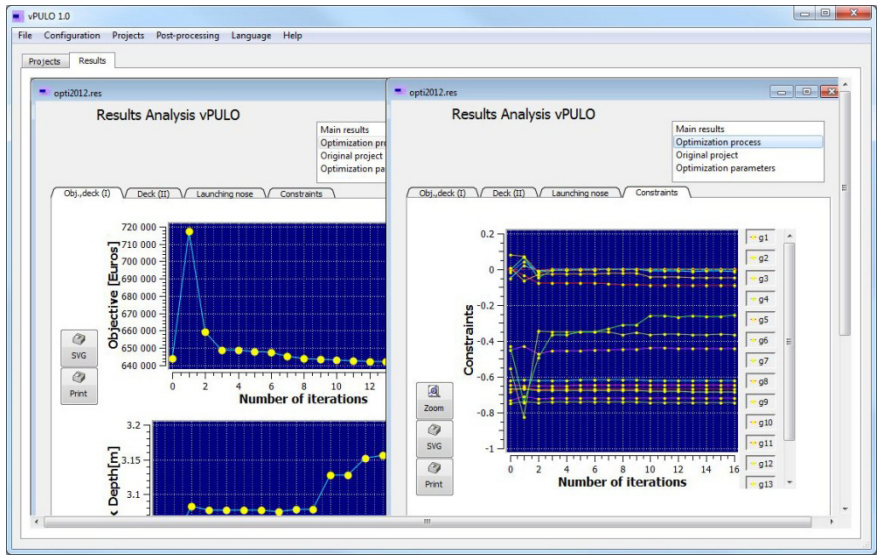

Figure 10: Evolution of objective function, design variables and constraints.

5 Conclusions

This article presents the simultaneous optimization of the deck cross-section, the centric prestressing forces, and the launching nose of prestressed concrete launched bridges, using software with graphical user interface. The main conclusions are the followings:

- The present techniques for dimensioning of launching noses are based on trial and error methods. Therefore, they are inaccurate and can lead to an error.
- Launched bridges are a suitable case for application of structural optimization methodologies that can overcome the limitations of conventional design methods.
- The optimization of a launched bridge requires searching simultaneously for the most appropriate dimension values of the launching nose and the deck cross-section as well as the centric prestressing forces so that the total construction cost of deck-nose system will be minimum, with the required codes satisfied.
- The application of numerical techniques to the optimization of launched bridge construction allows designers to take better decisions.
- User friendly software can help in introducing new design techniques. The software vPULO, with its graphical user interface makes it easy to obtain the optimal solution to the problem studied.

References

[1] Bouchon, E. and *et al*., *Guide des ponts poussés*, Association français de genie civil, Presses de l'ecole nationale des ponts et chausées, 1999.
[2] Göhler, B. and Pearson, B., Incrementally launched bridges: Design and construction, Wiley, New York, 2000.
[3] Rosignoli, M., *Bridge launching*, Thomas Telford, 2002.
[4] AASHTO, *Bridge construction practices using incremental launching*, American Association of State Highway and Transportation Officials, Highway Subcommittee on Bridge and Structures, 2007.
[5] Iglesias, C., *Algunas ideas sobre el predimensionamiento de puentes empujados*, Hormigón y Acero, Vol. 182, pp.111-128, 1992.
[6] Rosignoli, M., *Nose-deck interaction in launched prestressed concrete bridges*, J. Bridge Eng., Vol. 3 (1), pp.17-21, 1998.
[7] Choi, H.Y., Suh, S.K., Oh, M.S. and Oh, S.H., *Techniques of optimizing the launching nose in incremental launching method*, The 5th international symposium on steel structures, Seoul, South Corea, pp.954-961, 2009.
[8] Wang, W., Zheng, H. and Zeng, X., *Optimum design of launching nose during incremental launching construction of same-span continuous bridge,* World Academy of Science, Engineering and Tech., 72, 2010.
[9] Fontán, A.N., *Optimización de la sección transversal y del pico de lanzamiento de puentes lanzados de hormigón pretensado,* Doctoral Thesis, University of A Coruña, 2009.
[10] Fontán, A.N., Hernández, S., Baldomir, A. and Díaz, J.M., *Diseño óptimo del pico de lanzamiento de puentes lanzados de hormigón pretensado*, Rev. Int. Metod. Numer. Calc. Dise., Vol. 28 (2), 2012.
[11] DOT, *DOT Design Optimization Tools. User Manual. Version 5.0*, Vanderplaats Research and Development, Inc., 2001.
[12] EHE, *Instrucción de hormigón estructural*, Comisión permanente del hormigón, Ministerio de Fomento, Spain, 2008.
[13] Eurocódigo 3, *Proyecto de estructuras de acero,* AENOR, 2008.
[14] Hernández, S., *Métodos de diseño óptimo de estructuras*, Colegio de ingenieros de caminos, canales y puertos, 1990.
[15] Vanderplaats, G.N., *Numerical optimization techniques for engineering design: with applications*, 3ª edition, Vanderplaats Research and Development, inc., Colorado Springs, 2001.

Optimization of thick-walled shells based on solutions of inverse problems of the elastic theory for inhomogeneous bodies

V. I. Andreev
Department of Strength of Materials,
Moscow State University of Civil Engineering, Russia

Abstract

An inverse problem of elastic theory for inhomogeneous bodies is normally used for identification of the dependencies of a material's mechanical properties of coordinates where the stress state of the body will be specified. It is known that in thick-walled cylindrical or spherical shells under internal or external pressure the highest stresses are close to the inner surface of the shell. Several solutions of inverse problems (depending on the elastic modulus along the radius at which the equivalent stress in the shell will be constant) are obtained in this paper with the use of conventional strength theories. Corresponding shells could be called equal stress shells. If an investigator changes the elastic modulus of the material its mechanical properties change as well. It is shown that for some materials the investigator can create a model of an equal strength shell with an equivalent stress at each point, which is equal to the strength of the material. This paper is devoted to creating multi-layered shells in which the elastic modulus in each layer is determined by the results of solving inverse problems.
Keywords: elastic theory, inverse problem, thick-walled shells, inhomogeneous bodies, stress state, strength, equivalent stress, multilayer shells, maximum shear theory, maximum-strain-energy theory.

1 Introduction

The aim is to develop models of thick-walled shells which are close to equal strength. The modulus of elasticity of the material, which depends on the radius at which the corresponding equivalent stress will be constant at all points of the shell [1], is determined with the use of solutions of inverse elasticity problems

WIT Transactions on The Built Environment, Vol 125, © 2012 WIT Press
www.witpress.com, ISSN 1743-3509 (on-line)
doi:10.2495/OP120171

for inhomogeneous bodies for various strength theories. Analytical and numerical methods are used for the solution of inverse problems. A special so-called coefficient of efficiency of design β (the ratio of the maximum limiting pressure in an inhomogeneous shell (with the variable modulus of elasticity) to the corresponding pressure in a homogeneous shell) is introduced in this paper. We use the criterion of strength as given by Batrakov [2] and the model of Karpenko [5] for analysis of the corresponding shells. The coefficient β for different compositions of concrete and different loading conditions is normally within the interval 1.5–2.6.

2 Ideas

Fig. 1 shows a cross section of a thick-walled cylindrical shell, loaded inside with constant pressure p_a (fig. 1,*a*). For a homogeneous material (shown by dotted lines in fig. 1,*b*) the stress σ_θ reaches a maximum near the inner contour of the cylinder (fig. 1,*c*), and for a heterogeneous material (solid line), where $E = E(r)$, the diagram σ_θ aligns more closely to the constant value. The idea of the method of optimizing in the strength of the thick-walled shells consists in the creation of such shells from heterogeneous materials. For this purpose we solve the inverse problem of elasticity of inhomogeneous bodies for the respective shell. The essence of the inverse problem is the following. Assuming that for all points of the shell the equivalent stress σ_0, corresponding to a particular theory of strength, is constant, we can define the proper function $E(r)$. This shell is called an equal-stress shell.

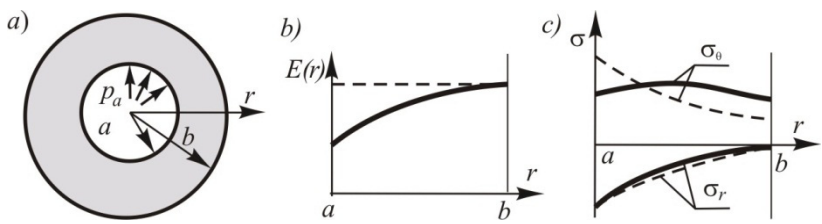

Figure 1: Stress state in a thick-walled cylinder under the action of internal pressure. —— nonhomogeneous material, - - - - homogeneous material.

3 The solutions of inverse problems for a thick-walled cylinder for two classical theories of strength

Below for example are the solutions of inverse problems for maximum shear theory and maximum-strain-energy theory.

3.1 The basic equations

The solution of the direct problem of the theory of elasticity of inhomogeneous bodies in cylindrical coordinates with axial symmetry is reduced to a differential equation [1]

$$\sigma_r'' + \left(\frac{3}{r} - \frac{E'}{E}\right)\sigma_r' - \frac{1-\nu}{r}\cdot\frac{E'}{E}\sigma_r = 0 \tag{1}$$

Here the modulus of elasticity *E=E(r).* The essence of the direct problem is to determine the stress state at a known function of *E(r)*. As mentioned above, the essence of solving the inverse problem is to determine the function *E(r)* in which the equivalent stress σ_0 (for each theory of strength its own) will be constant throughout the structure. We consider a thick-walled cylindrical shell, where the inner radius is equal to *a* and the external radius is equal to *b*, with the loaded constant internal (p_a) and external (p_b) pressures. In this case, the boundary conditions have the form:

$$r = a, \quad \sigma_r = -p_a; \qquad r = b, \quad \sigma_r = -p_b. \tag{2}$$

3.2 Maximum shear theory

3.2.1 Option 1

If circumferential stresses $\sigma_\theta > 0$ the principal stresses are defined as follows: $\sigma_1 = \sigma_\theta$, $\sigma_2 = \sigma_z = \nu(\sigma_r + \sigma_\theta)$ and $\sigma_3 = \sigma_r$. In view of this condition the equal-stress state is written in the form $\sigma_\theta - \sigma_r = \sigma_0 = const$. Substituting this into the equilibrium equation

$$\frac{d\sigma_r}{dr} + \frac{\sigma_r - \sigma_\theta}{r} = 0, \tag{3}$$

we obtain

$$\sigma_r' = \frac{\sigma_0}{r} \tag{4}$$

The solution of this differential equation is a function

$$\sigma_r = \sigma_0 \ln r + A \tag{5}$$

From the boundary conditions (2) we find the constants A and σ_0:

$$A = \frac{p_b \ln a - p_a \ln b}{\ln b - \ln a}; \quad \sigma_0 = \frac{p_a - p_b}{\ln b - \ln a} \tag{6}$$

From eqn (3) we obtain an expression for σ_θ:

$$\sigma_\theta = \sigma_0(1 + \ln r) + A \tag{7}$$

Substituting (5) in eqn (1), we obtain the equation for modulus $E(r)$:

$$E' - \frac{2\sigma_0}{r[\sigma_0(1 + k\cdot\ln r) + A\cdot k]}\cdot E = 0 \tag{8}$$

where $k = (1-2\nu)/(1-\nu)$.

After separation of variables in eqn (8), integrating and using the initial condition ($r = a$; $E = E_0$), we obtain the relationship $E(r)$:

$$E(r) = E_0 \left[\frac{(p_a - p_b)(1 + k \ln r) + k(p_b \ln a - p_a \ln b)}{(p_a - p_b)(1 + k \ln a) + k(p_b \ln a - p_a \ln b)} \right]^{\frac{2}{k}}. \quad (9)$$

3.2.2 Option 2

Under the action in the circumferential direction $\sigma_\theta < 0$ the principal stresses are equal: $\sigma_1 = \sigma_r$, $\sigma_2 = \sigma_z = \nu(\sigma_r + \sigma_\theta)$ and $\sigma_3 = \sigma_\theta$. With this in mind the equal-stress condition takes the form $\sigma_r - \sigma_\theta = \sigma_0 = const$. In this case we obtain a solution that coincides with the solution given in Option 1.

3.2.3 Option 3

Under the action in the circumferential direction $\sigma_\theta < 0$ the principal stresses can be determined also as follows: $\sigma_1 = \sigma_z = \nu(\sigma_r + \sigma_\theta)$, $\sigma_2 = \sigma_r$ and $\sigma_3 = \sigma_\theta$. With this in mind the equal-stress condition after some changing is the form: $[(1-k)\sigma_r - \sigma_\theta]/(2-k) = \sigma_0 = const$. Expressing from this equality σ_θ and substituting it into the equilibrium eqn (3), we obtain

$$\sigma_r' + k\frac{\sigma_r}{r} = -(2-k)\cdot\frac{\sigma_0}{r} \quad (10)$$

The solution of this differential equation is the function:

$$\sigma_r = \frac{A \cdot r^{-k} - (2-k)\sigma_0}{k} \quad (11)$$

We can define constants A and σ_0 using the boundary conditions (2):

$$A = k \cdot \frac{p_a - p_b}{b^{-k} - a^{-k}}; \quad \sigma_0 = \frac{k}{2-k} \cdot \frac{p_a b^{-k} - p_b a^{-k}}{b^{-k} - a^{-k}} \quad (12)$$

Substituting the stress (11) into the resolving eqn (1) we obtain a homogeneous linear differential equation for the distribution of the modulus of elasticity:

$$E' - \frac{A}{\sigma_0} \cdot r^{-(k+1)} \cdot E = 0 \quad (13)$$

After integrating eqn (13), with the condition ($r = a$; $E = E_0$) we obtain the dependence $E(r)$:

$$E(r) = E_0 \exp\left[-\frac{A}{k\sigma_0} \cdot \left(r^{-k} - a^{-k} \right) \right] \quad (14)$$

In fig. 2 diagrams of the dependence $E(r)$ are presented that are calculated using the values: $\nu_1 = 0.1$, $\nu_2 = 0.25$, $\nu_3 = 0.4$, $b/a = 2$, $p_a = 6$ MPa, $p_b = 12$ MPa.

For values of Poisson's ratio $\nu_1 = 0.1$ and $\nu_2 = 0.25$ the dependence $E(r)$ is determined by solving the optimization problem for a cylinder corresponding to option 3, since the stress relation to this variant is $\sigma_z > \sigma_r > \sigma_\theta$. However, for the value $\nu_3 = 0.4$ the solution of the optimization problem for a cylinder corresponds to option 1, since the stress relation to that decision has $\sigma_r > \sigma_z > \sigma_\theta$, taking into account amendments to the sign of the equivalent stress. As follows from fig. 2 the influence of Poisson's ratio for the distribution function $E(r)$ is significant. In fig. 3 as an example the distribution of stresses in the inhomogeneous (equal-stress) cylinder in the case $\nu_2 = 0.25$ is shown, as well as that in a homogeneous cylinder with the same sizes and loads.

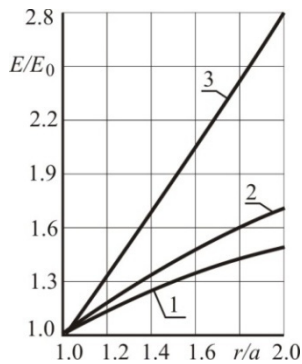

Figure 2: Distribution of the modulus of elasticity in the equal-stress cylinder. 1 – ν=0.1, 2 – ν=0.25, 3 – ν=0.4

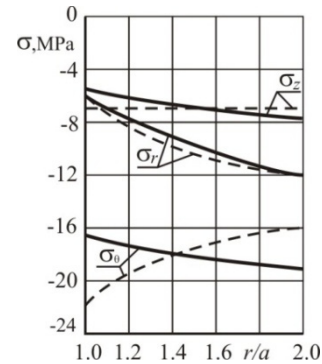

Figure 3: Stress diagrams in the equal-stress cylinder. —— nonhomogeneous material, - - - homogeneous material

Once again we will underline that the equivalent stress σ_0 at all points of the cylinder is the same. Thus, we have found the model of the equal-stress structure. However, such a cylinder is not equal-strength. To learn how to get the model of the equal-strength cylinder we will discuss things further.

3.3 Maximum-strain-energy theory

The fourth theory of strength in the coordinate system σ_1, σ_2 and σ_3 represents the surface of a circular cylinder

$$\sigma_1^2 + \sigma_2^2 + \sigma_3^2 - (\sigma_1\sigma_2 + \sigma_2\sigma_3 + \sigma_3\sigma_1) = \sigma_0^2 \qquad (15)$$

So depending on what type of structure (disk or cylinder) is calculated, the configuration of the surface determining the strength of the material of the

structure will vary. Therefore, to best present the whole picture it is useful to consider separately the calculation of the disk and the cylinder. Below we consider the construction of the equal-stress model of the cylinder.

The principal stresses in this case are defined by: $\sigma_1 = \sigma_z = \nu(\sigma_r + \sigma_\theta)$, $\sigma_2 = \sigma_r$ and $\sigma_3 = \sigma_\theta$. In view of this condition of equal-strength (15) can be rewritten as

$$\left(1-\nu+\nu^2\right)\sigma_r^2 - \left(1+2\nu-2\nu^2\right)\sigma_r\sigma_\theta + \left(1-\nu+\nu^2\right)\sigma_\theta^2 = \sigma_0^2 = const \qquad (16)$$

The eqn (16) describes an ellipse, so the solution is a necessary search using parametric expressions for the stresses:

$$\sigma_r = \sigma_0\left(\frac{2-k}{k}\sin\varphi - \frac{1}{\sqrt{3}}\cos\varphi\right), \quad \sigma_\theta = \sigma_0\left(\frac{2-k}{k}\sin\varphi + \frac{1}{\sqrt{3}}\cos\varphi\right) \qquad (17)$$

Substituting into the equilibrium eqn (1) the expression (17), we obtain

$$\frac{dr}{d\varphi} - r\cdot\left(\frac{\sqrt{3}}{2}\cdot\frac{2-k}{k} + \frac{1}{2}\operatorname{tg}\varphi\right) = 0 \qquad (18)$$

The solution of this differential equation is a function

$$r = A\exp\left(\frac{\sqrt{3}}{2}\cdot\frac{2-k}{k}\varphi\right)\Big/\sqrt{\cos\varphi} \qquad (19)$$

The constants A, σ_0 and the parameters φ_a, φ_b are defined in the general case numerically, using the boundary conditions (2). Substituting the stress σ_r from (17) and the expression for the coordinate r from (19) into the resolving eqn (1), after transformations we obtain an equation for determining the distribution of the modulus of elasticity $E(\varphi)$:

$$\frac{dE}{d\varphi} - \frac{2\sqrt{3}}{k}\cdot\frac{\cos\varphi}{\sqrt{3}\sin\varphi+\cos\varphi}\cdot E = 0 \qquad (20)$$

After separation of variables in eqn (20) and integrating with the initial condition ($\varphi = \varphi_a$; $E = E_0$), we find the function $E(\varphi)$:

$$E(\varphi) = C\exp\left(\frac{\sqrt{3}}{2k}\varphi\right)\left(\sqrt{3}\sin\varphi+\cos\varphi\right)^\alpha \qquad (21)$$

where

$$\alpha = \frac{3}{2k}; \quad C = E_0\left[\exp\left(\frac{\sqrt{3}}{2k}\varphi_a\right)\left(\sqrt{3}\sin\varphi_a+\cos\varphi_a\right)^\alpha\right]^{-1}.$$

Given that the parameter k depends on ν on the basis of expression (21), we can investigate the effect of Poisson's ratio on the character of the distribution

function $E(r)$. As a result of the calculation solutions were obtained which differ from those shown in fig. 2 by no more than 5%. Stress distributions in a nonhomogeneous structure for this theory of strength show similar curves to those in fig. 3.

This is not surprising since, as we know, the results of the strength of the maximum shear theory and the maximum-strain-energy theory in all problems of theory of elasticity do not give a contrast of more than 14%.

Summarizing the results obtained in section 3.3, it is possible to draw the following conclusions. Creating equal stress thick-walled shells is possible by changing the modulus of elasticity of the material. Thus, the received solutions can be applied to materials for which it should be possible to make modifications of the modulus of elasticity of materials. Such materials include fiberglass, polymers and other composites.

4 From equal-stress to equal-strength structures

4.1 Some mechanical properties of concrete

In order to build a model equal-strength structure it is necessary that with a change of structure of the material its strength changes more slowly than the modulus of elasticity. An example would be modified cement concrete. Table 1 presents the main characteristics of this concrete [2]. Another example is polymer concrete filled silica flour [3] (see Table 2). It is evident that in these materials with a significant change in modulus of elasticity the strength varies slightly.

Table 1: Mechanical properties of concrete with the addition of microsilica.

№	Quantity microsilica in the concrete mix, kg/m^3	Prizm strength R_b, MPa	Elasticity modulus E_b, 10^{-4} MPa
1	-	42,5	3,62
2	116	44,0	3,01
3	142	38,0	2,16

Table 2: Mechanical properties of polymer concrete filled silica flour.

№	Level of filling silica flour	Prizm strength R_b, MPa	Elasticity modulus E_b, 10^{-4} MPa
1	-	142	3,10
2	50	146	4,50
3	100	160	7,10
4	200	148	10,5
5	300	132	13,7

For the correlation of strength and stiffness properties of the material the dependence $R = f(E)$ is introduced which allows agreement amongst themselves of the strength and deformation characteristics of the material. This function approximates the experimental data for the selected material. Using this dependence, we can solve the inverse problem to model the equal-strength structure. Nevertheless the structure may not be equal-stress, but the condition of equal-strength is ensured by the equality of the equivalent stress σ_0 at each point of the body to the strength of the material R at this point.

4.2 The inverse problem for an equal-strength cylinder

This section describes the method of optimization of a cylindrical thick-walled shell of polymer-concrete based on the criterion of the strength of P. Balandin. This condition is confirmed experimentally for concrete in the field of all-round non-uniform compression [4]. The strength condition of P. Balandin in the coordinate system σ_1, σ_2 and σ_3 represents the surface of a paraboloid of revolution. Given the fact that the compressive stresses are contained within it with a minus sign, this expression is written as follows

$$\sigma_1^2 + \sigma_2^2 + \sigma_3^2 - (\sigma_1\sigma_2 + \sigma_2\sigma_3 + \sigma_3\sigma_1) + (R_b - R_{bt})(\sigma_1 + \sigma_2 + \sigma_3) = R_b R_{bt}, \quad (22)$$

where R_b is the design strength of concrete under axial compression (prism strength), and R_{bt} is the design strength of concrete under axial tension. Since the concrete works poorly in tension it is possible to put $R_{bt} = 0$ in (22). The application of this provision greatly simplifies the solution of the optimization problem. With this simplification expression (22) can be rewritten as:

$$\sigma_1^2 + \sigma_2^2 + \sigma_3^2 - (\sigma_1\sigma_2 + \sigma_2\sigma_3 + \sigma_3\sigma_1) + R_b(\sigma_1 + \sigma_2 + \sigma_3) = 0 \quad (23)$$

In concrete, as follows from [5], in the limit state under the action of compressive stresses Poisson's ratio can reach values close to 0.5. Therefore, for further calculations we take $\nu = 0{,}5$. Assuming that the cylinder is in the plane strain conditions, the principal stresses can be determined as follows: $\sigma_1 = \sigma_z = \nu(\sigma_r + \sigma_\theta)$, $\sigma_2 = \sigma_r$ and $\sigma_3 = \sigma_\theta$. With this in mind, the strength condition (23) takes the form:

$$0.75(\sigma_r)^2 - 1.5\sigma_r\sigma_\theta + 0.75(\sigma_\theta)^2 + 1.5R_b(\sigma_r + \sigma_\theta) = 0 \quad (24)$$

Eqn (24) describes a parabola in the implicit form, so the solutions need to be presented as a parametrical expression for the stresses σ_r and σ_θ [6]:

$$\sigma_r = -R_b(-0.5\varphi + 0.25\varphi^2), \quad \sigma_\theta = -R_b(0.5\varphi + 0.25\varphi^2). \quad (25)$$

The relationship between the strength and the rigidity properties of the material is given by

$$R_b = \rho + \omega E_b \tag{26}$$

where the coefficients ρ and ω are determined on the basis of experimental data. In solving the problem, we use the condition that the Poisson's ratio $\nu = 0{,}5$. From this it follows that in the plane strain condition

$$\varepsilon_r = -\varepsilon_\theta \tag{27}$$

Substituting (27) into the condition of compatibility of the strain components, we obtain the equation

$$\frac{d\varepsilon_\theta}{dr} + 2\frac{\varepsilon_\theta}{r} = 0 \tag{28}$$

The solution of eqn (28) is the expression

$$\varepsilon_\theta = \frac{\varepsilon_0}{r^2} \tag{29}$$

where ε_0 remains unknown.

To obtain the dependence of the modulus of elasticity of concrete E_b from the radius we will use the expression for the strain ε_θ

$$\varepsilon_\theta = \frac{1}{E_b} \cdot \left[(1-\nu)\sigma_\theta - \nu\sigma_r\right] \tag{30}$$

Substituting into (30) the value of Poisson's ratio $\nu = 0.5$, and the expression (29), (25) and (26), after transformations we obtain

$$E_b = \frac{\rho(1-2\varphi)r^3(\varphi)}{4\varepsilon_0 - \omega(1-2\varphi)\cdot r^3(\varphi)} \tag{31}$$

Substituting (26) and (31) into eqns (17), we obtain expressions for the stresses in terms of the parameter φ

$$\sigma_r = \frac{\rho\varepsilon_0\left(-5+12\varphi-4\varphi^2\right)}{3\left(4\varepsilon_0 - \omega(1-2\varphi)\cdot r^3(\varphi)\right)}, \quad \sigma_\theta = \frac{\rho\varepsilon_0\left(1-4\varphi^2\right)}{3\left(4\varepsilon_0 - \omega(1-2\varphi)\cdot r^3(\varphi)\right)}. \tag{32}$$

After substituting (32) in the equilibrium eqn (3) after transformations we obtain the nonlinear differential equation

$$\frac{dr}{d\varphi} = \frac{2}{3}\cdot\frac{8\varepsilon_0(3-2\varphi)r - \omega(1-2\varphi)^2 r^4}{(1-2\varphi)\left(16\varepsilon_0 + \omega(1-2\varphi)^2 r^3\right)} \tag{33}$$

where ε_0 is a constant defined by the expression

$$\varepsilon_0 = \frac{R_b^{(0)}}{4E_b^{(0)}}(1-2\varphi_a)a^3 \tag{34}$$

Here φ_a, $R_b^{(0)}$ and $E_b^{(0)}$ are the initial (at $r = a$) values of the parameter φ, the design strength of concrete under axial compression and the modulus of elasticity of concrete. Equality (34) is obtained by substituting the following quantities into (30):

$$\nu = 0.5\,,\ \varepsilon_\theta = \frac{\varepsilon_0}{a^3}\,,\ E_b = E_b^{(0)},$$

$$\sigma_r = \frac{R_b^{(0)}}{12}\left(-5 + 12\varphi_a - 4\varphi_a^2\right),\ \sigma_\theta = \frac{R_b^{(0)}}{12}\left(1 - 4\varphi_a^2\right) \tag{35}$$

To solve eqn (33) used the Runge-Kutta fourth order method.

4.3 Calculation example

Below, the solution for the thick-walled cylinder using the method given above on the basis of V. Paturoyev's experimental data [3] is presented.

The calculation was carried out using the following basic data: $E_b^{(0)} = 3.1\times10^4$ MPa, $R_b^{(0)} = 141.0$ MPa, $p_a/p_b = 1.5$, $b/a = 1.6$, $\nu = 0.5$. To determine the coefficients in the formula (26), we applied the standard mathematical functions of MathCAD 13, so therefore we obtained the following values: $\rho = 126.7$ MPa and $\omega = 4.6\cdot10^{-4}$.

For the first three lines of tab. 2. Fig. 4 shows the approximating dependence for polymer-concrete as well as the experimental points for which it is built.

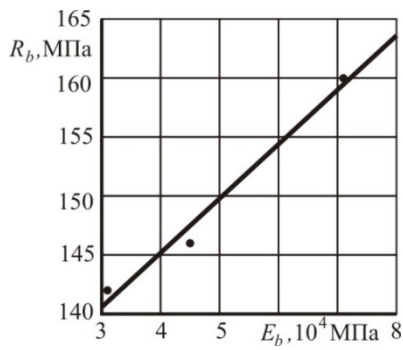

Figure 4: The relationship between strength and modulus of elasticity of polymer-concrete.

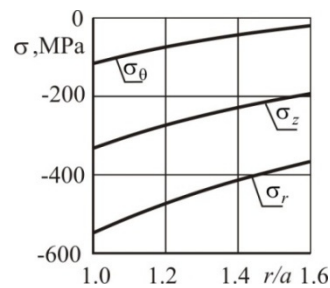

Figure 5: Stresses in an equal-strength polymer-concrete cylinder.

The solution of (33) is obtained by the Runge-Kutta fourth order method for the initial value of the argument $\varphi_a = -3.071$. The final value of the argument $\varphi_b = -2.222$. The values of the pressures on the cylinder are: $p_a = 549.1$ MPa

and $p_b = 366.0$ MPa respectively. The value of pressure p_a is found as follows. In the expression for the normal radial stress from (32) we substitute the values of the constants ρ and ω, the value of the parameter $\varphi = \varphi_a$, and also the value $r = a$. As a result we find $\sigma_r(r = a) = -549.1$ MPa. Using the first of relations (2) we find the value p_a specified above. The pressure p_b equals 1.5 p_a.

Stresses σ_r, σ_θ and σ_z are shown in fig. 5. The resulting load in the equal-strength cylinder can be compared with the load for a homogeneous structure. By condition (24) the greatest equivalent stress is reached at an inner surface of the cylinder. For a homogeneous structure the value of the internal pressure p_a^{hom} can be found by the formula

$$p_a^{hom} = -\frac{2R_b^{(0)}(s_r + s_\theta)}{(s_r - s_\theta)^2} \tag{36}$$

where $s_r = -1$ and $R_b^{(0)}$ is the value of the design strength of polymer-concrete at the point where $r = a$, $s_\theta = \left(b^2 + a^2 - 2b^2\left(p_b / p_a\right)\right) / \left(b^2 - a^2\right)$. The expression (36) is obtained as follows. We denote the stresses in the homogeneous cylinder as

$$\sigma_r = p_a^{hom} s_r \,;\; \sigma_\theta = p_a^{hom} s_\theta \tag{37}$$

where functions s_r and s_θ are obtained by solving the Lame problem for a thick-walled cylinder under boundary conditions

$$r = a,\;\; s_r = -1; \qquad r = b,\;\; s_\theta = -d. \tag{38}$$

Here d is the ratio of the external pressure to the value of internal pressure. The design strength is assumed to be constant

$$R_b = R_b^{(0)}. \tag{39}$$

After substituting expressions (37) and (38) into eqn (24) we can find the pressure p_a^{hom}.

Calculation by formula (36) gives the pressure p_a^{hom} =213.5MPa. Above, we have determined the limit load for the equal-strength inhomogeneous structure p_a^{inh} =549.1MPa. To determine the effect of the optimized model of the inhomogeneous equal-strength structure we introduce the efficiency ratio $\beta = p_a^{inh}/p_a^{hom}$, which shows how many times the external loads on the body can be increased, in comparison with the homogeneous analogue. For the equal-strength cylinder considered in this section β=2.57.

4.4 From the model to the structure

Creating a thick-walled cylinder where the modulus of elasticity varies along the radius by a continuous law is rather difficult.

One way of solving the direct problems of the theory of elasticity of inhomogeneous bodies is to replace the continuous function $E(r)$ with a piecewise-homogeneous function. By analogy, the creation of optimized thick-walled cylinders consisting of several layers is proposed. Thus the modulus of elasticity of the material in each layer is determined by solving the inverse problem given above in which the continuous function $E(r)$ is defined.

The solution of the problem for the multilayered cylinder is rather simple. In each layer it corresponds to the solution of a Lame problem, and for definition of the constants the boundary conditions (2) and the conditions of ideal contact on boundaries between layers are used:

$$u_i = u_{i+1}; \quad \sigma_{r,i} = \sigma_{r,i+1} \tag{40}$$

where i is the layer number, u is the radial displacement, and σ_r is the radial stress. One of the fundamental questions is – how to choose the value of E_i in the i-th layer. As shown in the analysis, in order to satisfy the condition of strength (23) at all points of the layer it is necessary that E_i is equal to the value of $E(r)$ at the left edge of the layer.

Stresses σ_r, σ_θ and σ_z for a three-layered cylinder are shown in fig. 6 and diagrams of equivalent stresses are given in fig. 7.

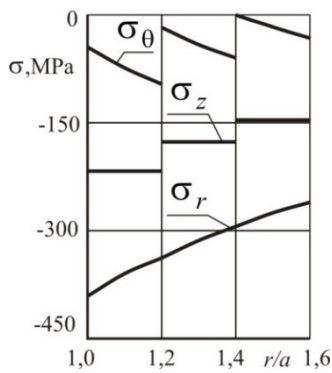

Figure 6: Stress distribution in a three-layer cylinder.

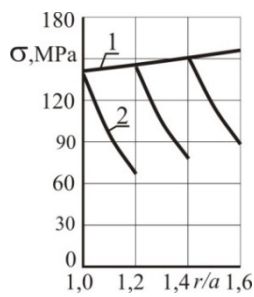

Figure 7: Strength R_b (1) and equivalent stress (2) in a three-layer cylinder.

Let us compare the resulting load on the piecewise-homogeneous cylinder with a load for a homogeneous structure. Using (36), we can find the value of internal pressure: p_a^{hom} =213.5MPa. Comparing this pressure with the load for a piecewise-homogeneous cylinder ($p_a = p_a^{(3)} = = -\sigma_r(r=a) = 391.5$ MPa) we obtain the value of the coefficient effectiveness: $\beta = p_a^{(3)}/p_a^{hom}$ =1.83.

Similar calculations for the cylinder, consisting of four and five layers, give the following results: $\beta = p_a^{(4)}/p_a^{hom} = 1.99$, $\beta = p_a^{(5)}/p_a^{hom} = 2.09$.

It is obvious that with increasing number of layers in the cylinder the coefficient β will be close to the value β = 2.57, which corresponds to a model with continuous heterogeneity. Thus the developed multilayer structures can be called *close to equal strength*.

5 Conclusions

In this paper based on solving the inverse problem of elasticity theory of inhomogeneous bodies we have developed a method of changing the definition of the modulus of elasticity along the radius at which the equivalent stress in a thick-walled cylinder at each point is equal to the strength of the material. This cylinder is an equal-strength structure. Since in practice to create such a cylinder is hard enough, we propose the construction of multi-layer structures, in which the modulus of elasticity in each layer is determined by solving the inverse problem. This cylinder is close to being an equal-strength structure.

Generally, such shells may be formed from various materials (concrete or reinforced concrete, steels, polymers, etc.). Practical applications of these shells will be the result of collaborative work of specialists in mechanics, chemists and technologists.

References

[1] Andreev V.I., *Nekotoryje zadachi i metody mehaniki neodnorodnyh tel*, Izdat. ASV: Moscow, 2002.
[2] Batrakov V.G., *Modificirovannyje betony. Teorija i praktika*, 2 Issue: Moscow, 1998.
[3] Paturojev V.V., *Polimerbeton*, Strojizdat: Moscow, 1987.
[4] Genijev G.A. and Kissuk V.N., K voprosu obobshchenija teorii prochnosti betona. *Beton i zhelezobeton*, **2,** pp. 16-19, 1965.
[5] Karpenko N.I., *Obshchie modeli mehaniki zhelezobetona.* Strojizdat: Moscow, 1996.
[6] Kamke E., *Differentialgleichungen*. Leipzig, 1959.

This page intentionally left blank

Performance based design of masonry infilled reinforced concrete frames for near-field earthquakes

A. Madan[1], D. Das[2] & A. Hashmi[3]
[1]*Department of Civil Engineering, Indian Institute of Technology, New Delhi, India*
[2]*Department of Civil Engineering, Durgapur, India*
[3]*Structural Engineer, Gulf Region*

Abstract

Performance Based Design (PBD) is an iterative exercise in which a preliminary trial design of the building structure is selected and if the selected trial design of the building structure does not conform to the desired performance objective, the trial design is revised. In this context, development of a fundamental approach for performance based seismic design of masonry infilled frames with minimum number of trials is an important objective. The paper presents a plastic design procedure based on the energy balance concept for PBD design of multi-story multi-bay masonry infilled reinforced concrete (R/C) frames subjected to near-field earthquakes. The proposed energy based plastic design procedure was implemented for trial performance based seismic design of representative masonry infilled reinforced concrete frames with various practically relevant distributions of masonry infill panels over the frame elevation. Non-linear dynamic analyses of the trial PBD of masonry infilled R/C frames was performed under the action of near-field earthquake ground motions. The results of non-linear dynamic analyses demonstrate that the proposed energy method is effective for performance based design of masonry infilled R/C frames under near-field as well as far-field earthquakes.
Keywords: masonry infilled frame, energy methods, near-fault ground motions, pushover analysis, nonlinear dynamic analysis, seismic demand.

WIT Transactions on The Built Environment, Vol 125,
www.witpress.com, ISSN 1743-3509 (on-line)
doi:10.2495/OP120181

1 Introduction

In the recent past, near-field earthquake ground motions with large velocity pulses have caused extensive damage to civil engineering structures. Unlike far-field earthquake ground motion records a ground motion recorded in the near-field region of a strike-slip earthquake (i.e., near the fault rupture of the earthquake) exhibits distinctive short duration long period velocity pulses with large peak ground velocities and accelerations [1, 2]. The force based design methodology followed by the current seismic design codes may be inherently deficient in ensuring the safety of building structures in such cases. In case of a masonry infilled reinforced concrete (R/C) framed building with an irregular distribution of masonry panels over the frame elevation, the seismic vulnerability of the building in the event of near-field earthquakes would be further multiplied.

2 Research significance

A review of literature on performance-based seismic engineering (PBSE) of building structures indicates that there is no reported research study on performance based design of masonry infilled reinforced concrete (R/C) frames using the energy approach. Moreover, none of the reported research studies on PBD of moment resisting frames using energy methods focus on the seismic performance of the frame under the action of near-field earthquakes. The paper presents an energy method for PBD of masonry infilled R/C frames subjected to near field earthquakes considering the commonly encountered seismically vulnerable distributions of masonry infill panels over the frame elevation, such as those in which the infill panels are discontinued at the ground level for functional purposes (e.g. providing parking spaces at the ground level) thus resulting in a 'soft story' at that level. One of the objectives of the study is to demonstrate the efficacy of the proposed energy method for PBD of masonry infilled R/C frames under the action of near-field as well as far-field earthquakes considering the influence of the distribution of masonry infill panels over the frame elevation on the seismic vulnerability of the frame.

3 Plastic design of multi-story multi-bay masonry infilled R/C frames based on energy balance concept

Based on the energy balance formulations available in literature [3–7], a plastic design procedure is proposed in the present study for the above mentioned PBD. The proposed plastic design procedure using the energy balance concept is based on the following additional assumptions:
(i) The plasticity in the R/C frame elements is assumed to be concentrated at the plastic hinges for purposes of arriving at the first trial performance based design.

(ii) The global yield mechanism of the multi-story multi-bay frame shown in Figure 1 (a) that is selected for the formulation of the plastic design procedure is the dominant plastic collapse mode of the masonry infilled R/C frame. The assumption is realistic if the transverse shear reinforcement in the R/C frame is designed and detailed to prevent shear failure of the R/C frame elements due to concentrated shear forces induced by the infill panels at the frame-infill interface, particularly near the beam-column joints.
(iii) The stiffness degradation, strength deterioration and hysteretic energy dissipation in the infill panels under cyclic load reversals during the earthquake may be neglected in the energy based plastic design. The assumption should result in conservative design since the lateral strength of the masonry infills is neglected in the plastic design process while the lateral stiffness and yield deformation of the masonry infilled R/C frame is considered in the proposed methodology taking into account the structural contribution of masonry infills.

For purposes of deriving the design input seismic energy as provided by Housner [4], the design pseudo-velocity (PSV) spectrum can be obtained [Figure 1(b)] using the elastic design pseudo-acceleration (PSA) spectrum provided by the seismic design codes as follows:

$$S_v = \frac{T}{2\pi} ag \tag{1}$$

where, T is the fundamental time period, g is acceleration due to gravity and a is the peak PSA, normalized with respect to g, which can be obtained from the elastic design PSA spectrum of the Indian seismic design code [8].

The design seismic base shear and earthquake forces at various levels are obtained using equations available in literature [5, 6], based on the assumption that the selected global yield mechanism shown in Figure 1(a) is maintained during the entire earthquake excitation. For the selected global yield mechanism [Figure 1(a)], the assumption may be explicitly incorporated in the design process by rewriting the equilibrium equation for the frame as follows:

$$\sum_{i=1}^{n} F_i h_i = \sum_{i=1}^{n} 2 n_b \beta_i M_{pbr} + (n_b + 1) M_{pc} \tag{2}$$

where, in this case, F_i is the design earthquake force at level i evaluated (as explained earlier), n_b is the number of bays, M_{pbr} is the common reference plastic moment for beams, β_i is a factor for proportioning the beam strength at level i, M_{pc} is the plastic moment of the columns at the base.

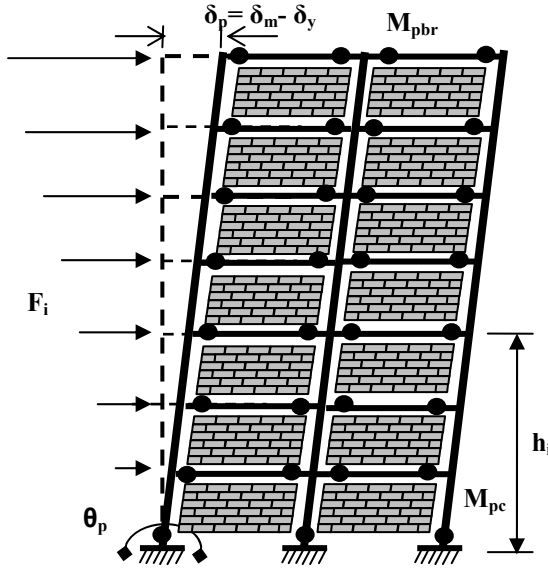

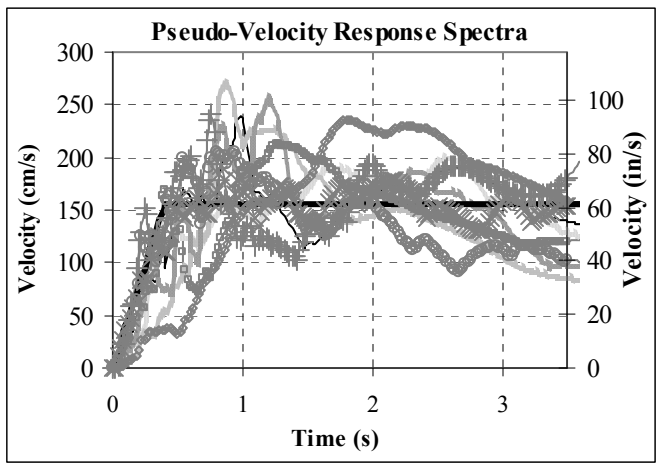

(b)

Figure 1: Key components of the energy balance concept: (a) multi bay frame with selected global plastic mechanism and (b) pseudo-velocity response spectra of the scaled earthquake ground motion records and design response spectrum.

The beam proportioning factors β_i in Equation (2) represents the ratio of the plastic moment capacity of beams at level i to a reference plastic moment M_{pbr} for the beams. Assuming suitable values of the proportioning factors β_i and the plastic moment M_{pc} of the columns at the base, Equation (2) can be solved to determine the common reference plastic moment M_{pbr} for the beams, the only unknown variable in the equation. The methodology proposed by Leelataviwat *et al*. [3] was used in the present study to select the beam proportioning factors β_i and the plastic moment M_{pc} of the columns in Equation (2).

4 Performance based seismic design of masonry infilled R/C frames using the energy approach

The proposed method was implemented for trial PBD of multi-story multi-bay frames considering the representative frame geometries as shown and explained in Table 1. For purposes of comparison, the frames are also designed in compliance with the prevalent code-specified force based design criteria.

4.1 Estimation of yield drifts of masonry infilled R/C frames for energy based plastic design

The proposed energy approach requires estimation of the yield drifts of the frames, since the yield drift of the frame equals the maximum elastic rotation for the yield mechanism of the frame. The yield drifts were estimated in the present study by performing a non-linear pushover analysis of the code-compliant designs of the infilled frames. The R/C frame with the representative geometry [Table 1] was designed in compliance with the force based design criteria specified by the current Indian seismic design code [8] for the various practically relevant distributions of masonry infill panels over the frame elevation. Figure 2(a) presents the design dimensions and reinforcement details of the code-compliant R/C frame.

Force-controlled non-linear static analysis (pushover analysis) of the code-compliant designs of masonry infilled R/C frames was performed by applying an incrementally increasing inverted triangular (linear) variation of lateral story forces considering the structural contribution of the masonry infill panels. The pushover analysis is based on rational and realistic non-linear macro-element models for the frame elements and masonry infills [9, 10]. Figure 2(b) illustrates the inelastic static lateral force-displacement response determined from the non-linear pushover analysis of the R/C frame for the different distributions of masonry infill. It may be noted that the lateral force and displacement in the plot are normalized with respect to the weight and height, respectively, of the frame, thus resulting in a plot of the horizontal seismic base shear coefficient versus the normalized top drift of the structure. The figure also shows the idealized trilinear capacity curves of the R/C frame for the different distribution of masonry infills. The point of initiation of the last linear branch of the idealized curves is

identified as the yield point and the corresponding deformation as the normalized yield deformation or the yield drift of the frame. It is apparent from Figure 2(b) that the distribution of masonry infill panels over the frame elevation significantly influences the yield drift of the R/C frame. It can be observed from the figure that the different distributions of masonry infill panels over the frame elevation considered in the present study may be ranked in the decreasing order of yield drift as: (i) bare frame (ii) masonry infilled frame with no infills at the ground level (iii) masonry infill frame with partially infilled ground story (iv) completely infilled frame.

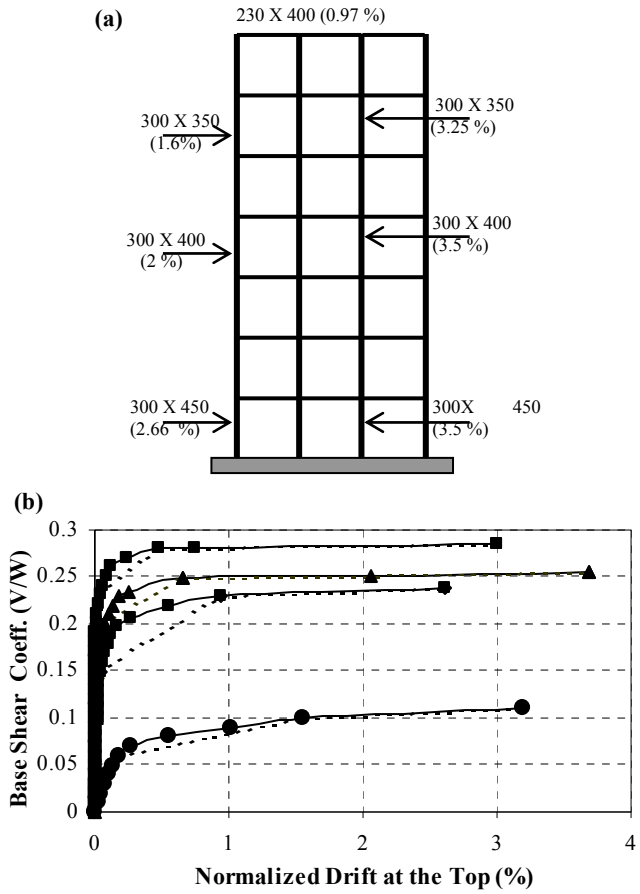

Figure 2: Design dimensions and details and capacity curves of code compliant r/c frame: (a) dimensions and reinforcement details of the code-compliant r/c frame and (b) capacity curves for the code-compliant masonry infilled r/c frames.

Table 1: Design Variables Computed in Course of the Proposed Energy Based Plastic Design Procedure for a Trial Performance Based Design of the Masonry Infilled R/C Frames with Target Drift of 2%.

Schematics of the Frame Elevation	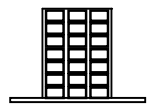			
Distribution of masonry in fill panels	Bare Frame	Infilled Frame without Infill Panels in the First Story	Infilled Frame with Partially Infilled First Story	Completely Infilled Frame
Assumed Elastic Rotation, Φ_e% (Yield Drift)	0.85	0.7	0.55	0.4
Structural ductility Factor, μ_s	2.352	2.857	3.636	5.0
Target rotation, Φ_t%	2	2	2	2
Plastic rotation Φ_p%	1.15	1.3	1.45	1.6
Time Period, T	0.735	0.63	0.63	0.63
Ductility Reduction Factor, R_u	2.352	2.85	3.636	5
Modification Factor, γ	0.669	0.577	0.474	0.36
Weight of Structure at any Level i, W_i	234	441	441	441
Shear proportioning Factor, β_i	2.08	2.13	2.13	2.13
Design Base Shear Parameter, α	2.942	4.511	11.97	5.55
Design pseudo-acceleration (g), a	1.359	1.587	1.587	1.587
Base Shear coefficient, V/W	0.372	0.302	0.227	0.158
Base Shear, V, kN (kips)	610 (137.1)	933 (209.6)	701.4 (157.6)	490.2 (110.1)
Plastic moment of column, M_{pc} at base of the structure, kNm (kips-in)	251 (2220.4)	384 (3396.9)	289.4 (2559.7)	202.2 (1788.7)
Reference Plastic Moment of Beam, M_{pbr}, kNm (kips-in)	132.1 (1168.8)	197.0 (1742.7)	148.2 (1310.8)	103.5 (915.6)
Elastic rotation (Yield Drift) computed from Non-linear Pushover Analysis of trial PBD of the Frame	0.88	0.65	0.55	0.51

4.2 Energy based plastic design of the representative multi-story multi-bay masonry infilled R/C frames for target performance levels

In order to validate the proposed PBD methodology using the energy approach, the R/C frame with the representative geometry shown in Figure 2(a) was designed using the proposed energy based plastic design procedure for the different distributions of masonry infill panels mentioned in a previous section. As the design is performance based, selecting a target drift is the foremost step in the design process. The masonry infilled R/C frames were designed for target inter-story drifts of 1%, 2% and 4% corresponding to the immediate occupancy (IO), life safety (LS) and collapse prevention (CP) performance limit states, respectively, in accordance with global acceptance criteria defined by ATC-40 [11] and FEMA-356 [12]. Table 1 summarizes the values of the salient design variables computed using the proposed energy based plastic design procedure for a specified target rotation of 2%. The implementation of the proposed procedure is demonstrated in the present paper by selecting a target drift of 2%.

As mentioned in Table 1, the assumed elastic rotations (i.e. yield drifts) estimated from non-linear pushover analysis are 0.4%, 0.7%, 0.55% and 0.85% for the four different masonry infill panel distributions. The target rotation is specified as 2% for purposes of performance based design. Thus, the plastic rotations are estimated as 1.6%, 1.3%, 1.45% and 1.15% respectively for the four cases, respectively. The structural ductility factor was estimated as the ratio of the ultimate or target rotation to the assumed elastic rotation of the frame. The natural time periods of the masonry infilled R/C frames and bare frame were estimated for the trial performance based design of the masonry infilled R/C frames by modelling the frame structures as equivalent single-degree-of-freedom systems wherein the stiffness of the system is estimated from the idealized trilinear capacity curve of the infilled frame obtained from the pushover analysis. The yield strength reduction factors for the R/C frames are obtained from the structural ductility factors for the corresponding time periods using the relationships proposed by Newmark and Hall [13]. The procedure for calculating the other design variables of the proposed method has been discussed in the earlier sections of the paper. Figure 3 displays the dimensions and reinforcement details of R/C frame elements obtained from the first trial of PBD using the proposed energy approach for a target drift of 2% for the different infill panel distributions

4.3 Nonlinear pushover analysis of the trial performance based designs of masonry infilled R/C frames

Pushover analyses of the PBDs of the infilled frames were performed to verify the elastic rotations (i.e. yield drifts) of the frames that were assumed in the proposed energy based plastic design procedure. The yield drifts computed from the pushover analyses are also mentioned in Table 1. It is evident from the table that the assumed elastic rotations are in close agreement with the computed yield drifts. It is also worthwhile to note that the normalized peak lateral forces for the

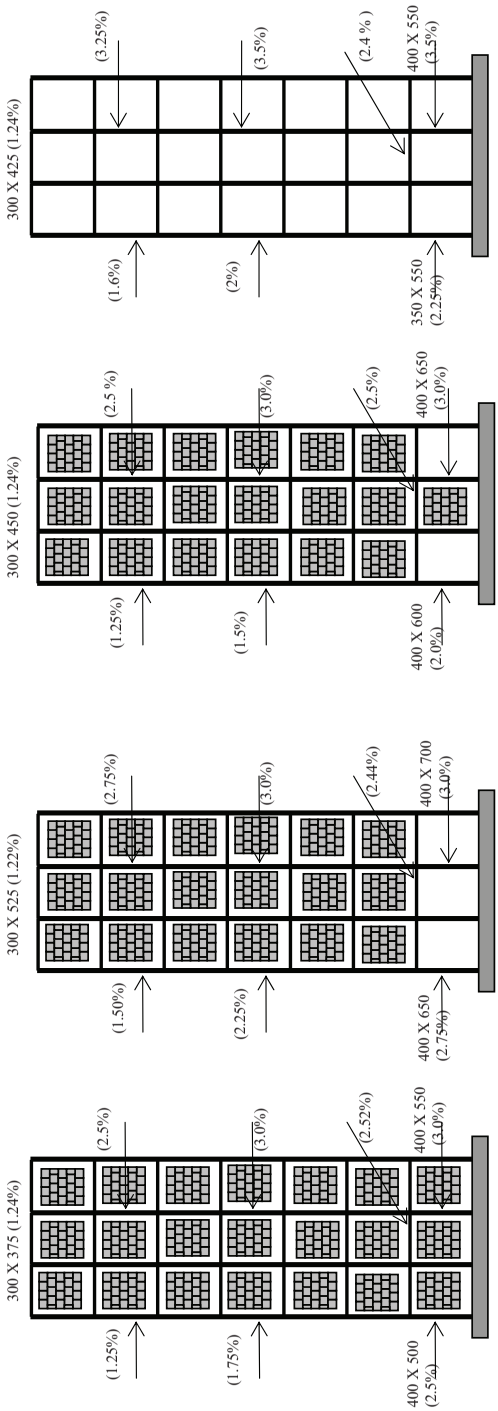

Figure 3: Dimensions and reinforcement details of the r/c frame designed by energy based approach for target drift of 2%.

trial performance based designs of the masonry infilled R/C frames determined from the pushover analyses show reasonably good agreement with the design seismic base shear coefficients obtained from the proposed energy based plastic design procedure.

5 Displacement based seismic analysis of trial performance based designs of masonry infilled R/C frames

In order to evaluate the seismic performance of the frames designed for the different target drift levels using the proposed procedure, non-linear dynamic analyses were performed using rational and realistic hysteretic models of the R/C frame elements and masonry infill panels [10]. The non-linear dynamic analysis was performed using eight recorded earthquake ground acceleration records and one synthetic accelerogram. The recorded earthquake ground motions of Bhuj (India, 2001), El Centro (1940), San Fernando (1971) and Chile (1985) earthquakes considered in the dynamic analysis are far-field ground motions, while the Northridge (1994), Tabas (Iran, 1978), Erzincan (Turkey, 1992) and Chi Chi (Taiwan, 1999) earthquake ground motions are near-field or near-fault ground motions. All the recorded ground motions used for the dynamic analysis were scaled to achieve the same intensity as that of the ideal design level (design basis) earthquake specified by the current Indian seismic design code. Using the definition of spectrum intensity by Housner [14] the synthetic ground motion was artificially generated to be compatible with the design response spectrum provided by the Indian seismic design code with an intensity equal to that of the ideal design level earthquake specified by the code. Figure 1(c) displays the pseudo-velocity response spectra of the scaled earthquake ground motion records used for the dynamic analysis. The figure also shows the idealized pseudo-velocity response spectrum conforming to current Indian seismic design criteria.

5.1 Results of seismic analysis of code compliant masonry infilled R/C frames

The variations of the peak normalized inter-story drifts in percentage terms over the height of the code-compliant designs of the masonry infilled R/C frame predicted by the non-linear dynamic analysis is shown in Fig 4(a). It can be observed from the figure that the maximum interstory drifts of frame with a ‘soft’ ground story range from 2.5% to 6%. The maximum inter-story drifts for the frame with a partially infilled ground story are marginally lower. In contrast, the maximum inter-story drifts of the completely infilled frame ranges between 1% and 4% for all the earthquake ground motions with the exception of one for which the maximum inter-story drift is 6%. The maximum inter-story drifts of the bare frame display a similar range as the corresponding completely infilled frame. The maximum inter-story drifts for the bare frame lie between 1% and 4% for all the earthquake ground motions with the exception of one for which the maximum inter-story drift is as large as 8%. Figure 4(a) indicates that the

prevalent force based design methodology followed by the current generation of seismic design codes largely disregard limitation of inter-story drifts and the related seismic damage.

5.2 Results of seismic analysis of the trial performance based designs of masonry infilled R/C frames for different target drifts

The plots of variation of the peak normalized inter-story drifts in percentage terms over the height of the trial PBD of the R/C frame designed for a target drift of 2% as predicted by the non-linear dynamic analysis is shown in Figure 4(b). It is apparent from Figure 4(b) that the maximum inter-story drifts of the trial PBDs of the R/C frame are within the target drift of 2% for all stories with the only exception of the bare frame in which the inter-story drift at the top level marginally exceeds the target drift. From the results presented in Figure 4(b), it can be concluded that the first trials of PBD of the masonry infilled R/C frames meet the target performance level for each distribution of masonry infill panels considered in the study. Hence, a second trial by refining the design is not required for any frame. The figure also shows that the application of the proposed procedure is successful in limiting the inter-story drifts within the target drift of 2% under the influence of near-field earthquakes as well far-field earthquakes. Therefore, it is hypothesized that the proposed performance based design methodology using the energy approach can be effectively implemented for achieving the desired performance level in masonry infilled R/C frames under near-field earthquakes as well. Moreover, further enhancement in seismic performance may be achieved by selecting a lower target drift in the proposed energy based plastic design procedure, for e.g. a target drift of 1% corresponding to immediate occupancy performance limit state.

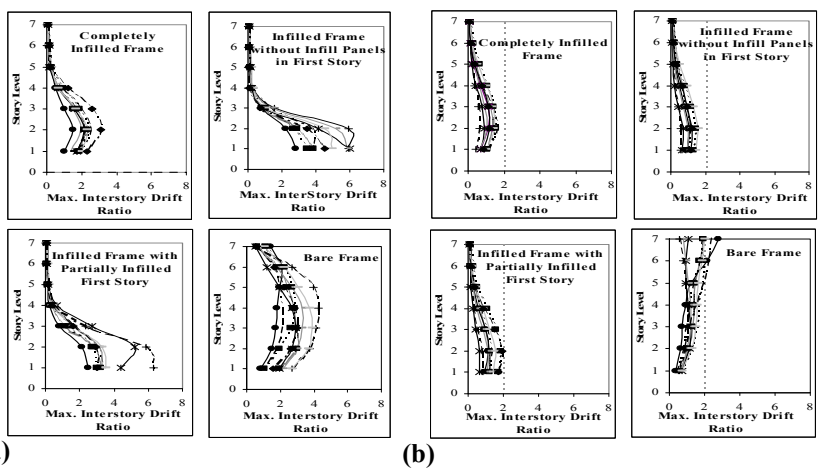

Figure 4: Peak normalized inter-story drifts (%) of the r/c frame designed using (a) code specified force based design procedure and (b) energy based plastic design procedure for target drift of 2%.

6 Conclusions

The paper presents a plastic design procedure based on the energy balance concept for performance based seismic design of multi-story multi-bay masonry infilled reinforced concrete (R/C) frames subjected to near-field earthquakes considering the commonly implemented distributions of masonry infill panels over the frame elevation. The results of non-linear dynamic analyses of the code-compliant designs of the masonry infilled R/C frames lead to the conclusion that the prevalent force based design methodology provided by the current generation of seismic design codes is inherently deficient in controlling the inter-story drifts and the related seismic damage under earthquake loads. An inherent limitation of the force based seismic design criteria specified by the present generation of seismic design codes is that the maximum plastic deformations are disregarded in the design formulation. The only specification in the seismic design criteria that considers the displacement demand on the structure is the check on drift limitations, which is accomplished by linear elastic methods. The incentives for retaining linear elastic analysis procedures in the current seismic design practice may be the simplicity of linear analysis techniques and the prevalent familiarity of engineers with force based design. Moreover, the current seismic design codes do not provide any explicit recommendations or guidelines that enable the engineer to predict the seismic performance of the final design or evaluate the margin of life safety achieved by conforming to the code specifications. The provision of strength reduction factor in the formulation for seismic base shear in the current seismic design codes implicitly assumes that the structure is capable of several cycles of inelastic deformation without loss of lateral strength due to intrinsic ductility of the structure. However, the force based design formulation does not specify any limitation on the maximum plastic drift of the structure.

The results of non-linear dynamic analyses of the trial performance based designs of the masonry infilled R/C frames with the various practically relevant distributions of masonry infill panels over the frame elevation lead to the conclusion that the first trials of performance based design of the masonry infilled R/C frames meet the target performance level for each distribution of masonry infill panels over the frame elevation considered in the study for all practical purposes. Hence, a second trial by refining the design may not be required for any distribution of masonry infill panels. A more important conclusion that can be derived from the results of non-linear dynamic analyses is that the application of the proposed energy based plastic design procedure for performance based seismic design is equally successful in limiting the inter-story drifts of the masonry infilled R/C frames within the specified target drifts under the influence of near-field earthquakes. The proposed performance based design methodology using the energy approach offers an engineering solution to the inverse problem of determining the design dimensions and reinforcement of the R/C frame members in a masonry infilled R/C framed buildings that are required to achieve the specified performance objective for the building structure for a given seismic hazard level. The proposed energy approach is more rational and realistic for performance based seismic design of building structures subjected to

near-field as well as far-field earthquakes since the approach is based on the fundamentals of energy balance.

References

[1] Yang, J. N., and Agrawal, A. K., "Semi-Active Hybrid Control for Nonlinear Buildings against Near-Field Earthquakes." *Engineering Structures*, Vol.94, 2002, pp.271-280.

[2] Roberts, M. W., and Lutes, L. D., 2003 "Potential for Structural Failure in the Seismic Near-field." Journal of Engineering Mechanics, ASCE, V.129, No.8, 2003, pp.927-934.

[3] Leelataviwat, S., Goel, S.C., and Stojadinovic, B., "Energy-Based Seismic Design of Structures using Yield Mechanism and Target Drift." Journal of Structural Engineering, V.128, No.8, 2002, pp.1046-1054.

[4] Housner, G.W., "Limit Design Of Structures To Resist Earthquakes." Proceeding of 1st world conference on earthquake engineering, Earthquake Engineering Research Institute, Oakland, California, 5, 1956, pp.1-13.

[5] Kato, B., and Akiyama, H., " Seismic Design of Steel Buildings" Journal of Structural Division, ASCE, V.108, No. 8, 1982, pp.1709-1721.

[6] Akiyama, H., "Earthquake-Resistant Limit-State Design of Buildings." University of Tokyo Press, Tokyo, 1985.

[7] Lee, S.S., and Goel, S.C., "Performance Based Design Of Steel Moment Frames Using Target Drift And Yield Mechanism." Research Report UMCEE 01-17, The University of Michigan, Ann Arbor, Michigan, 2001.

[8] BIS. "IS 1893-2002 (Part 1): Indian Standard Criteria for Earthquake Resistant Design of Structures, Part 1-General Provisions and Buildings." Bureau of Indian Standards, 2002.

[9] Madan, A., Reinhorn, A. M., Mander, J. B., Valles, R., "Modeling of Masonry Infill Panels for Structural Analysis." Journal of Structural Engineering, V.123, No.10, 1997, pp.1295-1302.

[10] Valles, R. E., Reinhorn, A. M., Kunnath, S. K., Li, C., and Madan, A., "IDARC Version 4.0 - A Program for the Inelastic Damage Analysis of Buildings." Technical Report NCEER-96-0010, SUNY/Buffalo, 1996.

[11] ATC-40., "Seismic Evaluation and Retrofit of Concrete Buildings." Report SSC 96-01, California Seismic Safety Commission, Applied Technology Council, CA, USA, 1996.

[12] FEMA-356 "Prestandard and Commentary for Seismic Rehabilitation of Buildings", Federal Emergency Management Agency (FEMA), Washington D. C., USA, 2000.

[13] Newmark, N.M., and Hall, W.J., "Earthquake Spectra and Design." Earthquake Engineering Research Institute, Oakland,California, 1982.

[14] Housner, G. W., "Behavior of structures during earthquakes." Journal of Engineering Mechanics, ASCE, V.85, No.4, 1959, pp.109-129.

This page intentionally left blank

Section 4
Aerospace structures

This page intentionally left blank

Uncertainty and reliability in aircraft design and optimization

S. Hernández, J. Díaz, M. Cid, A. Baldomir & L. Romera
Structural Mechanics Group, School of Civil Engineering, University of La Coruña, Spain

Abstract

Aircraft engineering is subjected to many classes of uncertainties due to the lack of proper definition of loads, behaviour of new materials or even due to the inaccuracies produced during manufacturing. Because of that, the most advanced methods of analysis and optimization need to be used during the dimensioning of aircraft structures. One way to increase the safety level of a design could be to increase the safety coefficients for load values or material strength, but this approach would lead to an unacceptable amount of material for the aircraft. More proper approaches can be applied using probabilistic analysis during the design phase. In that case, some of the parameters, such as loads, material properties of manufacturing tolerances are defined as random variables and a probabilistic analysis is carried out to identify the safety of the design. This approach can be also enhanced by introducing the concept of design optimization. In that case the optimum solution for an aircraft structure is obtained even considering the random nature of some of the design variables. In this paper these methodologies will be described and some examples of aircraft structures will be presented to show the potential in real problems.
Keywords: uncertainty quantification, reliability based design optimization.

1 Introduction

Reliability is related with the probability of verifying a certain condition. This is known as the probability of failure. In a probabilistic analysis, the uncertainties in the basic magnitudes of the structure are considered directly in the analysis, changing from fixed quantities to random variables (RV). The limit state function defines if a design belongs to the failure domain, where the limit state is not

WIT Transactions on The Built Environment, Vol 125, © 2012 WIT Press
www.witpress.com, ISSN 1743-3509 (on-line)
doi:10.2495/OP120191

verified, or to the security domain, where it is (figure 1). If $\mathbf{a}$ is the vector of basic variables which contains the n random variables of the structure, then the domains are defined as follows:

$$\text{Failure domain: } F = \{\mathbf{a} \mid g(\mathbf{a}) < 0\} \tag{1}$$

$$\text{Security domain: } S = \{\mathbf{a} \mid g(\mathbf{a}) \geqslant 0\} \tag{2}$$

The boundary between both domains is known as the failure surface or limit state surface, which generally is an hypersurface of $n-1$ dimensions in the n-dimensional space of basic variables. The safety margin is now defined as a random variable which can be identified with the value of the limit state function:

$$M = g(\mathbf{a}) \tag{3}$$

According to this, probability of failure p_f is formulated as:

$$p_f = P\left[g\left(\mathbf{a}\right) \leqslant 0\right] = \int_{g(\mathbf{a}) \leqslant 0} \cdots \int f_{\mathbf{A}}\left(\mathbf{a}\right) d\mathbf{a}, \tag{4}$$

where $f_{\mathbf{A}}\left(\mathbf{a}\right)$ is the joint probability density function of all the basic variables involved in the response of the system. Except in some particular cases, integral expression (4) cannot be resolved analytically, because of the nonlinearity of $f_{\mathbf{A}}\left(\mathbf{a}\right)$, and also due to the fact that the number of random variables usually employed is large, and therefore the dimension of the problem.

The uncertainty quantification methods selected in this work to assess the reliability of the structure are based on the Taylor series expansion of the limit state surface. Those methods require information about the value of the limit state function and its derivatives in the vicinity of the design point. A brief description of the algorithms is presented next.

2 Reliability analysis methods

2.1 First order second-moment methods

The FOSM or first order second-moment method uses an estimation of the first two statistical moments of the limit state function evaluated at $\boldsymbol{\mu}_{\mathbf{A}}$, the point defined by the mean value of the random variables [1]:

$$\mu_M = E\left[g(\mathbf{a})\right] \simeq g(\boldsymbol{\mu}_{\mathbf{A}}) \tag{5}$$

$$\sigma_M^2 = Var\left[g(\mathbf{a})\right] \simeq \sum_{i=1}^{n}\sum_{j=1}^{n} \frac{\partial g(\boldsymbol{\mu}_{\mathbf{A}})}{\partial a_i} \frac{\partial g(\boldsymbol{\mu}_{\mathbf{A}})}{\partial a_j} \sigma_{A_i A_j}, \tag{6}$$

where μ_M and σ_M are the mean value and the standard deviation of the limit state function, respectively. Reliability index β is defined from equations (5) and (6) as

$$\beta = \frac{\mu_M}{\sigma_M}, \tag{7}$$

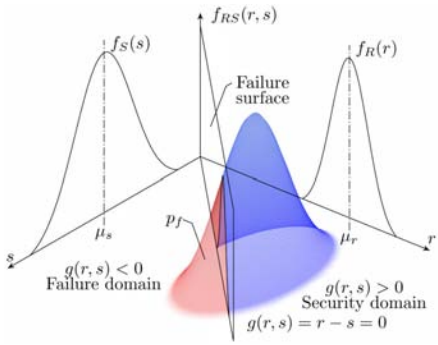

Figure 1: Failure and security domains.

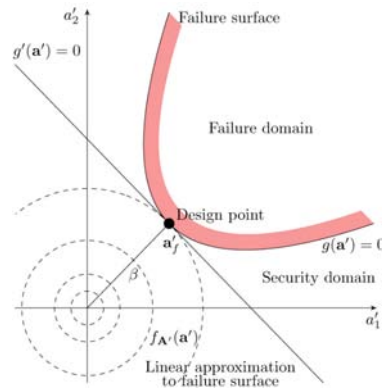

Figure 2: First order reliability method.

whereas the probability of failure p_f can be obtained as

$$p_f = 1 - \Phi(\beta), \tag{8}$$

where Φ is the cumulative distribution function of the standard normal variable.

2.2 First order reliability methods

The FORM or first order reliability method [2] consists in the search of the most probable point of failure (MPP) in the standardised domain of the random variables ($\mathbf{a}'$), in order to allow the substitution of the limit state function by its Taylor series expansion of first order at that point (figure 2),

$$g(\mathbf{a}') \simeq g(\mathbf{a}'_\mathbf{f}) + \nabla g(\mathbf{a}'_f)^T(\mathbf{a}' - \mathbf{a}'_f), \tag{9}$$

where $\mathbf{a}'_f$, the most probable point of failure, is the point of minimum distance from the origin to the limit state surface. Geometrically, the method approximates the limit state surface by the tangent hyperplane at the MPP. Reliability index is related now to the failure surface, but it is invariant with respect to the formulation of the limit state function:

$$\beta = -\frac{\mathbf{a}_f'^T \nabla g(\mathbf{a}'_f)}{\sqrt{\nabla g(\mathbf{a}'_f)^T \nabla g(\mathbf{a}'_f)}}. \tag{10}$$

2.3 Advanced mean value methods

These algorithms assume the approximation of the limit state surface by the tangent hyperplane at the point $\boldsymbol{\mu}_{\mathbf{A}}$. The first order expansion is known as AMV:

$$M = g(\mathbf{a}) \simeq g(\boldsymbol{\mu}_{\mathbf{A}}) + \nabla g(\boldsymbol{\mu}_{\mathbf{A}})^T(\mathbf{a} - \boldsymbol{\mu}_{\mathbf{A}}), \tag{11}$$

whereas AMV+ is an enhanced first order approximation which starts in $\boldsymbol{\mu}_{\mathbf{A}}$ and then iterates to obtain an estimation of the MPP ($\mathbf{a}^*$):

$$M = g(\mathbf{a}) \simeq g(\boldsymbol{a}^*) + \nabla g(\boldsymbol{a}^*)^T(\mathbf{a} - \boldsymbol{a}^*). \tag{12}$$

2.4 Two-point adaptive nonlinear approximation

The two-point adaptive nonlinear approximation (TANA3) is based on an exponential approximation which uses information of the current iteration k and also of the previous one $k-1$ [3]. According to that, the limit state surface can be approximated as

$$g(\mathbf{a}) \simeq g(\mathbf{a}_k) + \sum_{i=1}^{n} \frac{\partial g(\mathbf{a}_k)}{\partial a_i} \frac{(a_{i,k})^{(1-r_i)}}{r_i} \left(a_i^{r_i} - a_{i,k}^{r_i}\right) + \frac{\varepsilon_2}{2} \sum_{i=1}^{n} \left(a_i^{r_i} - a_{i,k}^{r_i}\right)^2, \tag{13}$$

where the nonlinear index r_i and the parameter ε_2 are defined as

$$r_i = 1 + \frac{\ln\left(\dfrac{\partial g(\mathbf{a}_{k-1})}{\partial a_i}\right) - \ln\left(\dfrac{\partial g(\mathbf{a}_k)}{\partial a_i}\right)}{\ln(a_{i,k-1}) - \ln(a_{i,k})}, \tag{14}$$

$$\varepsilon_2 = \frac{2\left[g(\mathbf{a}_{k-1}) - g(\mathbf{a}_k)\right]}{\sum_{i=1}^{n}\left(a_i^{r_i} - a_{i,k-1}^{r_i}\right)^2 + \sum_{i=1}^{n}\left(a_i^{r_i} - a_{i,k}^{r_i}\right)^2} - \frac{2\left[\sum_{i=1}^{n} \dfrac{a_{i,k}^{1-r_i}}{r_i} \dfrac{\partial g(\mathbf{a}_k)}{\partial a_i}\left(a_{i,k-1}^{r_i} - a_{i.k}^{r_i}\right)\right]}{\sum_{i=1}^{n}\left(a_i^{r_i} - a_{i,k-1}^{r_i}\right)^2 + \sum_{i=1}^{n}\left(a_i^{r_i} - a_{i,k}^{r_i}\right)^2} \tag{15}$$

3 Reliability based design optimization

Reliability based design optimization solves the problem of minimizing an objective function, usually related with the cost of the structure, like the weight, considering constraints defined in terms of uncertainty. The variables that characterize the problem can be divided into two types. Design variables, which are modified in the optimization cycle and random variables, which are the source of uncertainty.

RBDO is an active research topic and many authors have contributed so far. Some interesting references can be found in [4–8].

The formulation of a RBDO problem can be set out in different ways, depending on where the procedure to evaluate the reliability constraints is connected to the optimization process. Thus, bi-level or double loop approaches consider the reliability constraints within the optimization loop. On the other hand, mono-level approaches replace probabilistic constraints with approximate deterministic values, converting the double loop in a single loop. Finally, decoupled approach solves the RBDO problem as a sequence of deterministic optimization procedures.

In this work a double loop framework with a reliability index approach has been selected as methodology. The algorithm selected for the optimization loop is sequential quadratic programming

4 Application examples

This section demonstrates the performance of the selected reliability methods when applied in the context of a design optimization algorithm. Three different examples are presented. In all the cases, the probabilistic results are compared with the deterministic results, using in this case the mean values of the random variables.

4.1 Ten bar truss

Figure 3 shows the geometry of a ten bar truss structure. Two loads of the same value are applied and modelled with a random variable using a Gumbel distribution. The mean value is 255.5 kN, and the coefficient of variation (COV) is 0.15. The material is aluminum, having deterministic values the density and the Poisson's coefficient, with 2.77 t/m^3 and 0.3 respectively. The Young's modulus is considered as a random variable with a normal distribution, with mean 6.895×10^4 MPa and COV 0.05. Dimensions are deterministic and the parameter L is 9.144 m. The cross section areas are the design variables. They have an initial value of 153.938 cm^2, and are constrained by a lower and upper bound, with values of 10.425 cm^2 and 216.111 cm^2, respectively.

This structure will be optimized by means of minimizing its volume, considering deterministic optimization and reliability based design optimization. The maximum displacement in the node 5 is selected as constraint, so the deterministic problem is formulated as:

$$\min F(\boldsymbol{x}) \tag{16}$$

subject to:

$$w_5 \leqslant w_{max} \tag{17}$$

In this case, the maximum displacement allowed on node 5 is $w_{max} = -5.08$ cm. When considering reliability based design optimization, the constraints are

random quantities and the problem is formulated as:

$$\min F(\boldsymbol{x}) \tag{18}$$

subject to:

$$\beta_i \geqslant \beta_{min} \tag{19}$$

where $\beta_{min} = 3$, which corresponds with a probability of failure of 1.35×10^{-3}.

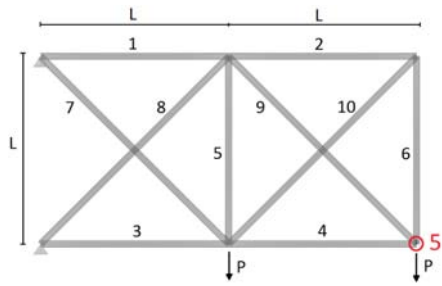

Figure 3: Ten bar truss structure.

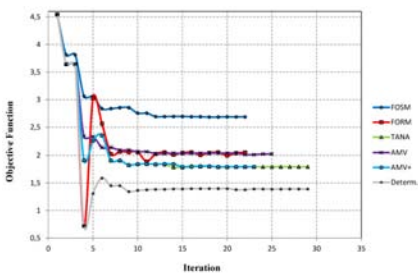

Figure 4: Ten bar truss objective function.

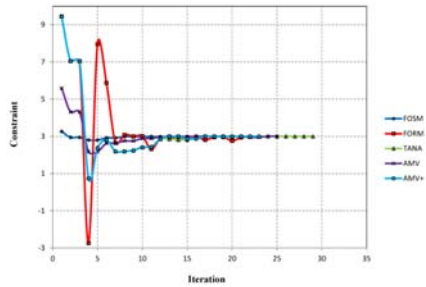

Figure 5: Ten bar truss reliability constraint.

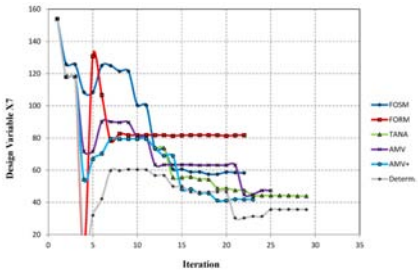

Figure 6: Convergence of design variable x_7.

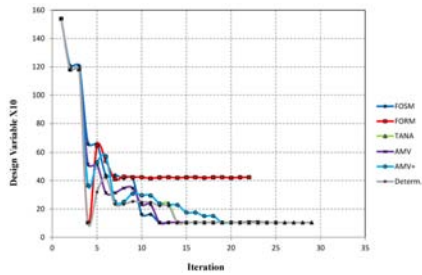

Figure 7: Convergence of design variable x_{10}.

Table 1: Ten bar truss results summary.

Method	FOSM	FORM	TANA	AMV	AMV+	Determ.
x_1	216.111	144.240	144.850	162.213	145.584	109.340
x_2	10.452	43.625	10.452	10.452	10.452	10.452
x_3	166.594	140.847	109.968	130.792	107.569	85.573
x_4	109.601	46.627	67.993	76.687	68.750	50.003
x_5	10.452	32.147	10.452	10.452	10.452	10.452
x_6	10.452	43.604	10.452	10.452	10.452	10.452
x_7	58.327	81.734	43.921	47.295	41.798	35.642
x_8	159.494	79.664	99.972	114.812	102.393	75.551
x_9	151.582	50.421	96.073	109.461	96.462	70.843
x_{10}	10.452	42.456	10.452	10.452	10.452	10.452
F	2.687	2.053	1.794	2.026	1.794	1.389
Iterations	22	22	29	25	23	29
Evaluations	3410	504,406	175,605	4590	197,676	869

As it is shown in figures 4 to 7 and in table 1, TANA and AMV+ methods reach similar objective function values and AMV has an increase of 13% in its objective function value with respect to them. In the case of the FOSM method, the result obtained has an increase of 50% with respect to TANA and AMV+, due to the differences on the value obtained for the reliability index at the initial design. As expected, deterministic design converges into a lower value. The most expensive methods are AMV+ and TANA with 197,000 and 175,000 evaluations, respectively. The methods requiring less iterations are FOSM and AMV, with 3400 and 4600 evaluations, respectively.

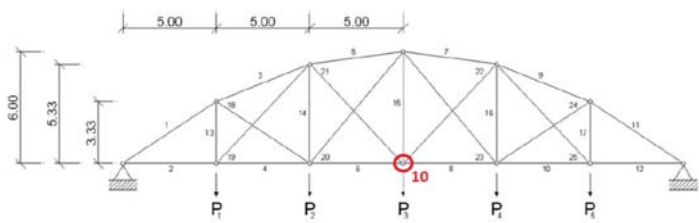

Figure 8: Twenty-five bar 2D truss structure.

Table 2: Twenty-five bar 2D truss design variables.

Variable	x_1	x_2	x_3	x_4	x_5	x_6	x_7	x_8	x_9	x_{10}	x_{11}	x_{12}	x_{13}
Initial point	15	0.5	15	0.5	15	0.5	2	0.1	2	2	0.1	0.1	2

Table 3: Twenty-five bar 2D truss results summary.

Method	FOSM	FORM	TANA	AMV	AMV+	Determ.
x_1	13.350	12.949	12.741	12.564	13.418	12.998
x_2	0.100	0.100	0.100	0.100	0.100	0.100
x_3	13.535	13.351	13.226	13.207	13.377	12.957
x_4	0.434	0.439	0.436	0.432	0.314	0.315
x_5	15.367	15.109	15.346	15.850	14.791	14.373
x_6	0.100	0.100	0.100	0.100	0.100	0.100
x_7	1.828	1.697	1.837	1.827	1.234	1.319
x_8	0.100	0.100	0.100	0.100	0.100	0.100
x_9	2.381	2.336	2.406	2.461	2.850	2.691
x_{10}	1.741	1.790	1.761	1.748	1.172	1.151
x_{11}	0.100	0.100	0.100	0.100	0.100	0.100
x_{12}	0.100	0.100	0.100	0.100	0.100	0.100
x_{13}	2.305	2.279	2.339	2.397	2.319	2.256
F	0.433	0.425	0.426	0.429	0.421	0.409
Iterations	17	18	17	14	42	30
Evaluations	1050	182,109	58,458	1175	213,441	602

4.2 Twenty-five bar 2D truss

Figure 8 shows the geometry of a 25 bar 2D truss structure. The load case in study is composed by five loads applied on the nodes of the lower bars. The value of these five loads is supposed to be equal, being a random variable with a Gumbel distribution. The mean value is 286.5 kN, and the COV is 0.1. The material used in this truss is steel, having deterministic values the density and the Poisson's coefficient, with 7.85 t/m^3 and 0.3, respectively. Young's modulus is a random variable with a normal distribution, with mean 2.1×10^5 MPa and COV 0.05. The dimensions of the truss are deterministic values and the design variables are the cross section areas of the bars, with the initial values shown in table 2, constrained by a lower and upper bound, with values 0.1 cm^2 and 1000 cm^2, respectively. The maximum displacement allowed on node 10 is -2.5 cm.

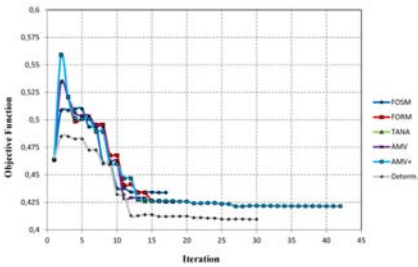

Figure 9: 25 bar 2D objective function.

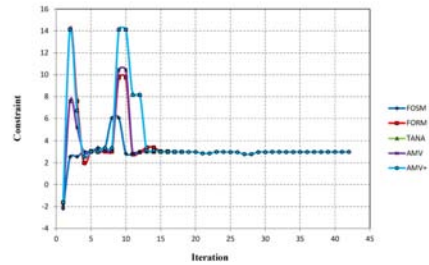

Figure 10: 25 bar 2D reliability constraint.

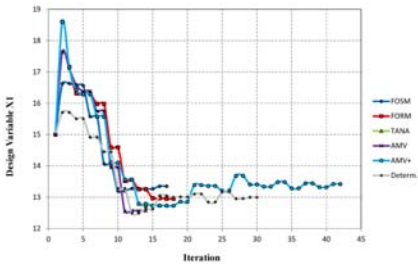

Figure 11: Convergence of design variable x_1.

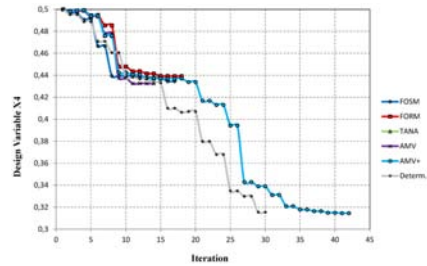

Figure 12: Convergence of design variable x_4.

As is shown in table 3 and figures 9 to 12, the five reliability methods reach similar design variable and objective function values, with a slightly higher objective function value in the case of the FOSM method, with a relative increase of 2%. The reason of this phenomenon is the different reliability index obtained with the FOSM method with respect to the others. It is also remarkable the fact that the deterministic optimization reaches a value only 4% lower. This is due to the low sensitivity that the loads have with respect to the structural displacements. In the AMV+ case, as it is shown in figure 9, the number of needed iterations is twice as much as the other methods, but in the last 30 the algorithm is converging around the neighbourhood of the solution, so the convergence is similar in all the cases, reaching acceptable values over the 15^{th} iteration. Focusing now on the number of needed evaluations, the FOSM and AMV methods are the least expensive, with only over 1100. TANA follows them with over 58,500 and FORM and AMV+ are the more expensive, with 182,000 and 213,000, respectively.

4.3 Twenty-five bar 3D truss

Figure 13 shows the geometry of a 25 bar 3D truss structure. Four loads are applied in nodes 1, 2, 3 and 6 with components $(0.1P, P, -P)$, $(0, P, -P)$, $(0.05P, 0, 0)$

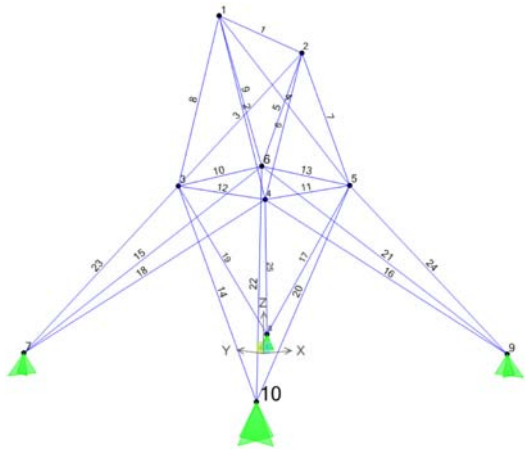

Figure 13: Twenty-five bar 3D truss structure.

and $(0.06P, 0, 0)$, respectively. The value P is taken as a random variable with a Gumbel distribution where the mean value is 25.58 kN and the COV is 0.15. The material is aluminum and its properties are the same as in the section 4.1. Design variables have an initial value of 19.634 cm^2, and are constrained by a lower and upper bound, with values 0.636 cm^2 and 50 cm^2, respectively. The maximum horizontal displacement allowed on node 2 in the y axis is -0.889 cm.

In this case, different results are obtained depending on the method (figures 14 to 17 and table 4). TANA and AMV+ methods reach similar objective function values, 0.213. In the case of the FOSM method the result obtained has an increase

Table 4: Twenty-five bar 3D truss results summary.

Method	FOSM	TANA	AMV	AMV+	Determ.
x_1	0.636	0.636	9.638	0.636	0.636
x_2	6.406	0.636	8.173	0.636	0.636
x_3	21.895	23.312	40.417	23.905	12.332
x_4	0.636	1.451	0.636	0.636	0.636
x_5	8.132	12.909	23.551	11.583	6.780
x_6	6.978	4.953	11.219	5.117	2.709
x_7	6.621	1.182	0.839	1.054	0.636
x_8	21.895	25.224	50	25.094	13.479
F	0.250	0.214	0.431	0.213	0.115
Iterations	41	47	27	45	58
Evaluations	3051	160,857	2668	153,267	1386

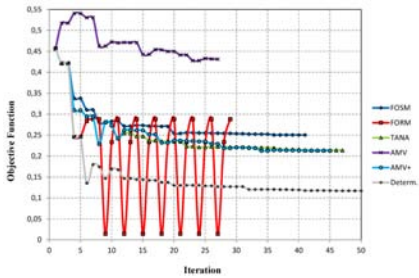

Figure 14: 25 bar 3D objective function.

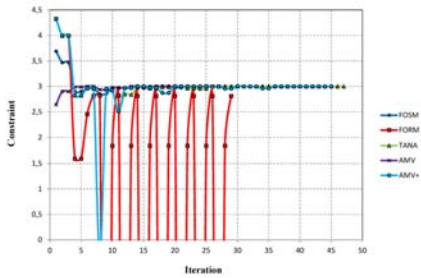

Figure 15: 25 bar 3D reliability constraint.

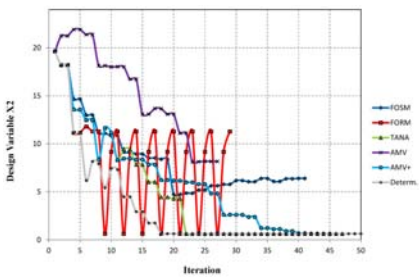

Figure 16: Convergence of design variable x_2.

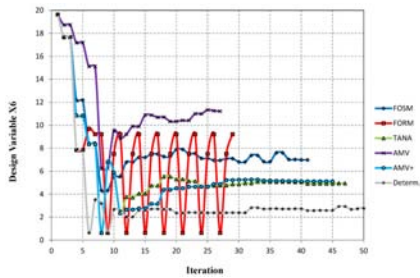

Figure 17: Convergence of design variable x_6.

of 17%, but in the AMV case, the objective function doubles those values, reaching 0.431. The reason is the different reliability index obtained with the AMV and FOSM method with respect to the others; for the initial point, the reliability index of each one of those methods has a value of 2.64 and 3.68, respectively, instead of 4.32 obtained with FORM, TANA and AMV+. This means that the probability of failure is higher and, therefore, the design variables and, consequently, the objective function will increase. It is also remarkable the fact that the FORM method does not reach convergence. As is shown in figure 14, from 8^{th} iteration starts to oscillate into three cyclical iterations. Deterministic optimization converges into a result 50% less than the obtained by RBDO.

All the methods reach convergence with a similar number of iterations with around 45, except AMV that finishes with only 27 iterations. Deterministic needs 58. Also, the most expensive methods, in terms of number of evaluations, are TANA and AMV+ with 160,000 and 153,000, respectively. The less computational intensive methods are the FOSM and AMV, with 3000 and 2600 evaluations, respectively.

5 Conclusions

In this work, a review of some existing procedures of reliability analysis and their capabilities has been carried out in a RBDO framework. Three examples have been used to illustrate the performance of the methods employed in the study. Finally, some conclusions can be drawn.

As a general conclusion it can be said that depending on the reliability method used, the results of the RBDO can have slight changes. In particular, FOSM and AMV methods converge to less accurate values of reliability index than the other methods. This fact has an influence in the optimization results, which offer different values for the objective function.

Also, some differences were appreciated in terms of computational cost. FOSM and AMV are the fastest methods and FORM is the one requiring most iterations and does not always converge. Finally, AMV+ and TANA offer a good compromise between accuracy and efficiency.

Acknowledgements

The research leading to these results has received funding from the Spanish Ministry of Science and Innovation (Ministerio de Ciencia e Innovación) under grant agreement DPI2010-16238. The authors fully acknowledge the support received.

References

[1] Cornell, C.A., A probability-based structural code. *Journal of the American Concrete Institute*, **66(12)**, pp. 974–985, 1969.
[2] Hasofer, A. and Lind, N., Exact and invariant second moment code format. *J Eng Mech Div-ASCE*, **100(1)**, pp. 111–121, 1974.
[3] Xu, S. and Grandhi, R., Effective two-point function approximation for design optimization. *AIAA journal*, **36**, pp. 2269 – 2275, 1998.
[4] Yao, W., Chen, X., Luo, W., Van Tooren, M. and Guo, J., Review of uncertainty-based multidisciplinary design optimization methods for aerospace vehicles. *Progress in Aerospace Sciences*, **47(6)**, pp. 450–479, 2011.
[5] Yang, R., Chuang, C., Gu, L. and Li, G., Numerical experiments of reliability-based optimization methods. *45 th AIAA/ASME/ASCE/AHS/ASC Structures, Structural Dynamics and Materials Conference*, 2004.
[6] Aoues, Y. and Chateauneuf, A., Benchmark study of numerical methods for reliability-based design optimization. *Structural and Multidisciplinary Optimization*, **41(2)**, pp. 277–294, 2009.
[7] Youn, B.D. and Choi, K.K., Selecting probabilistic approaches for reliability-based design optimization. *AIAA journal*, **42(1)**, pp. 124–131, 2004.
[8] Burton, S. and Hajela, P., Efficient reliability-based structural optimization through most probable failure point approximation. *45th AIAA/ASME/ASCE/AHS/ASC Structures, Structural Dynamics and Materials Conference*, 2004.

Welding sequence optimization of plasma arc for welded thin structures

M. B. Mohammed, W. Sun & T. H. Hyde
Division of Materials, Mechanics and Structures, Faculty of Engineering, University of Nottingham, UK

Abstract

Dividing the weld path into multiple seams that are welded sequentially in a specific order is one of the most important and cost effective distortion and residual stresses mitigation strategies. This is particularly important for welding fabrication of thin structures. The number of sequence options resulting from reordering seams increases explosively with the increase of the number of weld seams. Investigating all sequences using experimental, analytical or computational approaches requires substantial expenses in terms of time, resources and cost and in many situations is practically impossible. Therefore, welding industries tend to opt for small improvement and abandon the search for the absolute optimum welding sequence, e.g. the welding sequence that produces the absolute minimum welding induced distortion. This paper presents an optimization procedure to improving the effectiveness of the search for an optimized welding sequence. The optimization procedure is based on the principles of genetic algorithms (GA), in which the finite element (FE) analysis is used to produce the distortion information and direct the evolution of the GA within the optimization. The capability of the optimization procedure to identify an optimum welding sequence was demonstrated for the keyhole plasma arc welding (KPAW) of two Ti-6Al-4V thin structures, being a flat plate and a simplified replica of a portion of an aero-engine casing. The optimization procedure developed in this study was capable of minimizing the welding induced distortion by up to 55% and of improving the effectiveness of the search for an optimized welding sequence by up to 98%.
Keywords: welding sequence, optimization, genetic algorithms, plasma arc welding, finite element modelling.

WIT Transactions on The Built Environment, Vol 125,
www.witpress.com, ISSN 1743-3509 (on-line)
doi:10.2495/OP120201

1 Introduction

Welding generates distortion and residual stresses in structures as a result of the effects of shrinkage during cooling [1, 2]. These can lead to unacceptable inaccuracies and in-service defects, respectively [3]. A number of design-related and process-related mitigation strategies such as weld joint details, clamping, preheating and heat input are implemented to counteract this shrinkage effects [4].

Dividing the weld path into several seams that are welded sequentially in a specific order is one of the most important and cost effective distortion and residual stresses mitigation strategies [4]. The order (sequence) by which seams are welded alters the cooling patterns and as a result alters distortion and residual stresses evolution [3]. However, the number of sequences resulting from reordering weld seams increases explosively with increasing the number of weld seams which makes investigating all possible sequences using experimental, analytical or computational approaches substantially expensive [5]. Therefore, welding industries tend to opt for small improvement and abandon the search for the ultimate optimum welding sequence [4].

Previous research works have implemented various algorithms and methods in determining an optimum welding sequence. This includes the neural net alogrithm [5], the genetic and evolutionary alogrithm [1, 3, 6, 7] and the elstic net method [7]. These were all coded on the basis of the heuristic knowledge of welding experts in the robot welding industry while using FE modelling to calculate distortion. Distrotion was considered as the criterion determining the weld quality in these studies due to the fact that welding sequence has a minor effect on the resulting maximum residual stress values [1]. The heauristic knoweldge is however unique to the specific welding process of a specific structure which makes its emplementation across different welding processes and structures less resilient.

This paper presents the principles and application of the optimization procedure developed for improving the effectiveness of the search for an optimum welding sequence of thin structures. The optimization procedure is based on the principles of genetic algorithms (GA) and the finite element (FE) analysis software SYSWELD is used to produce the distortion information and direct the evolution of the GA in [8] within the optimization framework. The optimization procedure was demonstrated for the keyhole plasma arc welding (KPAW) of three thin Ti-6Al-4V structural components: a flat plate, a curved T-joint and a simplified replica of a portion of an aero-engine casing.

2 Principles of optimization using genetic algorithms

Genetic algorithms searches for an optimized solution by the evolution of the existing solution using the mechanics of natural selection and natural genetics [9]. That is, if we think of each seam in the welding process as a gene and we think of any sets of seams as individuals composed of a string of genes, then GA applies genetic operations that results in the evolution of these individuals to

produce fitter ones, i.e. optimized solutions. This is achieved by assigning fitness parameter to each solution and by selecting the existing optimum ones to go through the evolution process; also known as breeding. The three genetic operations associated with evolution are demonstrated below:

1. Crossover: Exchanging genes between the fittest breeding parents.

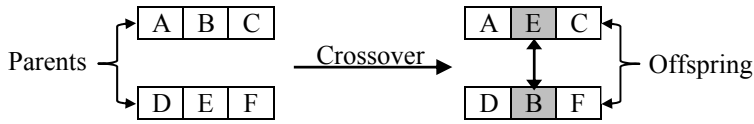

2. Mutation: Rearranging genes within each of the fittest breeding parents.

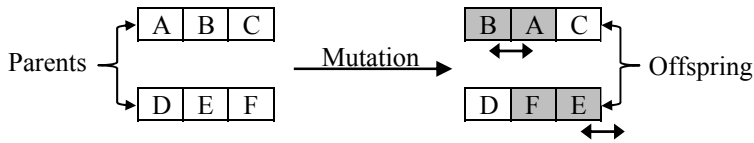

3. Reinsertion: This involves evolution by replacing parents with offspring.

GA is an effective tool to use in optimizing the distortion induced by seams welding sequence as the solution domain in GA is not limited by restrictive assumptions such as continuity and existence of derivatives.

3 FE modelling of KPAW of thin structures

The heat input required to establish the keyhole welding mode in plasma arc welding process is achieved by forcing plasma arc though a fine-bore nozzle at high velocities and high temperatures. KPAW process is superseded by laser and electron beam welding processes in terms of the power density these processes are capable of producing; KPAW process is however more cost effective and more tolerant of joint preparation [10].

The finite element models of the KPAW processes of two titanium alloy (Ti-6Al-4V) based thin structures were used to demonstrate the developed optimization procedure; these are a flat plate and a simplified replica of a portion of an aero-engine casing ().

The FE modelling of these thin structures was based on the work previously presented by Deshpande *et al.* [11] in which the KPAW processes modelling of bead on plate of the same material and thickness was developed and validated. The FE modelling was carried out using the commercially available welding specific software SYSWELD in which a 3D conical Gaussian heat source was used to model the heat input. The clamping conditions were defined by constraining the three velocity components (*Ux*, *Uy* and *Uz*) of the nodes in the clamped areas on the thin structures. Heat transfer by convection and radiation were also accounted for.

As illustrated in Figure 1(a), the flat plate has three seams while the aero-engine casing replica has four seams. Also, the FE modelling of the welding of the flat plate does not involve the joining of two separate plates; rather, the heat source representing the welding torch was applied along the mid-section of a single plate. Hence, distortions in the flat plate are purely generated due to the contribution of heating and cooling cycle in addition to clamping conditions. In the case of the simplified replica of a portion of an aero-engine casing the FE modelling of the welding involves the joining of the outer ring with the inner structure represented respectively by the solid and dotted lines as shown in Figure 1(b). This was incorporated in the FE model by adding a very thin layer (0.25 mm) of "chewing gum elements" at the interface between the two

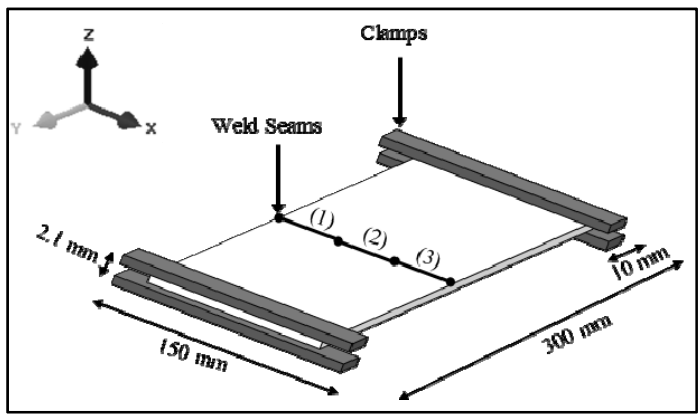

(a)

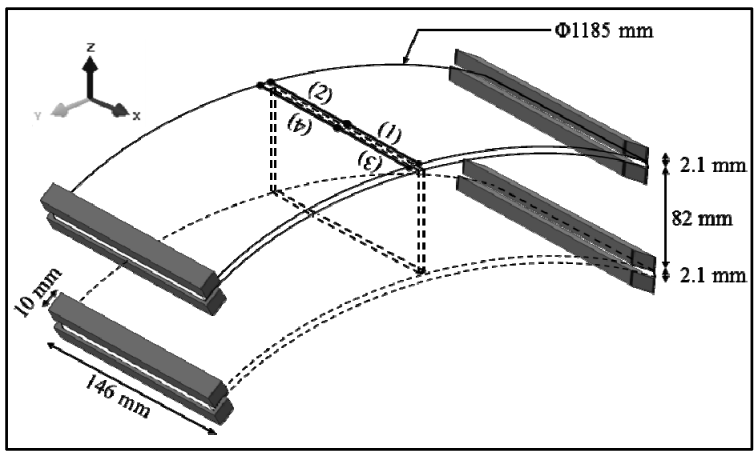

(b)

Figure 1: FE modelling set-up for the KPAW of Ti-6Al-4V (a) Flat plate; (b) Simplified replica of a portion of an aero-engine casing.

structures (Figure 2). These chewing gum elements have no stiffness, hence the name, and it undergoes transition from the no stiffness state to the state of taking on the mechanical behaviour of the Ti-6Al-4V once their temperature exceeds the melting point. This allows for the representation of the local mechanical interlocking between the welded structures as a result of the occurrence of fusion.

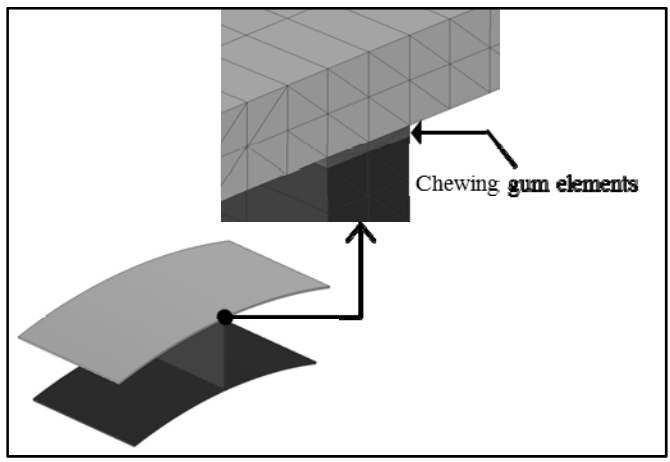

Figure 2: Interfacing welded structure using chewing gum elements to represent fusion.

4 Definition of welding sequence problem

The seams in the FE modelling of the flat and the simplified replica of a portion of an aero-engine casing are of equal length in both cases. While the direction of welding each seam can vary, each seam can be welded only once. Therefore, each welding sequence consists of a string containing all seams. The total number of possible welding sequences is the number of combinations that can be made by rearranging the orders and directions of seams. This is demonstrated in (Table 1) for the flat plate. As can be seen in Table 1, the order of welding a seam is represented by its position in the sequence; being 1st, 2nd, 3rd, etc. and the direction of welding a seam is represented by the (+) and (-) signs.

The total number of all possible welding sequences can be obtained using Equation (1) introduced in [1, 12] in which d is the number of directions for each seam (2 directions) and s is the total number of seams (3 and 4). As a result, there is a total of 48 and 384 possible welding sequences for the flat plate and the simplified replica of a portion of an aero-engine casing.

$$d^s \times s! \tag{1}$$

Table 1: Example of welding sequences resulting from rearranging the orders and directions of seams in the flat plate.

Sequence No.	Seams Welding Orders and Directions			Schematic
	1st	2nd	3rd	
1	+1	+2	+3	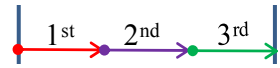
2	-2	+1	+3	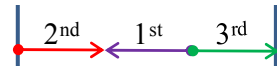
3	-3	-2	-1	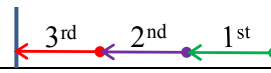

Identifying the absolute optimum welding sequence, i.e. the welding sequence that produces the absolute minimum distortion, can only be achieved by modelling all possible sequences. This is expensive in terms of computational efforts, time and the costs associated with it. Hence, there is a need for an optimization procedure to be employed in order to improve the effectiveness of identifying a welding sequence that can produce a minimum distortion.

5 Structure of welding sequence optimization procedure

The structure of the optimization procedure is composed of two interacting elements; genetic algorithms to optimize the search of an optimum welding sequence and FE modelling to assess and direct the search for an optimum welding sequence. The interaction between GA and FE modelling is developed on a MATLAB platform using the structure shown in Figure 3. As Figure 3 shows, GA is initially coded to create an initial population (parent sequences)

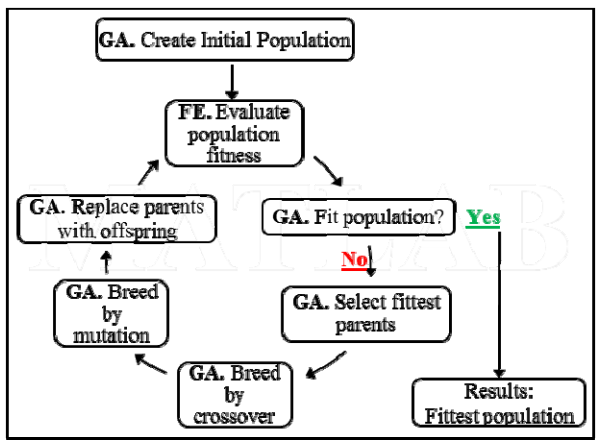

Figure 3: Structure of optimization procedure developed on MATLAB platform.

which will go through the process of genetic (seam) evolution. These initial parent sequences were coded to carry all genes in order to give each gene equal opportunity to survive and make it to the next generation. The parent sequences coded for the three seams in the flat plate and for the four seams in the simplified replica of a portion of an aero-engine casing are shown in Table 2.

Table 2: Parent sequences coded to bare all seams.

	Parent (1)				Parent (2)			
Three Seams	+1	+2	+3		-1	-2	-3	
Four Seams	+1	+2	+3	+4	-1	-2	-3	-4

The fitness of each of the parent sequences is then evaluated by calculating the distortion introduced by each of the parent sequences to the welded structure using FE modelling. This is achieved by the MATLAB code developed to modify the FE modelling input files to reflect the welding sequence created by GA and to feed the distortion results back to it. Because the distortion in the z-direction is dominant as shown in Figure 4 for the flat plate, the value of the objective function to be minimized in this optimization procedure was defined as the maximum displacement in the z-direction (*Uz*) as shown in Equation (2) where *i* is the i^{th} welding sequence.

$$\begin{aligned} Min \rightarrow Obj \cdot Fun(1) &= max\,|Uz| \\ &\vdots \\ Min \rightarrow Obj \cdot Fun(i) &= max\,|Uz| \end{aligned} \tag{2}$$

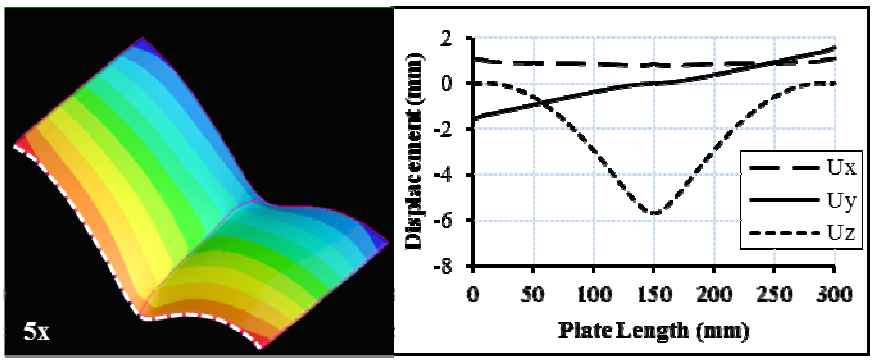

Figure 4: Displacements profiles along the white dotted line in the x, y and z directions in the flat plate.

The parent sequences are then assigned a rank on the basis of the distortion they induce; that is higher rank for minimum distortion. A new welding sequence (offspring welding sequence) is then generated as a result of the breeding of the

parent sequences by single gene crossover and single gene mutation. The fitness of the new offspring sequence is then assessed and a rank is assigned to it. The new offspring welding sequences replaces the parent sequence that has lower rank in order to ensure that only fitter parents are contributing to the evolution of the new generations, i.e. new optimized sequences.

The optimization procedure described above continues until the optimization criterion described in Equation (3) is met, where β=0.4; this minimizes the distortion by 40% relative to the maximum distortion identified during the optimization procedure. The value of β=0.4 was found to be effective in identifying an optimum welding sequence for the welds presented in this paper.

$$\frac{min(Obj \cdot Fun(1\ldots i))}{max(Obj \cdot Fun(1\ldots i))} \leq \beta \tag{3}$$

6 Results and discussions

Table 3 and Figure 5 show the results of the optimization procedure for the flat plate. As can be seen, an optimized welding sequence (-1 -3 +2) was identified in accordance with the optimization criterion described in Equation (3) in the fifth iteration. The optimized welding sequence produced a maximum absolute

Table 3: Evolution of the 3 seams welding sequence of flat plate in optimisation.

Iteration	Weld Sequence			|Uz| (mm)
1	-1	-2	-3	8.34
2	+2	+1	-3	6.98
3	+2	-1	-3	7.65
4	+2	-3	-1	8.01
5	-1	-3	+2	3.76

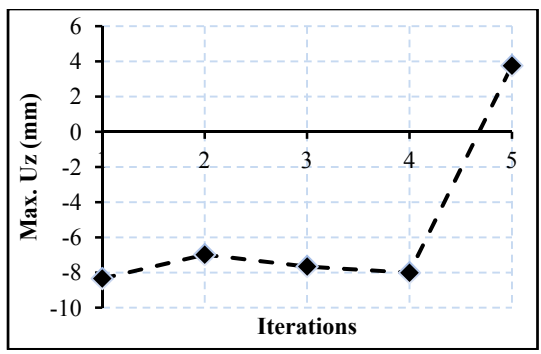

Figure 5: Maximum distortions in z-direction for the 3 seams welding sequence optimization of flat plate.

distortion of 3.76 mm which is less by about 55% of the maximum distortion that was produced by sequence (-1, -2, -3) in the first iteration. In this case, the optimization procedure was able to minimize distortion by about 55% by the FE modelling of 5 sequences out of a total of 48 possible sequences which saves about 90% of the time required for the FE modelling of all sequences.

The results of the optimization procedure for the simplified replica of a portion of an aero-engine casing are shown in Table 4 and Figure 6. The optimum welding sequence (+1 -4 +2 -3) was identified in the ninth iteration and produced a maximum distortion of 1.27 mm which is about 40% less than the distortion produced in the eighth iteration. Identifying an optimized welding sequence in the ninth iteration implies that about 98% of time required for the FE modelling of all possible welding sequences (384 sequences) was saved while achieving 40% reduction in welding induced distortion.

Table 4: Evolution of the 4 seams welding sequence of the simplified replica of a portion of an aero-engine casing.

Iteration	Weld Sequence				|Uz| (mm)
1	+2	-4	-3	+1	1.96
2	+1	-4	-3	-2	1.97
3	+1	-4	-2	-3	1.88
4	+1	-4	-2	+3	2.05
5	+2	-3	-1	+4	1.99
6	+1	-2	+4	-3	1.61
7	+1	+4	+2	+3	2.00
8	+2	-4	-1	-3	2.11
9	+1	-4	+2	-3	1.27

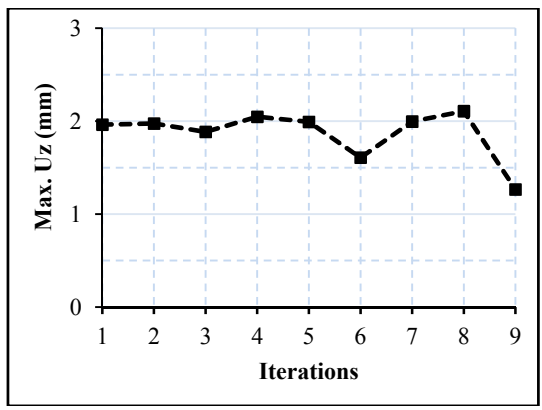

Figure 6: Maximum distortions in z-direction for the 4 seams welding sequence optimization of simplified replica of a portion of aero-engine casing.

Figure 7 shows a comparison between the distortions resulting from using continuous welding (no seams) and using optimized welding sequence for both of the flat plate and the simplified replica of a portion of an aero-engine casing. The comparison clearly shows that continuous welding did not result in reduced distortion hence validating the concept of dividing weld bead into several seams to minimize distortion.

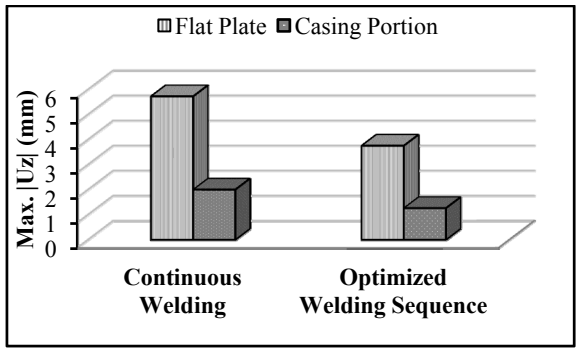

Figure 7: Comparison between distortions induced by continuous welding and the optimized welding sequences.

7 Conclusions

Welding induced distortion can be minimized by dividing the weld bead into small seams that are welded in a specific order. Identifying the absolute optimum welding sequence requires investigating all possible welding sequences which is expensive in terms of computational efforts, time and cost. An optimization procedure that was developed on the basis of the integration of GA and FE modelling in a MATLAB platform is proposed in this paper to improve the effectiveness of the search for an optimized welding sequence, i.e. the welding sequence that minimizes welding induced distortion. The optimization procedure was applied in the FE modelling of a KPAW of Ti-6Al-4V flat plate that has three seams and a simplified replica of a portion of an aero-engine casing that has 4 seams. The optimization procedure identified an optimum welding sequence that minimized distortion by about 55% in the fifth iteration for the former and about 40% in the ninth iteration for the latter. As a result a saving of up to 90% and 98% of FE modelling time has been achieved for both welding models, respectively. It was demonstrated that the optimized welding sequences minimized distortion in comparison to continuous welding.

The optimization procedure presented in this paper can be conveniently applied to other similar welding processes, such as laser and electron beam welding, and can also be coded to minimize other structural parameters such as residual stresses.

8 Future work

Figure 8 shows the full-size simplified replica of the aero-engine casing from which the portion presented in this paper was extracted. As can be seen in the figure, the full-size replica is composed of 12 portions. The distortion optimization of one portion presented in this paper is considered as a *local optimization*. Future work will focus on developing *global optimization* of welding induced distortion. That is, optimizing the order by which the 12 portions are welded to minimize the global distortion of the full-size structure. This will improve the robustness of the optimization procedure in solving practical welding induced distortion problems required in welding industries.

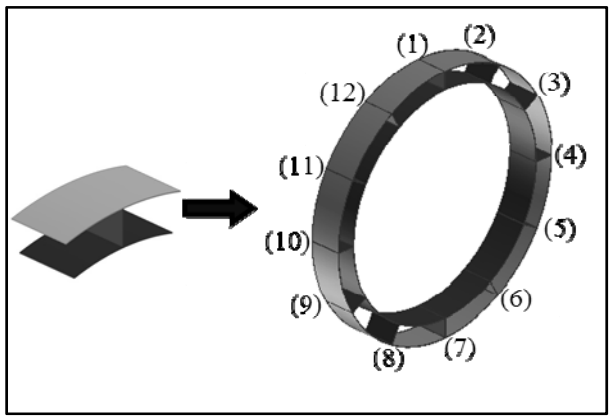

Figure 8: Full-size simplified replica of an aero-engine casing.

Acknowledgements

The authors of this paper would like to acknowledge the EPSRC for their financial support of the research work through the Nottingham Innovative Manufacturing Research Centre (NIMRC) at the University of Nottingham.

References

[1] Kadivar, M.H., K. Jafarpur, and G.H. Baradarn, *Optimizing welding sequence with genetic algorithm.* Journal of Computational Mechanics, 2000. **26**: p.514-519.
[2] Tsai, C.L., S.C. Park, and W.T. Cheng, *Welding distortion of a thin-plate panel structure.* Welding Research Supplement, 1999: p.156-165.
[3] Damsbo, M. and P.T. Ruhoff, *An evolutionary algorithm for welding tasl sequence ordering.* AISC'98, LNAI, 1998. **1476**: p.120-131.

[4] Nnaji, B.O., D. Gupta, and K.Y. Kim, *Welding distortion minimization for an aluminum alloy extruded beam structure using a 2D model*. Transactions of the ASME, 2004. **126**: p.52-63.
[5] Fukuda, S. and K. Yoshikawa, *Determination of welding sequence: a neural net approach.* Journal of Engineering Analysis with Boundary Elements, 1991. **7**(2): p.78-82.
[6] Kim, K.Y., D.W. Kim, and B.O. Nnaji, *Robot arc welding task sequencing using genetic algorithms.* IIE Transactions, 2002. **34**: p.865-880.
[7] Yang, H. and H. Shao, *Distortion-oriented welding path optimization based on elastic net method and genetic algorithm*. Journal of Materials Processing Technology, 2009. **209**: p.4407-4412.
[8] Hartmut, P., *GEATbx - Genetic and Evolutionary Algorithm Toolbox for use with Matlab*, 1994-2006.
[9] Goldberg, D.E., *Genetic Algorithms in Search, Optimization, and Machine Learning*1989: Addison-Wesley Publishing Company, Inc. 412.
[10] Wu, C.S., Q.X. Hu, and J.Q. Gao, *An adaptive heat source model for finite-element analysis of keyhole plasma arc welding.* Computational Materials Science, 2009. **46**: p.167-172.
[11] Deshpande, A.A., A.J. Short, W. Sun, D.G. McCartney, L. Xu, and T.H. Hyde. *Parameter idnetification for stable keyhole plasma arc welding of a Ti-6Al-4V sheet*. in *AeroMat* 2010. Bellevue, WA, USA.
[12] Voutchkov, I., A.J. Keane, A. Bhaskar, and T.M. Olsen, *Weld sequence optimization: The use of surrogate models for solving sequential combinatorial problems.* Journal of Computer Methods in Applied Mechanics and Engineering, 2005. **194**: p.3535-3551.

Section 5
Evolutionary methods in design optimization

This page intentionally left blank

Application of particle swarm optimization to the item packing problem

Y.-B. Shin & E. Kita
Graduate School of Information Science, Nagoya University, Japan

Abstract

The item packing problem is a class of optimization problems which involve attempting to pack items together inside a container, as densely as possible without the item overlap. This research focuses on the application of Particle Swarm Optimization (PSO) to the item packing problem in the two-dimensional region.

PSO has the potential solutions of the problem as particles. Particles in the swarm are updated according to the update rule with the velocity and position vectors. The position vectors of the item centers are taken as the design variables. The total number of items is maximized when all items are included inside a container without the item overlap. In the original PSO, the particle position vector is updated with the best position in all particles; i.e., global best position, and the local best position in previous positions of each particle; i.e., local best position. The present PSO algorithm utilizes, in addition to them, the second best position in all particles; i.e., global second-best position.

In the numerical example, the present algorithm is applied to the item packing problem within the two-dimensional region. The region figure is not regular and the square items are packed in the region. The comparison of the original and the present PSOs show that the present algorithm can find a better solution than the original PSO.

Keywords: particle swarm optimization, item packing problem, global best position, second global best position.

1 Introduction

Evolutionary computations are techniques implementing mechanisms inspired by biological evolution such as reproduction, mutation, recombination, natural selection and survival of the fittest; Genetic Algorithms [1–3], Simulated Annealing [4], Evolutionary Programming [5], Genetic Programming [6, 7], Particle Swarm Optimization [8, 9] and so on.

WIT Transactions on The Built Environment, Vol 125, © 2012 WIT Press
www.witpress.com, ISSN 1743-3509 (on-line)
doi:10.2495/OP120211

Genetic Algorithms (GA) [1–3] is very popular algorithm in the evolutionary computations. In GA [1–3], a population of chromosomes of candidate solutions to an optimization problem evolves toward better solutions by applying the genetic operators such as selection, crossover, mutation and so on. On the other, Genetic Programming [6, 7] and Grammatical Evolution [10–12] are designed for the different object. Their object is to find function representations for the unknown data sets and computer programs that perform a user-defined task. Particle Swarm Optimization (PSO), which has been presented in 1995 by Kennedy and Eberhart [8], is based on a metaphor of social interaction such as bird flocking and fish schooling. PSO is a population-based optimization algorithm, which could be implemented and applied easily to solve various function optimizations problem, or the problems that can be transformed to the function minimization or maximization problem.

In this study, we will apply PSO for solving two-dimensional packing problems. Packing problems are a class of optimization problems in mathematics which involve attempting to pack objects together (often inside a container), as densely as possible. There are many variations of this problem, such as two-dimensional packing, linear packing, packing by weight, packing by cost, and so on. We focus on the two-dimensional packing problems. Popular problems in two-dimensional packing are to packing circles or squares in a circle or a square. The problems are studied analytically and the maximum numbers of items are determined [13–15]. The application of PSO for solving packing problem has been presented by some researchers [16–19]. In this study, we consider that the packing regions have the arbitrarily shaped region and then, same items are packed in the region without their overlap. The design objective is to maximize the total number of the items packed in the region without the item overlap. The position vectors of the item centers are taken as the design variables. The problem is solved by the original and the present PSOs. In the PSO, the potential solutions of the optimization problem to be solved are defined as the particle position vectors. Then, the particle positions are updated by PSO update rules. In the original PSO, the particle position vector is updated by the best position of all particles; global best position, and the local best position in previous positions of each particle; personal best position. The improved PSO utilizes, in addition to them, the second best position of all particles; global second-best position [9].

The remaining part of this paper is organized as follows. The PSO algorithms and the optimization problem are explained in section 2 and 3, respectively. In section 4, the packing problem in two-dimensional regions is solved. Finally, the conclusions are summarized again in section 5.

2 PSO algorithms

2.1 Update rule of original PSO

PSO algorithm determines the potential solutions of the optimization problem as the swarm of the particles. Each particle in the swarm has a position vector

$\boldsymbol{x}_i(t)$ $(i = 1, 2, \ldots, N)$ and a velocity vector $\boldsymbol{v}_i(t)$ in the search space at time t. The particle position vector is defined as the set of the design variables of the optimization problem. Each particle has memory and therefore, can remember the best position in search space it ever visited. The satisfaction of the particle i for the design objective at time t is estimated by the objective function or the fitness function $f(\boldsymbol{x}_i(t))$.

The position at which each particle takes the best fitness function is known as the personal best position $\boldsymbol{x}_i^{pbest}(t)$ and the overall best out of all particles in the swarm is as the global best position $\boldsymbol{x}^{gbest}(t)$. In the original PSO, the velocity and position vectors of the particle i are updated according to the following formulas

$$\boldsymbol{x}_i(t+1) = \boldsymbol{x}_i(t) + \boldsymbol{v}_i(t+1) \tag{1}$$

$$\begin{aligned}\boldsymbol{v}_i(t+1) = w \cdot \boldsymbol{v}_i(t) + c_1 \cdot R_1 \cdot \{\boldsymbol{x}_i^{pbest}(t) - \boldsymbol{x}_i(t)\} \\ + c_2 \cdot R_2 \cdot \{\boldsymbol{x}^{gbest}(t) - \boldsymbol{x}_i(t)\}\end{aligned} \tag{2}$$

where w is the inertia weight, c_1 and c_2 are acceleration coefficient, and t is the iteration time. Besides, R_1 and R_2 are random numbers in the interval $[0, 1]$.

The inertia weight w governs how much of the velocity should be retained from the previous time step. Generally the inertia weight is not fixed but varied as the algorithm progresses. The inertia weight w, in this study, is generally updated by self-adapting formula as

$$w = w_{\max} - (w_{\max} - w_{\min}) \cdot \frac{t}{t_{\max}} \tag{3}$$

where the parameter $w_{\max}$ and $w_{\min}$ denote the maximum and minimum inertia weight, respectively. The parameter t and $t_{\max}$ are the iteration step and the maximum iteration steps in the simulation, respectively.

The parameters c_1 and c_2 determine the relative pull of $\boldsymbol{x}_i^{pbest}(t)$ and $\boldsymbol{x}^{gbest}(t)$. According to the recent work done by Clerc [20], the parameters are given as

$$c_1 = c_2 = 1.5. \tag{4}$$

2.2 Update rule with global second-best position

The original PSO have no handling mechanism for avoiding the convergence to the local optima. Therefore, the new update rule is introduced in this section.

Each particle has three memories and thus, can remember, the global best position $\boldsymbol{x}^{gbest}(t)$, the local best position $\boldsymbol{x}_i^{pbest}(t)$, and the second global best position $\boldsymbol{x}^{sgbest}(t)$. The use of the second global bestposition $\boldsymbol{x}^{sgbest}(t)$ attempts

to search diversity and change movement of particles. The velocity and position vectors are updated according to the following formulas.

$$\boldsymbol{x}_i(t+1) = \boldsymbol{x}_i(t+1) + \boldsymbol{v}_i(t+1) \tag{5}$$

$$\begin{aligned}\boldsymbol{v}_i(t+1) = w \cdot \boldsymbol{v}_i(t) &+ c_1 \cdot R_1 \cdot \{\boldsymbol{x}_i^{pbest}(t) - \boldsymbol{x}_i(t)\} \\ &+ c_2 \cdot R_2 \cdot \{\boldsymbol{x}^{gbest}(t) - \boldsymbol{x}_i(t)\} \\ &+ c_3 \cdot R_3 \cdot \{\boldsymbol{x}^{sgbest}(t) - \boldsymbol{x}_i(t)\}\end{aligned} \tag{6}$$

where w is the inertia weight, c_1, c_2 and c_3 are acceleration coefficient, and t is the iteration time. Besides, R_1, R_2 and R_3 are random numbers distributed in the interval$[0, 1]$. The parameter c_1 and c_2 are taken as the same values in the original PSO; $c_1 = c_2 = 1.5$. The parameter c_3 is determined from some numerical experiments, which is given as $c_3 = 1.9$.

2.3 Algorithm

PSO share the information of $\boldsymbol{x}_i^{pbest}$, $\boldsymbol{x}^{gbest}$ and $\boldsymbol{x}^{sgbest}$. Obviously, $\boldsymbol{x}^{sgbest}$ is worse than $\boldsymbol{x}^{gbest}$. If only equation (6) is used for updating particle velocity and position vectors, the results must be worse than that by the original PSO. Therefore, the present algorithm uses both update rules; equations (2) and (6). The switching of the update rules (2) and (6) is controlled according to the probability P_s. The process is as follows:

1. Initialize the position and velocity vectors of particles with random numbers.
2. Set $t = 1$.
3. For $i = 1, 2, \cdots, N$:
   (a) Evaluate fitness functions $f(\boldsymbol{x}_i(t))$ for the particle i.
   (b) If $f(\boldsymbol{x}_i(t)) > f(\boldsymbol{x}_i^{pbest})$, set $\boldsymbol{x}_i^{pbest} = \boldsymbol{x}_i(t)$.
4. Find the first- and second-best particles $\boldsymbol{x}^1$ and $\boldsymbol{x}^2$ among $\boldsymbol{x}^{gbest}$, $\boldsymbol{x}^{sgbest}$ and $\boldsymbol{x}_i(t)$ $(i = 1, 2, \ldots, N)$.
5. If $\boldsymbol{x}^1 > \boldsymbol{x}^{gbest}$, set $\boldsymbol{x}^{gbest} = \boldsymbol{x}^1$.
6. If $\boldsymbol{x}^2 > \boldsymbol{x}^{sgbest}$, set $\boldsymbol{x}^{sgbest} = \boldsymbol{x}^2$.
7. Generate random number r in the interval$[0, 1]$.
8. If $r > P_s$, update the velocity and position vectors of all particles according to equations (1) and (2), respectively.
9. If $r \leq P_s$, update the velocity and position vectors of all particles according to equations (5) and (6), respectively.
10. Set $t = t + 1$ and go to step 3 if $t \leq t_{\max}$.

3 Packing problem

3.1 Optimization problem

The packing problem can be formulated to maximize the number of items N included into a two-dimensional polygonal region P.

The objective function is defined as follows.

$$\max z \tag{7}$$

The design variables vector is defined as the set of the center position vectors of all items as follows.

$$\boldsymbol{x}_i = \{p_x^1, p_y^1, \cdots, p_x^k, p_y^k, \cdots, p_x^z, p_y^z\}^T \tag{8}$$

where the vector $\{p_x^k, p_y^k\}$ denotes the center position vector of the item k,

The constraint conditions are as follows.

$$g_1(k, P) = 0 \tag{9}$$

$$g_2(k, l) = 0 \tag{10}$$

$$0.5w \leq p_x^k \leq W - 0.5w \tag{11}$$

$$0.5h \leq p_y^k \leq H - 0.5h \tag{12}$$

where $k = 1, 2, \cdots, z; l = 1, 2, \cdots, z$. The parameters w and h are item sizes, and W and H are feasible space sizes. The function $g_1(k, P)$ estimates the inclusion of the item k in the region P, which is defined as follows:

$$g_1(k, P) = \begin{cases} 0 & \text{The item } k \text{ is included in the region } P. \\ 1 & \text{The item } k \text{ is not included in the region } P. \end{cases} \tag{13}$$

The function $g_2(k, l)$ estimates the overlap between the item k and the item l, which is defined as follows:

$$g_2(k, l) = \begin{cases} 0 & \text{The item } k \text{ and } l \text{ are not overlapped.} \\ 1 & \text{The item } k \text{ and } l \text{ are overlapped.} \end{cases} \tag{14}$$

3.2 PSO implementation

When the number of the items z is given, PSO solves the item packing problem within the packing region without violating the constraint conditions. In the optimization problem to be solved by PSO, the fitness function is defined as follows.

$$f(\boldsymbol{x}_i) = \frac{1}{1 + \sum_{k=1}^{z} \left\{ g_1(k, P) + \sum_{l=1}^{z, k \neq l} g_2(k, l) \right\}} \tag{15}$$

3.3 Optimization process

The process of the present algorithm is shown in Fig.1 and summarized as follows.

1. $z = 0$.
2. Set the threshold P_s and the maximum step size $t_{\max}$.

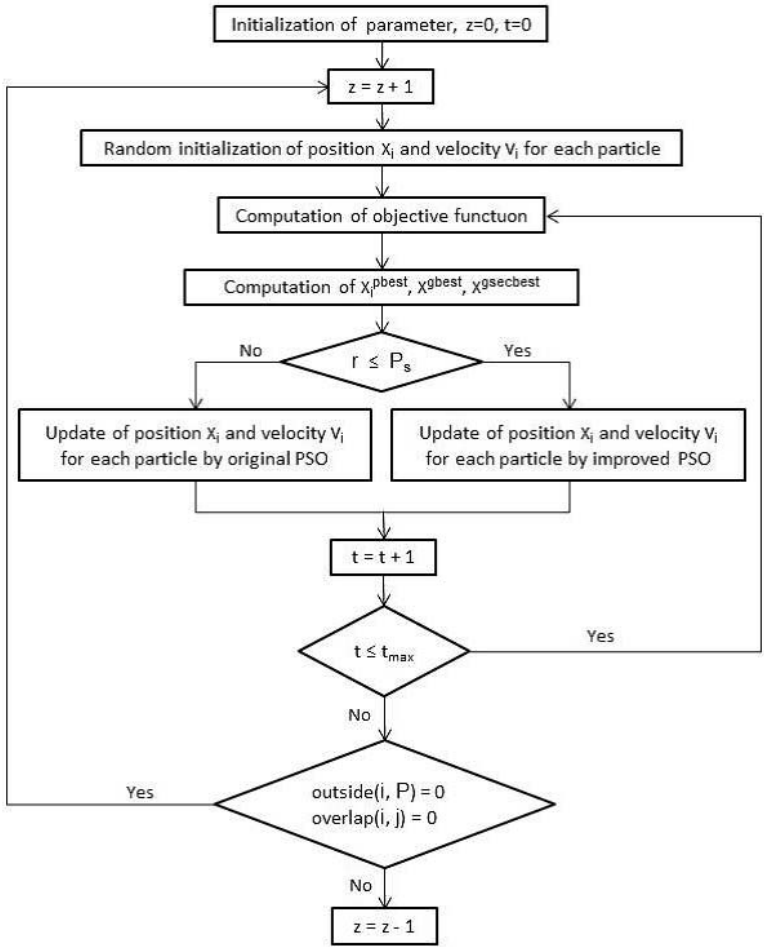

Figure 1: Flow chart of the parking problem by using improved PSO.

3. Update the item number by $z = z + 1$.
4. Perform PSO algorithm:
   (a) $t = 0$
   (b) Initialize a particle population with random position and velocity vectors.
   (c) Evaluate the fitness function for each particle $f(\boldsymbol{x}_i)$.
   (d) Estimate the $\boldsymbol{x}_i^{pbest}$, $\boldsymbol{x}^{gbest}$ and $\boldsymbol{x}^{gsbest}$.
   (e) If $f(\boldsymbol{x}^{gbest}) = 0$, go to Step 3.
   (f) Generate the random number r in $[0, 1]$.
   (g) If $r \le P_s$, update particles by equation (6), otherwise updated by equation (2).

(h) $t = t + 1$.
(i) If $t \leq t_{max}$, return to Step 4c.
5. If $g_1(i, P) = g_2(i, j) = 0$, return to Step 3.
6. Stop by $z = z - 1$.

4 Numerical examples

The packing region is shown in Figure 2. PSO parameters are listed in Table 1. Number of particles and maximum iteration steps are specified as $N = 200$ and $t_{\max} = 2000$, respectively. The other parameters are taken as $w = 0.9$, $c_1 = 1.5$, $c_2 = 1.5$, $c_3 = 1.9$, and $P_s = 0.1$.

The results are shown in Figure 3 and Table 2. The average values of the maximum item numbers are 12.07 in the original PSO and 13.99 in the present

Table 1: Parameters.

Number of particles	$N = 200$
Maximum iteration step	$t_{\max} = 2000$
Update rules parameters	$w_{\max} = 0.9, w_{\min} = 0.4$
	$c_1 = 1.5, c_2 = 1.5, c_3 = 1.9$

Table 2: Comparison of original and improved PSOs.

	Original PSO	Improved PSO
Average item number z	11.7	12.864
Average CPU time (seconds)	60.754	80.931
Success rate in $z \geq 13$	36.8%	73.8%

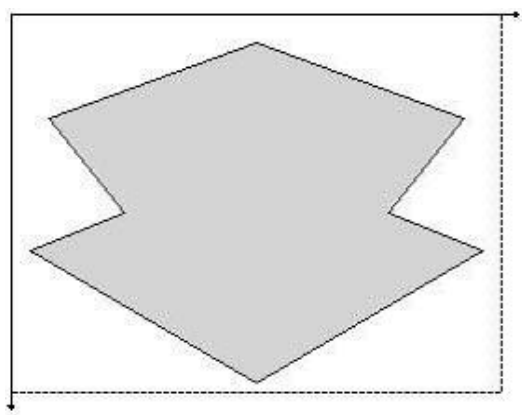

Figure 2: Packing region.

Table 3: Effect of parameter P_s in case B.

P_s	0.1	0.2	0.3	0.4	0.5	0.6
Item number	14.1	13.83	13.97	13.76	13.37	13.39
CPU time (seconds)	66.57	77.00	81.80	85.56	95.18	108.65

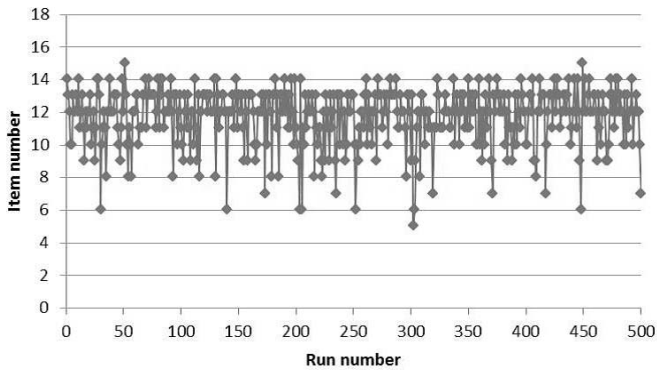

Figure 3: Maximum item numbers by original PSO.

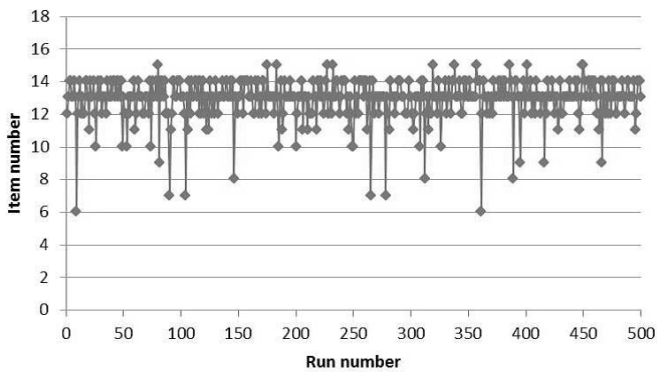

Figure 4: Maximum item numbers by present PSO.

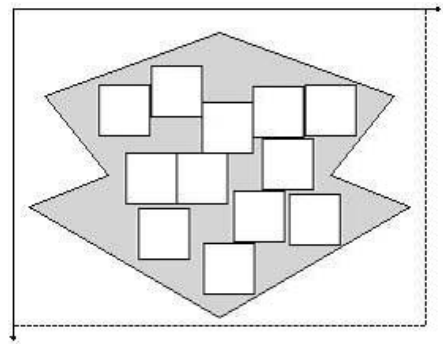

(a) z=12

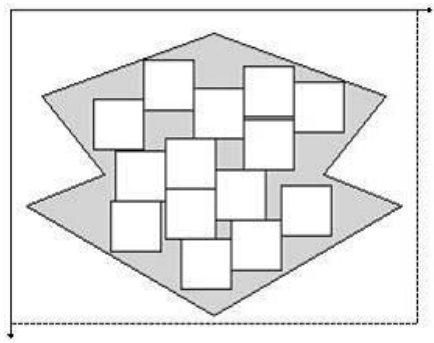

(b) z=14

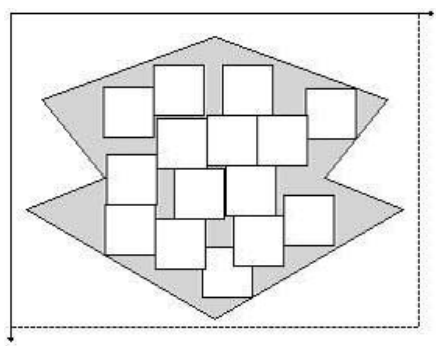

(c) z=15

Figure 5: Item placements in case of improved PSO.

PSO. The average CPU time is 35.198 and 65.124, respectively. The success rate is 19.8% and 75.2%, respectively. The use of the improved PSO can increase the item number improve the success rate although the CPU time is increased.

Next, the effect of the parameter P_s to the convergence property is discussed. The maximum number of items and the CPU times for the different parameter P_s are listed in Table 3. The results show that, at $P_s = 0.1$, the item number is largest and CPU time is shortest.

5 Conclusions

Application of Particle Swarm Optimization (PSO) for the two-dimensional packing problem was presented in this study. It was assumed that the packing region was not regularly but arbitrarily shaped. The square items were packed in the region as dense as possible without their overlapping. PSO was applied for solving the arrangement problem of the items in the region. The original PSO updates the particle position vectors by two information; the global best position and the local best position. The present algorithms uses, in addition to them, the second global best position. The present algorithm was applied for solving the item packing problem to the two-dimensional concave region. The results were compared with them by the original PSO. The average values of the maximum item numbers are 12.07 in the original PSO and 13.99 in the present PSO. Therefore, the present PSO can find better solution than the original PSO.

References

[1] J. H. Holland. *Adaptation in Natural and Artificial Systems*. The University of Michigan Press, 1 edition, 1975.
[2] D. E. Goldberg. *Genetic Algorithms in Search, Optimization and Machine Learning*. Addison Wesley, 1 edition, 1989.
[3] L. Davis. *Handbook of Genetic Algorithms*. Van Nostrand Reinhold, 1 edition, 1991.
[4] S. Kirkpatrick, C. D. Gelatt Jr., and M. P. Vecchi. Optimization by simulated annealing. *Science*, 220:671–680, 1983.
[5] D. B. Fogel and J. W. Atmar. *Proc. 1.st annual Conference on Evolutionary Programming*. Evolutionary Programming Society, 1992.
[6] J. R. Koza, editor. *Genetic Programming II*. The MIT Press, 1994.
[7] J. R. Koza, F. H. Bennett III, D. Andre, and M. A. Keane, editors. *Genetic Programming III*. Morgan Kaufmann Pub., 1999.
[8] J. Kennedy and R.C. Eberhart. Particle swarm optimization. In *Proceedings of IEEE the International Conference on Neural Networks*, volume 6, pages 1942–1948, 1995.
[9] Ryan Forbes and Mohammad Nayeem Teli. Particle swarm optimization on multi-funnel functions.

[10] C.Ryan, J.J.Collins, and M.O'Neill. Grammatical evolution: Evolving programs for an arbitrary language. In *Proceedings of 1st European Workshop on Genetic Programming*, pages 83–95. Springer-Verlag, 1998.
[11] C.Ryan and M.O'Neill. Crossover in grammatical evolution: A smooth operator? In *Proceedings of the European Conference on Genetic Programming*, pages 149–162. Springer-Verlag, 2000.
[12] C.Ryan and M.O'Neill. *Grammatical Evolution: Evolutionary Automatic Programming in an Arbitrary Language*. Springer-Verlag, 2003.
[13] Hallard T Croft, Falconer Kenneth J., and Guy Richard K. *Unsolved Problems in Geometry*. Springer-Verlag, 1991.
[14] J. Melissen. Packing 16, 17 or 18 circles in an equilateral triangle. *Discrete Mathematics*, 145:333–342, 1995.
[15] Erich Friedman. Packing unit squares in squares: a survey and new results. *The Electronic Journal of Combinatorics*, DS7, 2005.
[16] D. S. Liu, K. C. Tan, S. Y. Huang, C. K. Goh, and W. K. Ho. On solving multiobjective bin packing problems using evolutionary particle swarm optimization. *European Journal of Operational Research*, 190(2):357 – 382, 2008.
[17] Chen Zhao, Liu Lin, Cheng Hao, and Liu Xinbao. Solving the rectangular packing problem of the discrete particle swarm algorithm. In *Business and Information Management, 2008. ISBIM '08. International Seminar on*, volume 2, pages 26 –29, 2008.
[18] Chuan He, Yuan-Biao Zhang, Jian-Wen Wu, and Cheng Chang. Research of three-dimensional container-packing problems based on discrete particle swarm optimization algorithm. In *Test and Measurement, 2009. ICTM '09. International Conference on*, volume 2, pages 425 –428, dec. 2009.
[19] P. Thapatsuwan, J. Sepsirisuk, W. Chainate, and P. Pongcharoen. Modifying particle swarm optimisation and genetic algorithm for solving multiple container packing problems. In *Computer and Automation Engineering, 2009. ICCAE '09. International Conference on*, pages 137 –141, march 2009.
[20] M. Clerc. The swarm and the queen: towards a deterministic and adaptive particle swarm optimization. In *Proceedings of 1999 Congress on Evolutionary Computation*, volume 3, pages 1951–1957, 1999.

This page intentionally left blank

On the efficiency of bionic optimisation procedures

S. Gekeler, R. Steinbuch & C. Widmann
Reutlingen Research Institute, Reutlingen University, Germany

Abstract

Bionic optimisation strategies have proven to be efficient in many applications especially if there are many local maxima to be expected in parameter spaces of higher dimensions. In structural mechanics, the central question is whether one particular procedure is to be preferred generally or if there are different problem types where some procedures are more efficient than others. Evolutionary optimisation with some sub-strategies, particle swarm optimisation, and neural nets along with hybrid approaches that couple the aforementioned methods have been investigated to some extent. These approaches are not uniquely defined, but rather imply many variants regarding the definition and selection of next-generation members, varying parameters of the underlying processes and the criteria to switch the strategy. To measure the performance of the different approaches some simple test examples have been used. The indicator of the procedures performance was the number of individuals which needed to be studied in order to come up with a satisfactory solution. As our main concern was about problems with many optimisation parameters, artificial neural nets do not show sufficient convergence velocities in our class of optimisation studies. Evolutionary optimisation, its subclass of fern optimisation and particle swarm optimisation prove to be of comparable power when applied to the test problems. It should not be disregarded that for all these approaches some experience about the optimisation parameters has to be gathered. In consequence, the total number of runs or individuals necessary to do the final optimisation is essentially larger than the number of runs during this final optimisation. Good initial proposals prove to be the most important source for all optimisation processes.
Keywords: bionic optimisation, evolutionary optimisation, particle swarm optimisation, performance, structural mechanics.

WIT Transactions on The Built Environment, Vol 125,
www.witpress.com, ISSN 1743-3509 (on-line)
doi:10.2495/OP120221

1 Introduction

Optimisation deals with the modification of free parameters in given entities in order to come up with better values for given objectives or goals. In structural mechanics optimisation is often applied by the varying design data, e.g. the dimensions of a structure to improve the goal, e.g. to minimize the mass of a part or system or to reduce the energy consumption under service conditions.

The term "Bionic Optimisation" covers all the methods related to natural phenomena by which better variants of a given design are found. This implies that most natural processes use optimisation to adapt, survive and reproduce at given environmental conditions by better adapting to the situation. As there are infinite variants of applying this to technical problems, a strong classification of the observed phenomena is required in order to provide some understanding of the optimisation processes.

1.1 Terms and definitions

Before dealing with the different bionic optimisation strategies, some terms and definitions will help establish a common language. Care should be taken when reading papers by different authors or schools, as one term may be used for different subjects. Most authors accept that for an optimisation:

- We need a given *goal* or *objective z.*
- The objective z depends on a set of *free parameters* $p_1, p_2, \ldots p_n$.
- There are defined *limits* and *constraints* on the parameters values.
- *Restrictions* of the parameter combinations or of derived data like stresses or displacements exclude unacceptable or unfeasible solutions.
- We want find the *maximum* (or *minimum*) of $z(p_1, p_2, \ldots p_n)$.

Some discussion of the terms helps to better understand the following process.

- The *objective* or *goal* must be uniquely defined. We may not change the definition of the goal as this poses a new question and requires a new optimisation process.
- We need to find all parameters and their acceptable *value ranges* we might modify during the optimisation studies.
- The *parameter range* is the span of the free parameters' values given by lower and upper limits.
- The fewer free parameters we need to take into account, the faster the optimisation advances. Consequently, accepting some parameters as constant reduces the dimension of the solution space and accelerates the process.
- Restrictions like unacceptable system responses or unfeasible geometry must be taken into account. But occasionally restrictions limit the ranges of parameters to be searched. Such barriers have the potential to prevent the optimisation process from entering interesting regions.
- Finding the maximum of $z(p_1, p_2, \ldots p_n)$ is the same process as finding the minimum of the negative goal $-z(p_1, p_2, \ldots p_n)$. In consequence, there is no need to distinguish between the search of maxima or minima.

1.2 Gradient or derivative based optimisation

Gradient or derivative based optimisation methods are the most popular ways to find improvements of given situations. From an initial position, the derivatives of the objective $z(p_1, p_2, \ldots p_n)$ wrt. The free parameters are determined. Moving along this gradient has the tendency to yield local maxima in a small number of steps, as long as the search does not start to far away from the local maximum.

1.3 Bionic optimisation strategies

Bionic optimisation may be defined by many different approaches. Here we deal with some of the most commonly accepted classifications without taking into account all the many sub-classifications that might be found in the literature. The central approaches we are going to compare are

- Evolutionary Strategy (ES) [1, 2] - where paired or crossed parents have children by the combination and mutation of their properties. These children, or some of them, are parents in the next generation (Figure 1).

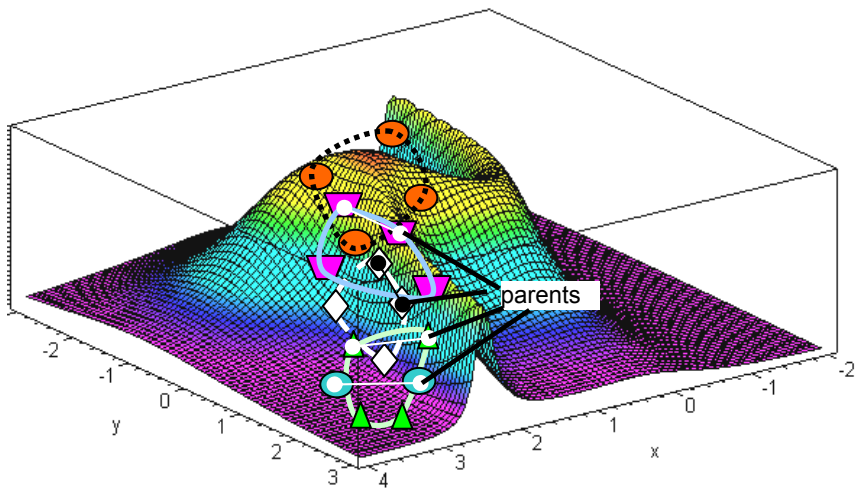

Figure 1: Evolutionary optimisation: 2 parents 4 kids.

- Fern Strategy (FS) - which may be regarded as a simplification of evolutionary optimisation. Individuals have offspring by mutation only but not by crossing properties with other members of the parent generation.
- Particle Swarm Optimisation (PSO) [3, 4] - where a population drifts through the possible solution space. The swarm's coherence is given by simple rules about the velocity of the individuals (Figure 2).
- Artificial Neural Nets (ANN) [6–8] - where training of the net yields an understanding of the solution space and allows the prediction of the system's response to given input. As ANN are not very efficient when applied to problems with many free parameters, we do not discuss them here [8].

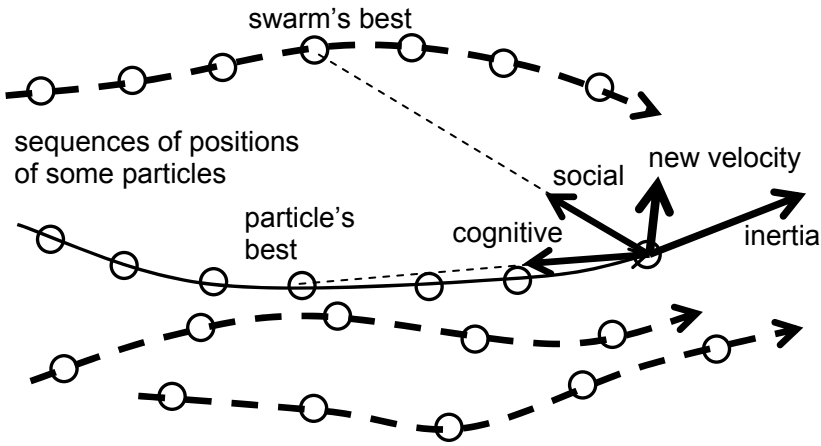

Figure 2: PSO, new velocity components of a particle.

1.4 Measuring the efficiency of procedures

To quantify the efficiency of the different optimisation strategies, we have to introduce a measure that allows us to uniquely define the amount of work required to achieve a predefined quality. From some experience we propose to use the number of individuals to be analysed before coming close to an accepted good value. This requires the knowledge of what a good solution would be, which is generally not known as soon as we start studying new problems.

1.5 Violation of boundary conditions

In all sequences of parameter sets that are based on random input, violations of the restrictions or boundary conditions may occur. Some problems are related to the fact that parameter combinations cause unfeasible geometries. Exceeding limits on physical responses, e.g. maximum stress or displacement have to be taken into account as well. There are different ways to deal with these inacceptable parameter sets.

The easiest way is to *remove all unacceptable individuals* from the list and to continue to produce members of the respective set until the required number of acceptable individuals is found. There is no reason not to use this selection type unless the cost of a specific function evaluation is too high to produce a number of individuals that may be essentially larger than the number of individuals required for the optimisation process.

Another way to keep the population near to the feasible range is to *punish all violation* of the given restrictions. A penalty multiplier weights the goal by the intensity of the violation. In consequence, punished individuals are less attractive for further reproduction, while the non-punished individuals have better chances to reproduce.

A third among many other ideas is to *fix the parameters* of the individual in violation to the border of the allowable space. This may be easily done for geometric input, but can be difficult if derived values like stresses or displacement are in question. In such cases, a reduction of the difference from a good individual's data may be used. If the parameters change less, the objective and the derived values may change less as well, so the violation may be avoided. We restrict our present study to the use of penalty functions for violations of the restrictions. The geometric input is set to the minimum or maximum value, if the randomly produced data exceed the respective limits. For PSO, we invert the particle's old velocity, if it violates given limits in addition to the penalty value. This combined approach has the advantage of simple applicability.

1.6 Hybrid strategies

In order to accelerate the optimisation process, it is not uncommon to use different strategies and to switch between them. This may be very efficient in many cases. We could start by using evolutionary optimisation so as to cover a region of the solution space and then change to particle swarms as soon as we feel we have reached the region of the best proposals [4]. During this study, where the main concern is about measuring the speed and efficiency of the different strategies, we avoid these hybrid methods, as their inclusion would lead to a large and confusing set of combinations and corresponding accelerations of the optimisation process.

2 Application of bionic optimisation strategies

The description of the approaches in section 1.2 needs to be improved upon to impart a qualified understanding of the studies.
- *Individuals* are the different elements of the parents and children sets.
- *Generation* is one step in the evolutionary processes, given by a set of parents.
- *Mutation* is the modification of an individual's parameters [2].
- The *mutation radius* is the maximum change of a parameter's value in a mutation step.

There are many other terms used in conjunction with bionic optimisation. As there is no generally accepted vocabulary, users are advised to check meanings carefully when reading papers from different authors [1, 2].

2.1 Evolutionary Strategy (ES)

In Evolutionary Optimisation two parents have one offspring by combining the properties of their DNA, here the values of the free parameters. This crossed DNA is subject to some random modification, the mutation. Some of the children will be better suited to adapt to the environmental challenges. Their chance to survive is superior to their siblings, so their genetic code becomes

dominant within the population. Therefore, these better children will be the next generation's parents. Some important things to note are:

- The *number of parents* should be sufficiently large to cover some or many possible parameter combinations, e.g. 0.5–5 times the number of parameters.
- The *number of children* should be 2–5 times the number of parents.
- *Pairing* selects two individuals to produce one common child.
- Should the *parents survive* to be parents in the next generation as well or not? Both approaches have their advantages and disadvantages.
- *Crossing*, the way by which two parents define the properties of one common child, and *mutation* may happen in different ways [2].
- The mutation radius may change during the course of the study
- *Selection* determines which Children of the current population (including the parents or not) should be the parents of the next generation.

ES tends to converge to the best solution if there are sufficiently large numbers of parents, children and generations and if the mutation radius is rather large. The number of individuals to be studied may become very large if the values driving the process are not set in a favourable range. Figure 3 plots the history of the goal of the three best and the worst parent for example F3 (cf. section 3.1).

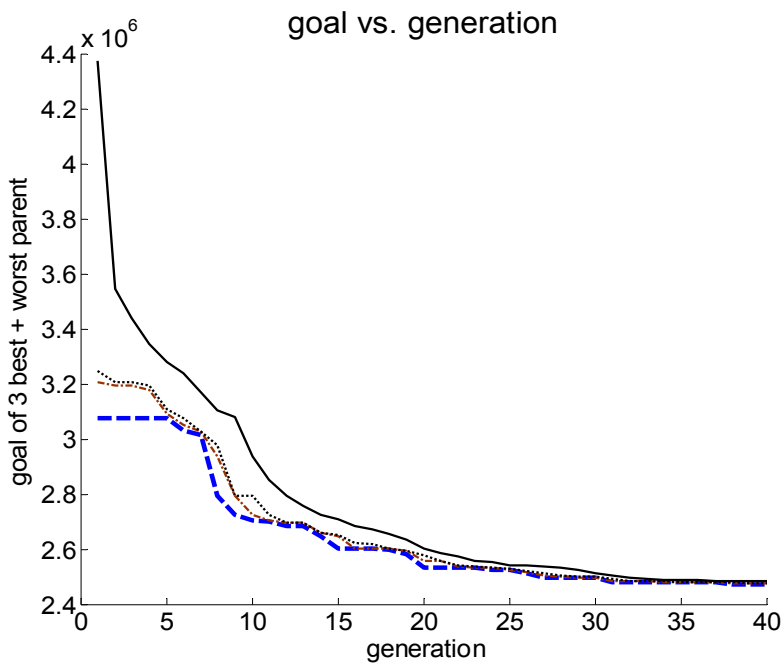

Figure 3: History of an evolutionary optimisation.

2.2 Ferns Strategy (FS)

Fern Optimisation is derived from the fact that ferns reproduce from the spores of one single parent. These spores do not have the same genetic properties as the parent. A certain mutation happens as in all duplication of the DNA.

- We define a limited number of initial designs - the parents - each given by a specific set of free parameters $p_1, p_2, \ldots p_n$.
- Each parent has a certain number of children, which are defined by a random mutation of their parent's parameters.
- This mutation radius may decrease during the course of the study.
- The best of the children will be the next generation's parents.
- This process is repeated for a certain number of generations.
- Sequences of parents and children which fail to come up with relatively good results are removed from the population to accelerate the process.
- The best individual of all offspring is the proposed optimum of the process.

As the solution space increases in size it becomes less probable that the coverage of the initial parts is sufficient to find very good designs. For smaller dimensions, FS is able to provide interesting results while remaining very easy to implement.

2.3 Particle Swarm Optimisation (PSO)

Particle Swarm Optimisation [3, 4] follows the observation that many groups of living beings have a tendency to behave like a complex being itself. The basic assumption of PSO is that the individuals know their position and velocity. In addition, they know where their best position during the process has been, and where the swarm's best position in the parameter space has been Then the process is defined by the following (c.f. Figure 2):

- Each individual continues in its direction of travel: the inertia tendency.
- It tries to return to the best position it ever assumed: the cognitive tendency.
- It tries to approach the best position for all individuals: the social tendency.
- These tendencies are weighted by some specific (c) and scalar or vector random (r) values and added to the inertia vector [4, 5].

$$\mathbf{v}_{new} = c_v \mathbf{v}_{old} + c_{cog} r_{cog} \mathbf{d}_{cog} + c_{soc} r_{soc} \mathbf{d}_{soc} \tag{1}$$

- The particle's position in the next step is found by adding the new velocity to its old position. This corresponds to the definition of a new generation in the other approaches.

$$\mathbf{x}_{new} = \mathbf{x}_{old} + \mathbf{v}_{new} \tag{2}$$

PSO has proven to be very successful if an appropriate set of particles and velocity-weighting factors $\{c_v, c_{cog}, c_{soc}\}$ has been used. Unfortunately, PSO has the tendency to stick to local minima if these parameters are not well chosen [5]. Figure 4 compares the results found at test example F3 for different weighting factors, c_v, and c_{soc} while the cognitive weight was $c_{cog} = 0.1$. There is a valley of efficient combinations of the coefficients. This valley is limited by steep hills indicating less efficient progress and weaker goals achieved by the PSO studies.

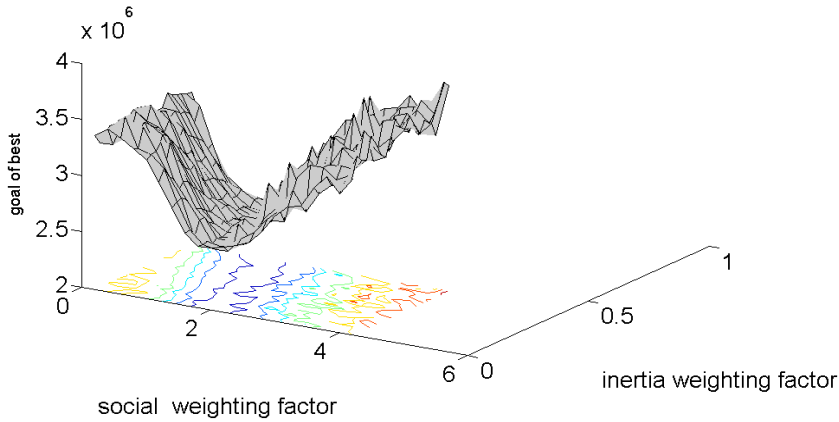

Figure 4: Dependency of the power of PSO of weighting factors for model F3.

3 Comparing the efficiency of bionic optimisation strategies

Optimisation is an expensive and time consuming process. We need to understand which procedure and which combinations of parameters may lead to a good and acceptable result within a reasonable amount of time.

3.1 Test examples

Figure 5 depicts the 5 test examples used while Table 1 summarizes their data. We want to minimize the mass of the frames by varying the rods' cross sections without exceeding their maximum stresses and displacements. The grid size of the examples is 1000 mm except for example 2 where the grid size is 360 inches. Example F2 used imperial units (in, kip) the other frames use mm and Newton.

Table 1: Data of test problems.

frame	params	grid size	Amax / Amin	E-Mod	σ_{max}	d_{max}
F1	6	1000 mm	600 / 20 mm^2	200 GPa	120 MPa	0.5 mm
F2	10	360 inch	35 / .1 inch^2	10 Msi	25 ksi	2.0 inch
F3	13	1000 mm	400 / 20 mm^2	200 GPa	50 MPa	0.5 mm
F4	58	1000 mm	400 / 20 mm^2	200 GPa	100 MPa	2.0 mm
F5	193	1000 mm	600 / 20 mm^2	200 GPa	450 MPa	20 mm

params: # of rods in frame
grid size: horizontal or vertical distance between the nodes
Amax, Amin: maximum and minimum allowed cross section area of the rods
E-Mod: Young's modulus
σ_{max}: maximum allowed stress in rod
d_{max}: maximum allowed displacement of nodes

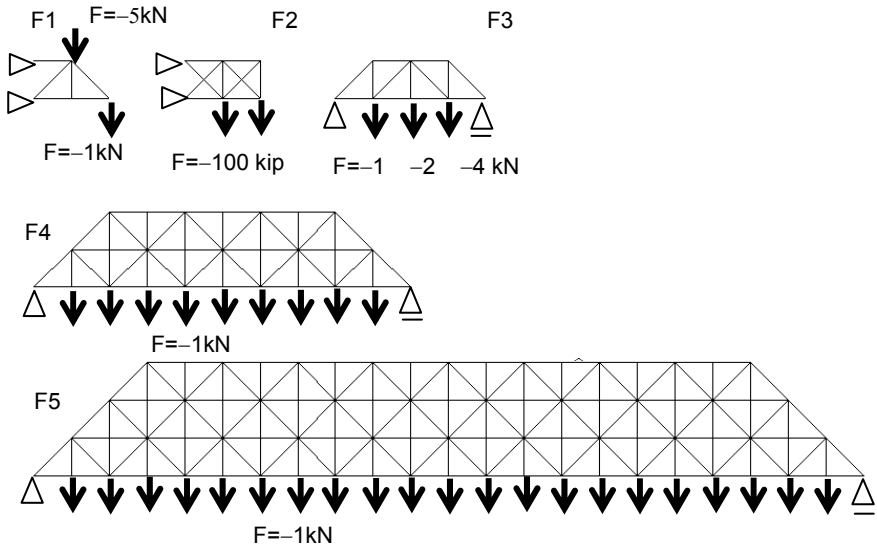

Figure 5: Test frames with loads and supports.

To come up with comparable results, we did a series of 20 loops for each problem and each strategy to avoid having only one or few very good or very bad results. On the other hand, the parameters we used were based on some experience with the underlying problems, so the number of runs presented does not come from naïvely starting a procedure, but includes some preliminary work which is impossible to quantify.

3.2 Input and results of the test examples

Table 2 lists the inputs of the test runs used. Table 3 and Figure 6 (individuals per loop) summarize the results of the test runs. The most important data are the number of individuals analysed to find a sufficient good design labelled as 'Individuals [1000]'. The number given multiplied by 1000 gives the total number of individuals required to find the proposed design. *mean* and *stddev* (standard deviation) and *best* are related to the results of the 20 runs. The ratio of the difference between the best and the average result divided by the standard-deviation (*reldev*) gives an idea of the stability of the strategy.

3.3 Interpretation of the results

ES, FS and PSO prove to be of a comparable efficiency when applied to the 4 smaller problems (F1, F2, F3, F4). Figure 6 indicates that there might be a nearly linear relation between the number of optimisation variables and the individuals required to find good proposals. For the largest problem F5 FS displays a performance that is essentially weaker than ES and PSO. ES and PSO seem to be

Table 2: Input parameters used.

2.1. ES

model	parents	kids	mut.rad.max	mut. Rad. min	generations
F1	10	20	.5	.05	60
F2	5	10	.5	.05	40
F3	5	10	.5	.05	50
F4	50	100	.5	.05	100
F5	100	200	.5	.05	200

2.2. FS

model	parents	kids/par.	mut.rad.max	mut. Rad. min	generations
F1	10	5	.5	.05	100
F2	10	4	.5	.05	50
F3	20	5	.5	.05	100
F4	100	5	.5	.05	200
F5	200	5	.5	.05	200

mutation radius reduced for ES and FS:
0% - 25% of generations: $r_{mut} = .50$
25% - 50% of generations: $r_{mut} = .20$
50% - 75% of generations: $r_{mut} = .10$
75% - 100% of generations: $r_{mut} = .05$

2.3.PSO

model	particles	generations
F1	10	30
F2	10	40
F3	20	80
F4	50	200
F5	800	70

Weighting factors:
c_v,= 0.08, c_{cog},= 0.005 c_{soc}= 2.0

of comparable power when applied to the problem class which we discuss. FS shows promising results if the number of parameters is not too large, but the random search in high dimensional spaces becomes less successful. The scatter indicator *reldev* proposes that PSO has a more stable tendency to find solutions near the best while ES and FS show a larger range after the 20 runs.

Some knowledge may be gleaned from the results of these series of studies. Foremost that optimisation, especially bionic optimisation, is a process that consumes large amounts of time and computing power.

The results presented in section 3.2 would not have been found without a large number of preliminary studies providing experience in the field of optimisation of frames.

The input characteristics used in the test runs is derived from these preliminary studies. For example the selection of the 3 weighting factors {c_v, c_g, c_s} for the PSO required some 100 000 runs (Figure 4). The proposal of the reduction of the mutation range for ES and FS is the result of many studies as well. The proposal to use a number of initial parents in the size of free variables for ES and PSO is based on many studies, as well as the idea to use a large number of initial parents and a small number of children in FS.

Table 3: Results of 20 optimisation runs per problem.

strategy	model	mean	stddev	best	reldev	Individuals [1000]
ES	F1	1.62e6	.716e3	1.62e6	1.50	12
	F2	6.33e4	4.50e3	5.47e4	1.90	8
	F3	2.56e6	6.99e4	2.48e6	1.11	20
	F4	1.03e7	4.18e5	8.65e6	3.92	200
	F5	1.98e7	1.07e6	1.58e7	3.65	800
FS	F1	1.66e6	4.49e4	1.62e6	0.81	28
	F2	6.39e4	4.43e3	5.45e4	2.09	25
	F3	2.50e6	2.29e4	2.47e6	1.19	46
	F4	9.91e6	2.77e5	9.39e6	1.86	189
	F5	2.33e7	4.18e5	2.25e7	2.15	2570
PSO	F1	1.65e6	1.71e4	1.62e6	1.61	6
	F2	5.87e4	5.61e3	5.15e4	1.27	8
	F3	2.50e6	2.53e4	2.48e6	1.02	32
	F4	8.90e6	1.68e5	8.68e6	1.22	200
	F5	1.54e7	0.18e4	1.53e7	1.70	1120

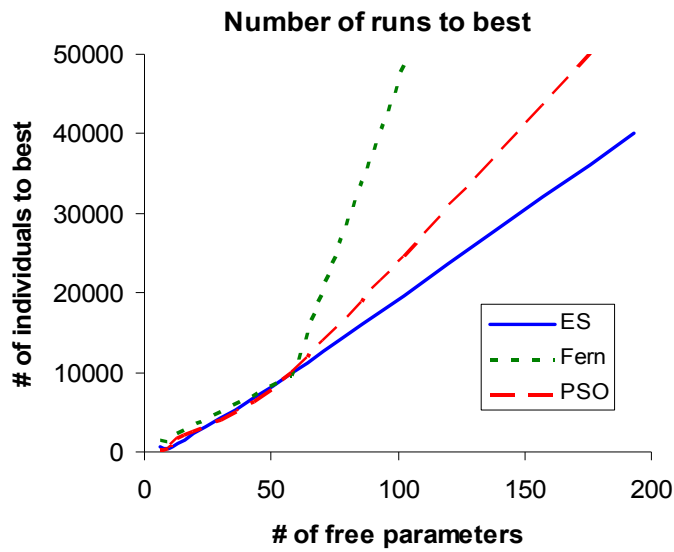

Figure 6: Efficiency of optimisation strategies.

One central fact about all optimisation may be learned from Figure 3. If there is a good initial design the number of optimisation runs to be done may decrease significantly. If an experienced engineer proposes an initial design with a goal of

e.g. 2.6 10^6, we need only 20 generations or 50% of the workload required to solve the task with a random initial design.

4 Conclusions

The quality of the initial proposals is the most important component of any optimisation. If experienced and motivated engineers propose designs that are close to the optimal ones there is a good chance that at least a local optimum will be found which is not too far away from the best solution possible. If we are close to good proposals, gradient methods will improve the parameters in short time and at reasonable effort.

As soon as we doubt that our initial designs are close to the optimal ones, ES or PSO have the capacity to propose of better designs. Nevertheless, the number of function evaluations may be large. Which of the two is to be preferred must be decided with some preliminary test. Often, the particle swarm shows a faster tendency towards the assumed best values, but some examples like those shown in Figure 4 indicate that the swarm might have the tendency to stick to local maxima like gradient methods.

Switching to gradient optimisation if a maximum is approached closely is always an interesting option. But experience has to be gathered there as well.

In every case, the optimisation of large problems is a time and resources consuming process. There is no way to avoid the evaluation of many individual solutions and there is no guarantee that the absolute best solution will be found at all.

Acknowledgements

Part of this work has been supported by the federal government and some companies that we have been working with. We gratefully acknowledge their financial and engineering support.

References

[1] Rechenberg, I. *Evolutionsstrategie '94*, Frommann-Holzboog, Stuttgart, (1994).
[2] Steinbuch, R. Successful Application of Evolutionary Algorithms in Engineering Design. *Special issue Vol 7, Journal of Bionic Engineering 7 Suppl* (2010), 199-□210.
[3] Coelho, L. D. S. and Mariani, V. C. Particle swarm optimization with quasi-Newton local search for solving economic dispatch problem, in *Proceedings—IEEE International Conference on Systems*, *Man and Cybernetics* (2007).
[4] Plevris, V., Papadrakakis, M. A Hybrid Particle Swarm-Gradient Algorithm for Global Structural Optimization. *Computer-Aided Civil and Infrastructure Engineering 26* (2011) 48–68.

[5] Perez, R. E. and Behdinan, K. (2007b), Particle swarm optimization in structural design, in F. T. S. Chan and M. K. Tiwari (eds.), *Swarm Intelligence: Focus on Ant and Particle Swarm Optimization*, Itech Education and Publishing,Vienna, Austria, pp.373–94.
[6] Berke L, Patnaik SN, Murthy PLN. Optimum design of aerospace structural components using neural netw*orks. Comput Struct 48 (1993): 1001–1010.*
[7] *Lagaros, N.D., Pap*adrakakis, M. Learning improvement of neural networks used in structural optimization. *Adv. in Engineering Software* 35 (2004) 9–25.
[8] Widmann, Ch.: *Strukturoptimierung mit Neuronalen Netzen*, Master Thesis, Reutlingen University, (2012).

This page intentionally left blank

Author Index

This page intentionally left blank

System Identification for Structural Health Monitoring

***I. TAKEWAKI**, Kyoto University, Japan; **M. NAKAMURA**, Technical Research Institute, Obayashi Corporation, Japan and **S. YOSHITOMI**, Kyoto University, Japan*

System Identification for Structural Health Monitoring is the first textbook on smart techniques of mechanical system identification using records from limited locations. The techniques explained in the book are based on rich content published in international journal papers by the authors, to which have been added introductory explanations to make the material accessible for a broad class of readers.

System identification (SI) techniques play an important role in investigating and reducing gaps between the constructed structural systems and their structural design models and in structural health monitoring for damage detection. A great amount of research has been conducted in SI.

There are two major branches of SI: modal-parameter and physical-parameter. The former is appropriate for identifying the overall mechanical properties of a structural system and exhibits stable characteristics in implementation. While the latter is important from different viewpoints, e.g. enhancement of reliability in active controlled structures or base-isolated structures, its development is limited due to the requirement for multiple measurements and the necessity of complicated manipulation. A mixed approach is often used in which physical parameters are identified from the modal parameters obtained by the modal-parameter SI. However, a sufficient number of modal parameters must be obtained in order for the unique and accurate identification of the physical parameters to take place. This requirement is usually hard to satisfy.

In spite of the importance of damping in the seismic-resistant design of buildings, it does not appear that its identification techniques have been developed sufficiently. Furthermore it is believed in general that the acceleration records for all the floors above a specific story are necessary in order to evaluate the story shear force that is required for stiffness-damping evaluation. This instrumentation may be unrealistic in multi-storied buildings.

To overcome this difficulty, the authors explain a unique system identification theory for a shear building model. They show that unique identification of story stiffnesses and viscous damping coefficients is possible when acceleration records at the floors just above and below a specific story are available.

ISBN: 978-1-84564-628-8 e-ISBN: 978-1-84564-629-5
Published 2011 / 272pp / £130.00

WITPRESS ...for scientists by scientists

Bridge Aeroelasticity

Sensitivity Analysis and Optimal Design

***J.A. JURADO, S. HERNÁNDEZ, F. NIETO** and **A. MOSQUERA**, University of A Coruña, Spain*

Long-span suspension and cable-stayed bridges are currently of great interest, a fact reflected in an ever-increasing number of bridges being built over bays, straits and estuaries. To address the need for more information on this type of structure, the authors have produced this book describing the current capability for analysis and design of such structures.

The book brings together cogently information that hitherto could only partially be found scattered in technical magazines, including the historical evolution and recent installations of long-span suspension and cable-stayed bridges. It discusses wind-induced phenomena as one of the main perils such structures have to withstand, specifically the instability known as flutter, and describes in a very comprehensive manner the most advanced methods to evaluate bridge safety under wind flow. Finally, it is the first book to present methodology for analysing the flutter speed of bridges both during and after construction. The authors' use of numerical optimisation methodologies for improving bridge design had never been considered before for this class of structure.

The book will be of interest to bridge design engineers and researchers, in academia, in engineering design and construction firms, and in government transportation departments.

Contents: Aeroelastic analysis and design optimisation of cable-supported Bridges; Cable-supported bridges since 1940: The Tacoma effect; Methodologies of flutter analysis for cable-supported bridges; Flutter analysis of suspension bridges during construction; Flutter analysis of completed cable-supported bridges; Sensitivity analysis of eigenvalue problems; Analytical sensitivity analysis of free vibration problems; Sensitivity analysis of flutter response for cable-supported bridges; Sensitivity of flutter response for suspension bridges under construction; Flutter response sensitivity of completed cable-supported bridges; A formulation of optimisation in bridge aeroelasticity; Optimisation of suspension bridges with aeroelastic and kinematic constraints.

High Performance Structures and Materials, Vol 10
ISBN: 978-1-84564-056-9 e-ISBN: 978-1-84564-334-8
Published 2011 / 368pp / £140.00

Structures Under Shock and Impact XII

Edited by: ***N. JONES****, The University of Liverpool, UK and* ***C.A. BREBBIA****, Wessex Institute of Technology, UK*

Of interest to engineers from civil, military, nuclear, offshore, aeronautical, transportation and other backgrounds, this book contains the proceedings of a well-established biennial conference on the subject that was first held in 1989.

The shock and impact behaviour of structures presents challenges to researchers not only because it has obvious time-dependent aspects, but also because it is difficult to specify the external dynamic loading characteristics and to obtain the full dynamic properties of materials. It is crucial that we find ways to share the contributions and understanding that are developing from various theoretical, numerical and experimental studies, as well as investigations into material properties under dynamic loading conditions. This book helps to meet that need.

Topics covered include: Impact and Blast Loading Characteristics; Protection of Structures from Blast Loads; Energy Absorbing Issues; Structural Crashworthiness; Hazard Mitigation and Assessment; Behaviour of Steel Structures; Behaviour of Structural Concrete; Material Response to High Rate Loading; Seismic Engineering Applications; Interaction Between Computational and Experimental Results; Innovative Materials and Material Systems; Fluid Structure Interaction.

WIT Transactions on The Built Environment, Vol 126
ISBN: 978-1-84564-612-7 e-ISBN: 978-1-84564-613-4
Forthcoming 2012 / apx 400pp / apx £172.00

This page intentionally left blank